FUNDAMENTAL CHARACTERISTICS AND BEHAVIOUR OF REINFORCED CONCRETE BRIDGE PIERS SUBJECTED TO REVERSED CYCLIC LOADING

By

FARBOD SAADAT

A Thesis
Presented to the University of Manitoba
in Partial Fulfillment of the
Requirements for the Degree of
M.Sc.
in the Department of Civil Engineering

Winnipeg, Manitoba

APRIL, 1984

FUNDAMENTAL CHARACTERISTICS AND BEHAVIOUR OF REINFORCED CONCRETE BRIDGE PIERS SUBJECTED TO REVERSED CYCLIC LOADING

by

Farbod Saadat

A thesis submitted to the Faculty of Graduate Studies of the University of Manitoba in partial fulfillment of the requirements of the degree of

MASTER OF SCIENCE

TABLE OF CONTENTS

ABSTRACT

A total of sixteen large-scale reinforced concrete specimens without web reinforcement were tested to study the behaviour of typical bridge piers subjected to deflection reversals large enough to cause extensive yielding of the longitudinal reinforcement. The different parameters considered included shear span-to-depth ratio, percentage of longitudinal reinforcement, frequency of the applied load, and axial compressive stresses. Each specimen was subjected to three cycles of deflection reversals, in increments equal to the yield deflection. The deflection was increased until the load-resisting capacity of the specimen was less than the yield load, which constituted failure of the specimens for the purpose of this program.

Based on parametric studies of the experimental results, a nondimensional factor was introduced to describe the fundamental behaviour of bridge pier structures within the described category. The proposed characteristic factor was used to derive expressions which would predict the ductility, maximum shear stress, energy dissipation capacity, energy absorption capacity, and the equivalent viscous damping coefficient for such members. Three modes of failure were observed. The modes were classified according to the range of the proposed characteristic factor, parallel to a rational categorization based on the maximum intensity of the applied shear stress.

The effect of the load frequency within the limited ranges considered in this program and the effect of axial compressive stresses on the behaviour of such members were also investigated. Finally,

an expression has been proposed for the prediction of the effective stiffness of the bridge piers subjected to reversed cyclic loading in the post-yielding range.

ACKNOWLEDGEMENTS

This study was carried out in the Department of Civil Engineering at the University of Manitoba with financial assistance from the Natural Sciences and Engineering Research Council of Canada. Dr. T. Higai, Associate Professor, Yamanishi University, Japan, was the principal investigator and in charge of laboratory work. He was assisted by Messrs. H. Ben-Omran, Ed Lemke, M. McVey and B. Turnbull. The comprehensive analysis of data presented in this thesis was carried out under the supervision of Dr. Sami Rizkalla, Associate Professor of Civil Engineering.

LIST OF TABLES

LIST OF FIGURES

NOTATIONS

a	Shear span
a/d	Shear span-to-depth ratio
b	Cross-sectional width
d	Effective depth of the section
d_c	Confined cross-sectional depth
EI	Equivalent flexural stiffness
E_c	Concrete modulus of elasticity
f_D	Damping force
f_s	Spring force
f_t	Concrete tensile strength
f_y	Yield strength of reinforcement
f_{sp}	Concrete splitting strength
f_{su}	Ultimate strength of reinforcement
f'_c	Concrete compressive strength
$f_{s,max}$	Maximum spring force
FR	Load frequency
I	Moment of inertia of the cross-section
I_g	Gross moment of inertia
I_{cr}	Moment of inertia of the cracked transformed section
I_{eff}	Effective moment of inertia
I_w	Work Index
I'_w	Modified Work Index
I''_w	Nonlinear Work Index
$(I''_w)_p$	Predicted Nonlinear Work Index

$I_{w_{ave}}$	Average Work Index
K	Nondimensional characteristic factor
k	Stiffness
M_a	Applied moment
M_{cr}	Cracking moment
n	Modulus ratio
N	Axial compressive load
NED	Normalized Energy Dissipation Capacity
p	Percentage of longitudinal reinforcement
P	Load
P_o	Maximum viscous damping force
P_y	Calculated yield load
P_{max}	Maximum load in the direction of failure
V	Rate of the applied deflection
v_c	Calculated shear strength under monotonic load
v_u	Maximum shear stress
v_y	Shear stress corresponding to yielding of longitudinal reinforcement at maximum moment section
W_a	Energy absorption capacity
W_d	Energy dissipation capacity
W_s	Strain energy stored
X	Displacement
X_{max}	Maximum displacement
μ	Displacement ductility factor
μ_ϕ	Curvature ductility factor
δ	Deflection
δy	Measured yield deflection

δ_u	Maximum deflection before failure
$\frac{\delta}{\delta y}$	Displacement ductility ratio
Δ	Dowel displacement
Δp	Pitch of the deflection increment
ϕ	Stiffness ratio
ϕp	Predicted stiffness ratio
ϕ_t	Measured stiffness ratio
ϕ_u	Curvature at ultimate
ϕ_y	Curvature at yielding of tension reinforcement
σ	Axial compressive stresses
ε_s	Steel strain
ε_y	Yield strain of longitudinal reinforcement
η_o	Axial load factor
η_{eq}	Equivalent viscous damping coefficient
$(\eta_{eq})_{pre}$	Predicted equivalent viscous damping coefficient
$(\eta_{eq})_{exp}$	Measured equivalent viscous damping coefficient
ω	Angular frequency
ω_n	Natural frequency

CHAPTER I

INTRODUCTION

1.1 INTRODUCTION

The behaviour of reinforced concrete building frame structures under reversed cyclic loading has been clarified to a certain extent. However, very little information is available concerning the response of reinforced concrete bridge piers subjected to large deflection reversals. Bridge piers are commonly lightly reinforced in both longitudinal and transverse directions. Unlike beams and columns, they fall into different categories in terms of shear span-to-depth ratio, as related to the percentage of longitudinal reinforcements and level of axial compressive stresses [37].

Failure of bridge piers must be prevented when they are subjected to extreme dynamic loading conditions. This requirement imposes additional demands on the structure to absorb and dissipate energy. Large portions of the imparted energy must be dissipated by inelastic deformation in piers. Thus, the sources of potential brittle failures, such as shear failure, should be prevented.

In order to study the shear behaviour of reinforced concrete bridge piers, a total of sixteen large-scale specimens were tested under large deflection reversals. Different parameters believed to have an influence on their behaviour were considered in this study.

1.2 OBJECTIVE OF THE INVESTIGATION

The main objective of this investigation is to study the shear behaviour of reinforced concrete bridge piers subjected to large

deflection reversals. Specifically, the influence of the following parameters on ductility, shear strength, mechanisms of stiffness degradation and energy dissipation, and modes of failure of reinforced concrete piers are examined:

(1) Shear span to depth ratio, a/d;

(2) Percentage of the longitudinal reinforcement, p;

(3) Load frequency, FR; and

(4) Level of axial compressive stresses, σ

An attempt was also made to derive expressions for prediction of the ductility, maximum shear stress, energy absorption and dissipation capacities based on the previously mentioned parameters. The study attempts to classify the modes of failure and also identify the fundamental characteristics of the bridge piers including damping and stiffness.

1.3 SCOPE OF THIS INVESTIGATION

In order to achieve the objective of this investigation, sixteen large-scale specimens were constructed and tested. Section properties, material properties, and construction details for these specimens were representative of typical bridge piers. The main parameters varied for these specimens were shear span-to-depth ratio, a/d, percentage of longitudinal reinforcement, p, load frequency, and level of axial compressive stresses.

This thesis begins with a comprehensive literature review in Chapter II. Design of specimens, fabrication techniques used in preparation of specimens, material properties, test set-up, loading apparatus, instrumentation and testing procedures are discussed in

Chapter III. The test results and observations for the sixteen specimens are presented in Chapter IV. Chapter V deals with the discussion of the results which leads to the introduction of a nondimensional characteristic factor to describe the fundamental behaviour and different modes of failure of bridge piers. This includes the ductility, strength, stiffness, and damping characteristics of such members. The effect of the load frequency and the presence of the axial compressive stresses on behaviour and ductility are also discussed in this chapter. Chapter VI presents the conclusion of this experimental study.

The instrumentation for each specimen, and data collected during testing, such as loads, deflections, shear strains, longitudinal steel strains, crack patterns, and hysteresis responses are published in a separate volume, Reference [4]. In addition, the detailed calculations of the energy dissipation capacity, work indices, equivalent viscous damping coefficient, and stiffness are contained in another separate volume, Reference [44].

CHAPTER II

LITERATURE REVIEW

2.1 INTRODUCTION

In order to ensure adequate ductility for reinforced concrete structures, sources of potential types of structural brittle failure, such as shear of concrete, should be eliminated. In earthquake design of frame structures, certain regions of the structure are chosen to form plastic hinges to dissipate seismic energy through inelastic deformations without substantial loss of strength. Furthermore, proportions of these members are generally controlled to force these hinges to form in the beams, which is known as the weak-beam-strong-column philosophy. However, in a bridge structure, this type of control may not be possible, since the inelastic deformations occur only in the piers, due to their relative stiffnesses compared to the bridge deck. Therefore, the reinforcement in the piers must be properly anchored and confinement of the concrete may also be required in some cases.

In general, the ductility of a structure depends on the design and locations of the plastic hinge regions in the members which maintain both flexural and shear capacity. Normally, the shear stresses for such members would not produce distress under unidirectional monotonic loading conditions up to failure. However, under repeated and reversed large deformations, shear distress may become evident and limit the ductility of such members. The main objective of this chapter is to study the behaviour of reinforced concrete members in shear. The first part of this chapter deals with static and monotonically increasing

loading conditions and discusses the effect of following parameters on the shear behaviour, including strength, ductility and mode of failure:

(a) shear span to depth ratio (a/d);

(b) longitudinal steel percentage (p); and

(c) axial load.

The second part of this chapter is devoted to the study of the effect of reversed cyclic loading.

2.2 BASIC MECHANISMS OF SHEAR TRANSFER

In general, the appreciation of some of the principal shear mechanisms in reinforced concrete is relatively recent. The main types of shear transfer in reinforced concrete are the following [1]:

(a) shear stress in the uncracked concrete;

(b) interface shear transfer;

(c) dowel action;

(d) arch action; and

(e) shear reinforcement.

The first three types constitute the main shear carrying mechanism for beams with $a/d > 3$, which is commonly known as beam action. However, for beams with $a/d < 3$ the arch action becomes the major shear resistance component. The extent of these mechanisms varies widely for various types of structural elements and the definite evaluation of the contribution of each individual component is as yet only tentative. For example, for rectangular beams without shear reinforcement, after the formation of the inclined crack, the proportion of the shear transferred by various mechanisms could range from

15 to 25% by dowel action, 20 to 40% by the uncracked concrete compression zone, and 33 to 50% by aggregates interlock or interface shear transfer [1,47].

Most modern design procedures assume that the total shear is resisted by the concrete in the compression zone, v_c, and by the vertical stirrups, v_s. However, some recent evidence indicates that the shear carried by the longitudinal steel, known as dowel action, and the interface shear transfer along the crack significantly affect the capacity and mode of failure [13,47].

2.3 FACTORS AFFECTING SHEAR STRENGTH

Many factors influence the shear behaviour and strength of reinforced concrete members. However, only the main parameters will be discussed in this chapter.

2.3.1 Effect of Shear Span-to-Depth Ratio, a/d

The shear span-to-depth ratio has been shown experimentally to be a highly influential factor in establishing shear strength [1,9,26,33]. For a typical rectangular reinforced concrete beam with a given percentage of longitudinal reinforcement, the effect of a/d on the shear capacity can be clearly seen in Fig. 2.1 from [9]. From this figure, four general categories of failure may be established. Each category will be discussed separately as follows:

(a) Deep Beams, $a/d \leq 1$

For a deep beam, shear stress has the predominant effect. After the formation of the cracks, this beam tends to behave like a tied arch. The load is carried by direct compression extending

around the line joining the applied load and the reaction, and by the tension in the longitudinal reinforcement. This tied-arch exhibits considerable reserve capacity. Several modes of failure are possible, such as anchorage failure of the tension reinforcements, crushing failure at the reactions, flexural failure and tension failure of the arch rib by cracking over the support, followed by crushing along the crack, as shown in Fig. 2.2 [50].

(b) Short Beams, $1 < a/d \leq 2.5$

In short beams, the ultimate shear capacity also exceeds the inclined cracking capacity, just as in the case of deep beams. Failure occurs at some load higher than that which caused the inclined crack to form. After the flexure-shear crack develops, the crack extends further into the compression zone as the load increases. It also propagates as a secondary crack toward the tension reinforcement and then progresses horizontally along that reinforcement. Failure eventually results, either by shear tension due to anchorage failure of the longitudinal tension reinforcement, or by shear tension failure as a result of crushing of the concrete in the compression zone at the location of the applied load (Fig. 2.3) [50].

(c) Intermediate Beams, $2.5 < a/d \leq 6$

For intermediate beams, vertical flexural cracks are initially formed and propagate to form flexure-shear cracks. At the sudden occurrence of the inclined crack, the beam is not able to redistribute the load, as in the case of smaller a/d ratios. In other words, the formation of the inclined crack represents the ultimate shear capacity of beams in this category, to which many investigators give the term diagonal tension failure, as shown in Fig. 2.4 from [50]. Reinforced concrete bridge piers generally fall into this category.

bridge piers generally fall into this category.

(d) Long Beams, a/d > 6

The failure of long beams starts with yielding of the tension reinforcement and ends by crushing of the concrete at the section of maximum bending moment, as shown in Fig. 2.5 from [50]. The ultimate strength of the beam is entirely dependent upon the magnitude of the maximum bending moment and is not affected by the magnitude of the shear force.

In order for the beams with reserve capacity to maintain a state of equilibrium, stresses must be redistributed after the formation of the inclined crack. Present knowledge of how the redistribution actually takes place is limited [50]. Therefore, for the design of all but deep beams, the shear capacity is assumed to be reached when the inclined crack forms.

Diagonal cracking strength is directly related to the principal tensile stress, which is a function of the ratio between the flexural tensile stress and the applied shear stress, $\frac{f_t}{v}$. The $\frac{f_t}{v}$ ratio is proportional to the ratio between the applied moment and shear, $\frac{M}{Vd}$, where d is the effective depth of the member [26]. This ratio is also equal to the shear span-to-depth ratio, a/d, where a is the shear span. Thus, the principal tensile stress is directly related to the a/d ratio, as confirmed by others [9,17,26,32,35,40,52].

The effect of the shear span-to-depth ratio, a/d, on the shear strength is shown in Fig. 2.6 for different percentages of longitudinal reinforcement [26]. It is evident that the shear strength increases with the decrease of a/d ratio. This is mainly due to compressive stresses or arch action mobilized with lower a/d ratios. This effect causes the substantial enhancement of ultimate shear

strength of R.C. members with a/d < 2.5 in particular.

A number of semirational expressions developed for predicting the flexure-shear cracking load of R.C. beams conclusively show the importance of a/d (or M/Vd) in diagonal cracking strength [1,25,33,34,36,42,54]. While there is a substantial reserve capacity after development of diagonal tension cracks in deep and short beams, the ultimate shear strength of the intermediate beams, 2.5 < a/d < 6, is essentially equal to diagonal cracking strength and failure occurs almost simultaneously with the formation of the diagonal tension crack [1]. Such failures are sudden, as confirmed by many experimental studies [9,26,31,33,41,54].

2.3.2 Effect of Percentage of Longitudinal Reinforcement, p

Flexural strength of R.C. members is most dependent on the percentage of longitudinal reinforcement, p. While the decrease of p reduces the flexural capacity of any given under-reinforced section sharply, it increases the ductility factor drastically. A high steel content, however, will mean narrower flexural cracks at a given load and this will enable aggregate interlock and dowel action to carry a larger load.

Kani [26] investigated the effect of p on modes of failure and shear strength of reinforced concrete beams. The test results of four series of beams with an ultimate concrete compressive strength of 26.2 MPa is given in a 3-D coordinate system in Fig. 2.7 from [26]. In this figure, the ratio between the ultimate moment capacity, M_u, and the flexural moment capacity of a member, M_{fl}, is related to the percentage of longitudinal reinforcement, p, and to the span-to-depth

ratio, a/d. It can be seen that the mode of failure is mainly dependent on the a/d ratio, but the relative strength valley will be shallower in the case of a smaller steel content, p. The valley of diagonal failure disappears completely for beams with $p \leq 0.5\%$, which means the failure of such beams is controlled by their flexural strength. With increasing values of p, the valley of diagonal failure deepens rapidly, with its range always limited by the two characteristic boundary points, D and T, where D denotes the transition point from flexural to compression shear failure, and T symbolizes the transition point between diagonal tension and flexural failure. If the a/d axis is considered, it can be seen that the reduced beam strength due to shear failure occurs only between a/d equal to D, which is nearly equal to a constant of 1.0, and the transition point, T, which varies with p. The minimum value of relative bending moment at failure was obtained in the vicinity of the shear span-to-depth ratio, $\frac{a}{d}$, of 2.5, and this was not influenced by p. Thus, in conclusion, the beam strength varies between 50 and 100% of the flexural capacity of the cross-section, and the exact strength depends on the combination of values of a/d and p.

The ductility of such members is inversely proportional to the percentage of the longitudinal reinforcement [38]. However, the addition of the compression steel will increase the ductility due to the reduction of the compression zone depth.

Mattock [32] studied the effect of longitudinal steel percentage, p, on the diagonal tension cracking. The test results indicated that the difference between the shear stresses required to initiate flexural cracks and those required to form diagonal cracks

is related to the transformed area of tension steel, np, as shown in Fig. 2.8 from [32]. The intensity of the principal stress is dependent on the depth of penetration of the flexural crack. The reduction of the compression zone depth will result in the increase of the principal stress for a given applied shear. The flexure crack will penetrate almost up to the neutral axis, the depth of which is a function of np. Therefore, the increase in the transformed area of tension steel, np, leads to the increase of the depth of the compression zone and, consequently, decreases the magnitude of the principal tensile stresses for a given applied load. Conversely, the load required to cause diagonal tension cracking increases with the increase of np. However, when the percentage of longitudinal reinforcement, p, is very small, the shear strength drops drastically [26, 32], as shown in Fig. 2.6.

For the design of reinforced concrete members, in order to calculate the concrete contribution, v_c, to shear resistance, the effect of p has been studied extensively. Tests [7,26,41] and analyses [1,32] have shown that the shear strength of R.C. members drops significantly if the longitudinal steel ratio, p, is decreased below 1.0 to 1.5% as shown in Fig. 2.9. For the analysis of the strength of beams a number of equations are proposed for the concrete contribution, v_c. Mattock [32] and Zsutty [54] have proposed two acceptable equations, while Rajagopalan and Ferguson [43] introduced the following equation based on the experimental results, as shown in Fig. 2.9 from [43].

$$v_c = (0.8 + 100\ p)\ \sqrt{f'_c} \leq 2.0\sqrt{f'_c}\ (\text{psi}) \qquad (2.1)$$

in which v_c is the nominal shear strength at which the initially formed flexural cracks will propagate into diagonal shear cracks.

Recently, Okamura and Higai [17] proposed a design equation for shear strength of reinforced concrete beams without web reinforcement. The proposed expression was derived based on an investigation of published test results. This equation is principally dependent on concrete strength, f'_c, reinforcement ratio, p, effective depth of cross section, d, and shear span-to-depth ratio, a/d. In this thesis, the shear strength, v_c, will be calculated according to this empirical equation, expressed as follows:

$$v_c = 0.2\ f'^{1/3}_c\ (0.75 + 1.4\frac{d}{a})\ (\ p + \frac{1}{d^{1/4}}\ - 1) \qquad \text{(MPa)} \qquad (2.2)$$

It should be noted that the shear strength, v_c, decreases under reversed cyclic loading, and Equation (2.2) is valid only under static and monotonic loading conditions.

2.3.3 Effect of Axial Load

Since shear is associated with the phenomenon of diagonal tension, it is expected that axial compression will increase, or conversely, axial tension will decrease the shear capacity of reinforced concrete members. Distress in concrete structures is often the result of the interaction of axial tension with transverse shear. This effect greatly influences the integrity of R.C. members without web reinforcement.

The behaviour of three identical beams subjected to three different loading combinations (transverse load and axial tension, transverse load only, and transverse load and axial compression) are compared in this section. The initial flexural cracks occur earliest in the beam with axial tension forces and extend further and are more nearly vertical in this beam. Mattock studied the effect of axial

load [16,32] and concluded that the axial load affects the initiation of the flexural shear cracks, but apparently does not affect the increment of shear between flexural cracking and diagonal cracking. Flexural shear cracks tend to incline at a smaller angle to the longitudinal axis in the presence of axial compression and may be almost vertical along most of the beam for the beams with axial tension, as shown in Fig. 2.10 from [32].

For typical under-reinforced members with web reinforcement, failure occurs due to crushing of the concrete in the compression zone after yielding of the web reinforcement crossing the diagonal cracks. Contribution of web reinforcement to the ultimate shear strength may be obtained from established truss analogy. The inclination of the diagonal tension cracks has been approximated by most design codes as 45° to the longitudinal axis of the member. In the case of members subjected to axial tension, fewer stirrups would be intercepted by a single diagonal tension crack. Accordingly, the contribution of the web reinforcement to shear strength might reasonably be expected to be less than in the case of a member without axial tension. However, experimental studies [16,32] have shown that the effectiveness of web reinforcement in resisting shear in reinforced concrete beams is not influenced by the presence of axial force.

The effect of axial load on diagonal tension cracking, v_c, and ultimate shear strength, v_u, as a function of the span-to-depth ratio, a/d, is shown in Fig. 2.11 from [16] for a group of simply supported beams. All beams have the same cross-section and the same amount of web reinforcement. The figure clearly indicates that the variations of v_u and v_c with a/d are similar. The results also suggest

that the contribution of web reinforcement (v_u - v_c), is independent of the axial force and the shear span-to-depth ratio, a/d.

Fig. 2.11 also shows the effect of axial forces on the concrete shear strength, v_c. This effect could be insignificant for slender beams subjected to axial tension [16]. Based on experimental studies [30], MacGregor revealed that the axial tension cracks which had formed prior to the application of the shear loading had very little effect on the behaviour and strength of beams. However, an independent study by Haddadin [16] concluded that the strength of beams was reduced due to the presence of axial tension cracks. The latter study recommended that the shear carried by the concrete be taken equal to zero if the average tensile stress exceeds 0.33 $\sqrt{f'_c}$.

Recently, several studies have attempted to use refined concrete failure theories to investigate shear failure mechanisms [1]. Many relationships have been proposed for the strength of concrete elements subjected to combined shear and axial stresses. These are based on either the Mohr Theory of Failure or the Kupfer, Hilsdorf, and Rusch diagrams. One of the proposed relationships is shown in Fig. 2.12 from [1]. This failure envelope presents all the combinations of shear and axial stresses for an element given in the same figure. The interaction diagram indicates the favorable effect of the compressive stresses up to an equivalent stress of 60% of the ultimate compressive strength of concrete, f'_c. Further increase of the axial compression, however, will reduce the ultimate shear resistance. This envelope also confirms that the addition of tensile stresses decreases the ultimate shear strength.

2.4 EFFECT OF REVERSED CYCLIC LOADING

When a beam is subjected to loading reversals, inclined cracks develop across the cracks caused by the preceding loads. Tests in which reversals of loading have been applied have shown that cross-inclined cracking occurring before yielding of shear reinforcement does not destroy the integrity of the member, but uncertainty exists regarding the effect of reversals on ultimate shear strength.

In this section, the behaviour of structural members subjected to deflection reversals will be discussed. This includes the study of strength and stiffness degradation characteristics as well as the effect of the loading pattern and load frequency.

2.4.1 Effect of the Loading History

Unfortunately, different investigators have used different loading patterns. Therefore, the result of the studies may not always be directly comparable. It is quite possible to produce different answers to questions of structural behaviour by varying the loading history [23].

Higashi, Ohkubo, and Ohtsuka [19] conducted a series of tests using two different loading patterns on companion specimens subjected to either three or ten load reversals at each deflection level. The results indicate that increasing the number of cycles did not alter the response substantially. Conversely, the response was significantly affected by the deflection limit. Where specimens were subjected to equal deformation levels in each direction, the strength degradation was more rapid and severe than when the deflection in one direction was limited. Both types of loading caused a more rapid decay

of strength than did monotonic loading.

Recently, Arakawa, et al. [2], studied experimentally the effect of load history on the strength, ductility and failure modes of columns. The results of this study showed that the deformation capacities of columns in structural systems were especially influenced by increasing the pitch of deflection amplitude for each cycle and the number of cycles. The ductility factors for the columns subjected to deflection increments equal to 10% of yield deflection, δy, were smaller than the columns subjected to deflection increments of δy. It was also indicated that the load-carrying capacity of the columns in the former case deteriorated quicker than that of the columns in the latter case. Also, the load-carrying capacity was generally slightly smaller in the former case.

2.4.2 Response of Reinforced Concrete Beams Under Load Reversals

Brown and Jirsa [11] investigated the behaviour of R.C. beams under load reversals and the effect of load history on the strength, ductility and mode of failure. In general, the loading part of the first cycle of the load-deflection relationship was a nearly bilinear curve which resembled the shape of the strain-stress curve for the reinforcement, as shown in Fig. 2.13 from [15]. However, the response in the reversed direction was curvilinear with a lower stiffness than the initial slope of the first half-cycle. The curvilinearity and reduced stiffness could be attributed to the cracking and slip between the concrete and reinforcement. The flexural tensile cracks formed during the first half-cycle had to be closed before development of the compression forces in the concrete. In addition, slip between

the steel and the concrete produced by large plastic deformations tended to reduce the stiffness under the first load reversals. It was also evident that the tension steel which yielded during the first half-cycle, no longer exhibited linear stress-strain characteristics after reversal of the applied load. This phenomenon is known as the Bauschinger effect [38].

The response in the second cycle was typical for the subsequent cycles. After the completion of the first cycle and yielding of the top and bottom reinforcements, the bond deterioration was approximately equal for both longitudinal bars. At this stage, the flexural and shear cracks extended across the entire depth of the beam, and concrete cover on both top and bottom surface had spalled off. The wide flexural cracks at the fixed end indicated that there was substantial plastic deformation of the reinforcement in the fixed end. Studies by Ismail [22] showed that yield strains in the longitudinal reinforcement penetrated quite extensively into the fixed end. This large deformation of the reinforcement anchored in the end block reduced the stiffness, but undoubtedly improved the energy-absorbing capacity of the beams.

In general, as the number of cycles increased, the load-deflection response exhibited a reduction of stiffness, as shown in Fig. 2.13. In particular, the stiffness decreased drastically at the early stages of the loading reversal, which is known as the pinching phenomenon. However, in the following stages, as the deflection increased, stiffness started to increase. The pinching of the curves towards the origin was the result of shear deformation and reduction of the stiffness during closure of flexural cracks initially formed in the previous cycles. The low initial stiffness substantially reduced

the energy absorbed in each cycle, particularly in the specimens with smaller span-to-depth ratios, i.e. a/d = 3. Similar results were observed by Bertero and McClure in tests of frames subjected to reversible loads [11].

2.4.3 Strength Decay of Reinforced Concrete Members Under Load Reversals

Experimental studies by Bertero, et al., [6,7] and Scribner and Wight [45] confirmed that the severity of pinching in the hysteresis response increases with the increase of applied shear stresses. Under load reversals in which the strains in the flexural steel exceed yielding range, some of the shear transfer mechanisms become ineffective. Several investigators have described in detail the problems associated with load reversals [5,6,11,40,47], as will be presented in the following discussion.

Fig. 2.14 illustrates four distinct stages of an idealized behaviour of a conventionally reinforced plastic hinge region [40]. In this example, it is assumed that the top and bottom flexural reinforcements are approximately equal. If the shear force is significant, extensive diagonal cracks will develop in the first inelastic load cycle, as shown in Fig. 2.14(a). Adequate web reinforcement will transfer the shear forces without yielding upon load reversal. However, a significant moment is required to close the previously formed flexural cracks. Fig. 2.14(b) shows the stage at which the bottom reinforcement has already yielded in tension without significant yielding of the top reinforcement to close the flexural cracks in the compression zone. At this stage, the significant shear force at the support has to be transferred by the dowel action across

the existing wide full-depth crack. Due to yielding of the top and bottom reinforcement, an appreciable shear displacement will occur, as shown in Fig. 2.15 from [38]. This displacement will lead to a considerable reduction in stiffness of the beam. Further increase of the applied shear will result in further sliding displacement until the critical crack closes at the top of the beam, as shown in Fig. 2.14(c). At this stage, shear can be transferred also across the concrete compression zone. The shear displacement, Δ , that has occurred before the closure of the crack results in uneven bearing of the concrete in the compression zone. Consequently, at a relatively low flexural compression stress level, grinding of the concrete at the crack interface will occur because of the lack of fit and the frictional shear load.

After several large inelastic load cycles, residual plastic tensile strains accumulated in the flexural reinforcement will become large. The shear may then need to be transferred entirely by the dowel action, as shown in Fig. 2.14(d). Large dowel displacements, loss of the concrete cover and the deterioration of the concrete around compression bars would eventually lead to the buckling of the longitudinal reinforcement. This will result in considerable reduction of the flexural and shear capacity of the beam.

In another experimental study [14], the distortions due to flexure and shear were determined separately in carefully instrumented beams. The study indicated that the shear distortions became highly significant as the shear stresses were increased and also when the imposed ductility was increased. In order to control the sliding shear displacement and the loss of energy dissipation capacity due to shear distortion, the shear stresses should be limited [14,45].

The dowel action could be improved by placing additional longitudinal reinforcement at the mid-depth of the section of the beam [45]. These mid-depth dowels will assist in redistributing the full-depth cracks which enhance the shear transfer by aggregate interlocking action. However, such an arrangement could increase the flexural strength of the plastic hinge section, which could result in an increase in the induced shear. The contribution of dowels to energy dissipation is generally insignificant [14,45].

2.4.4 Classification of Critical Regions of Structural Members

In studying the behaviour of reinforced concrete critical regions, it is convenient to classify them according to their controlling states of stress as follows:

(a) Inelastic behaviour controlled by bending (flexural critical regions);

(b) Inelastic behaviour controlled by high shear existing in the critical region, rather than bending; and

(c) Inelastic behaviour controlled by high axial compression and shear forces, rather than bending.

The major features of the results obtained from experimental studies reported on the behaviour of these types of critical regions will be summarized in the following paragraphs [6].

2.2.4.1 Behaviour of Flexural Critical Regions

Based on the analysis of a large number of experimental results, Bertero [6] summarized the behaviour of such regions as follows:

(a) Failure could occur due to the buckling of the longitudinal

reinforcement after extensive yielding due to flexure. In order to prevent the premature buckling of the main reinforcing bars, present code provisions on the spacing of lateral supports should be made more stringent. Test results and analytical studies indicate that the spacing of the transverse reinforcement should be reduced to, at most, 6 to 8 bar diameters of the main bars [8].

(b) The energy dissipation capacities of the beams could be increased by placing an equal amount of longitudinal reinforcement at the top and bottom layers of the critical region. Therefore, it would be advisable to use positive reinforcement in an amount greater than the 50% negative reinforcement currently allowed by the ACI code provisions.

(c) Since the slab contributes substantially to the increase in the initial stiffness and the negative moment capacity of the beam, energy absorption and energy dissipation capacities of a critical region are also increased. Thus, the strengthening effect of the slab should be included in the analytical models used for predicting the behaviour of this type of critical region.

(d) Despite the special precautions taken in providing anchorage for the main bars, the test results indicate significant pull-out of the rebars. In some cases, this pull-out contributes up to 40% of the measured total tip deflection [6]. The pull-out phenomenon of the longitudinal bars is a result of the degradation of bond stresses with repeated reversals of inelastic straining. Considering that the

anchorage provided to the main bars of the specimens tested exceeds the anchorage that can usually be provided in actual structures, it is clear that pull-out of the longitudinal bars can be one of the controlling parameters in the overall degradation of stiffness observed in real structures.

(e) Although there is some degradation of stiffness in the initial range of reloading during a reversal cycle, this becomes accentuated only after a high displacement takes place. The hysteresis loops for cycles of moderate reversals between the same peak deformations are quite stable.

(f) Most of the observed degradations in stiffness were a result of the Bauschinger effect [38] and the bond deterioration, while some were a result of the presence of shear.

2.4.4.2 Behaviour of Flexural Critical Regions with High Shear

Data available on the behaviour of critical regions subjected to reversals of combined flexure and high shear are very limited. Typical responses for two specimens subjected to different levels of shear stress are shown in Fig. 2.16 from [6], where some selected hysteresis loops corresponding to similar displacement ductility ratios are compared. These results were obtained for identical half-scale specimens, R-6, and R-5, with shear span-to-depth ratios, $\frac{a}{d}$, of 4.5 and 2.75, respectively. From the same figure, it can be seen that there is greater degradation of stiffness and energy dissipation in the case of R-5, which has been subjected to higher shear, than in the case of R-6. For the case of high shear, specimen R-5, the loops pinched towards the origin. This pinching effect is

due to the large degradation in shear resistance and stiffness during the initial stages of reloading. The deformation pattern of the short cantilever specimen, R-5, clearly displays the importance of shear distortions and the rotation of the beam as a rigid body. This rotation occurred as a result of the pull-out of the longitudinal bars from the end block, causing a fixed-end rotation which contributed to the tip deflection.

Typically, after a few reversals, the diagonal tension cracks produced by the shear not only crossed similar cracks resulting from the reversals of the shear, but also intersected and combined with the vertical flexural cracks. After severe reversals, one or two nearly vertical cracks remained open at zero load throughout the cross-section of the beam. At these cracks, the initial shear can be resisted only by the dowel action of the main bars, which is most inefficient. It accelerates the failure of the beam, which occurs in a mode that has been classified by Paulay [40] as sliding shear failure. Because it occurs after considerable flexural yielding of the main reinforcement, its mechanism is designated herein as a flexure-shear mechanism. From the results obtained on the effect of high shear reversals, the following conclusions can be drawn [6]:

(a) Increase in the shear forces at the critical regions of flexural members reduces their energy absorption and energy dissipation capacities.

(b) When the average shear stress at the critical region exceeds a stress value of $0.29\sqrt{f'_c}$ (MPa), the degradation in stiffness with a reversal of load becomes considerably greater than that for flexural critical regions with low shear stresses.

Degradation in strength occurs as the number of similar loading cycles increases. Failure of these regions results only after some significant flexural yielding of the longitudinal steel has taken place.

(c) The ability of the critical regions to maintain load and energy dissipation capacity and hysteresis loop stability could be significantly improved by reducing the spacing between the transverse reinforcements [6]. However, this may not always be the case if the concrete distress occurs along cracks parallel to the transverse reinforcement, which could reduce the efficiency of the shear reinforcement [11]. The degradation in strength, stiffness, energy absorption and energy dissipation per cycle increases rapidly when the shear stress approaches a specified stress level of 0.44 $\sqrt{f'_c}$ (MPa). In order to minimize these degradations, design of web reinforcement should be based on the following procedure:

(i) Neglect the concrete contribution in resisting shear [6,10]; and

(ii) Proportion the web reinforcement based on the load corresponding to the maximum bending capacities of the critical regions. Thus, the design should take into account the actual strength of the longitudinal reinforcement, including the strain-hardening range instead of the specified yield strength.

(d) Unfortunately, the degradation of the critical regions due to high intensity of shear stresses cannot be predicted

similarly to the case of pure flexure by only considering the bond deterioration and the Bauschinger effect. In order to avoid excessive damage under repeated loading reversals, the shear stress should be limited in magnitude to a value lower than $0.83 \sqrt{f'_c}$ (MPa) which is recommended by the current codes.

(e) By using inclined web reinforcements in combination with vertical stirrups it is possible to minimize the degradation of stiffness and to obtain stable hysteresis loops for a displacement ductility exceeding a value of 4 [39].

(f) The use of inclined web reinforcements permitted the development of a maximum effective plastic hinge rotation of similar magnitude to the values which could be obtained for compact steel beams.

(g) The pull-out of the longitudinal bars increases the tip deflection significantly. This phenomenon increases with the severity of the loading and the number of cycles of reversal.

2.4.4.3 Behaviour of Critical Regions with High Axial and Shear Forces

Where failure occurs prior to the achievement of flexural yielding, the failure is generally of a brittle nature. For reversed cyclic loading this failure is characterized by a rather rapid degradation of the shear strength. This can be seen in Fig. 2.17 from [24] for the specimen with a shear span-to-depth ratio of 1.4. Where flexural yielding occurs, adequate ductility is generally obtained. However, in the case of columns, plastic hinges are usually

avoided based on the weak beam-strong column design philosophy. Therefore, it is essential to prevent shear failure in the column before flexural yielding of the beam [7].

Arakawa, et al. [2,3], studied the effect of the variation of axial load on the ductility of columns. It was concluded that the ductility factor, μ, increases with decreasing axial load factor as shown in Fig. 2.18, where η_o is the axial load factor defined as the ratio between the magnitude of axial applied compressive stresses, σ, and the compressive strength of concrete, f'_c. Yamada and Yagi [51] tested specimens in double curvature, illustrated in Fig. 2.19. They concluded that the transition from flexural yielding to shear failure occurs at a critical a/d ratio which is a function of axial load, material properties and amount of longitudinal reinforcement. In general, shear failure is likely to occur for a shear span-to-depth ratio less than 2. To provide adequate deformation capacity for the case of shear failure, Yamada and Yagi recommended a minimum transverse reinforcement ratio of 1%. Zagajeski et al. [52], tested column specimens of the type shown in Fig. 2.17 with a shear span-to-depth ratio of 7.5. Both tie and spiral reinforcements were used. Spiral reinforcement was more effective in preventing shear failures. However, bond failure occurred due to spalling off of the concrete cover. The study indicated that the shear behaviour of columns is heavily dependent on the loading history. It was also found that increase of the transverse reinforcement significantly improved the lateral deformation capacity of the assemblage.

Paulay [39] applied reversed cycles of high shearing force to deep beams restrained at each end. In the first few cycles the

beams behaved as predicted by the ACI code sections 11.4.2 and 11.6.2, but as load cycling continued, the shear carried by the concrete decreased. Following yielding of the web reinforcement, a high percentage of the applied load was carried by the arch action. Failure generally occurred by crushing of the concrete at the ends of the arch. A significant decrease in stiffness was observed as the test progressed.

2.4.5 Relationship Between Work Index and Shear Resistance in Critical Regions

Gosian, et al. [15], proposed an approach for estimating the relationship between the severity of the applied load measured by the work index, I_w, and the shear resistance in plastic hinge regions. In order to determine the work index, they introduced a simplified method, rather than computing the actual area under the hysteresis loops. The load-deflection curves were normalized with respect to the calculated yield load, p_y, and the yield deflection, δ_y, respectively. The maximum deflection and load ratios were determined for each cycle from the normalized load-deflection curves. The work index was then determined using the following expression:

$$I_w = \sum_{i=1}^{n} \frac{P_i \, \delta_i}{P_y \, \delta_y} \qquad (2.3)$$

where P_i and δ_i are the maximum applied load and deflection at the ith cycle, respectively, and n is the number of cycles in which the ratio $\frac{P_i}{P_y} \geq 0.75$.

The study indicated that the work index is sensitive to the shear span-to-confined depth ratio, $\frac{a}{d_c}$, and to the level of axial compressive stress, $\frac{N}{A_c}$, where N and A_c are the axial compressive force and the confined cross-sectional area of the member, respectively. The core dimensions were used due to spalling off of the concrete at the early loading stages. Fig. 2.19 from [15] shows the load deflection curves of similar specimens with shear span-to-confined depth ratios varying from 3.2 to 6.2. It can be seen that the pinching of the curves towards the origin becomes more severe with the reduction of the level of axial compressive stresses and shear span-to-confined depth ratio. To account for these new parameters a modified work index, I'_w, was introduced as follows (metric):

$$I'_w = I_w \left(1 - \frac{d_c}{a}\right) \left(1 - 0.102 \frac{N}{A_c}\right) \qquad (2.4)$$

The relationship between the modified work index, I'_w, and the measured maximum shear stress resistance is shown in Fig. 2.21 from [15]. Using the modified work index as a means for evaluating the severity of the applied load, the maximum allowable shear stress can be estimated. According to the same figure, to achieve a performance equivalent to 5 cycles at a deflection limit of 5 times the yield deflection, the shear stresses should not exceed $0.5 \sqrt{f'_c}$ (MPa). In this case, the transverse reinforcement should be designed to provide a capacity approximately equal to that provided by the concrete, i.e., as recommended by other investigators [5]:

$$p_w f_y = \frac{A_v}{S b_c} f_y \geq 0.5 \sqrt{f'_c} \text{ (MPa)} \qquad (2.5)$$

where p_w is the percentage of transverse reinforcement, f_y is the yield strength, S is the stirrup spacing, b_c is the core width, and

A_v is the total area of transverse steel.

2.4.6 Effect of the Loading Frequency

Recently, Arakawa, et al. [3], investigated experimentally the effect of the loading frequency on the load-carrying capacity and the inelastic behaviour of columns. In their test, the loading frequency was varied between 0.05 and 1.5 HZ. Test results revealed no differences in modes of failure with the variation of the load frequency. However, the load-carrying capacity for the columns subjected to low frequencies appeared to deteriorate faster than the columns subjected to higher frequencies. It was also concluded that, for a constant rate of applied deflection, V (mm/sec), the ductility factor decreases with the increase of the loading frequency, FR, as shown in Fig. 2.21. However, for a constant deflection increment, Δp (mm/cycle), the effect of the rate of the imposed deflection, v, on the ductility factor, μ, is insignificant, as shown in Fig. 2.22.

2.4.7 Equivalent Viscous Damping Coefficient, η_{eq}

The process by which vibration steadily diminishes in amplitude is called damping. In damping, the energy of the vibrating system is dissipated as friction or heat. The mechanism of damping can take any of several forms, and often more than one form may be present at a time [46].

Fluid damping may be either viscous or turbulent. In viscous damping, the damping force is proportional to velocity. Solid damping or hysteretic damping is caused by the internal friction or hysteresis when a solid is deformed. Stress amplitude is a measure of solid

damping.

The most commonly used damping mechanism is viscous damping, in which the damping force is proportional to velocity. Strictly, this is only valid for damping such as that caused by the laminar flow of a viscous fluid through a slot [46]. Other forms of damping may approximate viscous damping if the dissipative forces are small. The use of viscous damping has the advantage of linearizing the equation of motion;

$$m\ddot{X} + C\dot{X} + KX = - m\ddot{a} \qquad (2.6)$$

in which, m is the mass, C is the viscous damping coefficient, K is the stiffness of the structural member and $\ddot{a}$ is the acceleration of the ground motion.

If instrumentation is available to measure the phase relationship between the input force and the resulting displacements, the damping can be evaluated from a test run only at resonance [12]. The procedure involves establishing resonance by adjusting the input frequency until the response is 90° out of phase with the applied loading. Then the applied load is exactly balanced by the damping force, so that if the relationship between the applied load and the resulting displacements is plotted for one loading cycle, as shown in Fig. 2.23, the result can be interpreted as the damping-force-displacement diagram.

If the structure has linear viscous damping, the curve will be an ellipse, as shown by the dashed line in Fig. 2.24. In this case, the damping coefficient can be determined directly from the ratio of the maximum damping force, f_{Dmax}, to the maximum velocity, $\dot{X}_{max}$:

$$C = \frac{f_{D,max}}{\dot{X}_{max}} = \frac{P_o}{\omega X_{max}} \qquad (2.7)$$

where it is noted that the maximum velocity is given by the product of frequency, ω, and displacement amplitude, X_{max}. If the damping is not linear viscous, the shape of the force-displacement diagram will not be elliptical. A curve like the solid line in Fig. 2.24 might have been obtained, for example. In this case, an equivalent viscous damping coefficient can be defined which would cause the same energy loss per cycle as in the observed force-displacement diagram. In other words, the equivalent viscous damper is associated with the elliptical force-displacement diagram having the same area and maximum displacements as the actual force-displacement diagram. In this sense, the dashed-line curve in Fig. 2.24 is equivalent to the solid-line curve. Then the equivalent applied force amplitude is given by

$$P_o = \frac{W_D}{\pi X_{max}} \qquad (2.8)$$

where W_D is the area under the damping force-displacement diagram, i.e., energy loss per cycle. Substituting this into Eq. (2.7) leads to an expression for the equivalent viscous damping coefficient in terms of the energy loss per cycle:

$$C_{eq} = \frac{W_D}{\pi \omega X^2_{max}} \qquad (2.9)$$

In most cases, it is more convenient to define the damping in terms of the critical damping ratio than as a damping coefficient. For this purpose, it is also necessary to define a measure of the critical damping coefficient of the structure, and this can be expressed in terms of the mass and frequency or in the alternate form involving stiffness, K, and frequency:

$$C_c = 2m\omega_n \tag{2.10}$$

or

$$C_c = \frac{2K}{\omega} \tag{2.11}$$

where C_c is the critical damping coefficient, and ω_n is the natural frequency of the structure.

This latter expression is more convenient because the stiffness of the structure can be measured by the same instrumentation used to measure the damping energy loss per cycle, merely by operating the system very slowly at essentially static conditions. The static-force-displacement diagram obtained in this way will be of the form shown in Fig. 2.25 if the structure is linearly elastic, and the stiffness is represented by the slope of the curve. Alternatively, the stiffness may be expressed by the area under the force-displacement diagram, W_s, as follows:

$$K = \frac{2W_s}{X^2_{max}} \tag{2.12}$$

Thus the damping ratio can be obtained by combining Eqs. (2.9), (2.11), and (2.12).

$$\eta_{eq} = \frac{C}{C_c} = \frac{W_D}{4\pi W_s} \tag{2.13}$$

The damping ratio defined by Eq. (2.13) appears to be independent of frequency. It depends directly on the ratio of damping-energy loss per cycle to the maximum strain energy stored at maximum displacement. However, for any given viscous-damping mechanism, the energy loss in the system will be proportional to the harmonic frequency, as will be the damping ratio.

The equivalent viscous damping concept expressed by Eq. (2.13) has also been applied to nonlinear systems [34], considering the area enclosed by the hysteresis loop as the damping energy loss during a cycle, W_D, and the area of the triangle as the maximum strain energy stored at maximum displacement, W_S, as shown in Fig. 2.25. Although the equivalent viscous damping coefficient, η_{eq}, provides a practical means of evaluating the damping characteristics of a vibrating system, its applications are as yet tentative [23,33].

2.5 GENERAL REMARKS

Based on the detailed discussions covered in this chapter, the following is a brief summary of the shear behaviour of reinforced concrete numbers under different loading conditions.

For statically and monotonically loaded beams, the current codes suggest that portions of the shear are carried by the uncracked concrete above the inclined cracks, dowel action of the longitudinal reinforcement, and interface shear transfer across the crack. For static and unidirectional cyclic loading, the codes provide conservative strength values.

For beams subjected to a reversed cyclic loading condition, the presence of the x-shaped cracks reduces the shear resistance due to cracking of the compression zone and residual tensile strains in the compression reinforcement, which prevent the complete closure of the cracks in the compression zone. The interface shear transfer is also reduced by the "working back and forth" action along the cracks as the load is cycled. Finally, dowel action will carry the load if splitting along the longitudinal bars is restrained by closely

spaced stirrups. Based on this reasoning, Bresler [10] has proposed that stirrups be provided for the full shear force in beams where load reversals take place.

CHAPTER III

EXPERIMENTAL PROGRAM

3.1 INTRODUCTION

The purpose of this experimental program was to study the shear behaviour of typical bridge piers subjected to large deflection reversals, such as those which would result from seismic excitation. In order to achieve this goal, it is essential that the material properties, construction details and boundary conditions are similar to a prototype bridge pier. This simulation also includes the range of shear span-to-depth ratio, $\frac{a}{d}$, percentage of longitudinal reinforcement, p, and magnitude of axial compressive stresses, σ.

In order for bridge piers to withstand a sudden seismic energy input, they are required to resist cyclic deflection reversals large enough to cause extensive yielding of the longitudinal reinforcement. This requirement led to the choice of the loading pattern shown in Fig. 3.1 for this experimental program.

A total of 16 reinforced concrete specimens without web reinforcement were tested to examine the effect of different parameters believed to influence the shear strength, ductility, stiffness and failure mechanism of such members, as given in Table 3.1.

3.2 DESIGN CRITERIA FOR THE SPECIMENS

In order to obtain data on the response of bridge piers subjected to large deflection reversals, three series of reinforced concrete specimens representative of bridge pier prototypes were designed and tested. The relationship between the specimen and the bridge piers

is shown in Fig. 3.2. The scale of the specimens was constrained by the capacity of the testing apparatus available in the structural laboratory at the University of Manitoba. On the other hand, the response of small specimens using fine aggregates could not necessarily be extrapolated to the prototype structure, in which the interface shear transfer across larger sized aggregates is bound to be less effective [48]. Therefore, normal weight concrete with a maximum aggregate size of 20 mm was used in the fabrication of the specimens to provide adequate simulation of the interface shear transfer. The width of the specimen was controlled by the minimum deformed bar diameter available and the minimum concrete cover specified by the code.

In order to standardize the formwork and the test set-up, the shear span length, a, was kept constant for all the specimens as shown in Fig. 3.2. The choice of the length of shear span, a, was controlled by the stroke capacity of the testing machine, which is limited to a range of ± 75 mm under a maximum load of 1,000 KN. The required stroke range is a function of the multiple of the deflection at the location of applied load necessary to cause yielding of the longitudinal reinforcement at the maximum moment section, which is a function of the shear span length, a. Based on these considerations, a shear span length of 1,150 mm was fixed for all the specimens.

The dimensions of the end block of the specimens were designed to provide a large flexural rigidity simulating the fixation and the boundary conditions provided by the foundation of a typical reinforced concrete bridge pier. The block was also proportioned to provide enough

embedment length for the longitudinal bars to avoid any probable slippage of longitudinal reinforcement through the end block. In addition, the end block provided an anchorage system for the specimen to the structural floor in the laboratory, as shown in Fig. 3.2.

3.2.1 Selection of the Specimen Variables

The main parameters varied were the shear span-to-depth ratio, $\frac{a}{d}$, the percentage of longitudinal reinforcement, p, the frequency of loading, FR, and the magnitude of axial compressive stresses, σ. The selection of these variables was mainly based on the results of a survey of single column bridge piers conducted in Japan in 1980 [36]. The survey revealed that the typical span-to-depth ratio, $\frac{a}{d}$, for bridge piers is greater than 3, the percentage of longitudinal reinforcement, p, is usually less than 1%, the average axial compressive stress, σ, ranges between 1 and 2 MPa, and the percentage of transverse reinforcement is less than 0.1%. Table 3.2 compares these characteristics of bridge pier columns to typical values of building columns. The differences in the range of the main parameters suggest possible changes in the mode of failure and ductility, which underline the need for an independent investigation. The selection of the specimen variables in this experimental program will be discussed individually in the following sections:

3.2.1.1 Shear Span-to-Depth Ratio, a/d

The effective depth, d, of the specimens was varied to allow for the variation of shear span-to-depth ratio, a/d, as given in Table 3.1. The selected range of a/d was between 3.29 and 6.05 as typical values for such members [36]. Intermediate-range $\frac{a}{d}$ values of 4.11

and 5.00 was also selected to study the trend of the variations of strength, ductility, stiffness and the mode of failure in this range.

3.2.1.2 Percentage of Longitudinal Reinforcement, p

The percentage of the longitudinal reinforcement, p, influences the ratio between the shear strength, v_c, calculated based on Eq. (2.2), and the shear stress corresponding to yielding of longitudinal reinforcement at the maximum moment location, v_y, as shown in Fig. 3.4 from [4]. The values of p were selected to ensure that the shear failure would take place after the yielding of the longitudinal reinforcement, i.e., $v_c/v_y > 1$. The chosen percentages of steel, p, are given in Table 3.1 for all the specimens tested in this program. These values cover the typical range for such members as proposed in Table 3.2 and go beyond that range to study the effect of higher percentages of steel. To ensure yielding of the longitudinal steel prior to shear failure, the selected values of p were less than 1.1% for specimens with a/d of 3.29, and less than 1.9% for specimens with a/d values of 6.05. The lower limits of p were selected to avoid large ratios of v_c/v_y, which would lead to flexural failure, which is beyond the scope of this investigation.

3.2.1.3 Frequency of Loading, FR

The majority of the past investigations of the behaviour of reinforced concrete members under reversed loading conditions have been conducted using static loading ranges to facilitate complete data collection on the response of the member and to observe such behaviour as crack propagation. The effect of the load frequency should be investigated before using the static test results in designing reinforced concrete structures subjected to seismic loading conditions. The load

frequency should include the range of frequency of typical seismic motion for bridge piers, which could vary between 0.5 and 10 HZ [20].

The original objective of testing specimens in series II was to examine the effect of load frequency in the previously mentioned range. Unfortunately, due to the limitation of the stroke capacity of the MTS testing machine, the maximum frequency was limited to 0.2 HZ and 0.1 HZ for a/d values of 3.29 and 6.05, respectively. Thus, the objective of series II was confined to a relatively low frequency range. Four specimens were tested with different load frequencies between 0.01 and 0.2 HZ, as given in Table 3.1. These tests could be considered as pilot tests for future extension of this experimental program.

3.2.1.4 Level of Axial Compressive Stresses, σ

Two specimens were tested with an equivalent axial compressive stress, σ , of 0.98 MPa to simulate the actual loading condition of the prototype as recommended in Table 3.2.

3.2.2 Design Procedure

The dimensions and reinforcement details of the end block for all the specimens were identical, as shown in Fig. 3.3. The length of the shear span of 1,150 mm and the width of 500 mm of the cantilever part of the specimen were also fixed for all the specimens in this program.

Based on a nominal concrete compressive strength, f'_c , of 30 MPa and a yield strength of steel, f_y, of 343 MPa, the specimens were designed as follows:

(a) The effective depth, d, was calculated based on the selected

values of a/d using the specified constant shear span length, a.

(b) For an assumed ratio of $v_c / v_y > 1$, the percentage of longitudinal tension steel, p, was determined based on the section and material properties previously specified. This was done by assuming a value of p and calculating the values of v_c and v_y. Several iterations were required to approach the desired values of v_c/v_y ration. The relationships between v_c, the ratio of v_c/v_y, the shear stresses corresponding to ultimate flexural capacity, v_f, and the percentage of the longitudinal reinforcement, p, are given in Fig. 3.4 for different a/d values.

3.3 TEST SPECIMENS

The experimental program consisted of three series of specimens. Series I was subdivided into two subseries I-A and I-B. A summary of the section properties of all specimens tested in different series is given in Table 3.1. Reinforcement details and instrumentations of individual specimens can be found in Reference [4], Appendix (B.2). The typical reinforcement details for all specimens are shown in Fig. 3.3. It should be noted that equal top and bottom reinforcement was used to provide equal resistance in either directions. The objectives and the range of the variables in each series will be discussed separately in the following sections. Specimens in all series except for Series II were tested under static loading conditions.

3.3.1 Subseries I-A

The main objective of this subseries was to examine the effect of shear span-to-depth ratio, a/d, on the mode of failure, ductility, shear strength, and stiffness of reinforced concrete piers. Based on Higai's test results on small size specimens [18], the ductility factor, μ, is a function of the v_c/v_y ratio. In order to examine this conclusion, three specimens (1-1, 1-2, and 1-3 with a/d values of 3.29, 5.0 and 6.05, respectively, as given in Table 3.1), were tested. The effective depth, d, was varied from 350 mm to 190 mm since a constant shear span length of 1,150 mm was used for all the specimens. The percentage of the longitudinal steel, p, was also varied between 0.51 and 1.26% to maintain an almost constant value of v_c/v_y of 1.6. According to the previous study [18], the ductility factor for all three specimens in this subseries should be identical.

3.3.2 Subseries I-B

Based on the test results of subseries I-A, it was observed that the mode of failure and the ductility factor are not only functions of v_c/v_y, but are also affected by the value of shear span to depth ratio, a/d. Since the effect of a/d and p cannot be separated, seven specimens were tested in subseries I-B to study the effect of a/d and p separately.

Three of these specimens (1-4, 1-5, and 1-6) were designed for a constant value of a/d equal to 6.05, and variable p ranging between 0.95 and 1.9%. Accordingly, the corresponding v_c/v_y ratios of these specimens varied between 1.44 and 2.22.

Three specimens (1-7, 1-8, and 1-9) were designed with a

constant a/d ratio of 3.29, and variable p ranging between 0.4 and 0.86%. The corresponding v_c/v_y ratios of these specimens varied between 1.24 and 1.95. Only one additional specimen, 1-10, was designed for an intermediate range of a/d of 4.11, with a p of 0.64%, and v_c/v_y of 1.82.

3.2.3 Series II

The objective of this series was to study the effect of load frequency on the behaviour of such members. Three specimens (2-1, 2-2, and 2-3) were designed for constant a/d of 3.29 and p of 0.51% and tested under different load frequencies of 0.1, 0.2, and 0.05 HZ, respectively. These specimens are comparable to specimen 1-1 tested in subseries I-A under a load frequency of 0.0004 HZ. An additional specimen, 2-5, was designed for an a/d value of 6.05, percentage of steel, p, of 1.26%, and tested under a load frequency of 0.1 HZ. This specimen is comparable to specimen 1-3 tested in subseries I-A under a load frequency of 0.0004 HZ, which is static loading condition.

3.2.4 Series III

The objective of this series was to study the effect of axial compressive stresses on the overall behaviour of reinforced concrete piers. Two specimens, 3-1 and 3-3, with identical section properties to specimens 1-1 and 1-3, respectively, were tested for comparison in the presence of an equivalent axial compressive stress, σ, of 0.98 MPa. The level of axial compressive stress applied, σ, is typical to bridge piers as recommended in [36] and is not comparable to that of typical building columns.

3.4 FABRICATION OF TEST SPECIMENS

This section deals with the fabrication of the form-work, construction details, and casting of concrete.

3.4.1 Construction of Form-work

The shape of the form-work for a typical specimen is shown in Fig. 3.5. The side of the specimen facing the bottom of the form-work will be referred to as face A, and the opposite side as face B throughout this thesis. Face A will be mainly used to observe the formation of the cracks during the test, and face B will be instrumented to measure the strains and the deflections.

Basically, the concrete form-work was made of 20mm plywood sheets, reinforced with 2x2 stiffners and braced, as shown in Fig. 3.5. The form-work mainly consisted of two parts. The first part was the cantilever part projected from the second part, the end block. Four 60 mm diameter holes were provided on either side of the end block to allow for the placement of polyvinyl chloride (P.V.C.) pipes. These pipes are used to provide ducts through which high-strength steel bolts fix the end block to the testing floor. Another eight 60-mm-diameter holes were provided at the end of the cantilever part, using the same P.V.C. pipes. These holes were used to attach a pin connection between the MTS hydraulic actuator and the specimen. Two 20mm holes were also provided at the end block to allow for the threaded inserts which were used for handling of the specimen. The forms were specially designed to be reused for different specimens.

3.4.2 Preparation of the Specimen

Electrical resistance strain gauges, as well as linear variable differential transducers (LVDT's), were installed to measure the steel strain at different locations. Prior to casting, 6mm diameter steel studs were attached to the longitudinal bars to support the LVDT's. The studs were long enough to reach the surface of the concrete. A spacer made of polyethylene tubing was placed over each stud leaving about a 3mm gap between the stud and the concrete, as shown in Fig. 3.6. This was provided to allow for the measurement of average steel strain without interference from the surrounding concrete. A typical stud, as shown in Fig. 3.7, was welded to a steel ring which was attached to the outer longitudinal bar using 5mm diameter screws. This procedure was used to avoid welding the stud to the reinforcement, which could result in local changes in material properties.

The rebars were assembled into two cages, one for the end block, and the other for the cantilever part. These cages were tied together, as shown in Fig. 3.8, and finally mounted in the form, as shown in Fig. 3.9.

The forms were oiled before placing the reinforcement to allow for reuse and smoother concrete surfaces. Plastic chairs and welding guides were used to support the reinforcement and provide the required concrete cover. Two structural connection inserts (Richmond type LF-W) were embedded into surface B of the end block for attaching a steel bracket used to support the LVDT at the tip of the cantilever. This LVDT is used to measure the deflection at the location of the applied load.

3.4.3 Casting of Concrete

Once the reinforcement was in place, concrete was cast and trowelled as shown in Fig. 3.10. Two pencil-type 25mm diameter vibrators were used during casting of concrete. Two anchorage inserts were placed in the concrete after initial setting. The specimens were left in the open air for about two hours, then covered with wet burlap and plastic sheets. The forms were stripped one day after casting, but the specimens remained covered for a total of seven days. Then the specimens were rotated 90° to their testing position, and cured in the open air for at least two weeks before testing. The age of each specimen at the time of testing is listed in Table 3.3.

With each specimen, six standard 152.4 x 304.8mm concrete test cylinders were cast to determine the concrete strengths. The cylinders were cured under the same conditions as the test specimens. Three of the cylinders were then tested to determine the compressive strength, f'_c, and stress-strain curve for the concrete. The concrete strain was measured with 200mm gauge length compressometers. The remaining three cylinders were tested to determine the splitting strength, f_{sp}. The average compressive and splitting strengths are summarized for each specimen in Table 3.3. The modulus of elasticity was calculated based on the measured stress-strain curves obtained from the compression test of the control cylinders. The cylinders were usually tested at the same time as the corresponding specimen. Reference [4], Appendix (A.1) contains the stress-strain plots for the concrete used for each specimen.

3.5 MATERIAL PROPERTIES

3.5.1 Concrete

All concrete used had a nominal design compressive strength of 30 MPa, and was ready-mixed concrete from a local concrete mix plant. The curing was accelerated by a Pozzolith type 100 HE admixture to produce high early strength. Normal density aggregate was used with the coarse aggregate obtained from glacial outwash deposits of Lake Agassiz in the Bird's Hill, Manitoba. The mix was of the following composition:

Water	155 kg
Cement "normal Portland"	366 kg
Sand	760 kg
Aggregate "20 mm"	1160 kg
Admixture "pozzolith, type 100 HE"	5490 ml
Water/cement ratio by weight	0.423

3.5.2 Reinforcing Steel

Reinforcement used in the specimens consisted of hot rolled deformed bars conforming to CSA G30-12-72, grade 300 MPa. Bar sizes used were No. 10M, 15M and 20M. Specimens from each size were tested in tension to determine yield strength, and ultimate tensile strength. The modulus of elasticity for each size was obtained by mounting two 5mm long electric resistance strain gauges opposite to each other on smoothly filed sides of the bar. It should be noted that care was taken in filing the deformed bars so that only the actual protrusions were removed. All steel specimens showed a typical ductile behaviour, having a well-defined yield point and cup-cone fracture.

The average results of the specimen tests are listed in Table 3.4, and stress-strain plots for each size of reinforcing steel may be found in Reference [4], Appendix (A.1).

3.6 TEST SET-UP

A typical test set-up is shown in Fig. 3.11. The specimen was fixed to the testing floor by using four 31.8mm high tensile strength bolts which were inserted through the holes in the end block and threaded into the testing floor. Cement paste with a water/cement ratio of 0.32 was used for levelling the end block, and providing proper contact between the end block and the testing floor. The end block was fixed to the floor using a large torque wrench. Steel bearing plates (200x200x33 mm), and thin lead plates were used to distribute the bolt forces to the concrete surface to avoid local crushing of concrete.

In the case of specimens 1-8, 1-9, and 1-10 of subseries I-B, the test set-up was modified to minimize the lateral rotational movement of the cantilever. This was done through the provision of a bracing system attached at the end of the cantilever, as shown in Fig. 3.12. The bracing system was provided with Teflon strips to reduce the friction between the braces and the specimen.

3.7 LOADING APPARATUS

The vertical reversing load was applied using an electric-servo type MTS testing machine. The load and stroke capacities of this type of machine are ± 1000 KN and ± 75 mm, respectively, under static loading condition. However, under dynamic loading condition the stroke capacity

is dependent on the load frequency, as shown in Fig. 3.13. The machine has a closed-loop system, and it can be controlled by any of the three feed-back signals: load, stroke, and strain. However, in this actuator was supported by a specially designed frame bolted to the testing floor as shown in Fig. 3.14. The actuator has two universal joints, one at the top and one at the bottom, to allow rotation of the actuator, which ensures that the applied load is always perpendicular to the specimen. The specimen was pinned-connected to the actuator using four bolts and two (500 x 300 x 33mm) steel bearing plates. In order to avoid local crushing of the concrete, lead plates were used between the steel plates and the concrete surface.

For specimens tested in Series III, the compression load was applied using a specially designed load frame equipped with two hydraulic jacks, and totally independent of the MTS machine, as shown in Fig. 3.15. The loading frame consists of two rigid beams connected by two Dewedage bars reacting against a pair of hydraulic jacks supported by the concrete. A pin connection was provided to allow for the rotation of the cantilever in the vertical plane, as connected by two Dewedage bars reacting against a pair of hydraulic jacks supported by the concrete. A pin connection was provided to allow for the rotation of the cantilever in the vertical plane, as shown in Fig. 3.16. A bearing plate was used to distribute the applied axial load over the cross-section at the free end. A load cell was also used to measure the total applied compression force during the test. The hydraulic jacks were connected to an electric pump and pressure regulator to maintain a constant axial compression load during the test, as shown in Fig. 3.17.

3.8 TESTING PROCEDURE

The reversed cyclic load pattern used in this experimental program is shown in Fig. 3.1 . The specimen was loaded downward (negative load) up to a load equal to the calculated yield load, p_y, using the load control mode of the machine at a rate of loading of 0.4 KN/sec. The corresponding deflection at the load point, δ_y, was measured for the specimen. Then, the specimen was unloaded back to its original position using the same rate of loading. Using the deflection control mode, the specimen was loaded upward (positive load) to a deflection equal to the yield deflection, δ_y. The specimen was unloaded and the same procedure was repeated for two more cycles of deflection reversals. After the completion of three cycles, the deflection limit was increased by an increment of δ_y and three cycles of deflection reversals were applied. This procedure was repeated until the load-resisting capacity of the specimen decreased to less than the yield load, p_y, which indicated failure of the specimen. Load, deflection, and strain readings were recorded while load or deflection was kept constant at different intervals. The frequency of loading using the deflection control mode for each specimen is given in Table 3.1 .

For specimens in Series II, the first half cycle was loaded similarly to the procedures described previously. After the completion of the first half cycle, the deflection control was used to apply a reversed sine wave loading with a deflection increment of δ_y every three cycles. The calculation of the yield load for the specimens in Series I and II is given in Reference [4], Appendix (A).

In the case of Series III, the axial load was applied first and monitored with the reading of digital volt-meters before the

application of the vertical load. The calculation of the yield load for the specimens in this series is given in Reference [4], Appendix (B).

3.9 INSTRUMENTATION

The strains of the longitudinal steel were measured using electric resistance strain gauges. The position of these gauges for a typical specimen is shown in Fig. 3.18. The number of strain gauges used changed slightly from one specimen to the other during the program based on the need for data required to explain the mode of failure. Detailed locations of the strain gauges for each specimen can be found in Reference [4], Appendix (B).

In order to measure the average steel strain, LVDT's were mounted on the steel studs projected from the longitudinal reinforcement, as shown in Fig. 3.19 for a typical specimen. Again, the arrangement of the LVDT's changed during the test program. The arrangement for all the specimens can be found in Reference [4], Appendix (B).

Three ± ¼ inch travel LVDT's were installed for some specimens, as shown in Fig. 3.20, to measure the average shear strains near the fixed end. Based on the strain measurements in three directions, the principal strains were calculated using Mohr's circle, as explained in Reference [4], Appendix (F).

An additional LVDT was mounted on a steel bracket, as shown in Fig. 3.21, to measure the deflection at the location of the applied load. A schematic diagram for the instrumentation in Series I and III is given in Fig. 3.22, and that for series II is given in Fig. 3.23.

3.10 DATA ACQUISITION

Loads and deflections of the specimens were monitored on the digital display of the MTS machine and recorded continuously by an X-Y plotter. The latter served as the main indicator for the loading progress. Crack propagation was observed and marked using a magnifying lens, and sketches were plotted as the cracks progressed.

In the loading tests of Series I and III, all the values of loads, deflections, shear strains, and steel strains were measured and recorded using a Hewlett-Packard "H.P. 9825A" based data acquisition system. It consisted of a controller, digital multimeter, scanner and printer, as shown in Fig. 3.24. This unit could receive and process inputs up to 120 channels. Data were stored during testing on cassette tape cartridges. For each cycle of loading, between 30 and 40 sets of measurements were recorded, depending on the magnitude of the yield load, p_y. The schematic diagram of the data acquisition system is shown in Fig. 3.25.

In the loading test of Series II, deflection and steel strains were measured and recorded continuously with dynamic strain amplifiers (Intertechnology 2100 system), and ultraviolet recorder (U.V. recorder) as shown in Fig. 3.26. Crack propagation was observed and marked after the completion of three cycles of loading at each deflection limit.

CHAPTER IV

TEST RESULTS

4.1 INTRODUCTION

This chapter summarizes the observations and test results for each of the sixteen specimens tested in this program. Details of the test results are contained in Reference [4], Appendix (C). These results include the readings such as load, deflection, and strains collected during testing of each specimen. The hysteresis loops and crack patterns are also given in Reference [4], Appendices (D) and (E), respectively. A summary of the experimental results is given in Table 4.1. The first digit for the designation of the failure cycle in this table indicates the deflection increment and the final digit refers to the cycle number for that increment.

4.2 DEFINITION OF DUCTILITY FACTOR AND FAILURE

Ductility factor is commonly defined as the ratio between the ultimate deflection at failure, δ_u, and the yield deflection, δ_y. Such a definition is general and should be supplemented by the definition of failure. In this experimental program, a specimen is considered to have failed when it fails to sustain a load equal to the yield load, P_y, as shown in Fig. 4.1. Since all the specimens in this program are subjected to three cycles of reversals at each deflection increment, different cases of failure may occur, which will be dealt with in the following discussion.

A specimen may be able to sustain a load exceeding the yield load, P_y, in the first cycle, but fails to carry a load equal to yield

load in the second or third cycle, as shown in Fig. 4.2. In this case, since the specimen completed the first cycle of the (n-1)th deflection increment without failure, therefore the ductility factor is equal to n. If the load carrying capacity in the first cycle of the (n+1)th deflection increment is less than P_y even at the (n) δ_y deflection, as shown in Fig. 4.3, this indicates that the specimen has actually failed in the fourth cycle of the nth deflection increment. Therefore the ductility factor in this case is equal to n-1.

4.3 SERIES I

The specimens in this series were divided into two subseries, I-A and I-B, according to the objectives discussed in sections 3.3.1 and 3.3.2.

4.3.1 Subseries I-A

This subseries consists of three specimens (1-1, 1-2, and 1-3) with shear span-to-depth ratio, a/d, of 3.29, 5.0, and 6.05 respectively. The percentage of steel, p, was varied to maintain a constant ratio of the shear strength, v_c, to the yield shear stress, v_y. These specimens were used to study the effect of a/d on the behaviour and deformation capacity of the reinforced concrete piers.

4.3.1.1 Specimen 1-1

Specimen 1-1 had a shear span-to-depth ratio, a/d, of 3.29 and a percentage of longitudinal reinforcement, p, of 0.51%. The calculated yield load, P_y, and the measured yield deflection, δ_y, were 83.9 KN, and 3.77 mm, respectively.

During the three cycles of the first deflection increment, 1 δ_y, four flexural cracks developed due to loading in each direction, as shown in Fig. 4.4. During the three cycles of the second deflection increment, 2 δ_y, some of the flexural cracks extended to form flexural shear cracks. At the third deflection increment, one of the flexural shear cracks extended to form a major diagonal crack under the negative load. Another flexural shear crack extended under the positive load of the fourth deflection increment, 4 δ_y, to form an additional major crack. This crack crossed the previously formed diagonal tension crack and formed an x-shaped crack, as shown in Fig. 4.5. The width of the x-shaped crack increased during the successive deflection increment, 5 δ_y, up to 5.5 mm and 3.5 mm in the third cycle, 5 $\delta_y/3$, under negative and positive loads, respectively. Maximum measured negative and positive loads during the first cycle of this deflection increment were -98.26 KN (1.17 P_y) and 108.31 KN (1.29 P_y), respectively. Measured steel strains indicated yielding of the top and bottom longitudinal reinforcement at the d-section by the end of this deflection increment.

At the first cycle of the sixth deflection increment, 6 $\delta_y/1$, shown in Fig. 4.6, the width of the x-shaped crack increased to 6 mm and 4 mm at applied loads of -70 KN (0.83 P_y) and + 58 KN (0.69 P_y), respectively. The specimen was able to sustain a maximum load of -80.6 KN under a negative deflection of -18.02 mm during the first cycle. This load is equivalent to 96% of the yield load, P_y, and the corresponding deflection represents only 4.78 times the yield deflection, δ_y. However, as the deflection was increased to 6 δ_y, a significant reduction of the specimen load-carrying capacity was observed. Since

the failure of the specimen occurred at a deflection less than 5 δ_y in this cyle, the ductility factor is equal to 4 for this specimen. The failure was due to the widening of the x-shaped crack.

4.3.1.2 Specimen 1-2

Specimen 1-2 had a shear span-to-depth ratio, a/d, of 5.0 and a percentage of longitudinal reinforcement, p, of 0.96%. The calculated yield load, P_y, and the measured yield deflection, δ_y, were 65.8 KN and 6.7 mm, respectively.

During the first deflection increment, 1 δ_y, four flexural cracks formed under the negative load and three flexural cracks under the positive load. The initiated flexural cracks extended to form flexural shear cracks during the second deflection increment, 2 δ_y, as shown in Fig. 4.7. The measured steel strain at this deflection increment indicated yielding of the top and bottom longitudinal reinforcement at d-section. During the three cycles of the third deflection increment, 3 δ_y, the x-shaped crack developed fully, as shown in Fig. 4.8. The width of the x-shaped crack increased during the first cycle of the fourth deflection increment, 4 δ_y. Under the positive load, however, the newly formed cracks extended to form additional diagonal cracks adjacent to the x-shaped crack as shown in Fig. 4.9. A maximum positive load of 80.03 KN (1.22 P_y) was recorded at the first cycle of this deflection increment, 4 δ_y/1. During this deflection increment, the strains of the top and bottom longitudinal reinforcements measured at 1.5d and 2d sections were approximately 80% of the yield steel strains, ε_y.

During the first cycle of the fifth deflection increment,

5 δ_y/1, the average measured crack width of the x-shaped crack was 7 mm. Also during this cycle, the negative load increased with increasing deflection, up to a deflection equal to 24.02 mm (3.6 δ_y) with a corresponding load of 63.7 KN (0.96 P_y). Beyond this point, the load started to decrease with increasing deflection and a value of 59.6 KN (0.78 P_y) was recorded at a corresponding deflection of 33.5 mm (5 δ_y). According to the definitions of failure and ductility, the specimen failed to sustain a load more than P_y in this cycle and the ductility factor is equal to 3. However, when the specimen was loaded in the opposite direction, a second diagonal crack formed suddenly with a considerably larger width compared to the existing x-shaped crack. In addition, the bottom concrete cover close to the maximum moment section spalled off. This was accompanied with a sudden drop of positive load from 77 KN (1.2 P_y) to 33 KN (0.5 P_y). Based on these observations, it was concluded that the mode of failure of this specimen was different from that of specimen 1-1 due to the formation of the second diagonal crack under the positive load during the first cycle, as shown in Fig. 4.10.

4.3.1.3 Specimen 1-3

This specimen had a shear span-to-depth ratio, a/d, of 6.05 and a percentage of longitudinal reinforcement, p, of 1.26%. The calculated yield load, P_y, and the measured yield deflection, δ_y, were 57.8 KN and 8.56 mm, respectively.

During the three cycles of the first deflection increment, 1 δ_y, seven and nine flexural cracks formed under the negative and positive loads, respectively. No additional cracks initiated during

the second deflection increment, 2 δ_y. However, an x-shaped diagonal crack developed fully during the first cycle of the successive deflection increment, 3 $\delta_y/1$, as shown in Fig. 4.11. The top and bottom longitudinal reinforcements yielded at d-section during this deflection increment. A maximum load of 71.69 KN (1.24 P_y) was recorded in the positive direction.

The specimen sustained a load higher than the yield load, p_y, in the negative direction of the first cycle of the fourth deflection mm (3.74 δ_y). Therefore, the ductility factor for this specimen which failed in the 4 $\delta_y/1$ cycle is equal to 3, according to the definition. of 27.5 mm (3.2δ_y). Then, the load started to decrease with increasing deflection due to the formation of a second diagonal crack adjacent to the x-shaped crack. The width of this crack was increased suddenly leading to a sudden drop in the positive load from 72 KN (1.25 P_y) to 57 KN (0.99 P_y), as shown in Fig. 4.12. The load continued to drop to a value of 36.68 KN (0.63 P_y) at a corresponding deflection of 32.01 mm (3.74 δ_y). Therefore, the ductility factor for this specimen failed in 4 $\delta_y/1$ cycle is equal to 3, according to the definition.

4.3.2 Subseries I-B

The objective for this subseries is to investigate the effect of the percentage of steel, p, on the shear behaviour and ductility of reinforced concrete piers. This subseries consists of seven specimens. Three of these specimens were designed for a constant value for a/d of 6.05 and v_c/v_y ratios varying between 1.44 and 2.22 as the percentage of steel varied between 0.95 and 1.9%. Another three specimens had an a/d value of 3.29 and v_c/v_y ratios varying between

1.24 and 1.95 as the percentage of steel varied between 0.40 and 0.86%. The remaining specimen had an a/d value of 4.11, a v_c/v_y ratio of 1.82 and a percentage of steel of 0.64%.

Experimental results and calculated values for these specimens are given in Table 4.1. The test observations for each specimen will be presented separately in the following sections, retaining the same pattern and notation used for series I-A.

4.3.2.1 Specimen 1-4

This specimen had a shear span-to-depth ratio, a/d, of 6.05 and a percentage of longitudinal reinforcement, p, of 1.90%. The calculated yield load, P_y, and the measured yield deflection, δ_y, were 83.7 KN and 8.4 mm, respectively. After the three cycles of 1 δ_y, a total of nine to ten flexural cracks formed under both the negative and the positive loads. These cracks were distributed across a distance of approximately 4.5d from the maximum moment section.

The first diagonal crack initiated under the positive load in the first cycle, 2 $\delta_y/1$, as an extension of the flexural crack at a distance d from the maximum moment section. Under the negative load of the second cycle, 2 $\delta_y/2$, the other diagonal crack developed to form an x-shaped crack at a distance d from the maximum moment section. During the same cycle, a secondary crack parallel to the bottom reinforcement formed as a result of splitting action between the steel and concrete at a distance 2d from the maximum moment section, as shown in Fig. 4.13. During the third cycle, 2 $\delta_y/3$, the measured steel strains indicated yielding of the bottom reinforcement of the d-section. However, only one of the two measured steel strains for the top

reinforcement indicated yielding at the same section. Maximum loads during this deflection increment increased up to -93.41 KN (1.12 P_y) and +92.02 KN (1.10 P_y) in the negative and positive directions, respectively.

During the 3 δ_y/1 cycle, one of the arms of the x-shaped crack extended to join the secondary crack parallel to the bottom reinforcement, as shown in Fig. 4.8. An additional diagonal crack also initiated within a distance of 1.6 to 2d as an extension of one of the flexural cracks initiated previously. One of the two strain gauge readings of the bottom reinforcement at 2d-section indicated yielding during this deflection increment.

Under the negative load of the first cycle of the fourth deflection increment, 4 δ_y/1, the diagonal crack width increased, and a complete yielding of the top and bottom reinforcements at 2d-section was recorded. The load in the positive direction was increased by increasing the deflection up to a value of 49.39 KN (0.59 P_y) at a corresponding deflection of 8.65 mm (1.03 δ_y). The load started to decrease with increasing deflection to a value of 37.08 KN (0.44 p_y) at the maximum deflection of this increment, 4 δ_y. At the same time the secondary crack parallel to the top and bottom reinforcement was joined by a diagonal crack extending within a distance of 1.6d to 1.85d, as shown in Fig. 4.15. Since the positive load corresponding to a deflection of 3 δ_y was less than p_y, the specimen failed in this cycle, 4 δ_y/1, but the ductility factor for this specimen is equal to 2. The failure was due to the formation of a second diagonal crack.

4.3.2.2 Specimen 1-5

This specimen had a shear span-to-depth ratio, a/d of 6.05

and a percentage of the longitudinal reinforcement, p, of 0.95%. The calculated yield load, P_y, and the measured yield deflection, δ_y, were 43.8 KN and 6.9 mm, respectively. During the three cycles of $1\delta_y$, seven and five flexural cracks formed under the negative and positive loads, respectively. The majority of these cracks extended to form flexural-shear cracks during cycling of this deflection increment, as shown in Fig. 4.16.

During the first cycle of the second deflection increment, $2\delta_y/1$, one additiional flexural crack formed under the positive load at a distance of 3.7d from the maximum moment section, as shown in Fig. 4.17. During the three cycles of $2\delta_y$, only one of the two measured steel strains for the bottom reinforcement indicated yielding at the d-section.

During the first cycle of third deflection increment, $3\delta_y/1$, an x-shaped crack initiated within a distance d from the maximum moment section, as shown in Fig. 4.18. The measured steel strains indicated yielding of the bottom reinforcement at the d-section. The x-shaped crack developed fully during the fourth deflection increment, $4\delta_y$, as shown in Fig. 4.19. In addition, a secondary crack parallel to the bottom longitudinal reinforcement formed under the positive load within a distance 1.8d from the maximum moment section. Under the negative and positive loads of the third cycle, $4\delta_y/3$, the maximum widths of the x-shaped crack were 2 mm and 3 mm, respectively. The measured steel strains during the first cycle, $4\delta_y/1$, indicated yielding of the top longitudinal reinforcement at the d-section.

During the first cycle of fifth deflection increment, $5\delta_y/1$, the widths of the x-shaped crack under the maximum negative and

positive load increased to approximately 3.5 mm and 5 mm, respectively, as shown in Fig. 4.20. Maximum negative and positive loads also increased during this deflection increment up to -49.12 (1.12 P_y) and +54.23 KN (1.24 P_y), respectively.

The width of the x-shaped crack increased to 5 mm at the maximum applied load and the crack remained open even at the instant of unloading during the first cycle, $6\delta_y/1$. Spalling off of the bottom concrete cover across a distance approximately 2d from the maximum moment section was also observed. Only one of the two strain gauge readings from the top and bottom reinforcements indicated yielding of the steel at the 2d-section. During the second cycle, $6\delta_y/2$, the width of the flexural-shear crack at a distance 2d from the maximum moment section increased under the negative load. Buckling of the bottom longitudinal reinforcement was observed at a distance d from the maximum moment section, especially after spalling off of the concrete cover, as shown in Fig. 4.21. The load in the negative direction was increased by increasing the deflection up to a value of -35.11 KN (0.8 P_y) at a corresponding deflection of -28.12 mm (4.08 δ_y). The load started to decrease with increasing deflection to a value of -34.56 KN (0.79 p_y) at the maximum deflection of this increment, $6\delta_y$. The bottom longitudinal reinforcement continued to buckle under the negative load and straighten out due to the reversed load to the positive direction. One of the two measurements of steel strains indicated yielding of the top and bottom longitudinal reinforcements at the 2-d section.

4.3.2.3 Specimen 1-6

This specimen had a shear span-to-depth ratio, a/d, of 6.05 and a percentage of longitudinal reinforcement, p, of 1.58%. The calculated yield load, P_y, and the measured yield deflection, δ_y, were 70.8 KN and 8.5 mm, respectively. During the three cycles of yield deflection, $1\delta_y$, a total of ten flexural cracks formed under the negative and positive loads. After the third cycle of this deflection increment, $1\delta_y/3$, an x-shaped crack started to form.

During the first cycle of this deflection increment, $2\delta_y/1$, the measured steel strains indicated yielding of the top longitudinal reinforcement at the d-section. However, only one of the two measured steel strains for the bottom longitudinal reinforcement indicated yielding at the same section. The x-shaped crack developed fully by the end of the second cycle, $2\delta_y/2$, as shown in Fig. 4.22. Maximum negative and positive loads increased during this deflection increment up to -78.11 KN (1.10 P_y) and +78.74 KN (1.11 P_y), respectively.

During the third cycle of the third deflection increment, $3\delta_y/3$, the width of the x-shaped crack increased to approximately 5 mm. A secondary crack parallel to the bottom reinforcement also formed, as shown in Fig. 4.23. Under the negative load, in this cycle, a maximum load of -70.22 KN (0.99 P_y) was recorded. During the first cycle of the fourth deflection increment, $4\delta_y/1$, the specimen sustained a negative load of -72.04 KN (1.02 P_y), corresponding to the maximum deflection of -34 mm ($4\delta_y$). However, the specimen sustained only a load of +45.28 KN (0.64 P_y) at the maximum deflection, $4\delta_y$, in the positive direction. At the same time, one of the arms of the x-shaped crack widened and extended to join the secondary crack along the bottom

longitudinal reinforcement, as shown in Fig. 4.24. The specimen was considered to have failed under the positive load of the first cycle of this deflection increment, $4\delta_y/1$. The measurements of strains indicated yielding of longitudinal reinforcements of the 2d-section during $4\delta_y/1$ cycle and before the failure of the specimen. The ductility factor for this specimen is equal to 2.

4.3.2.4 Specimen 1-7

This specimen had a shear span-to-depth ratio, a/d, of 3.29 and a percentage of longitudinal reinforcement, p, of 0.40%. The calculated yield load, P_y, and the measured yield deflection, δ_y, were 66.1 KN and 2.66 mm, respectively. During the three cycles of $1\delta_y$, three to four flexural cracks formed under each load direction across a distance of 1.4 times the effective depth, d, as shown in Fig. 4.25. During the three cycles of the second deflection increment, $2\delta_y$, the propagation of the cracks was insignificant. Similarly, the crack formation during the third deflection increment, $3\delta_y$, was insignificant, as shown in Fig. 4.26.

During the three cycles of the fourth deflection increment, $4\delta_y$, the width of the flexural crack at the maximum moment section increased to 3 mm, as shown in Fig. 4.27. Maximum negative and positive loads also increased up to -69.77 KN (1.06 P_y) and +79.65 KN (1.2 P_y), respectively. During the fifth deflection increment, $5\delta_y$, the flexural cracks initiated previously extended to form flexural-shear cracks, as shown in Fig. 4.28. In addition, small secondary cracks, formed along the top longitudinal reinforcement near the maximum moment section. A major diagonal crack formed under the negative load within a distance

of 0.73 d from the maximum moment section. During the same cycle new flexural cracks formed under the same load direction at a distance of 2.07 d from the maximum moment section.

During the sixth deflection increment, $6\delta_y$, the width of the flexural crack at the maximum moment section increased to approximately 4 to 5 mm under the positive load direction, as shown in Fig. 4.29. Maximum negative and positive loads increased up to -73.65 KN (1.11 P_y) and +82.82 KN (1.25 P_y), respectively. During the following deflection increment, $7\delta_y$, formation of new cracks was insignificant compared to the increase in the width of the existing flexural cracks and spalling off of the concrete cover near the maximum moment sections, as shown in Fig. 4.30. The negative load started to decrease to a maximum of -66.1 KN ($1P_y$), corresponding to the maximum deflection of the third deflection increment, $7\delta_y/3$.

During the eighth deflection increment, $8\delta_y$, the width of the flexural crack increased to 9 mm at the maximum moment section and spalling off of the concrete cover was also observed, as shown in Fig. 4.31. The negative load corresponding to the maximum deflection of the second cycle of this deflection increment, $8\delta_y/2$, was less than P_y. Therefore, the specimen was considered to have failed under the negative load of $8\delta_y/2$ and the ductility factor is equal to 7. The widening of the flexural crack at the maximum moment section led to a large vertical relative movement along the flexural crack, as shown in Fig. 4.32. This large vertical relative movement was considered to be the cause of failure, which has been categorized as sliding shear failure [47].

4.3.2.5 Specimen 1-8

This specimen had a shear span-to-depth ratio, a/d, of 3.29 and a percentage of the longitudinal reinforcement, p, of 0.46%. The calculated yield load, P_y, and the measured yield deflection, δ_y, were 74.8 KN and 2.77 mm, respectively. During the first cycle, $1\delta_y/1$, six flexural cracks formed under the negative load. One of the flexural cracks, at a distance of 0.94d, extended to form a diagonal crack. Under the positive load of the same cycle, three flexural cracks formed, as shown in Fig. 4.33.

The crack pattern remained without any significant change for the first and second cycles of the second deflection increment, $2\delta_y/1$ and $2\delta_y/2$. In the third cycle, $3\delta_y/2$, one flexural crack formed under the positive load at a distance of 1.44d from the maximum moment section. During three cycles of the third deflection increment, $3\delta_y$, a major diagonal crack formed under the positive load as an extension to a previously existing flexural crack at a distance of 0.93d from the maximum moment section, as shown in Fig. 4.34. During the fourth deflection increment, $4\delta_y$, the crack pattern remained the same, but an increase in the flexural crack width near the maximum moment section was observed.

During the three cycles of the fifth deflection increment, $5\delta_y$, a secondary crack formed along the top reinforcement within a distance of 0.43d from the maximum moment section. In addition, the widths of most of the flexural-shear cracks near the maximum moment section increased, as shown in Fig. 4.35. Maximum negative and positive loads recorded during this deflection increment also increased to -82.77 KN (1.11 P_y) and +90.35 KN (1.21 P_y), respectively.

During the second cycle of the sixth deflection increment, $6\delta_y/2$, the width of the flexural crack at 0.29d was approximately 4 mm. In the third cycle, $6\delta_y/3$, the previously existing flexural crack at the 2d-section extended under the negative load and formed a flexural-shear crack. Maximum negative and positive loads recorded during this deflection increment were -84.1 KN (1.12 P_y) and +91.51 KN (1.22 P_y), respectively.

During the seventh deflection increment, $7\delta_y$, an x-shaped crack developed fully, as shown in Fig. 4.36. The measured width of the flexural crack at the maximum moment section was approximately 5 mm. Maximum negative and positive loads recorded were -87.05 KN (1.16 P_y) and + 90.72 KN (1.21 P_y), respectively. The eighth deflection increment, $8\delta_y$, was accompanied with a large vertical relative movement near the maximum moment section and spalling off of the concrete cover, as shown in Fig. 4.37.

A large chunk of the concrete at the maximum moment section spalled off as the deflection was increased to $9\delta_y$, as shown in Fig. 4.38. At the maximum deflection of the second and third cycles, $9\delta_y/2$ and $9\delta_y/3$, the specimen sustained only a maximum load of -71.8 KN (0.96 P_y) and -66.92 KN (0.89 P_y), respectively. The specimen was considered to have failed under the negative load of $9\delta_y/2$. Hence the ductility factor for this specimen is equal to 8. The failure was due to the large vertical relative movement at the maximum moment section.

4.3.2.6 Specimen 1-9

This specimen had a shear span-to-depth ratio, a/d, of 3.29

and a percentage of longitudinal reinforcement, p, of 0.86%. The calculated yield load, P_y, and the measured yield deflection, δ_y, were 140.7 KN and 4.68 mm, respectively. Five to six flexural cracks formed under each load direction of the first cycle, $1\delta_y/1$. These cracks extended to form flexural-shear cracks during the same cycle as shown in Fig. 4.39. During the first cycle of the next deflection increment, $2\delta_y/1$, minor crack propagation occurred. But, during the second and third cycles, $2\delta_y/2$ and $2\delta_y/3$, critical diagonal cracks formed under both load directions. These two diagonal cracks intersected at a distance approximately 0.5d from the maximum moment section to form an x-shaped crack, as shown in Fig. 4.40. Secondary cracks along the top reinforcement also formed during this deflection increment. Maximum negative and positive loads increased up to -151.7 KN (1.08 P_y) and +150.66 KN (1.07 P_y), respectively.

Under the positive load of the first cycle of the third deflection increment, $3\delta_y/1$, another diagonal crack formed as an extension of a previously existing flexural crack at a distance of 1.11d from the maximum moment section. During the third cycle, $3\delta_y/3$, and under the positive load direction, a secondary crack along the bottom reinforcement formed, as shown in Fig. 4.41. The measured width of the x-shaped crack was approximately 2 mm. Both measurements of steel strains at d-section indicated yielding of the top longitudinal reinforcement. However, only one of the two readings of steel strain indicated yielding of the bottom reinforcement at the same section.

The specimen was able to maintain a negative load of -146.6 KN (1.04 P_y) in the first cycle of the fourth deflection increment, $4\delta_y/1$. The width of the x-shaped crack was approximately 8 mm. In

the positive direction of the same cycle, $4\delta_y/1$, the load dropped from 142.79 KN (1.02 P_y) to 96.56 KN (0.69 P_y) at deflections of 12.1 mm (2.59 δ_y) and 18.8 mm ($4\delta_y$), respectively. At the same time, the diagonal crack at 1.11d extended up to the maximum moment section, as shown in Fig. 4.42. Since the load dropped to a value less than the yield load, P_y, under a deflection less than $3\delta_y$, the specimen was considered to have failed under the positive load of the first cycle, $4\delta_y/1$. The ductility factor for this specimen is equal to 2.

4.3.2.7 Specimen 1-10

This specimen had a shear span-to-depth ratio, a/d, of 4.11 and a percentage of the longitudinal reinforcement, p, of 0.64%. The calculated yield load, P_y, and the measured yield deflection, δ_y, were 68 KN and 4.21 mm, respectively. Approximately five flexural cracks formed under each load direction of the first cycle, $1\delta_y/1$. The flexural cracks at a distance of 1.6d extended to form flexural-shear cracks during the same cycle, as shown in Fig. 4.43. All strain readings indicated yielding of the top and bottom reinforcements at the maximum moment section. The cracking pattern remained almost the same after the three cycles of the second deflection increment, $2\delta_y$.

During the third deflection increment, $3\delta_y$, the flexural crack at 0.29d extended diagonally to the maximum moment section, as shown in Fig. 4.44. The width of the flexural crack was approximately 2 mm at the maximum moment section. Under the negative load of the first cycle of the next deflection increment, $4\delta_y/1$, an additional flexural-shear crack formed at 0.6d from the maximum moment section,

as shown in Fig. 4.45. The width of the flexural crack at the maximum moment section increased to 4 mm. Maximum negative and positive loads also increased to -73.2 KN (1.08 P_y) and +78.6 KN (1.16 P_y), respectively.

During the fifth deflection increment, $5\delta_y$, another flexural shear crack formed under the positive load, as shown in Fig. 4.46. In addition, the flexural crack width increased to a value of 5 mm at the maximum moment section. During the sixth deflection increment, $6\delta_y$, a new flexural-crack initiated under the positive load at a distance of 2.64d from the maximum moment section. Steel strain readings indicated the yielding of the bottom longitudinal reinforcement of the d-section, while the measured strains of the top reinforcement were close to the steel yield strain, δ_y, at the same section. Maximum negative and positive loads increased up to -74.14 KN (1.09 P_y) and +82.76 KN (1.22 P_y), respectively.

During the three cycles of the seventh deflection increment, $7\delta_y$, vertical relative movement and increasing width of the cracks within a distance of 0.7d were observed. Chunks of concrete near the maximum moment section started to spall off, as shown in Fig. 4.47. The strain gauges readings at the d-section indicated yielding of both the top and bottom longitudinal reinforcements. The maximum load corresponding to the maximum deflection of the third cycle, $7\delta_y/3$, was -64.84 KN (0.95 P_y).

During the first cycle of the eighth deflection increment, $8\delta_y/1$, the vertical relative movement at the maximum moment section was more noticeable. Spalling off of the concrete was also observed, as shown in Fig. 4.48. The specimen was considered to have failed

at the third cycle of the seventh deflection increment, $7\delta_y/3$. Therefore, the ductility factor for this specimen is equal to 6.

4.4 SERIES II

Four specimens were tested in this series to investigate the effect of the load frequency on the mode of failure, ductility, strength, and stiffness of reinforced concrete bridge piers. Three specimens were designed for a constant a/d value of 3.29 and a constant p of 0.51%. One specimen with a/d = 6.05 and p = 1.26% was also tested in this series. The load was applied continuously and cycled three times at each deflection increment. The load frequency varied between 0.01 and 0.2 HZ. The crack propagation was marked under zero deflection after the completion of the three cycles of loading for each deflection increment. The results for these specimens were comparable to those in subseries I-A with similar values of a/d and p, and tested under a low load frequency of 0.0004 HZ. A summary of the test results and calculated values for the specimens in this series is given in Table 4.1. The test observations for each specimen will be presented separately in the following subsections, retaining the same pattern and notations used for the specimens in Series I.

4.4.1 Specimen 2-1

This specimen had a shear span-to-depth ratio, a/d , of 3.29 and a percentage of longitudinal reinforcement, p, of 0.51% identical to specimen 1-1. The specimen was tested undr a load frequency of 0.01 HZ. The calculated yield load, P_y, and the measured yield deflection, δ_y, were 83.8 KN and 3.74 mm, respectively.

During the three cycles of the first deflection increment, $1\delta_y$, three and four flexural cracks formed under the positive and negative loads, respectively. Some of these cracks extended to form flexural-shear cracks. During the second deflection increment, $2\delta_y$, another flexural crack formed at the maximum moment section and extended to form a flexural-shear crack. A major x-shaped crack developed fully during the third deflection increment, $3\delta_y$. Furthermore, two new flexural cracks formed under the positive load.

At the first cycle of the fourth deflection increment, $4\delta_y/1$, the specimen was able to sustain a load greater than the yield load, P_y, in the positive and negative directions. Readings of both strain gauges located at the d-section indicated yielding of the bottom longitudinal reinforcement. At the second cycle, $4\delta_y/2$, the specimen was able to sustain a load greater than P_y in the positive direction, but failed to carry a load equal to P_y in the negative direction. The maximum recorded negative load was -74 KN (0.88 P_y), corresponding to the maximum deflection of -14.96 mm ($4\delta_y$). Therefore, the specimen was considered to have failed at this cycle. The significant increase in width of the x-shaped crack was observed prior to failure, as shown in Fig. 4.49. This behaviour was considered to be the cause of the failure, as was the case for specimen 1-1. The ductility factor for this specimen is equal to 3.

4.4.2 Specimen 2-2

This specimen had a shear span-to-depth ratio, a/d, of 3.29 and a percentage of longitudinal reinforcement, p, of 0.51%. The specimen was tested at a load frequency of 0.2 HZ. The calculated

yield load, P_y, and the measured yield deflection, δ_y, were 83.8 KN and 3.8 mm, respectively.

During the first deflection increment, $1\delta_y$, three or four flexural cracks formed under each load direction. Some of these cracks extended to form flexural-shear cracks. During the second deflection increment, $2\delta_y$, only one additional flexural crack formed at the maximum moment section. However, the formation of the x-shaped crack almost completed by the end of the third deflection increment, $3\delta_y$. During the fourth deflection increment, $4\delta_y$, the x-shaped crack developed fully. In addition, four flexural cracks formed and then extended to develop flexural-shear cracks. The maximum loads during this increment were lower than those in the third deflection increment. However, the specimen maintained a maximum load higher than P_y, corresponding to the maximum deflection of $4\delta_y$. The readings of all the strain gauges located at the d-section indicated yielding of the top and bottom longitudinal reinforcements.

At the first cycle of the fifth deflection increment, $5\delta_y/1$, the specimen sustained a load greater than P_y in both directions. The width of the x-shaped crack increased during this cycle. At the second cycle, $5\delta_y/2$, the specimen failed to maintain a maximum load higher than P_y in the negative direction. The maximum negative load was -64 KN (0.76 P_y), corresponding to the maximum deflection. The crack pattern at failure was similar to that for specimen 2-1, as shown in Fig. 4.50. The widening of the x-shaped crack was considered to be the cause of failure. The ductility factor for this specimen is equal to 4.

4.4.3 Specimen 2-3

This specimen had a shear span-to-depth ratio, a/d, of 3.29 and a percentage of longitudinal reinforcement, p, of 0.51%. The specimen was tested at a load frequency of 0.05 HZ. The calculated yield load, P_y, and the measured yield deflection, δ_y, were 83.3 KN and 3.33 mm, respectively.

During the three cycles of the first deflection increment, $1\delta_y$, three flexural cracks formed under each load direction, as shown in Fig. 4.51. During the second deflection increment, $2\delta_y$, a full-depth flexural crack formed at the maximum moment section.

During the third deflection increment, $3\delta_y$, two new flexural cracks initiated and extended to form flexure-shear cracks. In addition, a secondary crack formed along the top reinforcement, as shown in Fig. 4.52. An x-shaped crack developed fully by the end of the third cycle of the fourth deflection increment, $4\delta_y/3$, as shown in Fig. 4.53. The reading of all the strain gauges at the d-section indicated yielding of the top reinforcement during the fifth deflection increment, $5\delta_y$. At the maximum deflection of the third cycle, $5\delta_y/3$, as shown in Fig. 4.54, the corresponding load was 81 KN (0.97 P_y). At the maximum deflection of the first cycle of the sixth deflection increment, $6\delta_y/1$, the specimen sustained only a load of -63 KN (0.76 P_y). The failure was due to the widening of the x-shaped crack, as shown in Fig. 4.55. The ductility factor for this specimen is equal to 4.

4.4.4 Specimen 2-5

This specimen had a shear span-to-depth ratio, a/d, of 6.05 and a percentage of longitudinal reinforcement, p, of 1.26%. The

specimen was tested at a load frequency of 0.1 HZ. The calculated yield load, P_y, and the measured yield deflection, δ_y, were 58.8 KN and 6.54 mm, respectively.

During the first deflection increment, $1\delta_y$, six flexural cracks formed under each load direction across a distance of 4.2d, as shown in Fig. 4.56. One more flexural crack formed under the positive load during the second deflection increment, $2\delta_y$. In addition, some of the flexural cracks within a distance of 1.7d extended to form flexural-shear cracks, as shown in Fig. 4.57. During the first cycle of the third deflection increment, $3\delta_y/1$, yielding of the top and bottom reinforcements at the d-section were recorded. Complete formation of a diagonal crack was also observed within a distance d from the maximum moment section under the positive load, as shown in Fig. 4.58. During the fourth deflection increment, $4\delta_y$, an x-shaped crack developed fully, as shown in Fig. 4.59. During the successive deflection increment, $5\delta_y$, secondary cracks formed along the top and bottom reinforcements. These secondary cracks joined together by a flexural-shear crack, as shown in Fig. 4.60.

At the second cycle of the sixth deflection increment, $6\delta_y/2$, the positive load corresponding to the maximum deflection was +58 KN (0.99 P_y). However, the load in the negative direction dropped suddenly to -28 KN (0.48 P_y), corresponding to the maximum deflection, $6\delta_y$, as shown in the hysteresis loop of this specimen in Reference [4], Appendix (D). Since the decrease in the maximum load in the negative direction was greater compared to that in the positive direction, the specimen was considered to have failed under the negative load after the first cycle, $6\delta_y/1$. Therefore, the ductility factor for this

specimen is equal to 5. The continuation of the loading test for three continuous cycles caused some difficulties in observation of the crack pattern at the failure cycle. However, the development of a second diagonal crack was considered to be the cause of failure.

4.5 SERIES III

The objective of this series was to investigate the effect of axial compressive stresses on the mode of failure, ductility, and strength of the reinforced concrete bridge piers. This series consists of two specimens, 3-1 and 3-3, with a/d ratios of 3.29 and 6.05, respectively. These specimens were tested under static loading condition and in the presence of axial compressive stresses of 0.98 MPa. The test observations for each specimen will be presented in the following subsections, retaining the same rotations used for the specimens in series I and II.

4.5.1 Specimen 3-1

This specimen had a shear span-to-depth ratio, a/d, of 3.29 and a percentage of longitudinal reinforcement, p, of 0.51%, identical to specimen 1-1. However, specimen 3-1 was subjected to an axial compressive force, N, of 196.2 KN which produced a constant axial compressive stress of 0.98 MPa throughout the test. The calculated yield load, P_y, and the measured yield deflection, δ_y, were 108.7 KN and 3.55 mm, respectively.

During the three cycles of the first deflection increment, $1\delta_y$, four flexural cracks formed under each load direction. Some of these cracks extended to form flexural-shear cracks. During the second

deflection increment, $2\delta_y$, the width of the flexural cracks increased to approximately 2 mm under the negative load. Furthermore, a diagonal crack initiated under the positive load, as shown in Fig. 4.61. The readings of strain gauges located at the maximum moment section indicated yielding of the top and bottom longitudinal reinforcements. An x-shaped crack started to develop from the existing diagonal cracks during the third deflection increment, $3\delta_y$, as shown in Fig. 4.62. Maximum negative and positive loads were -113.7 KN (1.05 p_y) and +127.6 KN (1.17 P_y), respectively.

During the fourth deflection increment, $4\delta_y$, another flexural crack formed under the positive load at 2.07d from the maximum moment section. Reading of strain gauges located at the d-section indicated yielding of the bottom reinforcement. The x-shaped crack developed fully during the second cycle of the fifth deflection increment, $5\delta_y/2$, as shown in Fig. 4.63. Widths of the x-shaped crack were 3 and 5 mm under the negative and positive loads of the third cycle, $5\delta_y/3$, respectively. Reading of strain gauges located at the d-section indicated yielding of both the top and bottom reinforcements. Maximum negative and positive loads were -119.4 KN (1.1 P_y) and +126.1 KN (1.16 P_y), respectively. At the first cycle of the sixth deflection increment, $6\delta_y/1$, shown in Fig. 4.64, the width of the x-shaped crack increased to 6 mm under the positive load. During the second cycle, $6\delta_y/2$, the width of the x-shaped increased further and the maximum positive load decreased to a value of +71.2 KN (0.66 P_y), corresponding to the maximum deflection of 21.3 mm ($6\delta_y$). The specimen failed at this cycle, due to the widening of the x-shaped crack, as shown in Fig. 4.65. The ductility factor for this specimen is equal to 5.

4.5.2 Specimen 3-3

This specimen had a shear span-to-depth ratio, a/d of 6.05 and a percentage of longitudinal reinforcement, p, of 1.26%, identical to specimen 1-3. However, specimen 3-3 was subjected to an axial compressive force, N, of 112.8, which produced a uniform axial compressive stress of 0.98 MPa throughout the test. The calculated yield load, P_y, and the measured yield deflection, δ_y, were 64.7 KN and 8.14 mm, respectively.

During the three cycles of the first deflection increment, $1\delta_y$, five and eight flexural cracks formed under the negative and positive load directions, respectively, as shown in Fig. 4.66. During the second deflection increment, $2\delta_y$, an additional flexural crack formed under each load direction at a distance of 2.2d from the maximum moment section. Some of the flexural cracks formed previously extended to form flexural-shear cracks, as shown in Fig. 4.67. Furthermore, an x-shaped crack formed in this deflection increment and developed fully during the following deflection increment, $3\delta_y$. Readings of all strain gauges located at the d-section indicated yielding of the top and bottom longitudinal reinforcements during the third cycle, $3\delta_y/3$. Maximum negative and positive loads were -68.5 KN (1.06 P_y) and +75.5 KN (1.17 P_y), respectively.

During the fourth deflection increment, $4\delta_y$, a second diagonal crack formed, extending between distances of 1.3d to 1.8d. This crack extended to join the x-shaped crack, as shown in Fig. 4.68. In addition, the width of the x-shaped crack increased to 2 and 3 mm under the positive and negative load, respectively. During the second cycle of the fifth deflection increment, $5\delta_y/2$, the maximum negative load

corresponding to the maximum deflection of $5\delta_y$ decreased drasticallly to -23.8 (0.37 P_y). At the same time, readings of the strain gauges located at the 2 d-section indicated yielding of the top longitudinal reinforcement. The specimen was considered to have failed under the negative load of the second cycle, $5\delta_y/2$, due to the widening of the x-shaped crack, although the width of the second diagonal crack was approximately 1 mm, as shown in Fig. 4.69. Therefore, the ductility factor for this specimen is equal to 4.

CHAPTER V

DISCUSSION OF EXPERIMENTAL RESULTS

5.1 INTRODUCTION

The main objective of this chapter is to clarify the criteria of shear failure of reinforced concrete bridge piers subjected to deflection reversals large enough to cause extensive yielding of longitudinal reinforcement. The categorization of crack patterns observed for the tested specimens as related to the mode of failure will be discussed in Section 5.2. Based on the measured steel strains, the relationship between the extent of yielding of the longitudinal reinforcement and the mode of failure are presented in Section 5.3. A nondimensional factor will be introduced in Section 5.4 to describe the fundamental behaviour of bridge piers such as ductility, energy dissipation capacity, maximum shear stress, work index, and damping characteristics. Each of these will be discussed individually in Sections 5.4, 5.5, 5.6, 5.8, 5.9, and 5.11, respectively. The nondimensional characteristic factor will be used to derive expressions for prediction of each of the previously mentioned variables. A rational classification of the mode of failure based on the intensity of applied shear stresses will be presented in Section 5.7, parallel to a categorization on the basis of the characteristic factor. The effect of load frequency and axial compressive load on the behaviour and the ductility of bridge piers will be dealt with in Sections 5.9 and 5.10, respectively. Finally, the stiffness of reinforced concrete bridge piers in the post-yielding range will be examined in Section 5.12.

5.2 CRACK PATTERN

The successive crack patterns including the final pattern for each specimen are given in Reference [4], Appendix (E). Sketches for the major crack pattern configuration for each specimen tested in Series I of this program are given in Figures 5.1 to 5.4. In these figures, the direction of the load at failure is shown for each specimen.

Diagonal tension cracks normally formed as extensions of the initiated flexural cracks under each load direction. Due to the nature of the applied reversed cyclic loading, the diagonal cracks intersected each other to form x-shaped cracks for most of the specimens. The test observations presented in Chapter IV indicated the importance of the x-shaped cracks, and the yielding of the longitudinal reinforcement as related to the mode of failure. For this reason, the locations of the x-shaped crack in each specimen will be compared. The length of the flexural cracking zone as related to the yielding of the longitudinal reinforcement will also be compared for all the specimens.

In the following discussion, the specimens will be categorized according to the value of the shear span-to-depth ratio, a/d. For each category, the effect of the percentage of the longitudinal reinforcement, p, on the shape of the crack pattern will be discussed as related to the mode of failure.

5.2.1 Specimens With $3.29 \leq a/d \leq 4.1$

The typical crack configuration for this category is shown in Fig. 5.1.a. The failure in this case occurred mainly due to the

widening of the x-shaped crack. Normally, following this mechanism, a secondary crack parallel to the longitudinal reinforcement formed in the tension side, corresponding to the direction of the failure load, as shown in Fig. 5.1.a. The x-shaped crack generally occurred within a distance equal to the effective depth, d, measured from the maximum moment section. For this category the length of the flexural crack zone varied between 1.6d and 2.16d. The above information about the exact location of the cracks is shown in Figs. 5.1 and 5.2 and listed in Tables 5.1 and 5.2.

For specimens with relatively low percentages of steel, i.e., specimens 1-8 and 1-10, the x-shaped diagonal crack was also formed within the d-section, as shown in Figures 5.1.b and 5.2.c. While the width of the diagonal cracks remained very small, the failure was mainly due to the large vertical relative movement at the maximum moment section, as shown in Fig. 4. 30. For specimen 1-7, with the lowest percentage of steel in this category, 0.4%, only one arm of the x-shaped crack formed, as shown in Fig. 5.1.c. This could be attributed to the low intensity of the applied shear in this specimen. The failure of this specimen was also due to the large vertical movement at the maximum moment section, which has been categorized as sliding shear failure [40].

For specimens with a relatively large percentage of longitudinal reinforcement in this category, i.e., specimen 1-9, both the x-shaped crack and secondary cracks formed at a location similar to the typical specimen, as shown in Fig. 5.1.d. However, the failure occurred due to the formation of a second diagonal crack initiated at 1.41d and extended to the maximum moment section.

5.2.2 Specimens With $5 \leq a/d \leq 6.05$

For specimens with a/d values of 5.0 and 6.05, the x-shaped crack formed at a distance approximately d from the maximum moment section. A secondary crack formed in the tension side corresponding to the direction of the failure load, as shown in Fig. 5.4.a. Typical failure occurred due to the initiation of a second diagonal crack at an approximate distance of 2d, as shown in Fig. 4.12. The crack configurations of all the specimens in this category tested in Series I are given in Figures 5.3 and 5.4.

For a specimen with a relatively low percentage of steel in this category, specimen 1-5, the failure was due to local buckling of the longitudinal reinforcement at the location of the x-shaped crack, as shown in Fig. 4.18. The formation of a second diagonal crack was not observed. The length of the flexural crack zone of the specimens in this category varied between 3.58d and 4.5d with an average value of approximately 4d. This indicates that the length of the flexural crack zone relative to the effective depth, d, is longer for specimens with large values of a/d.

The observed crack configurations at failure clearly indicate the significant effect of the percentage of longitudinal reinforcement within a given range of a/d. This confirms the theory that both a/d and p greatly influence the mode of failure, and that a combination of their effects is necessary to identify the failure mechanisms for reinforced concrete bridge piers.

5.3 STRAIN OF LONGITUDINAL REINFORCEMENT

In this experimental program, the strains of the longitudinal

reinforcements were measured at the maximum moment section, and at other various locations, as specified previously in section 3.9. Under the calculated yield load, P_y, the readings of the strain gauges placed at the maximum moment section were approximately equal to the steel yield strain, δ_y, at the first cycle of the first deflection increment, $1\delta_y/1$. These strain readings exceeded the steel yield strain at the first cycle of the second deflection increment, $2\delta_y/1$. The average measured steel strains at different locations in the direction of failure are shown in Figs. 5.5 to 5.7 for all the specimens tested in Series I of this program. The strain values are based on the average of the reading of two strain gauges placed at the same location. Occasionally, the strain values were based on one strain gauge only, due to the instability of the second gauge. In the same figures, the yield strain is given by a horizontal line and its value is based on the material properties given in Table 3.4. In addition, the cycle at which the specimen failed is presented by a vertical line in the same figures. Additional information about the steel strain can be found in Table 5.2, and the exact readings of the strain gauges are given in Reference [4], Appendix (C).

In the following discussion, the specimens will be categorized according to the value of the shear span-to-depth ratio, a/d. For each category, the influence of the percentage of the longitudinal reinforcement, p, on the extent of yielding of the longitudinal reinforcement will be discussed as related to the mode of failure.

5.3.1 Specimens With $3.29 \leq a/d \leq 4.1$

In this range of a/d, the strains of the longitudinal

reinforcements of a typical specimen, specimen 1-1, were measured at the location of the maximum moment section and at the d-section only. The strain of the longitudinal reinforcement at the d-section for this specimen is shown in Fig. 5.5.a. This figure clearly indicates that the longitudinal reinforcement yields at d-section during the failure cycle. This implies that the load carrying capacity of the specimen is decreased to less than P_y, due to yielding of the reinforcement at or near the location of the x-shaped crack. However, for specimens with relatively low percentage of steel in this category, specimens 1-7, and 1-8, which failed due to large vertical relative movement at the maximum moment section, no yielding of the longitudinal reinforcement at the d-section was observed before failure, as shown in Figs. 5.5.b and 5.5.c, respectively. For specimen 1-10, with percentage of steel of 0.64% and a/d value of 4.1, which also failed due to sliding shear, yielding of the longitudinal reinforcement at d-section was measured prior to failure, as shown in Fig. 5.5.d. This could be the reason for the formation of the diagonal crack closer to the maximum moment section in comparison to specimens 1-7 and 1-8.

For specimen 1-9, with a relatively high percentage of steel and a/d of 3.29, although a second diagonal crack formed in addition to the x-shaped crack, the longitudinal reinforcement yielded only at the d-section, as shown in Fig. 5.5.e. The failure occurred after the yielding of the longitudinal reinforcement under the same deflection increment, as was the case for the typical specimen. Based on the above discussion, the extent of yielding of the longitudinal reinforcement could be used in classification of the mode of failure for such members.

5.3.2 Specimens With $5.0 \leq a/d \leq 6.05$

The strains of the longitudinal reinforcement were typically measured at d, 1.5d and 2d sections, as shown in Fig. 5.6 for specimen 1-2. The typical specimens in this category were able to sustain one or two more deflection increments after yielding of the longitudinal reinforcement at the d-section, as shown in Figures 5.7.a, b, c. The specimens failed due to the formation of a second diagonal crack after the yielding of the longitudinal reinforcement at the 2d-section. The average strains measured at different locations in these specimens are shown in the same figures.

For specimen 1-5, with the lowest percentage of steel in this category, the failure occurred due to the buckling of the longitudinal reinforcement within the location of the x-shaped crack. This specimen was able to sustain two more deflection increments after yielding of the longitudinal reinforcement at the d-section, as shown in Fig. 5.7.d. The strain of the longitudinal reinforcement at the 2d-section was approximately 95% of the yield strain, ε_y.

Since the strain measurements were not continuously recorded for specimens tested in Series I and III, the maximum strain may not have been recorded for these specimens. However, the strain of steel for specimens in Series II, e.g., specimen 2-5, shown in Fig. 5.8, was recorded continuously by U.V. recorder. The continuous strain measurements indicated the yielding of steel at the 2d section before the peak deflection of the failure cycle, $6\delta_y/2$, was attained. This strain might not have been recorded if the strain measurements were taken in certain intervals. For this reason, the yielding of the longitudinal reinforcement at the 2d-section is considered to have

occurred, in general, for all the specimens in this category.

5.4 DUCTILITY

The ductility factor, μ, which expresses the deformation capacity of the structural members, is defined in this study as the ratio between the maximum deflection before failure, δ_u, and the deflection at yielding, δ_y. The ductility factor for all specimens tested in this program is given in Table 4.1. It is clear that the magnitudes of the ductility factors are relatively low since the specimens were designed to fail in shear. The test results indicated that ductility decreases with the increase of the percentage of longitudinal steel, p. Since all the specimens failed in shear, the ductility is also influenced by the shear span-to-depth ratio, a/d, and the tensile strength of the concrete, f_t [18].

The deformation capacity of members could also be measured by the curvature ductility factor, μ_ϕ, which is the ratio between the curvature at ultimate, ϕ_u, and the yield curvature, ϕ_y. The curvature ductility of doubly reinforced beams and columns subjected to monotonic loading, determined analytically [42], could be used to evaluate the displacement ductility factor, μ [38]. However, no expression has yet been introduced for the evaluation of the ductility factor under reversed cyclic loading conditions. While the flexural capacity of reinforced concrete bridge piers decreases gradually under deflection reversals, the shear strength decay is more abrupt. The following discussion is an attempt to introduce a mathematical expression to predict the ductility factor of the reinforced concrete bridge piers without web reinforcement.

5.4.1 Prediction of Ductility Factor, μ

Based on the experimental results, it was concluded that the ductility factor, μ, decreases with the increase of the percentage of longitudinal reinforcement, p. The ductility factor also decreases with the reduction of the shear span-to-depth ratio, a/d, since a smaller a/d value requires a larger load to cause yielding of the tension reinforcement and consequently produces higher shear stresses. It has also been established that the ductility factor increases with the reduction of the yield strength of the longitudinal reinforcement, f_y, [38]. Based on the above discussion, the ductility factor should be related to the previously mentioned variables as follows:

$$\mu \alpha \frac{a/d}{pf_y} \qquad (5.1)$$

For the specimens tested in Series I of this program, the relationship between the ductility factor, μ, and the combined variables $\frac{a/d}{pf_y}$ is shown in Fig. 5.9.. In the same figure, the best fitting curve to the data, using simple linear regression analysis, is also shown as a solid line. The experimental results revealed a considerable scattering of the data, especially in the high-ductility region. The fluctuation of data could be attributed to the absence of any consideration of the effect of the concrete strength. Since the diagonal tension cracks initiated as the applied principal tensile stresses exceed the tensile strength of the concrete, the concrete tensile strength, f_t, should be included in the parameters mentioned in Equation 5.1. Accordingly, the ductility factor, μ, is related to the above parameter as follows:

$$\mu \alpha \frac{a/d \cdot f_t}{pf_y} \qquad (5.2)$$

However, internationally, the tensile strength of concrete, f_t, is evaluated in terms of the square root of the ultimate compressive strength of concrete, $\sqrt{f'_c}$. Thus, the tensile strength of concrete, f_t, may be replaced by f'_c and the proposed variable may be rewritten as follows: $\frac{a/d\ \sqrt{f'_c}}{pf_y}$. Fig. 5.10 shows the relationship between the ductility factor and the dimensionless variable $\frac{a/d\ \sqrt{f'_c}}{pf_y}$. The scatter of data points in high-ductility range is less pronounced in this case compared to the previous analysis shown in Fig. 5.8. Recent advances in predicting the cracking strength of concrete [21] proposed expressions for concrete tensile strength, f_t, as follows:

$$f_t = 0.6 f_{sp} \qquad (5.3a)$$

or

$$f_t = f'^{2/3}_c \qquad (5.3b)$$

where f_{sp} is the measured concrete splitting strength. The relationship between the ductility factor, μ, and the proposed variable $\frac{a/d\ f_t}{pf_y}$, for all the specimens in Series I, using Equation 5.3a for the concrete tensile strength of concrete, f_t, is given in Fig. 5.11. Using this approach clearly indicated a definite trend for the experimental data and reduced the scattering effect, especially at high values of the ductility factor.

The strong agreement of the proposed relationship in Fig. 5.11 is attested to by the residual square value of 0.978, in comparison to 1.0 for a perfect relationship. The ratio between the predicted and measured values of 1.01 and the coefficient of variance of 9% also indicate a very high degree of predictive accuracy of the proposed expression.

A multiple linear regression analysis of the experimental

results of Series I was also performed to examine the relative weight of the various parameters proposed in quation 5.2. Based on this analysis, the relationship between the ductility factor and these parameters could be expressed as follows:

$$\mu = 0.38\ (pf_y)^{-1.74}\ (a/d)^{1.93}\ (f_t)^{1.43} \qquad (5.4)$$

where f_t was calculated based on Equation 5.3a. The corresponding mean and coefficient of variance of 1.00 and 11%, respectively, indicate a very good agreement between the predicted and experimental values of the ductility factor. The variation of exponents of the above parameters in Equation 5.4 also suggests the use of the nondimensional characteristic factor, K, where

$$K = \frac{a/d\ .\ f_t}{pf_y} \qquad (5.5)$$

Based on Fig. 5.3, the relationship between K and μ can be written as follows:

$$\mu = \frac{1}{0.8 - 0.13\ K} \qquad (5.6)$$

If one accepts only integer values for the ductility factor, the characteristic factor, K, of 2.3 was found for a ductility factor of two, which was established as the lower bound of the characteristic factor in the proposed equation. At the other extreme, the maximum value of K was obtained by considering a very flexible member, i.e., μ approaching a very large number. The corresponding value of K was 6.15. Therefore, the proposed relationship between ductility and the characteristic factor can be introduced for the range of K between 2.3 and 5.3. This range includes members failing in shear and excludes flexural failure mechanisms.

In a re-examination of the validity of the proposed equation

for prediction of the ductility factor, the ductility factors of five specimens without web reinforcement, tested by Higai [18] and Uragami, et al. [49], is compared with the predictions of Equation 5.6 in Fig. 5.11. Two of the specimens, 1 and 5, were tested under similar loading history, while the other three specimens (H1, H2 and U2) were tested under 2 cycles and 1 cycle of loading reversals at each deflection increment, respectively. Despite the differences in loading history and testing procedure, there is a reasonable agreement between the test results and the predictions of Equation 5.6.

5.4.2 Prediction of Ductility Factor Based on Intensity of Applied Shear Stresses

The intensity of shear stresses is one of the most important factors affecting the behaviour of reinforced concrete piers subjected to large deflection reversals. In particular, the increase of intensity of shear stresses prompts earlier formation of diagonal tension cracks. The intensity of shear also increases the pinching phenomenon of the hysteresis due to shearing deformations and consequently reduces the energy dissipation capacity and the ductility factor of such structural members. Thus, the ductility factor is inversely proportional to the intensity of the applied shear stresses.

The relationship between the ductility factor, μ, and the normalized applied yield shear stress in terms of the concrete tensile strength, $\frac{v_y}{f_t}$, for all the specimens in Series I is shown in Fig. 5.12. The experimental results indicate a definite trend which could be expressed mathematically using linear regression analysis as follows:

$$\mu = \frac{1}{2\,\frac{v_y}{f_t} - 0.2} \qquad (5.5)$$

where f_t is the tensile strength of concrete calculated based on Equation 5.3a. The excellent agreement between the measured and predicted values is reflected by the mean and coefficient of variance values of 1.02 and 9%, respectively.

The proposed expression exhibits extremely high deformation capacity for very low yield shear stresses in the range of approximately 10% of the tensile strength of the concrete. The proposed equation is valid for the entire range of the ductility factor, including the flexural failure range. In the low range of the ductility factor, the proposed relationship results in a ductility factor of unity for a high yield shear stress of approximately 60% of the tensile strength of the concrete. The ductility factor gradually approaches zero with further increases of the shear stress beyond the 60% limit of tensile strength.

In order to re-examine the validity of Equation 5.5, the ductility factors of two specimens without web reinforcement, tested by Higai [18], are compared with the predictions of this equation in Fig. 5.12. It can be seen that the predicted and the measured values are in good agreement for one of the specimens. However, considerable difference between the predicted and the measured values exists for the other specimen. This may be attributed to the differences in the specimen dimensions and the testing procedures.

5.5 MAXIMUM SHEAR STRESS

The maximum shear stress, v_u, for each specimen was calculated based on the maximum measured load, which was modified to account for the self weight of the specimen. Thus,

$$v_u = \frac{P_{max}}{bd} \tag{5.7}$$

where P_{max} is the modified measured load in the direction of failure, and b and d are the width and the effective depth of the member, respectively. The calculated values of the maximum shear stress, v_u, for all the specimens tested in this program are given in Table 4.1.

The relationship between the maximum shear stress, v_u, and the percentage of the longitudinal reinforcement, p, for all the specimens tested in Series I is shown in Fig. 5.13. The maximum shear stress, v_u, is higher for specimens with a/d of 3.29 in comparison to other specimens with higher a/d ratios. The maximum shear stress will also increase by increasing the percentage of the longitudinal reinforcement, p, for a given value of a/d.

Multiple linear regression analysis of the normalized maximum shear stress with respect to the concrete tensile strength, $\frac{v_u}{f_t}$, for the specimens tested in Series I versus the fundamental variables results in the following expression:

$$\frac{v_u}{f_t} = 0.93\ (pf_y)^{0.86}\ (\frac{a}{d})^{-0.89}\ (f_t)^{-0.94} \tag{5.8}$$

The resultant mean and coefficient of variance values are 1.0 and 5%, respectively. The powers of the variables in this expression are very close to each other. This would suggest that a similar relationship exists between $\frac{v_u}{f_t}$ and the characteristic factor, K.

5.5.1 The Relationship between Maximum Shear Stress and Yield Shear Stress

The lower bound for the intensity of shear stresses exerted on a specimen subjected to deflection reversals is the yield shear stress. The yield shear stress is assessed by dividing the yield load, P_y, by the effective area, bd, where b and d are the width and the depth of the section, respectively. On the other hand, the upper bound is the maximum shear stress, v_u, calculated based on Equation (5.6). The ratio of $\frac{v_u}{v_y}$ for all the specimens tested in Series I, as it is related to the percentage of steel, p, is shown in Fig. 5.14. It is clear that the ratio $\frac{v_u}{v_y}$ is independent of the percentage of steel, with an average value of 1.15 for the different ranges of shear span-to-depth ratio a/d. These results indicate that yielding of the longitudinal reinforcement significantly affects shear failure under reversed loading.

5.5.2 The Prediction of Maximum Shear Stress Based on Characteristic Factor

The normalized maximum shear stress, v_u, with respect to the concrete tensile strength, f_t, is related to the characteristic factor, K, as shown in Fig. 5.15. The tensile strength of the concrete was calculated based on Equation 5.2a. The solid line in the figure represents the best fitting curve for the experimental data which can be expressed mathematically as follows:

$$\frac{v_u}{f_t} = \frac{0.71}{K^{0.74}} \qquad (5.8)$$

The excellent agreement between the measured and predicted values is reflected by the mean and coefficient of variance values of 0.99 and 2.5%, respectively. This expression confirms that the maximum shear stress, v_u, is directly proportional to pf_y and inversely proportional to a/d, as shown in Fig. 5.16. It can also be seen that the maximum shear stress under deflection reversals diminishes with the reduction of the percentage of longitudinal reinforcement, p, while the reduction of shear span-to-depth ratio, a/d, enhances the maximum shear stress.

The above relationship also provides a very useful means of classifying the modes of failure, as will be discussed in the following section.

5.6 MODES OF FAILURE

The appearance of the crack configuration discussed in Section 5.2 failed to indicate a clear trend which could be used to classify the mode of failure for such members. The extent of yielding of the longitudinal reinforcement was the only common observation which could be used to classify the different failure mechanisms. This observation confirms the hypothesis that yielding of the longitudinal reinforcement would prompt the deterioration of the interface shear transfer under the reversed loading condition for members without web reinforcement [29].

Using the proposed characteristic factor, K, it was possible to classify the mode of failure accordingly, as shown in Fig. 5.11.

Based on the range of the K values, the critical crack pattern and the extent of yielding of the longitudinal reinforcement could be predicted. In addition, based on the relationship between the normalized maximum shear stress, $\frac{v_u}{f_t}$, and the characteristic factor, K, the range of intensity of shear stresses for each mode of failure was established, as shown in Fig. 5.16. As a result, for any given specimen, using the intensity of shear stresses, $\frac{v_u}{f_t}$, which can easily be calculated, the mode of failure under deflection reversals of the previously described pattern may be predicted. The various ranges of intensity of shear corresponding to the three different modes of shear failure were tentatively established and further testing is needed to confirm the limits, especially in the intermediate range of K.

The proposed classification of mode of failure can be summarized as follows:

Mode (1): Failure is mainly due to a large vertical relative movement at the maximum moment section, caused by the localization of the yielding of the longitudinal reinforcement at this section. This mode is typical for K values between 4.8 and 5.3.

Mode (2): This failure mode is characterized by yielding of the longitudinal reinforcement within a distance d from the maximum moment section. The failure is mainly caused by widening of the x-shaped diagonal crack or buckling of the longitudinal reinforcement within the same distance. This mode is typical for K values between 4 and 4.8.

Mode (3): The failure is characterized by the yielding of the longitudinal reinforcement within a distance 2d from the maximum moment section. Failure is mainly due to the initiation and widening of a second diagonal crack. This mode is typical for K-values between 2.3 and 4.

5.7 ENERGY DISSIPATION CAPACITY

The ability of any structure to withstand large deflection reversals is solely dependent on its energy dissipation capacity, because the energy dissipation provides a measure of the inelastic performance of a structure under load reversals. The dissipated energy is the difference between the energy expended during load application and that recovered during unloading. Energy dissipation capacity, W_d, is thus defined as the accumulation of areas enclosed by the hysteresis loops prior to failure. The normalized energy dissipation capacity of a specimen, NED, was determined by normalizing the accumulated energy dissipation with respect to the elastic applied energy in the first cycle.

5.7.1 The Relationship Between Ductility Factor and Normalized Energy Dissipation

The normalized energy dissipation capacities, NED, for all the specimens tested in Series I and III were determined based on the numerically recorded values of loads and deflections using a computer program, as given in Table 5.3. However, for specimens in Series II, NED was calculated using the planimeter and the hysteresis response, as given in the same table. Details of these calculations are contained in Appendix (A), Reference [44]. Based on the experimental data the relationship between NED and μ was established,

as shown in Fig. 5.17. The solid line represents the best fit to the experimental data with mean and standard deviation values of 1.00 and 0.12, respectively. This relationship could be expressed mathematically as follows:

$$NED = 5.75\ (\mu)^{1.67} \tag{5.9}$$

Thus, energy dissipation capacity and ductility factor are closely related. This equation results in zero ductility for zero energy dissipation capacity. The energy dissipated is equal to zero in an elastic range, $P < P_y$. For reinforced concrete members, this range constitutes the linear portion of the load-deflection response, which is limited to approximately 40 to 50% of the yield load. The ductility factor in this case would be less than one (0.4 to 0.5). The typical failure mechanism would be a result of fatigue which requires a large number of cycles.

5.7.2 The Relationship Between Normalized Energy Dissipation and Characteristic Factor

Since the ductility factor has been shown to be a function of the characteristic factor, K, the normalized energy dissipation capacity could also be expressed in terms of the characteristic factor as follows:

$$NED = \frac{10^5}{(280 - 45.5K)^{5/3}} \tag{5.10}$$

The proposed equation is compared with the experimental data as shown in Fig. 5.18. The mean and standard deviation values obtained are within the acceptable range at 1.03 and 0.21, respectively.

5.8 EFFECT OF LOAD FREQUENCY

A total of four specimens, Series II, were tested with different frequencies, as given in Table 3.1. The behaviour of these specimens was compared to the behaviour of two specimens tested earlier under the very low frequency of 0.0004 HZ, equivalent to a static load in Series I.

The appearance of the crack patterns at failure for the different a/d categories were approximately similar to those specimens tested under an equivalent static load, as shown in Figures 5.19 and 5.20. Details of the location and range of the cracks for all the specimens tested in this series is given in Table 5.4.

Failure of specimens 2-1 and 2-3 occurred due to the widening of the x-shaped diagonal crack just after yielding of the longitudinal reinforcement, similarly to specimen 1-1. However, for specimen 2-2, which was tested under the highest frequency, 0.2 HZ, yielding of the longitudinal reinforcement at the d-section was observed at the first cycle of the fourth deflection, while the specimen failed during the fifth deflection increment. This observation suggests a possible change in the failure criteria under higher load frequencies. For the a/d value of 6.05, specimen 2-5 failed just after yielding of the longitudinal reinforcement at the 2d-section, similarly to specimen 1-3. The relationship between failure and yielding of longitudinal reinforcement for all the specimens in this series is given in Table 5.5.

The maximum shear stresses of specimens 2-1, 2-2, and 2-3 were approximately equal to that of specimen 1-1, as given in Table 4.1. For the higher range of a/d, the maximum shear stress of specimen

2-5 is slightly higher than that for specimen 1-3, as shown in Fig. 5.21. These results reflect the insignificant effect of the load frequency on the maximum shear stress of the specimens in both a/d categories.

Similarly to specimen 1-1, a ductility factor of 4 was obtained for both specimens 2-2 and 2-3, as shown in Fig. 5.22. The concrete honeycombs observed at the maximum moment section of specimen 2-1 could contribute to the reduction of the ductility factor obtained for this specimen.

For specimen 2-5, the measured deflection, δ_y, under the same calculated yield load was lower in comparison to the identical specimen 1-3. This could be attributed to the possible torsional movement of specimen 2-5. The change in the yield deflection magnitude, which would definitely alter the ductility, could be the explanation for the two different values obtained for the ductility factors, as shown in Fig. 5.23.

5.9 EFFECT OF AXIAL LOAD

Two specimens, 3-1 and 3-3, as representative of both the lower and higher ranges of a/d, were subjected to an axial compressive stress of 0.98 MPa and tested in this program. The behaviour of these two specimens is compared to identical specimens, 1-1 and 1-3 respectively, tested without the presence of the axial load. The effect of axial compressive stresses on crack patterns is given in Fig. 5.24. The location and range of the cracks, and the relationship between failure and yielding of longitudinal reinforcement for specimens in this series are given in Tables 5.6 and 5.7, respectively.

Specimen 3-1 failed due to the widening of the x-shaped diagonal crack after yielding of the longitudinal reinforcement at the d-section as shown in Fig. 5.26, similarly to specimen 1-1. As in the case of the identical specimen, 1-3, the failure of specimen 3-3 occurred after yielding of the longitudinal reinforcement at the 2d-section, as shown in Fig. 5.27. However, the appearance of the failure in terms of the crack pattern, was slightly different. In specimen 1-3, the failure was due to the formation of a second diagonal crack at the 2d-section (failure mode 3). In contrast, the failure of specimen 3-3 was mainly due to the widening of the x-shaped diagonal crack at the d-section (mode 2).

This indicates that the failure mode of the members with large a/d values is significantly affected by the presence of axial compression stress due to the increase of the maximum shear stress resistance. However, only one specimen was tested in this range and further investigation is required before any general conclusions can be drawn.

5.10 WORK INDEX

The work index, I_w, was introduced by Gosian, et al. [15], as a means to evaluate the response of different specimens subjected to various loading histories and severities of the applied load. The discussion of the work index has been presented in Section 2.4.5. As previously mentioned, the work index was also modified to include the influences of the shear span-to-depth ratio, a/d, and axial compressive stresses, σ, on the energy absorption during successive cycles of deflection reversals.

5.10.1 Relationship Between the Work Indices

The work index, I_w, defined as the normalized energy absorbed, was based on an assumed linear elastic hysteresis response. It did not take into account the effect of the nonlinearity of the load-deflection hysteresis. Thus, a nonlinear work index, I''_w, is introduced based on the actual hysteresis response. In order to determine I''_w, a computer program was used to calculate the areas under load-deflection curves which were numerically recorded for the specimens tested in Series I and III of this program. The calculated values of the work index, I_w, modified work index, I'_w, and the nonlinear work index, I''_w, for all the specimens tested in this program are given in Table 5.3. Details of the calculations are contained in Appendix (B), Reference [44].

The relationship between I'_w and I''_w values for the specimens tested in Series I of this program is shown in Fig. 5.28. In the same figure, the solid line represents the best fitting straight line relationship and the dotted lines are the 95% confidence limits, which indicate an excellent agreement between the two values. This straight-line relationship existing between the two values allows the determination of I''_w in terms of I'_w as follows:

$$I''_w = 2.25\ I'_w - 7.31 \qquad (5.11)$$

The resultant mean and coefficient of variance of the ratios between the predicted values and the measured values are 1.00 and 5%, respectively. Such agreement suggests that I'_w represents with a high degree of accuracy the actual energy absorption capacity, I''_w. This eliminates the need for the cumbersome and time-consuming process of determining the actual energy absorbed based on the nonlinear response.

However, since the original work index, I_w, has been used by many investigators [2,3,15], a relationship between I''_w and I_w would be more useful. Thus, the relationship between I''_w and I_w values for all the specimens tested in Series I was examined, as shown in Fig. 5.29. In this figure, the solid line represents the best fitting straight-line relationship which can be expressed as follows:

$$I''_w = 1.61\ I_w \qquad (5.12)$$

The resultant mean and coefficient of variance are 1.02 and 6%, respectively.

The comparison of the two figures 5.28 and 5.29 indicated that Equation 5.11 is as useful for prediction of the nonlinear

work index, I''_w, as Equation 5.12. However, I_w used in Equation 5.12 is more widely recognized compared to I'_w introduced by Gosian, et al. [15], which is used in Equation 5.11. Therefore, I''_w can be predicted simply based on the original work index, I_w, using Equation 5.12. The effect of the shear span-to-confined depth ratio, $\frac{a}{d_c}$, introduced in the modified work index, I'_w, is insignificant for typical reinforced concrete bridge piers. However, it should be noted that the intensities of the applied shear stresses in this program were quite small and the modification factor, $(1 - \frac{d_c}{a})$, does not vary greatly due to the limited range of a/d_c. Thus, the effect of the shear span-to-confined depth ratio, a/d_c, is expected to become evident for smaller values of a/d_c, corresponding to higher applied shear stresses.

Based on the simple regression analysis of the data, the modified work index, I'_w, for all the specimens tested in Series I can be determined satisfactorily using the following expression:

$$I'_w = 0.75\ I_w \qquad (5.13)$$

The resultant mean and coefficient of variance values are 0.95 and 8%, respectively. The same expression could be obtained based on the assumption that the load-deflection curves are parabolic.

5.10.2 Various Parameters Affecting the Work Index, I_w

A parametric study of the work index, I_w, was conducted based on the multiple regression analysis of the experimental values of I_w as related to the fundamental variables pf_y, a/d, and f_t. The result indicates the following relationship:

$$I_w = 4.52\ (pf_y)^{-2.15}\ (a/d)^{2.0}\ (f_t)^{1.85} \qquad (5.14)$$

The corresponding mean and coefficient of variance are 1.03 and 22.3%, respectively. It should be noted that the absolute power of the variables are almost the same. This would suggest that the work index, I_w, can also be expressed in terms of the characteristic factor, K.

In order to examine the results of the multiple regression analysis, each parameter was examined individually. The results as compared to the experimental data are given in Figures 5.30, 5.31 and 5.32. It is interesting to note that in the low range of pf_y the work index, I_w, is very sensitive to the variations of pf_y. This implies that the energy absorption capacity is increased drastically by the reduction of the percentage of steel, p, or the steel yield strength, f_y, in the low range of pf_y.

5.10.3 The Relationship Between the Work Indices and Characteristic Factor

The relationship between the work index, I_w, and the characteristic factor, K, for all the specimens tested in Series I is shown in Fig. 5.33. Based on linear regression analysis, the best fitting curve is also shown by a solid line. The equation for this curve could be expressed mathematically as follows:

$$I_w = 4.17\ e^{0.62K} \qquad (5.15)$$

The resultant mean and coefficient of variance values of 1.00 and 18%, respectively, indicate a good agreement between the predicted and the measured values of the work index.

The relationship between the modified work index, I_w', and the characteristic factor, K, for all the specimens tested in Series I of this program is shown in Fig. 5.34. The solid line represents

the best fitting curve to the experimental data and can be mathematically expressed as follows:

$$I'_w = 3.73\ e^{0.59K} \qquad (5.16)$$

The mean and coefficient of variance values obtained are 1.01 and 19%, respectively.

Since I''_w and I'_w are linearly related as expressed by Equation 5.11, an expression could readily be derived to relate I''_w and K. However, a direct relationship between these two variables was established, as shown in Fig. 5.35, using linear regression analysis for the experimental data. The solid line shown in the figure represents the best fitting curve and can be mathematically expressed as follows:

$$I''_w = 5.88\ e^{0.65K} \qquad (5.17)$$

The resultant mean and coefficient of variance values are 1.00 and 19%, respectively.

5.10.4 The Relationships Between Maximum Shear Stress and the Work Indices

The maximum shear stress, v_u, of a structural member obviously depends on the degree of severity of the applied energy, which could be represented by the work index, I_w, or modified work index, I'_w, or nonlinear work index, I''_w, as discussed in Section 2.4.5. The relationships between the normalized maximum shear stress with respect to the tensile strength of concrete, $\frac{v_u}{f_t}$, and the work indices, based on the experimental data, are given in Figures 5.36, 5.37, and 5.38.

Fig. 5.36 depicts the relationship between the normalized maximum shear stress, $\frac{v_u}{f_t}$, and the work index, I_w. The solid line

representing the best fitting curve to the experimental data can be expressed mathematically as follows:

$$\frac{v_u}{f_t} = \frac{1.08}{I_w^{0.36}} \qquad (5.18)$$

The corresponding mean and coefficient of variance values of 1.00 and 9%, indicate an excellent agreement between the predicted and measured values.

Fig. 5.37 shows the same relationship between the normalized maximum shear stress, $\frac{v_u}{f_t}$, and the modified work index, I'_w. The solid line representing the best fitting curve to the experimental data can be expressed mathematically as follows:

$$\frac{v_u}{f_t} = \frac{1.05}{(I'_w)^{0.37}} \qquad (5.19)$$

The resultant mean and coefficient of variance values are 1.01 and 9%, respectively.

Similarly, the relationship between the normalized maximum shear stress, $\frac{v_u}{f_t}$, and the nonlinear work index, I''_w, was established as shown in Fig. 5.38. The solid line representing the best fitting curve to the experimental data can be expressed mathematically as follows:

$$\frac{v_u}{f_t} = \frac{1.18}{I''^{\,0.34}_w} \qquad (5.20)$$

The corresponding mean and coefficient of variance values are 1.01 and 9%, respectively.

However, the determination of the nonlinear work index, I''_w, is quite cumbersome and also requires the complete hysteresis response. But I''_w may be predicted with reasonable accuracy using

Equation 5.20, which is based on the characteristic factor, K. The relationship between the normalized maximum shear stress, $\frac{v_u}{f_t}$, and the predicted nonlinear work index, $(I''_w)_p$, was established as shown in Fig. 5.39. The solid line in the figure represents the best fitting curve and it can be expressed mathematically as follows:

$$\frac{v_u}{f_t} = \frac{1.32}{(I''_w)_p^{0.37}} \qquad (5.21)$$

The resultant mean and coefficient of variance values are 1.00 and 4%, respectively. It is interesting to note that this equation has a much smaller coefficient of variance compared to Equation 5.20 which is based on the measured hysteresis response.

Based on either of the three Equations 5.18, 5.19, and 5.21, it is now possible to predict the maximum shear stress of a pier without web reinforcement, v_u, for any level of desired deformation capacity. For example, assume that a pier without web reinforcement is required to provide energy absorption such that it can withstand a deflection of five times the yield deflection with a deflection history as shown in Fig. 3.1, and the load capacity should be always more than 75% of the yield load. The corresponding work index in this case is approximately equal to 45, which would translate into a maximum shear stress of approximately 27% of the tensile strength of the concrete, according to Equation 5.18. This value also represents the concrete contribution in resisting shear for pier structural members with web reinforcement. However, for such members with web reinforcement, this concrete contribution may be enhanced due to the presence of transverse reinforcement, which prevents opening of the diagonal cracks and increases the effect of the aggregate interlocking

action.

The comparison between Equation 5.19, proposed for bridge piers without web reinforcement, and the experimental results for the specimens with web reinforcement collected by Gosian, et al. [15], is shown in Fig. 5.40. The ductility factors, μ, corresponding to different ranges of I'_w based on Equation 5.19 for specimens without web reinforcement are given in the same figure. The figure indicates the insignificant effect of the concrete contribution for members with web reinforcement subjected to reversed cyclic loading. This conclusion confirms the recommendation given by Gosian, et al. [15], to ignore the concrete contribution and design the transverse reinforcement to carry a shear force not less than the maximum shear force imposed on the section. However, for bridge piers which are very lightly transversely reinforced, as discussed in Section 3.2.1, the concrete contribution represents the major component for resisting shear. Therefore, it is recommended that the intensity of the shear stresses corresponding to the yield load should be limited to $\sqrt{f'_c}$ (psi) in design of the bridge piers to ensure reasonable energy absorption capacity and performance under deflection reversals.

The comparison between the equations introduced in this section and Equation 5.8, all useful for the prediction of maximum shear stress, v_u, would suggest that Equation 5.8 is more desirable since it is related to the characteristic factor, K, which can be determined readily on the basis of the fundamental variables, pf_y, a/d, and f_t.

5.10.5 The Relationship Between the Ductility Factor and the Work Index

The ductility factor, μ, versus the work index, I_w, for all the specimens tested in Series I, is shown in Fig. 5.41. The relationship between the two variables was established based on linear regression analysis as shown by the solid line in the same figure. The mathematical expression of this best fitting curve takes the following form:

$$\mu = 0.26\ (I_w)^{0.7} \qquad (5.22)$$

The resultant mean and coefficient of variance are 1.01 and 12%, respectively. Similar relationships were also established between the ductility factor, μ, and the modified work index, I'_w, and the nonlinear work index, I''_w, predicted by Equation 5.17, as shown in Figures 5.42 and 5.43, respectively.

Based on Equation 5.22, the zero ductility factor corresponds to zero work index, which represents members unable to absorb energy, or with trivial deformation capacities. For a minimum ductility factor of one, the corresponding work index, based on Equation 5.22, is 6. This reflects the ability of the member to withstand 3 cycles with a deflection equivalent to the yield deflection, δ_y, in addition to one complete cycle with a maximum deflection of twice the yield deflection, $2\delta_y$. The failure occurs during the second cycle of $2\delta_y$.

It should be noted that the proposed expression is based on the loading pattern used in this experimental program and further research is needed to examine its applicability for different loading histories.

An attempt to minimize the effect of the loading pattern could be made by including the number of cycles to failure, n. An average work index, $I_{w_{ave}}$, could be introduced as follows:

$$I_{w_{ave}} = \frac{I_w}{n} \tag{5.23}$$

The relationship between the ductility factor and the average work index is shown in Fig. 5.44. The solid line represents the best fitting curve to the experimental data. The mathematical expression of this curve takes the following form:

$$\mu = \frac{2}{3} (I_{w_{ave}})^{3/2} \tag{5.24}$$

The resultant mean and coefficient of variance of 1.02 and 11.8%, respectively, indicates an excellent agreement between the predicted and measured values. A comparison between the results of ten specimens with light transverse reinforcement of 0.3% tested by Arakawa et al. [3], and the predictions of Equation 5.24 is shown in Fig. 5.45. It can be seen that the above equation underestimates the ductility factor of all these specimens. Thus, the proposed relationship developed for reinforced concrete bridge piers without web reinforcement could be considered as the lower bound for a family of curves with different percentages of web reinforcement. A similar expression was introduced by Arakawa et al. [3], for reinforced concrete columns with 0.3% web reinforcement as follows:

$$\mu = 1.85\ I_{w_{ave}} - 0.85 \tag{5.25}$$

The comparison between the results of all the specimens tested in Series I of this program without web reinforcement and Equation 5.25 is shown in Fig. 5.46. The solid line representing Equation 5.25 is obviously an upper bound to the results of all the specimens shown.

5.11 Equivalent Viscous Damping Coefficient

As discussed in Section 2.4.7, the equivalent viscous damping coefficient, η_{eq}, is proportional to the ratio of energy dissipation capacity, W_d, to energy absorption capacity, W_a, of the R.C. members tested. Energy is dissipated mainly through residual inelastic deformations which cannot be eliminated by the removal of the load. Cracking of the concrete, however, reduces the energy dissipation capacity, initially through the opening of the flexural cracks which do not close in early stages of load reversals, and later by the formation of diagonal cracks, causing the pinching of the load-deflection curves towards the origin. The equivalent viscous damping coefficient, η_{eq}, for each specimen tested in Series I is given in Table 5.3.

The histories of the equivalent viscous damping coefficient, η_{eq}, for all the specimens tested in Series I are given in Reference [44], Appendix (C). The study of these histories of η_{eq} indicates that the equivalent damping coefficient starts to decrease after the full development of x-shaped crack. Fig. 5.47 shows a typical history of the equivalent damping coefficient as it is related to the imposed deflection and also its relationship with the formation of diagonal cracks and yielding of the reinforcement at d-section. In this figure, the solid line is based on the values of η_{eq} representing the damping characteristics of the specimen at each given deflection increment individually. However, if the accumulated energy dissipated and energy absorbed up to each deflection increment are used, there would not be any drop in the equivalent damping coefficient, η_{eq}, before failure, as shown in the same figure by the dotted line. Therefore, the

accumulated damping coefficient increases with the increase of the deflection until failure.

5.11.1 The Prediction of the Equivalent Viscous Damping Coefficient at Ultimate

Since the energy dissipation capacity, W_d, and the energy absorption capacity, W_a, have been shown to be functions of the characteristic factor, K, the equivalent damping coefficient at ultimate should also be related to K. Based on the experimental results the relationship between η_{eq} at ultimate and K was established as shown in Fig. 5.48. The solid line represents the best fitting curve to the test results and can be expressed mathematically as follows:

$$\eta_{eq} = 0.12 \sqrt{K} \qquad (5.26)$$

The corresponding mean and standard deviation values of 1.01 and 0.09 respectively, indicate an excellent agreement between the predicted values and the test results as shown in Fig. 5.49.

To examine the effects of various parameters such as pf_y, $\frac{a}{d}$ and f_t on the ultimate equivalent damping coefficient individually, a multiple regression analysis of the experimental data was performed. The results can be expressed mathematically as follows:

$$\eta_{eq} = \frac{0.073\ (a/d)^{0.75}\ (f_t)^{0.36}}{(pf_y)^{0.48}} \qquad (5.27)$$

The resultant mean and coefficient of variance of 1.00 and 7%, respectively, compare favorably with the corresponding values for Equation 5.26. However, the difference is insignificant and therefore does not justify the use of Equation 5.27 for practical purposes, considering the complexity of this expression. From

Equation 5.27 it can be concluded that the equivalent damping coefficient is generally most affected by the variations of steel percentage of pf_y, especially in the low range of the steel percentage.

5.11.2 History of the Equivalent Viscous Damping Coefficient

The comparison of the accumulated equivalent damping coefficient histories of all the ten tested specimens of Series I, given in Appendix (C) of Reference [44] indicates that the representative values of η_{eq} up to any deflection increment are comparable for different specimens. Using all the data points, the histories of all these specimens can be represented by a single curve with reasonable predictive accuracy independent of their fundamental variables (pf_y, $\frac{a}{d}$, and f_t), as shown in Fig. 5.50. The best fitting curve was found using linear regression analysis. The relationship can be expressed mathematically as follows:

$$\eta_{eq} = 0.22 - \frac{0.15}{\delta / \delta y} \qquad (5.28)$$

in which, δ is the deflection limit up to which the equivalent damping coefficient is sought. Fig. 5.51 shows the ratios between the predicted values based on Equation 5.28 and the experimental results for all ten specimens in Series I. The corresponding mean and coefficient of variance were 0.99 and 11%, respectively which indicates a very good agreement with the test results. The agreement was even slightly improved when only the ultimate values of η_{eq} were compared, as shown in Fig. 5.52.

The prediction of the history of the equivalent damping coefficient is deemed to be very useful in an iterative dynamic analysis of the response to any input excitation.

5.11.3 Effect of Load Frequency

The comparison of the histories of the equivalent damping coefficient for the static case and the low-frequency dynamic cases, as shown in Figure 5.33, revealed no significant effect of the frequency in this range. Therefore, the proposed history of η_{eq} could also be representative in this case, as shown by solid line in the same figures. However, there is a slight difference between the dynamic tests and the static one for small deflection range ($\delta < 2\delta y$) which could be attributed to the higher strength and stiffness of the specimens under dynamic loading condition.

5.12 EQUIVALENT FLEXURAL STIFFNESS

The changes of damping coefficient and stiffness are the two fundamental parameters which influence the response of bridge piers to strong seismic motion. These two parameters are closely related to the maximum imposed displacement. The damping characteristics of R.C. piers have been discussed in Section 5.11. The change of the overall stiffness could be attributed to the combination of cracking and local spalling of the concrete, as well as slippage and reduction of modulus of elasticity of the steel. Under strong seismic excitation, excursions into the inelastic range lead to a significant reduction in the natural frequency of reinforced concrete structures.

For deflection calculations at service load conditions, the flexural stiffness, EI, of reinforced concrete members could be predicted using the following expression for effective moment of inertia, I_{eff} and the concrete modulus of elasticity, E_c, adapted

by the ACI and Canadian Codes:

$$I_{eff} = \left(\frac{M_{cr}}{M_a}\right)^3 I_g + \left[1 - \left(\frac{M_{cr}}{M_a}\right)^3\right] I_{cr} \qquad (5.29.a)$$

$$E_c = 4730 \sqrt{f'_c} \quad \text{(MPa)} \qquad (5.29.b)$$

where, M_{cr} is the cracking moment, M_a is the applied moment at the maximum moment section, I_g is the gross moment of inertia, and I_{cr} is the moment of inertia of the crack transformed section. This expression provides an effective moment of inertia, taking into account the variation of cracking conditions along the member. The comparison between the computed deflections based on Eq. 5.29 and some of the experimental results reported has indicated good agreement at service load levels up to 70% of the yield load, P_y [28]. However, at higher load levels the scatter appears and increases as the load approaches the ultimate load under unidirectional loading condition.

Under deflection reversals large enough to cause yielding of the longitudinal reinforcement, extensive cracking of the concrete occurs both at the top and the bottom surfaces of the beam, which leads to a substantial reduction of the stiffness. In general, the total tip deflection of a pier could be attributed to three components: flexural deformation, slippage of the longitudinal reinforcement, and shear deformation. The deflection due to flexural deformation constitutes the main portion of the total deflection. However, in some cases the deformation due to anchorage slip of the longitudinal reinforcement might contribute up to 30% of the total deflection. Shear deformations could be significant for short piers with shear span-to-depth ratio, a/d, less than 2.5. In this experimental program, proper anchorage was provided for longitudinal reinforcements to

minimize the effect of the slippage on the tip deflection.

The main objective of this section is to introduce an equivalent flexural stiffness which could be used to predict the deflection of R.C. members subjected to reversed cyclic loading condition.

5.12.1 Various Parameters Affecting the Stiffness

The stiffness of a reinforced concrete pier changes continuously with the variation of the applied load. However, the slope of the secant line at any point on the load-deflection curve could represent the equivalent flexural stiffness, EI, at that level. Based on the experimental results, the equivalent flexural stiffnesses for all the specimens tested in Series I of this program were determined at different deflection increments, as given in Table 5.8. Details of the calculation of the stiffness for each specimen are given in Appendix (D) of Reference [44]. Fig. 5.54 shows the variation of the stiffness histories for specimens in Series I with shear span-to-depth ratios of 3.29 and 6.05. Since the shear span, a, is constant for all the specimens, the a/d ratio in fact represents the influence of the effective depth, d, of the cross-section. It is apparent from the figure that the effective depth is the main parameter affecting the stiffness of the specimens. In general, increasing the percentage of the longitudinal reinforcement, p, increases the compression zone depth under a given load and consequently increases the overall stiffness of the member. However, based on Fig. 5. 54, this effect is insignificant compared to the influence of a/d.

The effect of the modulus of elasticity of the concrete, E_c, due to the variation of the concrete compressive strength, f'_c, is not reflected in Fig. 5.54, because of the limited range of compressive strength of concrete used in this program.

A multiple linear regression analysis of the experimental results at the first deflection increment, $1\delta y$, for all the specimens in Series I indicated a relationship between EI and the fundamental variables as follows:

$$EI = 122.2 \left(\frac{d}{a}\right)^{2.11} (pf_y)^{0.14} (f_t)^{0.26} \qquad (5.30)$$

where all the variables are in metric units. The mean and coefficient of variance were found to be 1.01 and 5.7%, respectively. This expression also emphasizes the significant effect of the effective depth, d, compared to the other variables.

5.12.2 Equivalent Flexural Stiffness at Post-Yielding Range

The effective stiffness, E_cI_{eff}, of reinforced concrete members in post-cracking range prior to the yielding of the longitudinal reinforcement could be determined based on Eq. 5.29. However, in the post-yielding range the reduction of the stiffness is drastic due to the repeated excursions into the inelastic range under reversed cyclic loading. The stiffness ratio, ϕ, between the equivalent flexural stiffness in the post-yielding range, EI, and the effective stiffness based on the equations proposed by the codes for service load conditions, E_cI_{eff}, for all the specimens tested in Series I are given in Table 5.8. The details of the calculations are contained in Appendix (D), Reference [44].

The multiple linear regression analysis of the data conducted

based on the average stiffness ration, ϕ, at different deflection increments indicated the following expression:

$$\phi = 0.153\ (a/d)^{0.39}\ (\frac{\delta y}{\delta})^{0.84}\ (pf_y)^{0.25}\ (f_t)^{0.51} \quad (5.31)$$

where $\delta/\delta y$ is the displacement ductility ratio. The mean and coefficient of variance of 1.01 and 12.7%, respectively, reflect an excellent agreement between the predicted and the measured values. The results based on the statistical indicator T-test also revealed the insignificant effects of tensile strength of the concrete, f_t, and the longitudinal reinforcement indicated by (pf_y) parameter. However, based on Eq. 5.31, $\frac{\delta}{\delta y}$ parameter appears to be the most influential parameter affecting the behaviour of such members. Thus, another expression was derived for the stiffness ratio, ϕ, as related to $\frac{\delta}{\delta y}$ and $\frac{a}{d}$ only, as shown in Fig. 5.55 by the solid line. This relationship takes the following mathematical form:

$$\phi = 0.17\ (\frac{a}{d})^{0.78}\ (\frac{\delta y}{\delta})^{0.85} \quad (5.32)$$

The ratios between the predicted and the measured values, $\frac{\phi p}{\phi_t}$, at different deflection increments are plotted in Fig. 5.56 The corresponding mean and coefficient of variance of 0.99 and 12.9%, respectively, indicate the same predictive accuracy as Eq. 5.31. Thus, Eq. 5.32 is considered to be superior to the former expression for the prediction of the stiffness ratio, ϕ. The stiffness ratio, ϕ, for different specimens with a/d ratios of 3.29 and 6.05 are compared in Figures 5.57 and 5.58. While no significant effect of p is recognized for specimens with moderate amount of longitudinal reinforcement, a considerable reduction in stiffness ratio is observed for one specimen, 1-7, with very low percentage of steel. However, the lower stiffness could also be attributed to the effect of the

lower tensile strength, f_t, for this specimen.

5.12.3 Evaluation of the Deflection Under Cyclic Loading Condition

The deterioration of the equivalent flexural stiffness of a reinforced concrete pier due to the repetition of a specified deflection reversal occurs gradually. However, the reduction of the equivalent flexural stiffness with the increased deflection is much more drastic, as reflected by Eq. 5.32. Based on this equation, the deflection of a reinforced concrete pier subjected to a deflection pattern, as shown in Fig. 3.1, could be calculated using the following expression:

$$\delta = \left[\frac{P\,(a)^{2.22}\,(d)^{0.78}}{0.51\,(\delta y)^{0.85}\,E_c I_{eff}} \right]^{6.67} \qquad (5.33)$$

where P is the maximum applied load, δ is the resultant deflection under cyclic loading condition, and I_{eff} is the effective moment of inertia calculated based on Eq. 5.29 for the applied load P. By calculating the ultimate deflection, δ_u, corresponding to a maximum load 1.15 P_y, the ductility factor, μ, could be estimated.

Conversely, under any given deflection, δ, the load carrying capacity of a pier could be determined by an iterative procedure using the following expression:

$$P = \frac{3\phi E_c I_{eff}}{a^3}\,\delta \qquad (5.34)$$

The iteration starts by assuming a load carrying capacity equal to the yield load, P_y, for the calculation of I_{eff}. Using Eq. 5.34, the value of P can be calculated and a new value of I_{eff} will be found accordingly. After a few iterations, convergence should be reached,

because P varied in a fairly narrow range, $P_y < P < 1.25\ P_y$.

Based on either of the previously mentioned procedures, the load-deflection curve at post-yielding range could be predicted as shown in Fig. 5.59 for a typical specimen tested in this program. The agreement between the predicted and the measured values is satisfactory.

CHAPTER VI

CONCLUSIONS

A total of sixteen large scale specimens representative of actual bridge piers were tested and analyzed to investigate their shear behaviour under large deflection reversals. Based on the results of this experimental program, the following observations and conclusions may be drawn:

1. Under large deflection reversals, two diagonal cracks intersect each other to form an x-shaped crack within a distance approximately equal to the effective depth of the section, d, measured from the location of the maximum moment section.
2. The ratio of the maximum shear stress, v_u, to the yield shear stress, v_y, is found to be approximately constant and independent of both the percentage of longitudinal reinforcement and the shear span-to-depth ratio. This result indicates the significant effect of yielding of the longitudinal reinforcement on the shear failure under large deflection reversals.
3. The extent of the yielding of the longitudinal reinforcement is related to the mode of failure and it can be used to explain different failure mechanisms of such members.
4. The fundamental behaviour of bridge pier structures can be fully described using a proposed nondimensional characteristic factor, K, in terms of the shear span-to-depth ratio, a/d, concrete tensile strength, f_t, percentage of longitudinal reinforcement, p, and the yield strength of the steel, f_y,

as follows:

$$K = \frac{(a/d)\ f_t}{p f_y}$$

5. The proposed factor, K, was used to derive expressions which would predict the ductility, maximum shear stress, energy dissipation and energy absorption capacities and equivalent viscous damping coefficient of such members.
6. The mode of failure is significantly affected by shear span-to-depth ratio, a/d, and the percentage of longitudinal reinforcement, p.
7. Using the proposed characteristic factor, K, it was possible to classify the failure mechanisms into three different distinct modes of failure. This classification was accomplished parallel to a rational categorization of these failure modes based on the maximum intensity of the applied shear stresses.
8. An expression was also proposed for the prediction of ductility factor based on the intensity of applied shear stresses.
9. The ductility factor and the energy dissipation capacity are closely related.
10. The load frequency within the range considered in this program, 0.0004 to 0.2 HZ, appeared to have an insignificant effect on the mode of failure, maximum shear stress, and ductility. However, the test results indicate possible changes in failure criteria under higher frequencies.
11. The results of the two specimens tested in the presence of the axial compressive load indicated that the axial compressive

stresses reduce the deterioration of the interface shear transfer across the cracks, which increases the maximum shear stress capacity and ductility of the member.

12. The failure modes of members with large a/d values are affected by the presence of axial compressive stresses.

13. Due to the limited ranges of the load frequency and axial compressive stress in this study, further investigation is required into the effects of values higher than those considered in this program.

14. A nonlinear work index, I_w'', was introduced to represent the real energy absorption capacity. An expression was also derived for the prediction of this index using the characteristic factor, K.

15. The comparison between the commonly used work index, I_w, and the nonlinear work index indicated an excellent agreement. Thus, the work index could adequately represent the real energy absorption capacity of reinforced concrete bridge piers.

16. The work indices and the maximum shear stress capacity are closely related. Therefore, the work index, I_w, could be used as a good representative of the severity of the applied load.

17. A relationship was established between the ductility factor and the average work index, $I_{w_{ave}}$, to allow for the prediction of the deformation capacity of such members subjected to various degrees of severities of the applied load.

18. Expressions were proposed for the prediction of the equivalent viscous damping coefficient and the equivalent flexural

stiffness of such members in the post-yielding range. This information could be used for the investigation of the dynamic response of these members in future.

REFERENCES

1. ACI-ASCE Committee 426 (1973), "The Shear Strength of Reinforced Concrete Members", ASCE Journal, Str. Division, ST6, June 1973.

2. Arakawa, T., et al. (1981), "Evaluation of Deformational Behaviour of Reinforced Concrete Columns Under Cyclic Loading", Transactions of the Japan Concrete Institute, Vol. 3, 1981, pp, 391-398.

3. Arakawa, T., et al. (1982), "Effect of the Rate of Cyclic Loading on the Load-Carrying Capacity and Inelastic Behaviour of Reinforced Concrete Columns", Transaction of the Japan Concrete Institute Vol. 4, 1982, pp. 485-492.

4. Ben-Omran, H., Higai, T., Rizkalla, S., and Saadat, F. (1983), "Behaviour of Reinforced Concrete Bridge Piers Subjected to Large Deflection Reversal, Volume II", Department of Civil Engineering, University of Manitoba, Winnipeg, November 1983.

5. Bertero, V.V., and Popov, E.P. (1975), "Hysteretic Behaviour of Ductile Moment Resisting R.C. Frame Components", Report No. EERC 75-16, University of California, Berkeley, Calif., April 1975.

6. Bertero, V.V., and Popov, E.P., "Seismic Behaviour of Ductile Moment-Resisting R.C. Frames", Special Publication of ACI SP 53.11, pp. 247-291.

7. Bertero, V.V., and Popov, E.P. (1974), "Hysteretic Behaviour of R.C. Flexural Members with Special Web Reinforcement". Report No. EERC 74.9, E.Q. Eng. Research Centre, Univ. of Calif., Berkeley, CA, 1974, p. 134.

8. Bertero, V.V. and Collins, R.G. (1973), "Investigation of the Failures of the Oliveview Stair Towers During the San Fernando E.Q. and their Implications on Seismic Design", E.Q. Eng. Research Center, Univ. of Calif., Berkeley, Report No. EERC 73-26, Dec. 1973, pp 282.

9. Bresler and MacGregor (1967), "Review of Concrete Beams Failing in Shear", ASCE 1967 (ST1) February, pp. 343-372.

10. Bresler, B. (1972), "Behaviour of Structural Elements, A Review", Proceedings of the Disaster Mitigation Workshop, University of California, Aug. 1972.

11. Brown, R.H. and Jirsa, J.O. (1974), "Shear Transfer of Reinforced Concrete Beams Under Reversed Loading", Special Publication SP-42, Shear in Reinforced Concrete, ACI, Detroit,

Mich. 1974, pp. 347-357.

12. Clough, "Dynamics of Structures", McGraw Hill Publications, pp. 70-77.

13. Fenwick, R.C. and Paulay, T. (1968), "Mechanisms of Shear Resistance of Concrete Beams", ASCE, Str. Division, Oct. 1968, ST 10, pp. 2325-2351.

14. Fenwick, R.C. and Feng, A. (1979), "The Behaviour of R.C. Beams Under Cyclic Loading", Dept. of C.E. Report No. 176, Univ. of Auckland, NZ, 1979, p. 52.

15. Gosain, N.K., Brown, R.H. and Jirsa, J.O. (1979), "Shear Requirements for Load Reversals on R.C. Members", ACI Journal, July 1977, ST7, pp. 1461-1476.

16. Haddadin, K.J., Hong, S. and Mattock, A.H. (1971), "Stirrup Effectiveness", Proc. of ASCE, Str. Division, Sept. 1971 pp. 2277-2297.

17. Higai, T. (1978), "Fundamental Study on Shear Failure of Reinforced Concrete Beams", Transaction of JSCE, Vol. 10, 1978, pp. 339-343.

18. Higai, T. (1982), "Shear Failure of Reinforced Concrete Under Large Deflection Reversals", Yamanashi University Report, Japan.

19. Higashi, Y., Ohkubo, M. and Ohtsuka, M. (1977), "Excursions on Restoring Force Characteristics and Failure Modes of Reinforced Concrete Columns", Paper No. 11-23, Sixth World Conference on Earthquake Engineering, New Delhi, January 1977.

20. Higashi, Y. and Hirosawa, M., "Experimental Research on Ductility of R.C. Short Columns under Cyclic Lateral Load", Preliminary Report for International Association of Bridge and Structural Engs., Symposium on Design and Safety of R.C. Compression Members, Quebec 1974.

21. Hwang, L. and Rizkalla, S. (1983), "Effective Tensile Stress-strain Characteristics for Reinforced Concrete, Proceedings of the Canadian Structural Concrete Conference, June 1-3, Ottawa, Ontario.

22. Ismail, Mohamed A.F. (1962), "Bond Deterioration in R.C. under Cyclic Loading", Ph.D. Thesis, C.E. Dept., Univ. of Ill., Urbana, Jan. 1962.

23. Jacobsen, Lyndik, S., "Damping in Composite Structures", ASCE Journal, 1948.

24. Jirsa, James O., "Applicability of Bridges of Experimental Seismic Test Results Performed on Subassemblages of Buildings", Workshop on Earthquake Resistance of Highway Bridges.

25. Kani, G.N.J. (1967), "How Safe Are Our Large R.C. Beams", ACI Journal, March 1967.

26. Kani, G.N.J. (1966), "Basic Facts Concerning Shear Failure", ACI Proceedings 63, June 1966, pp. 675-692, Discussion pp. 1511-1528.

27. Johns, Kenneth C. and Belanger, Michel D. (1981), "Dynamic Stiffness of Concrete Beams", ACI Journal, May/June 1981, pp. 201-205.

28. Kripanarayanan, K.M. and Branson, D.E. (1972), "Short-Time Deflection of Beams Under Single and Repeated Load Cycles", ACI Journal, Feb. 1972, pp. 110-117.

29. Laible, J.P., "Experimental Investigation of Seismic Shear Transfer Across Cracks in Concrete Nuclear Containment Vessels", ACI, SP53, 1977.

30. MacGregor, James G. and Hanson, John M. (1969), "Proposed Changes in Shear Provisions for R.C. and Prestressed Concrete Beams", ACI Proceedings 66, April 1969, pp. 276-288. Discussion, pp. 849-851.

31. Manual, R.F. (1974), "Failure of Deep Beams", Shear in R.C., Vol. 2 (SP.42), ACI 1974, pp. 425-440.

32. Mattock, Alan H. (1969), "Diagonal Tension Cracking in Concrete Beams with Axial Forces", Proc. of ASCE, Str. Division, ST9, Sept. 1969, pp. 1887-1899.

33. Morrow & Viest, "Shear Strength of R.C. Frame Members Without Web Reinforcement", ACI Journal, Mar. 1957, pp. 835-869.

34. Mutsuyashi, H. and Machida, A. (1982), "Dynamic Properties of Reinforced Concrete Piers", Transactions of the Japan Concrete Institute, Vol. 4, 1982, pp. 429-436.

35. Okamura, H. and Higai, T., "Proposed Design Equation for Shear Strength of Reinforced Concrete Beams Without Web Reinforcement", Proc. of JSCE, No. 300, August 1980, pp. 131-141.

36. Okubo, T. and Iwasaki, T. (1979), "Summary of Experimental and Analytical Seismic Research Recently Performed on Highway Bridges", Proceedings of a Workshop on Earthquake Resistance of Highway Bridges, Applied Technology Council, January 1979, pp. 548-565.

37. Ozaka, Y. and Ohta, M., "Experimental Study on the Behaviour of Reinforced Concrete Bridge Piers Under Seismic Alternating Loads", A.I.C.A.P. - C.E.P. Symposium on Structural Concrete Under Seismic Actions, Rome, May 1979.

38. Park, R. and Paulay, T. (1975), "Reinforced Concrete Structures", 1975, a Wiley-Interscience Publication.

39. Paulay, T. (1971), "Coupling Beams of R.C. Shear Walls", ASCE, Vol. 97, No. ST3, March 1971, pp. 843-862.

40. Paulay, T. (1971), "Simulate Seismic Loading of Spandrel Beams", Journal of the Structural Division, ASCE, Vol. 97, No. ST9, Proc. Paper 8365, Sept. 1971, pp. 2407-2419.

41. Placas and Regan (1971), "Shear Failure of R.C. Beams", ACI Journal, Oct. 1971.

42. Priestley, M.J.N. and Park, R. (1979), "Seismic Resistance of Reinforced Concrete Bridge Columns", Proceedings of a Workshop on Earthquake Resistance of Highway Bridges, Applied Technology Council, January 1979, pp. 254-283.

43. Rajagopalan, K.S. and Ferguson, P.M., "Exploratory Shear Tests Examining Percentage of Longitudinal Steel", ACI Journal, Aug. 1968, pp. 834.

44. Saadat, F., Higai, T. and Rizkalla, S. (1984), "Fundamental Characteristics and Behaviour of Reinforced Concrete Bridge Piers Subjected to Reversed Cyclic Loading, Volume II", Department of Civil Engineering, University of Manitoba, Winnipeg, May 1984.

45. Scribner, C.F. and Wight, J.K. (1980), "Strength Decay in R.C. Beams Under Load Reversals", ACI Journal, April 1980, ST4, pp. 861-876.

46. Steidel, Jr., R.F., "An Introduction to Mechanical Vibrations", Second Edition, McGraw Hill Publication.

47. Taylor, H.P.J. (1972), "Shear Strength of Large Beams", ASCE 98, Nov. 1972, pp. 2473-2490.

48. Taylor, H.P.J., "Investigation of the Forces Carried Across Cracks In Reinforced Concrete Beams in Shear by Interlock of Aggregate", Technical Report 42.477, Cement and Concrete Association, London, England, 1970, pp. 22.

49. Uragami, M., Hashimoto, C. and Chou, L., "Resolution of the Deflection of R.C. Bridge Pier Due to Static Cyclic Loading", University of Tokyo.

50. Wang C.K., and Salmon, C.G. (1979), "Reinforced Concrete Design, 1979, pp. 111-120.

51. Yamada, M. and Yagi, S. (1973), "Shear Explosion of R.C. Short Columns", Fifth World Conference on E.Q. Eng., Paper No. 90, Rome, 1973.

52. Zagajeski, S.W., Bertero, V.V. and Bouwkawp, J.G. (1978), "Hysteretic Behaviour of R.C. Columns Subjected to High Axial and Cyclic Shear Forces", Report No. UCB/EERL-78105, Univ. of Calif. Berkeley, April 1978.

53. Zia, Paul and Johnson, David (1971), "Analysis of Dowel Action", ASCE 97, May 1971 (ST5), pp. 1611-1630.

54. Zsutty, T.C., "Beam Shear Strength Prediction by Analysis of Existing Data", ACI Journal, Nov. 1968, pp. 943-951.

TABLE 3.1

Variables Considered in the Experimental Program

Series	Spec. No.	bxd (mm)	Longitudinal Reinforcement	p%	a/d	P_y (KN)	v_c (MPa)	v_y (MPa)	$\frac{v_c}{v_y}$	Frequency of Loading (HZ)	Axial Compression Stress (MPa)
	1-1	500x350	3-20 M	0.51	3.29	83.9	0.80	0.48	1.67	0.0004	None
I-A	1-2	500x230	3-20 M 1-15 M	0.96	5.0	65.8	0.96	0.57	1.68	"	"
	1-3	500x190	4-20 M	1.26	6.05	57.8	1.06	0.61	1.74	"	"
	1-4	500x190	6-20 M	1.89	6.05	83.70	1.27	0.88	1.44	0.0004	None
	1-5	"	3-20 M	0.95	"	43.80	1.02	0.46	2.22	"	"
	1-6	"	5-20 M	1.58	"	70.80	1.12	0.75	1.49	"	"
	1-7	500x350	2-20 M 1-10 M	0.40	3.29	66.10	0.74	0.38	1.95	"	"
I-B	1-8	"	2-20 M 1-15 M	0.46	"	74.80	0.77	0.43	1.79	"	"
	1-9	"	5-20 M	0.86	"	140.70	0.99	0.80	1.24	"	"
	1-10	500x280	3-20 M	0.64	4.11	68.0	0.89	0.49	1.82	"	"
	2-1	500x350	3-20 M	0.51	3.29	83.8	0.77	0.48	1.60	0.01	None
	2-2	"	"	"	"	"	0.77	"	1.60	0.2	"
II	2-3	"	"	"	"	"	0.78	"	1.60	0.05	"
	2-5	500x190	4-20 M	1.26	6.05	58.8	1.10	0.62	1.77	0.1	"
III	3-1	500x350	3-20 M	0.51	3.29	108.70	0.84	0.62	1.35	0.0004	0.98
	3-3	500x190	4-20 M	1.26	6.05	64.76	1.18	0.68	1.74	"	0.98

Table 3.2 A Comparison between Building Columns and Bridge Pier Columns

Structures	Shear Span Ratio	Steel Ratio (%)		Normal Stress $\sigma_N = \frac{N}{A_c}$ (kgf/cm^2)	Remarks
		Tension Bar, P_t	Hoop, P_w		
Buildings	1-3	1-2	0.2-1.2	20-120	Columns Experimented
Bridge Piers	>3	<1	<0.1	10-20	Actual Pier Columns

TABLE 3. 3

AGE AND CONCRETE PROPERTIES

Series No.		Spec. No.	Age at Testing (days)	Concrete Compressive Strength, f'_c, (MPa)	Concrete Tensile Splitting Strength, f_{sp}, (MPa)	Concrete Modulus of Elasticity E_c (MPa)
I	I-A	1-1	55	37	3.9	26513
		1-2	22	35	3.5	25081
		1-3	68	36	3.8	28265
	I-B	1-4	28	40	4.3	28557
		1-5	35	42	4.0	29560
		1-6	48	33	3.4	24319
		1-7	15	38	3.6	27519
		1-8	17	38	4.2	29722
		1-9	25	41	4.2	29507
		1-10	38	41	4.4	29204
II		2-1	26	34	3.1	25994
		2-2	28	34	2.9	25842
		2-3	29	35	4.0	26172
		2-5	19	40	3.9	32012
III		3-1	23	36	3.4	24492
		3-3	22	41	4.2	28312

TABLE 3.4

REINFORCEMENT STEEL PROPERTIES

Series No.		Spec. No.	Percentage of Long. Reinf. P %	Type of Long. Steel	Yield Stress f_y (MPa)	Weighted Average f_y (MPa)	Ultimate Tensile Stress f_{su} (MPa)	Weighted Average f_{su} (MPa)	Modulus of Elasticity E_s (MPa)
I	I-A	1-1	0.51	3-20 M	343	343	556	556	178,892
		1-2	0.96	(3-20 M, 1-15 M)	(341, 371)	349	(533, 574)	544	(179,667, 179,339)
		1-3	1.26	4-20 M	343	343	556	556	178,892
	I-B	1-4	1.89	6-20 M	341	341	533	533	179,667
		1-5	0.95	3-20 M	341	341	533	533	179,667
		1-6	1.58	5-20 M	342	342	536	536	178,087
		1-7	0.40	(2-20 M, 1-10 M)	(342, 355)	344	(536, 536)	536	178,087
		1-8	0.46	(2-20 M, 1-15 M)	(343, 342)	343	(531, 530)	531	(182,719, 183,722)
		1-9	0.86	5-20 M	343	343	531	531	182,719
		1-10	0.64	3-20 M	343	343	531	531	182,719
II		2-1	0.51	3-20 M	343	343	551	551	175,834
		2-2	0.51	3-20 M	343	343	551	551	175,834
		2-3	0.51	3-20 M	341	341	533	533	179,667
		2-5	1.26	4-20 M	350	350	541	541	184,891
III		3-1	0.51	3-20 M	342	342	536	536	178,087
		3-3	1.26	4-20 M	342	342	536	536	178,087

TABLE 4.1

Test Results

Series	Spec. No.	f'_c (MPa)	f_y (MPa)	f_t (MPa)	K	δ_y (mm)	P_{max} (KN)	v_u (MPa)	$\frac{v_u}{v_y}$	Failure Cycle	Yielding Location	μ
I-A	1-1	37	343	2.34	4.33	3.77	-103.76	0.59	1.23	-6δy/1	1d	4
	1-2	35	341	2.10	3.19	6.70	- 73.43	0.64	1.12	-5δy/1	1.5d	3
	1-3	36	343	2.28	3.17	8.56	68.29	0.72	1.18	+4δy/1	1d	3
I-B	1-4	40	341	2.58	2.4	8.40	88.64	0.93	1.06	+4δy/1	2d	2
	1-5	42	341	2.40	4.54	6.90	- 52.52	0.55	1.20	-6δy/2	2d	5
	1-6	33	342	2.04	2.28	8.50	75.34	0.80	1.07	+4δy/1	2d	2
	1-7	38	342	2.16	5.14	2.66	- 79.15	0.45	1.18	-8δy/2	-	7
	1-8	38	343	2.52	5.24	2.77	- 92.15	0.53	1.23	-9δy/3	-	8
	1-9	41	343	2.52	2.82	4.68	145.55	0.83	1.04	+4δy/1	1d	2
	1-10	41	343	2.64	4.88	4.21	- 78.83	0.57	1.16	-8δy/1	1d	6
II	2-1	34	343	2.00	3.76	3.74	- 99.5	0.59	1.23	-4δy/2	1d	3
	2-2	34	343	2.00	3.76	3.80	-107.5	0.61	1.27	-5δy/2	1d	4
	2-3	35	341	2.04	3.86	3.33	-101.5	0.58	1.21	-6δy/1	1d	4
	2-5	40	350	2.23	3.06	6.54	- 74.0	0.78	1.26	-6δy/2	2d	5
III	3-1	36	342	2.04	3.85	3.55	+122.12	0.70	1.13	+6δy/2	1d	5
	3-3	41	342	2.52	3.54	8.14	- 73.62	0.77	1.13	-5δy/2	2d	4

TABLE 5.1

LOCATION AND RANGE OF CRACKS - SERIES I

Spec. No.	a/d	p (%)	Load Direction	Initiating Flexural Crack	X-Shaped Diagonal Crack at (h/2)	Length of the Flexural Crack Zone
1-1	3.29	0.51	-	0.49d	0.43d	1.6d
			+	1.0 d	0.46d	1.79d
1-8	3.29	0.46	-	0.94d	0.79d	1.99d
			+	0.93d	0.57d	1.44d
1-7	3.29	0.40	-	0.5 d	0.54d	2.07d
			+	-	-	1.63d
1-9	3.29	0.86	-	0.7 d	0.57d	2.04d
			+	0.76d	0.36d	2.04d
1-10	4.11	0.64	-	-	-	1.88d
			+	-	-	2.64d
1-2	5.0	0.96	-	0.78d	0.70d	3.52d
			+	0.70d	0.43d	3.35d
1-3	6.05	1.26	-	1.05d	0.66d	3.68d
			+	0.74d	0.58d	3.89d
1-6	6.05	1.58	-	1.00d	1.00d	4.47d
			+	1.21d	1.00d	4.50d
1-4	6.05	1.90	-	1.11d	0.89d	4.42d
			+	1.0 d	0.74d	4.00d
1-5	6.05	0.95	-	0.92d	0.47d	3.58d
			+	1.11d	0.71d	3.89d

TABLE 5.2 RELATIONSHIP BETWEEN FAILURE AND YIELDING OF LONGITUDINAL REINFORCEMENT

SERIES - I

Spec. No.	a/d	p (%)	μ	Failure Cycle	YIELDING OF STEEL			
					d-Section	1.5d-section	2d-section	3d-section
1-1	3.29	0.51	4	$-6\delta y/1$	$6\delta y/1$	-	-	-
1-7	3.29	0.40	7	$-8\delta_y/2$	$\varepsilon_s < \varepsilon_y$	$\varepsilon_s < \varepsilon_y$	$\varepsilon_s < \varepsilon_y$	-
1-8	3.29	0.46	8	$-9\delta_y/3$	$\varepsilon_s < \varepsilon_y$	$\varepsilon_s < \varepsilon_y$	$\varepsilon_s < \varepsilon_y$	-
1-9	3.29	0.86	2	$+4\delta_y/1$	$3\delta_y/2$	$\varepsilon_s < \varepsilon_y$	$\varepsilon_s < \varepsilon_y$	-
1-10	4.11	0.64	6	$-8\delta_y/1$	$8\delta_y/1$	$\varepsilon_s < \varepsilon_y$	$\varepsilon_s < \varepsilon_y$	-
1-2	5.0	0.96	3	$-5\delta_y/1$	$3\delta_y/1$	$5\delta_y-1$	$\varepsilon_s < \varepsilon_y$	-
1-3	6.05	1.26	3	$+4\delta_y/1$	$2\delta_y/1$	-	-	-
1-4	6.05	1.90	2	$+4\delta_y/1$	$2\delta_y/3$	-	$4\delta_y-1$	$\varepsilon_s < \varepsilon_y$
1-5	6.05	0.95	5	$-6\delta_y/2$	$4\delta_y/1$	-	$*6\delta_y/1$	$\varepsilon_s < \varepsilon_y$
1-6	6.05	1.58	2	$+4\delta_y/1$	$3\delta_y/1$	-	$4\delta_y/1$	$\varepsilon_s < \varepsilon_y$

*One strain gauge reading > ε_y

TABLE 5.3 Calculated Test Results

	Spec. No.	W_d (KN-M)	NED	I_w	I_w'	I_w''	$(I_w)_{ave}$	$\frac{v_u}{f_t}$	η_{eq}
SUBSERIES I-A	1-1	18.39	58.16	63.06	45.53	95.35	3.82	0.253	0.178
	1-2	17.63	40.05	34.88	28.15	57.37	2.79	0.304	0.195
	1-3	10.21	20.68	22.02	18.76	33.29	2.32	0.315	0.165
SUBSERIES I-B	1-4	13.8	18.75	20.93	17.83	31.69	2.20	0.362	0.158
	1-5	24.2	80.75	57.95	49.37	101.18	3.62	0.230	0.220
	1-6	13.6	22.6	20.73	17.66	31.82	2.18	0.389	0.170
	1-7	23.59	134.16	102.26	73.83	161.87	4.65	0.209	0.193
	1-8	38.4	185.3	130.05	93.90	206.46	5.20	0.211	0.200
	1-9	12.7	19.3	20.52	14.82	29.63	2.16	0.329	0.147
	1-10	40.6	141.8	92.42	76.34	159.25	4.40	0.216	0.225
SERIES II	2-1	7.64	24.38	24.53	-	-	2.45	0.289	0.156
	2-2	15.01	47.14	41.06	-	-	3.16	0.335	0.184
	2-3	14.81	53.07	45.09	-	-	3.22	0.229	0.189
	2-5	26.43	68.73	58.37	-	-	3.65	0.308	0.185
SERIES III	3-1	23.20	60.12	58.56	46.76	90.67	3.55	0.342	0.167
	3-3	26.00	49.31	37.97	35.63	63.90	2.92	0.307	0.209

TABLE 5.4

LOCATION AND RANGE OF THE CRACKS - SERIES II

Spec. No.	a/d	Rate of Loading (Hz)	Load Direction	Initiating Flexural Crack	X-Shaped Diagonal Crack at (h/2)	Length of the Flexural cracks Zone
2-1	3.29	0.01	- +	0.77d 0.54d	0.66d 0.31d	1.33d 1.93d
2-2	~	0.2	- +	0.83d 0.79d	0.76d 0.56d	1.51d 1.60d
2-3	~	0.05	- +	0.59d 0.57d	0.63d 0.63d	1.4 d 1.46d
			AVE.	0.68d	0.59d	1.54d
1-1	~	0.0004	- +	0.49d 1.0 d	0.43d 0.46d	1.6 d 1.79d
			AVE.	0.75d	0.45d	1.7 d
2-5	6.05	0.1	- +	0.89d 0.58d	1.05d 0.5d	4.16d 3.95d
			AVE.	0.74d	0.78d	4.06d
1-3	~	0.0004	- +	1.05d 0.74d	0.66d 0.58d	3.68d 3.89d
			AVE.	0.9 d	0.62d	3.79d

TABLE 5.5 RELATIONSHIP BETWEEN FAILURE AND YIELDING OF LONGITUDINAL REINFORCEMENT - SERIES II

Spec No.	a/d	p (%)	Rate of loading (HZ)	μ	Failure cycle	Yielding of Steel		
						d-section	1.5d-section	2d-section
1-1	3.29	0.51	0.0004	4	$-6\delta_y/1$	$6\delta_y/1$	-	-
2-1	~	~	0.01	3	$-4\delta_y/2$	$4\delta_y/1$	$\varepsilon_s < \varepsilon_y$	$\varepsilon_s << \varepsilon_y$
2-2	~	~	0.2	4	$-5\delta_y/2$	$4\delta_y/1$	$\varepsilon_s < \varepsilon_y$	$\varepsilon_s << \varepsilon_y$
2-3	~	~	0.05	4	$-6\delta_y/1$	$6\delta_y/1$	$\varepsilon_s < \varepsilon_y$	$\varepsilon_s << \varepsilon_y$
1-3	6.05	1.26	0.0004	3	$+4\delta_y/1$	$2\delta_y/1$	-	-
2-5	~	~	0.1	5	$-6\delta_y/2$	$3\delta_y/3$	-	$6\delta_y/2$

TABLE 5.6

LOCATION AND RANGE OF THE CRACK - SERIES III

Spec. No.	a/d	Axial Comp. Stress (MPa)	Local Direction	Initiating Flexural Crack	X-Shaped Diagonal Crack at (h/2)	Length of the Flexural Crack Zone
3-1	3.29	0.98	-	0.83d	0.61d	1.94d
			+	0.79d	0.66d	2.11d
			AVE.	0.81d	0.64d	2.03d
1-1	3.29	0.0	-	0.49d	0.43d	1.6d
			+	1.00d	0.46d	1.79d
			AVE.	0.75d	0.45d	1.70d
3-3	6.05	0.98	-	0.76d	0.66d	4.08d
			+	0.95d	0.79d	4.16d
			AVE.	0.86d	0.73d	4.12d
1-3	6.05	0.0	-	1.05d	0.66d	3.68d
			+	0.74d	0.58d	3.89d
			AVE.	0.9d	0.62d	3.79d

TABLE 5.7 RELATIONSHIP BETWEEN FAILURE AND YIELDING OF LONGITUDINAL REINFORCEMENT - SERIES III

Spec No.	a/d	p(%)	Axial compressive stress (MPa)	μ	Failure cycle	Yielding of steel		
						d-section	1.5d-section	2d-section
1-1	3.29	0.51	0.0	4	$-6\delta_y/1$	$6\delta_y/1$	-	-
3-1	~	~	0.98	5	$+6\delta_y/2$	$4\delta_y/1$	$\varepsilon_s < \varepsilon_y$	$\varepsilon_s << \varepsilon_y$
1-3	6.05	1.26	0.0	3	$+4\delta_y/1$	$2\delta_y/1$	-	-
3-3	~	~	0.98	4	$-5\delta_y/2$	$3\delta_y/1$	-	$5\delta_y/1$

TABLE 5.8 CALCULATED EQUIVALENT FLEXURAL STIFFNESS RATIO, ϕ

Specimen	$1\delta y$	$2\delta y$	$3\delta y$	$4\delta y$	$5\delta y$	$6\delta y$	$7\delta y$	$8\delta y$	$9\delta y$
1-1	0.460	0.292	0.218	0.166	0.138				
1-2	0.729	0.375	0.241	0.192					
1-3	0.784	0.419	0.280						
1-4	0.691	0.396	0.260						
1-5	0.839	0.408	0.290	0.212	0.178				
1-6	0.801	0.435	0.284						
1-7	0.365	0.229	0.110	0.138	0.121	0.100	0.081		
1-8	0.539	0.284	0.215	0.117	0.147	0.126	0.062	0.091	0.068
1-9	0.486	0.297	0.211						
1-10	0.672	0.334	0.236	0.189	0.160	0.137	0.114		

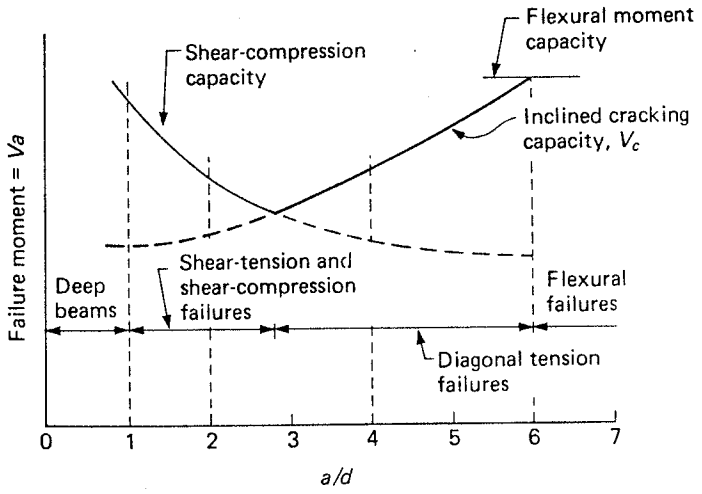

Fig. 2.1 VARIATION IN SHEAR CAPACITY WITH a/d FOR RECTANGULAR BEAMS

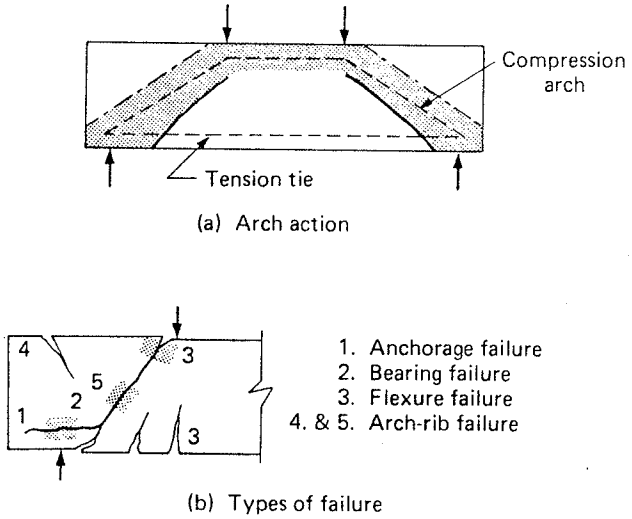

Fig. 2.2 MODES OF FAILURE IN DEEP BEAMS

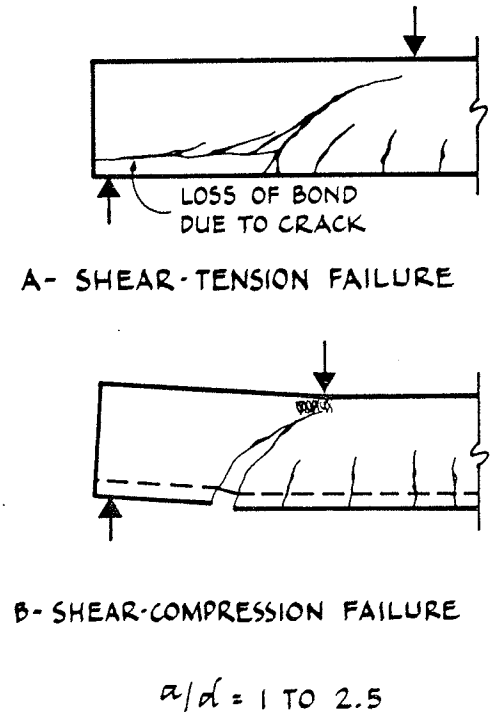

Fig. 2.3 TYPICAL SHEAR FAILURES IN SHORT BEAMS

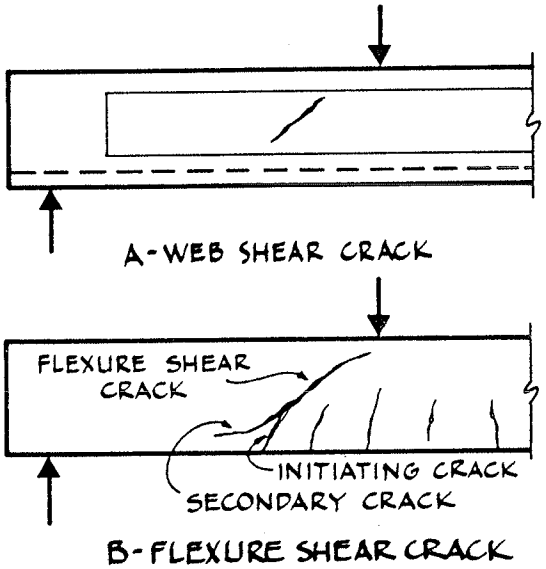

Fig. 2.4 TYPES OF INCLINED CRACK

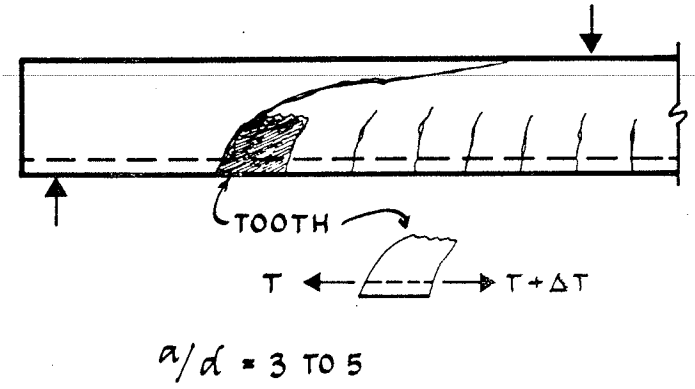

Fig. 2.5 TOOTH CRACKING FAILURE AND DIAGONAL TENSION FAILURE

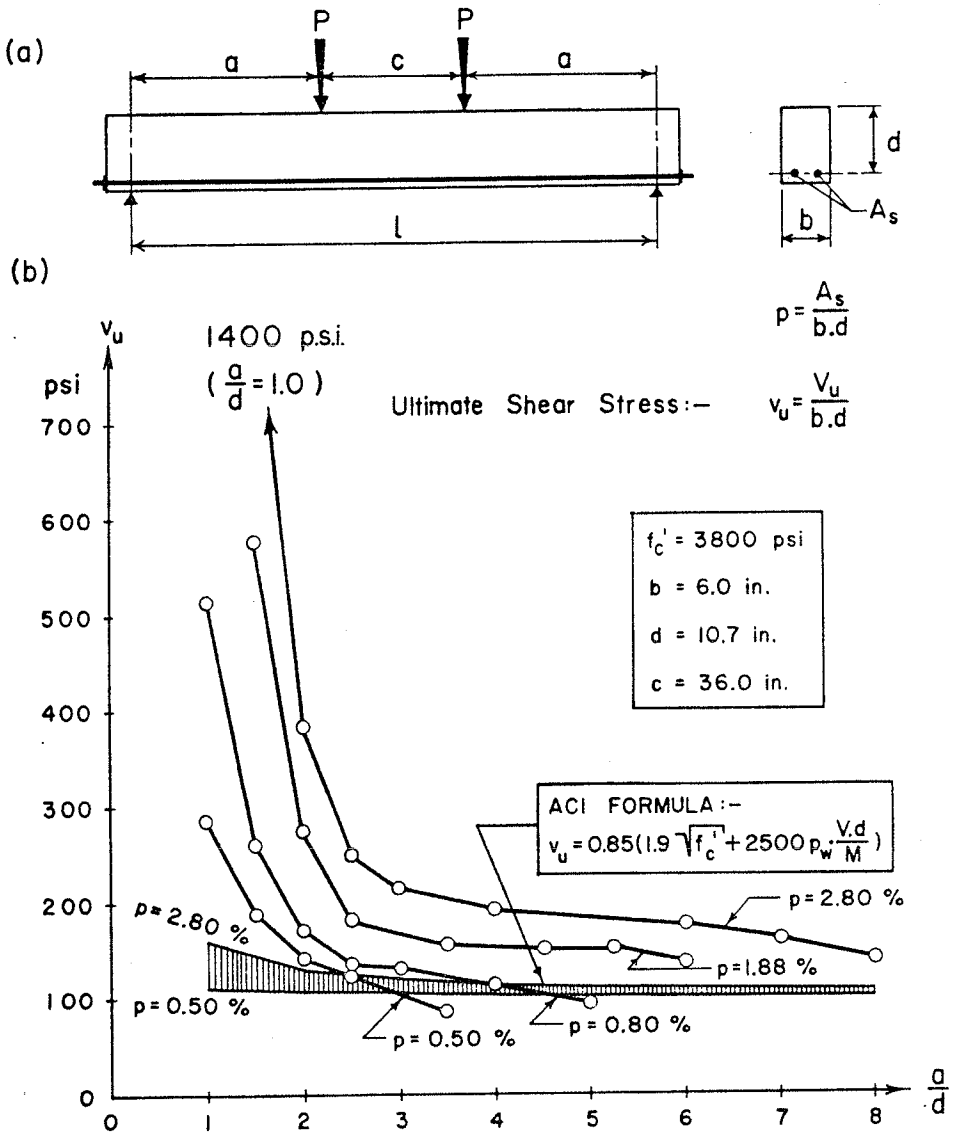

Fig. 2.6 THE EFFECT OF a/d ON SHEAR STRENGTH

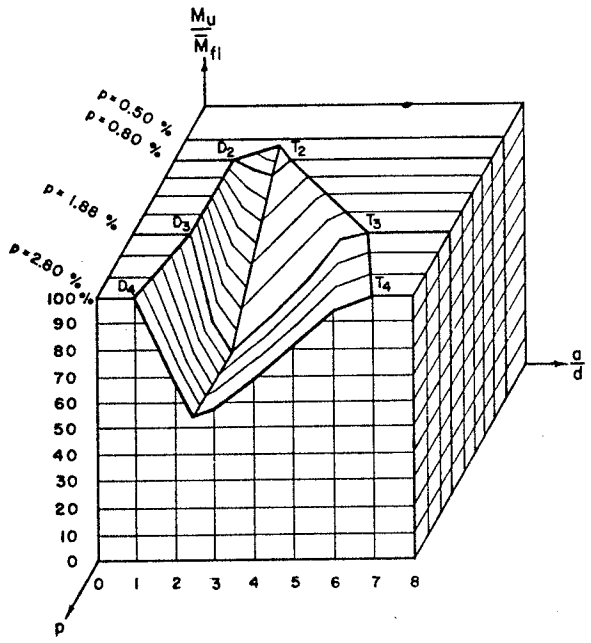

Fig. 2.7 RELATIVE BEAM STRENGTH, M_u/M_{fl}, VERSUS a/d AND p

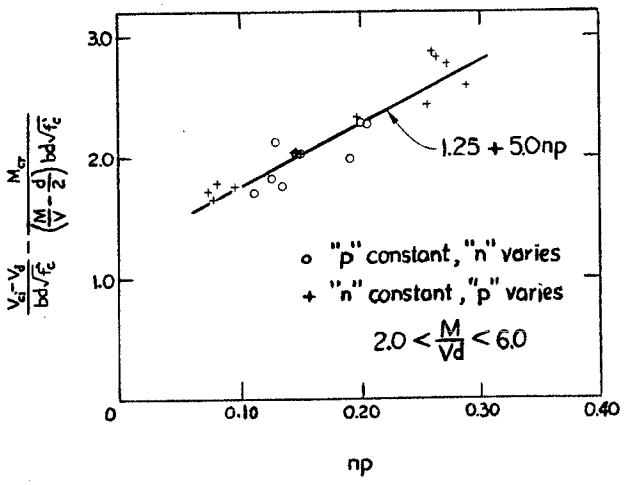

Fig. 2.8 VARIATION OF SHEAR STRESS INCREMENT BETWEEN FLEXURAL AND DIAGONAL TENSION CRACKING, WITH VARIATION OF PRODUCT OF MODULAR RATIO, n, AND FLEXURAL TENSION REINFORCEMENT RATIO, p

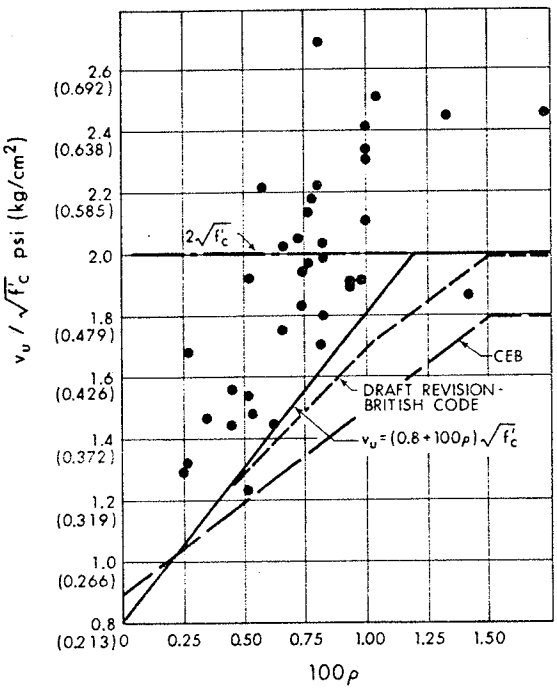

Fig. 2.9 EFFECT OF LONGITUDINAL REINFORCEMENT RATIO, p, ON CONCRETE CONTRIBUTION, v_c

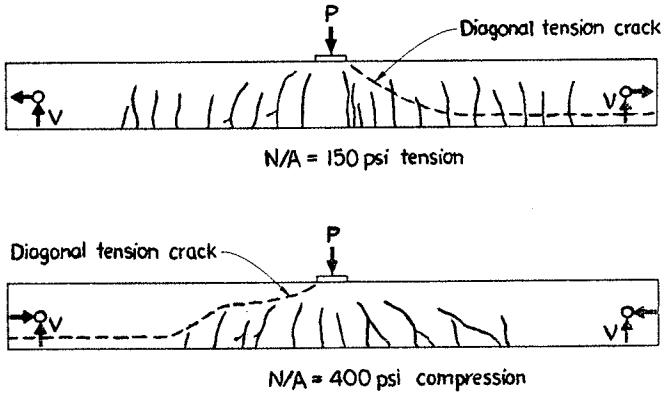

Fig. 2.10 EFFECT OF AXIAL LOAD

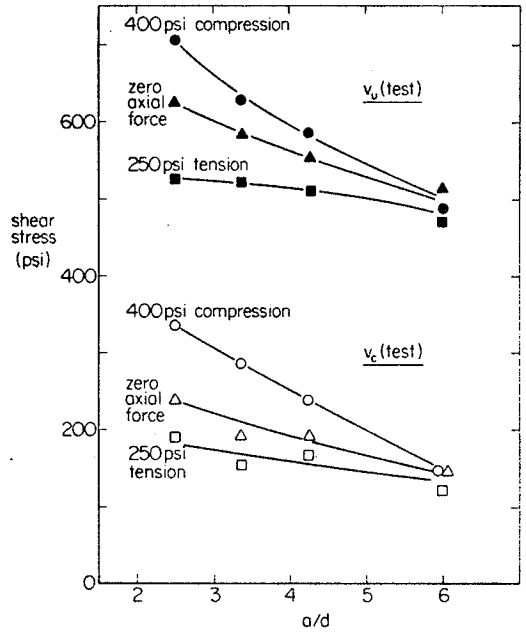

Fig. 2.11 EFFECT OF AXIAL LOAD ON DIAGONAL TENSION CRACKING, v_c, AND ULTIMATE SHEAR STRENGTH, v_u

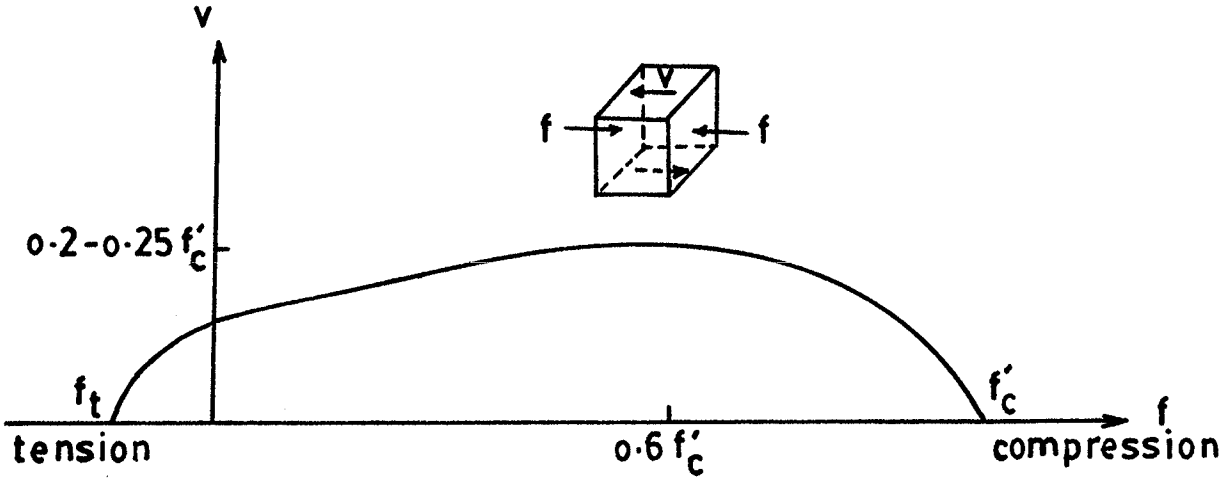

Fig. 2.12 FAILURE ENVELOPE OF CONCRETE SUBJECTED TO AXIAL AND SHEAR STRESSES

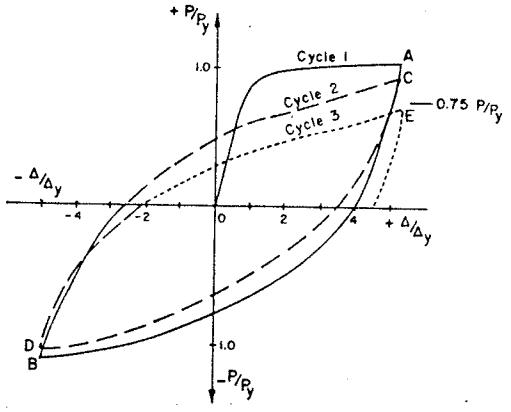

Fig. 2.13 LOAD-DEFLECTION HYSTERESIS

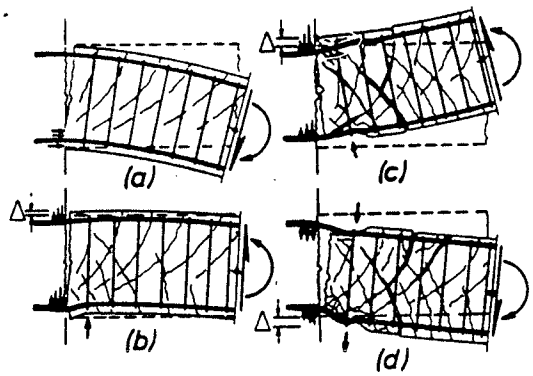

Fig. 2.14 SIGNIFICANT STAGES OF THE DEVELOPMENT OF A PLASTIC HINGE DUE TO REVERSED CYCLIC LOADING

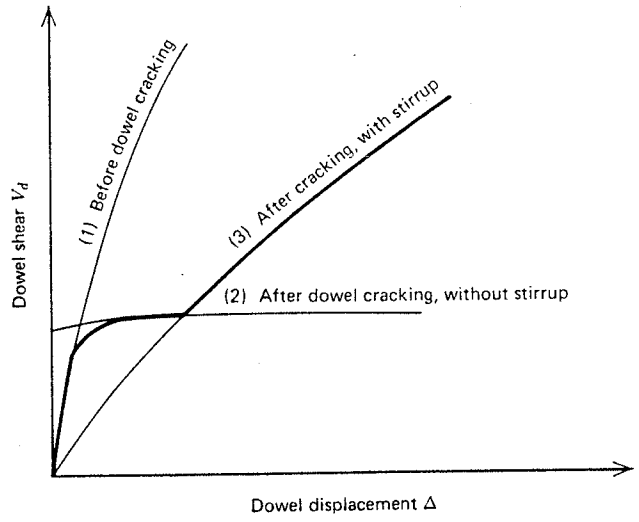

Fig. 2.15 DOWEL SHEAR-DOWEL DISPLACEMENT RELATIONSHIP

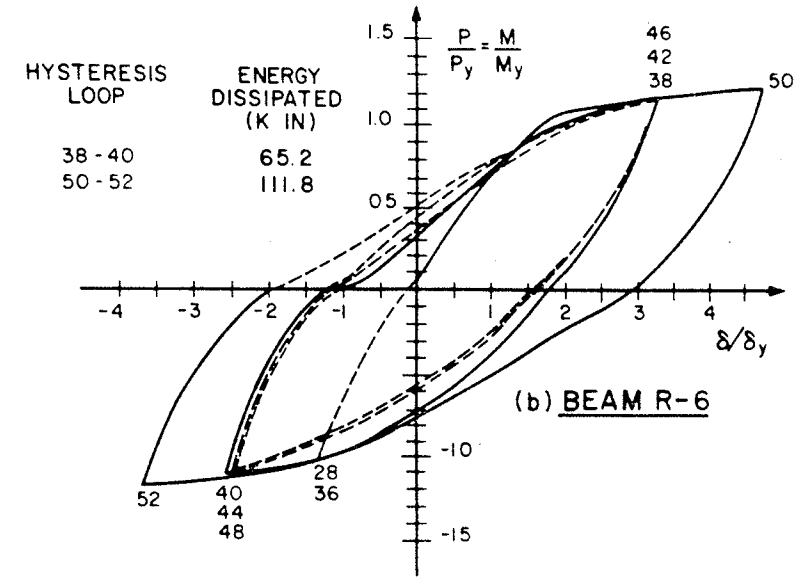

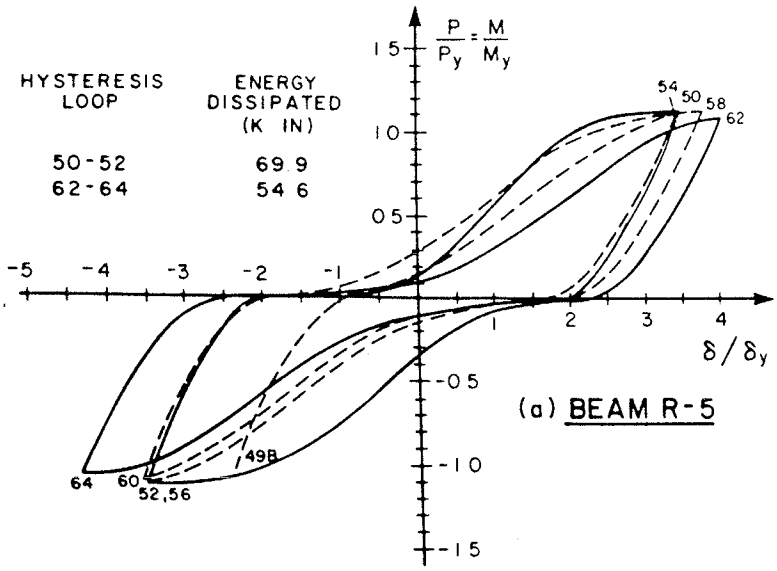

Fig. 2.16 COMPARISON OF HYSTERESIS BEHAVIOUR AT SIMILAR DISPLACEMENT DUCTILITY RATIOS, ILLUSTRATING EFFECT OF SHEAR ON ENERGY DISSIPATION CAPACITY

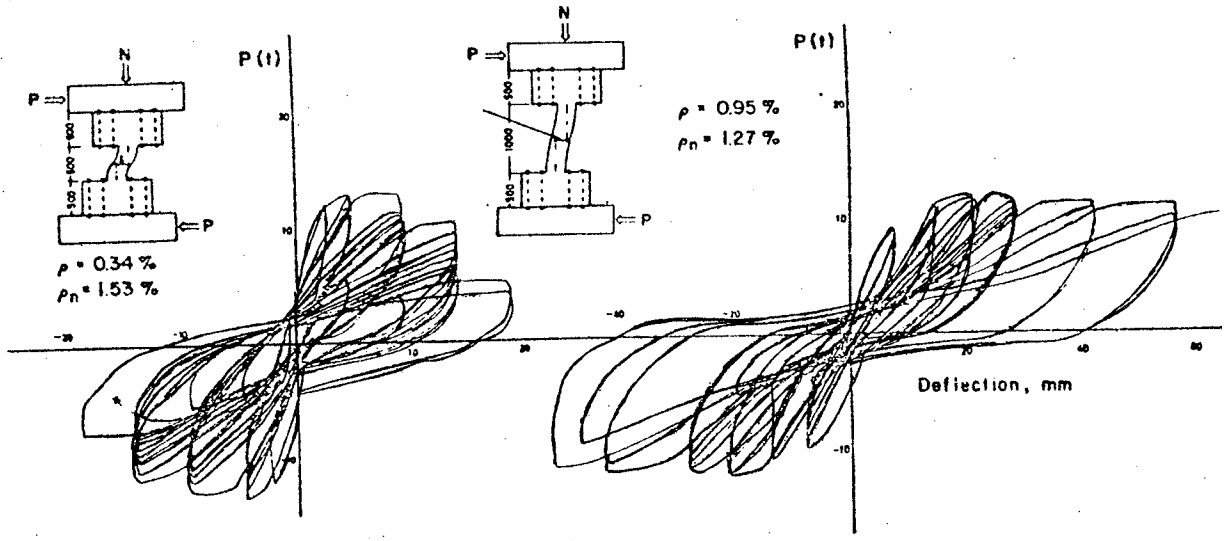

Fig. 2.17 LATERAL SHEAR-DEFORMATION CURVES

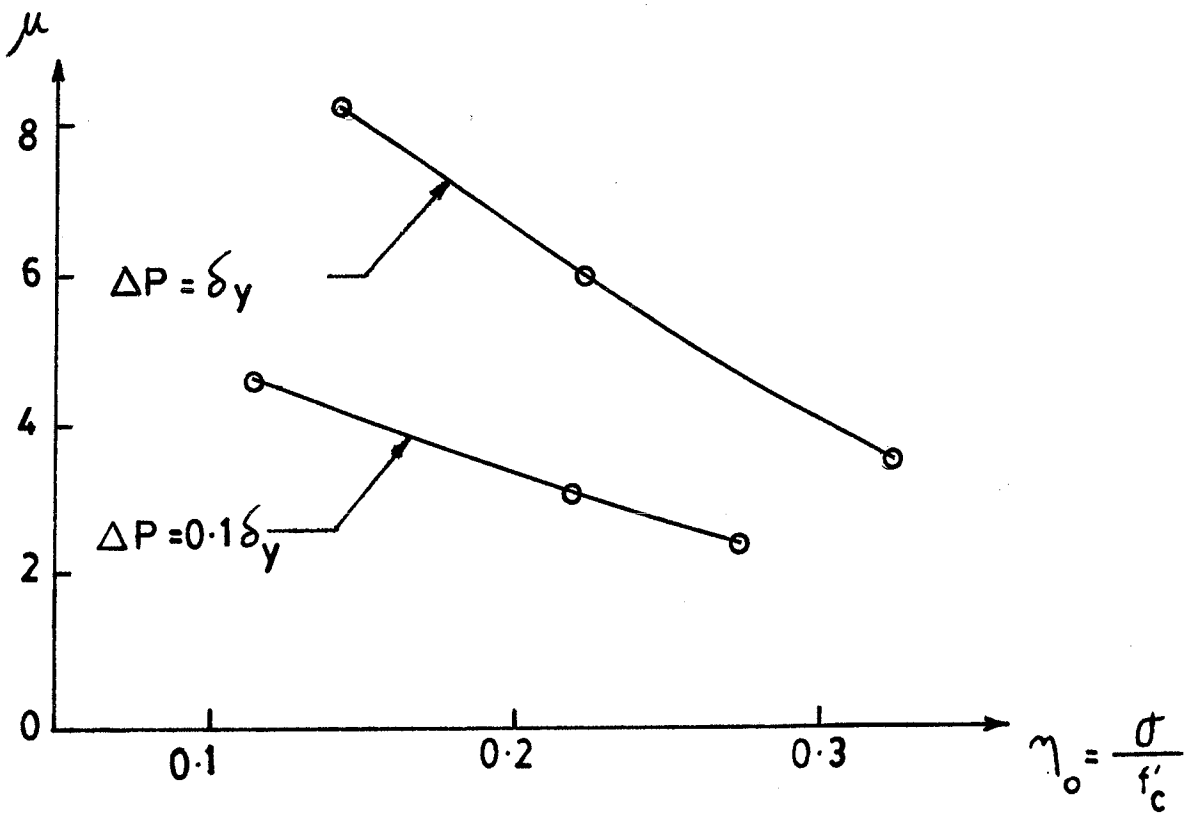

Fig. 2.18 RELATIONSHIP BETWEEN DUCTILITY FACTOR AND LEVEL OF AXIAL COMPRESSIVE STRESSES [3]

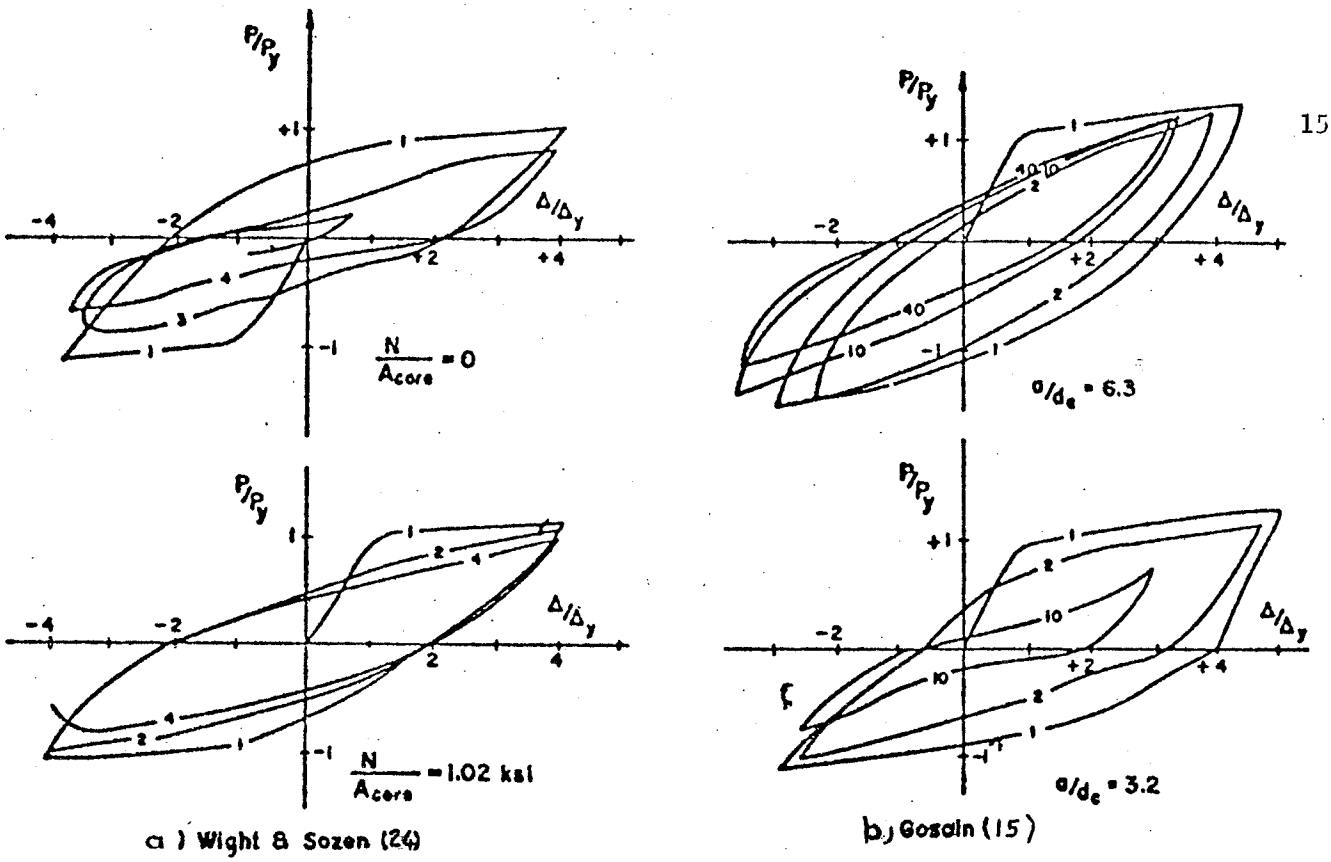

Fig. 2.19 INFLUENCE OF AXIAL COMPRESSIVE STRESSES, $\frac{N}{A_c}$, AND SHEAR SPAN TO CONFINED DEPTH, $\frac{a}{d_c}$, ON RESPONSE

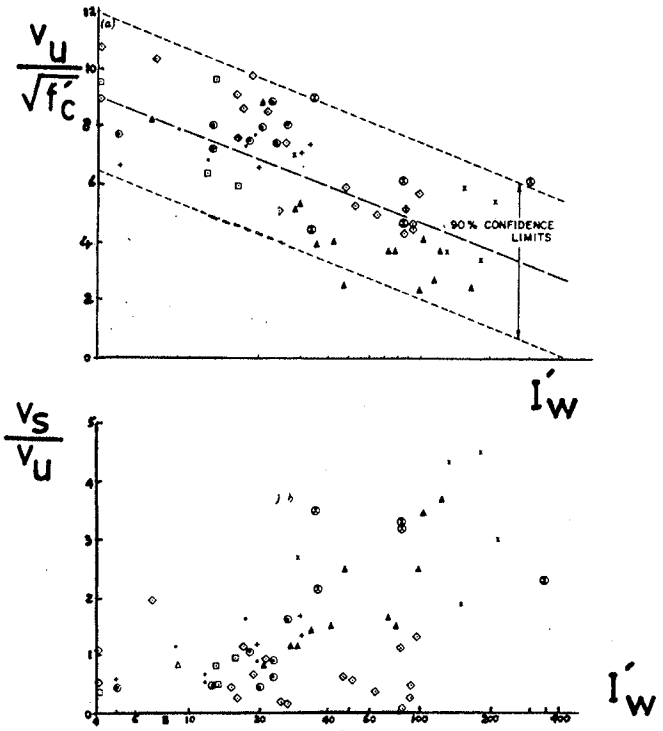

Fig. 2.20 VARIATION OF MODIFIED WORK INDEX, I_w', WITH ULTIMATE SHEAR STRESS

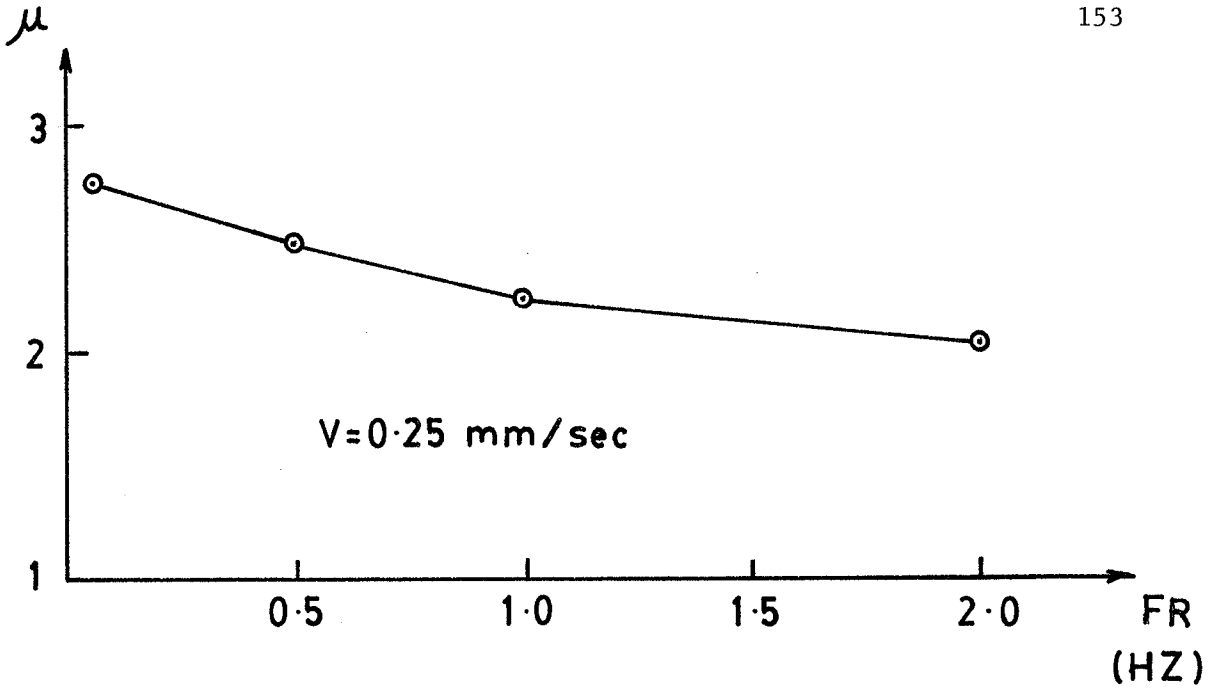

Fig. 2.21 RELATIONSHIP BETWEEN DUCTILITY FACTOR, μ, AND LOAD FREQUENCY, FR

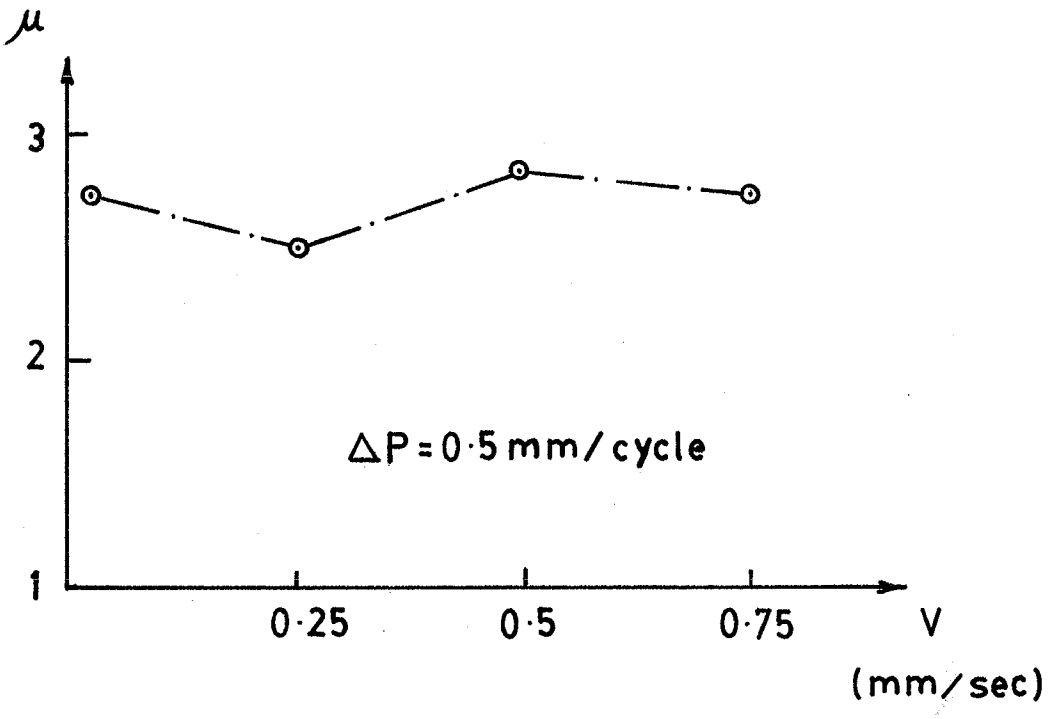

Fig. 2.22 RELATIONSHIP BETWEEN DUCTILITY FACTOR, μ, AND RATE OF THE APPLIED DEFLECTION, v

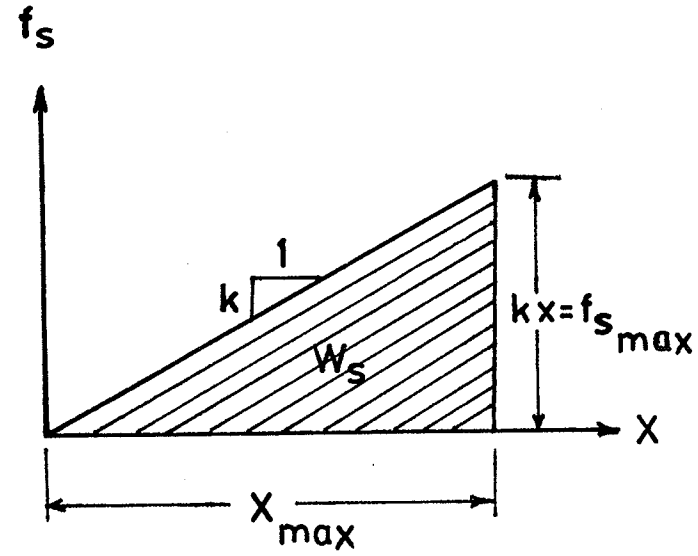

Fig. 2.23 RELATIONSHIP BETWEEN VISCOUS AND ACTUAL DAMPING FORCE-DISPLACEMENT DIAGRAMS

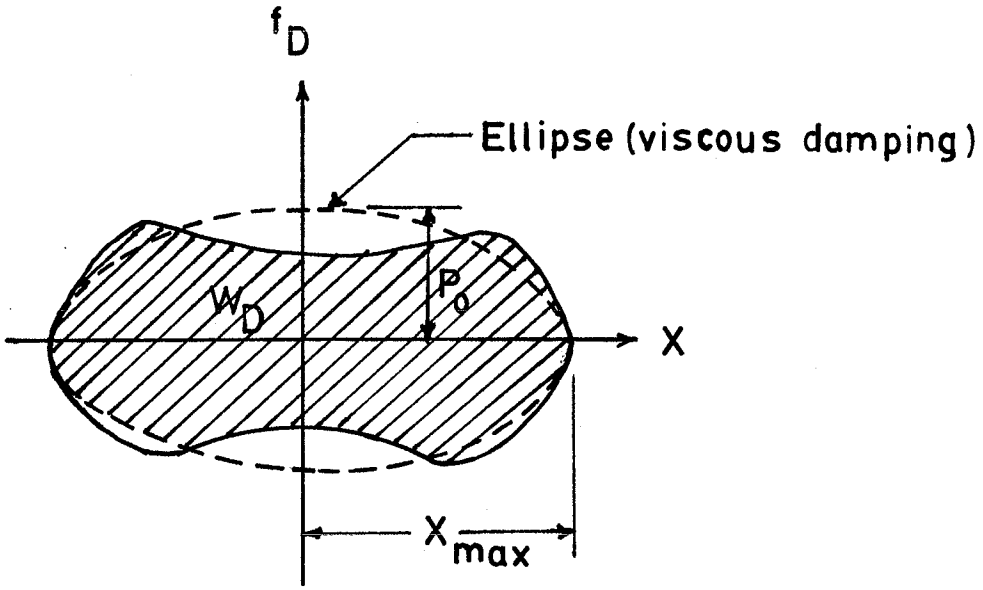

Fig. 2.24 STATIC FORCE-DISPLACEMENT DIAGRAM OF A LINEARLY ELASTIC SYSTEM

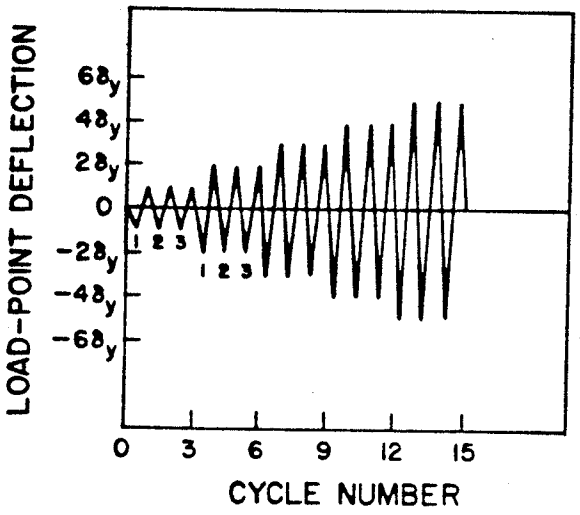

Fig. 3.1 LOAD PATTERN

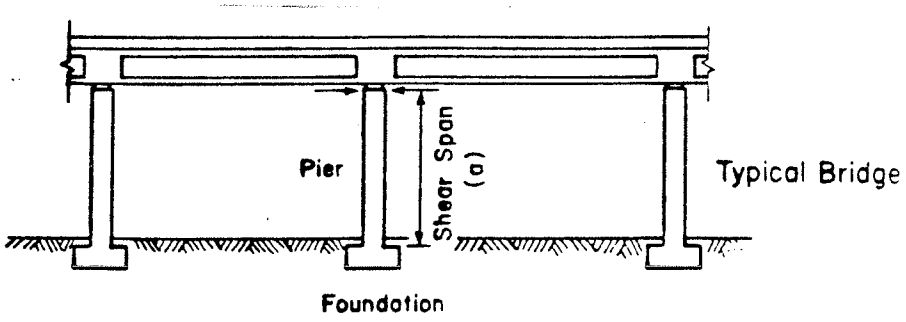

A-Typical Bridge Piers

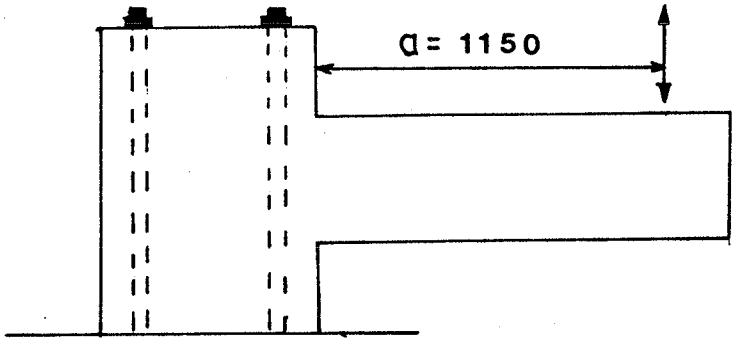

B- Typical Specimen

Fig. 3.2. RELATIONSHIP BETWEEN A TYPICAL SPECIMEN AND BRIDGE PIERS.

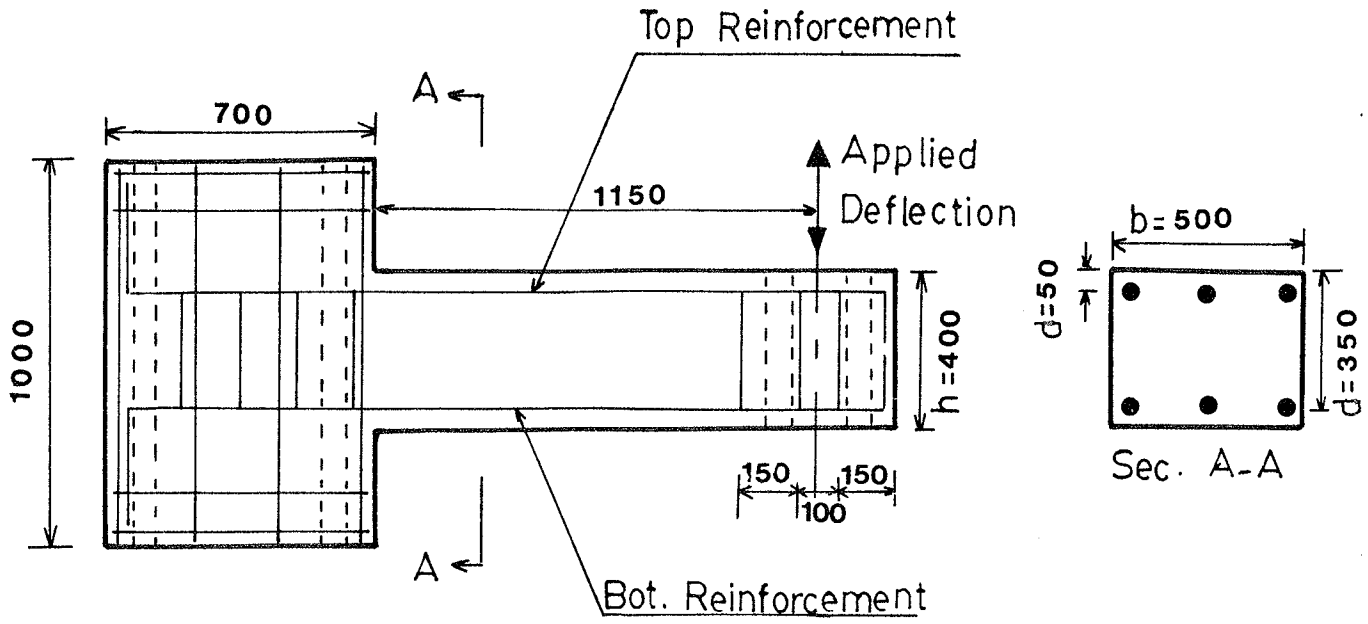

a- Elevation

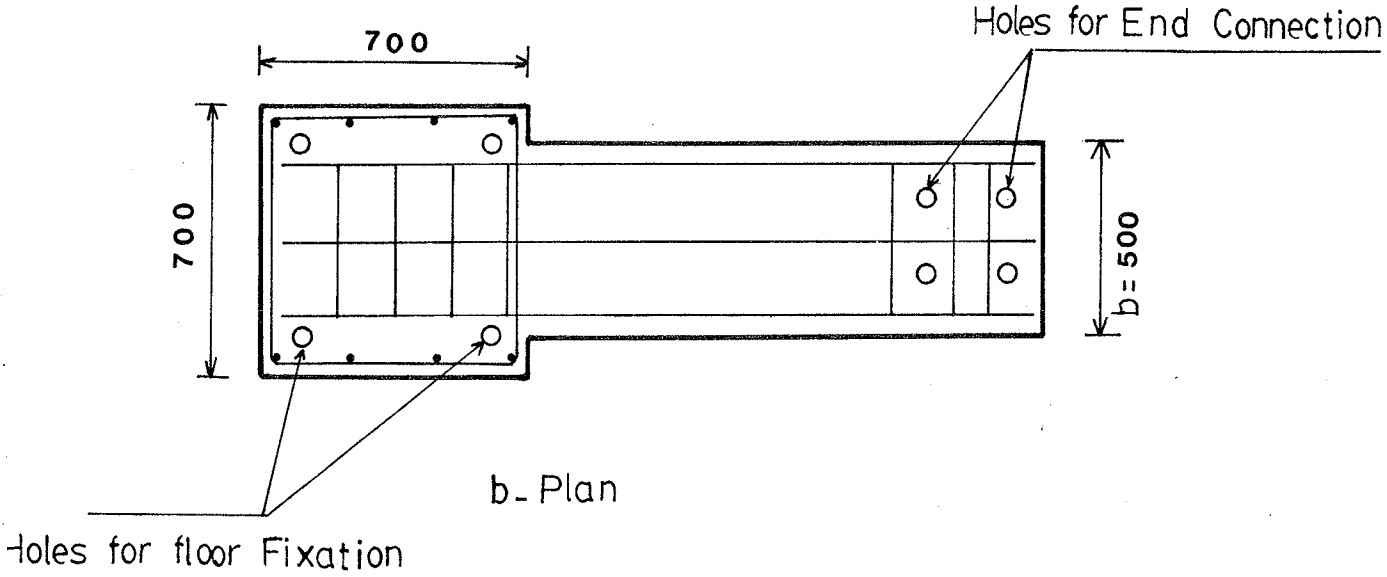

Fig. 3.3. REINFORCEMENT DETAILS AND DIMENSION OF A TYPICAL SPECIMEN.

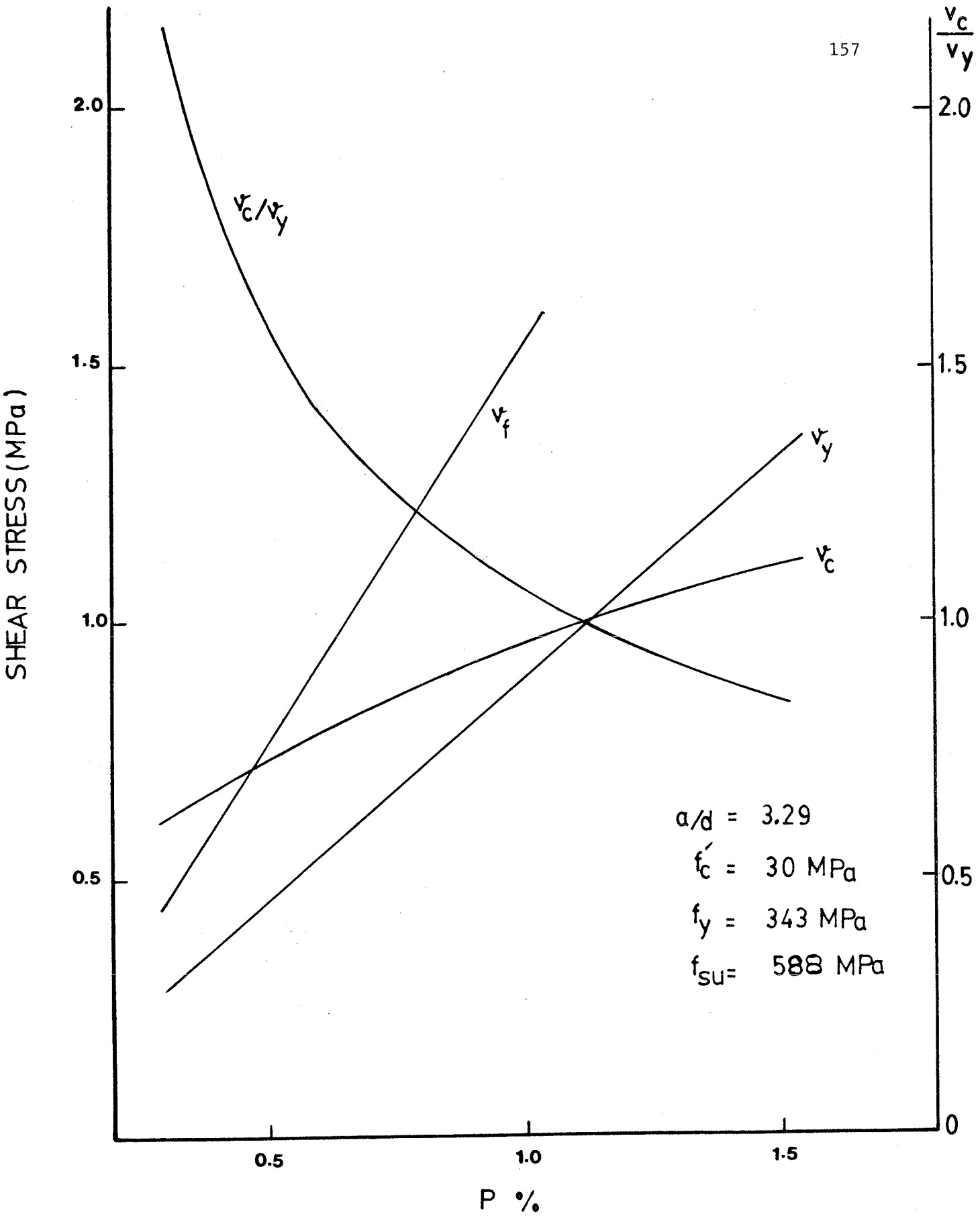

Fig. 3.4.a. CALCULATED SHEAR STRESS VERSUS p FOR a/d VALUE of 3.29.

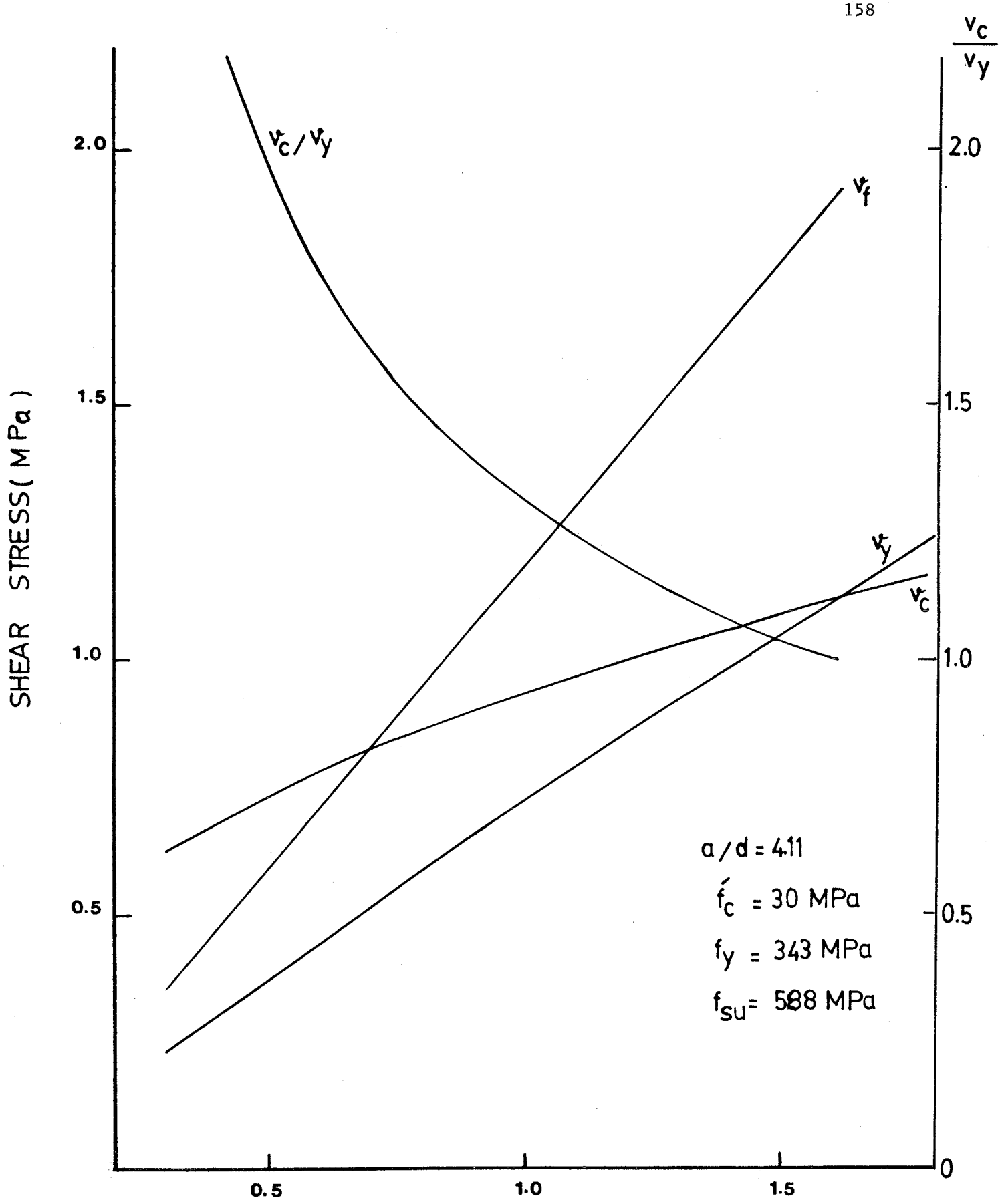

Fig. 3.4.b. CALCULATED SHEAR STRESS VERSUS p FOR a/d VALUE OF 4.11.

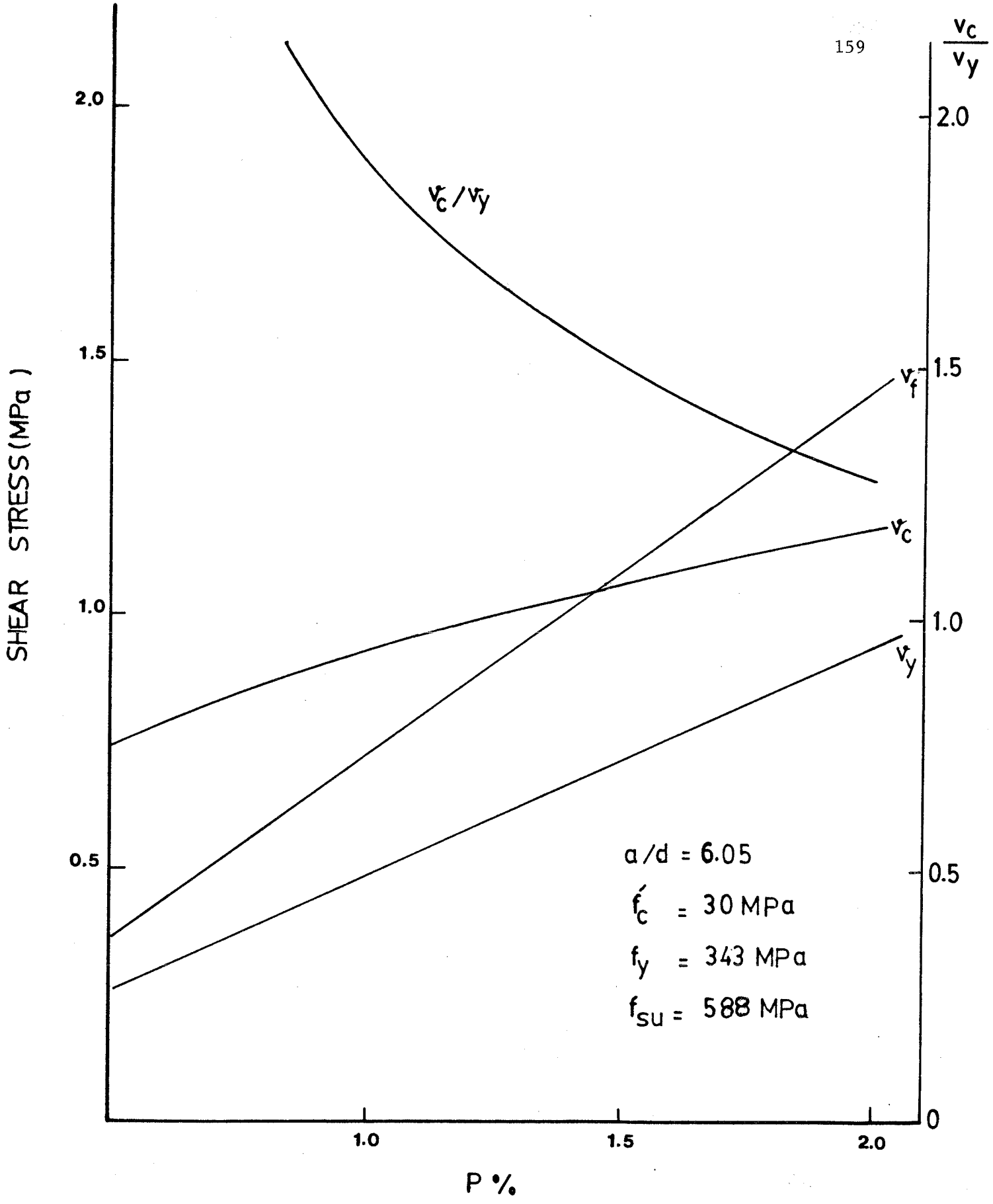

Fig. 3.4.c. CALCULATED SHEAR STRESS VERSUS p FOR a/d VALUE of 6.05.

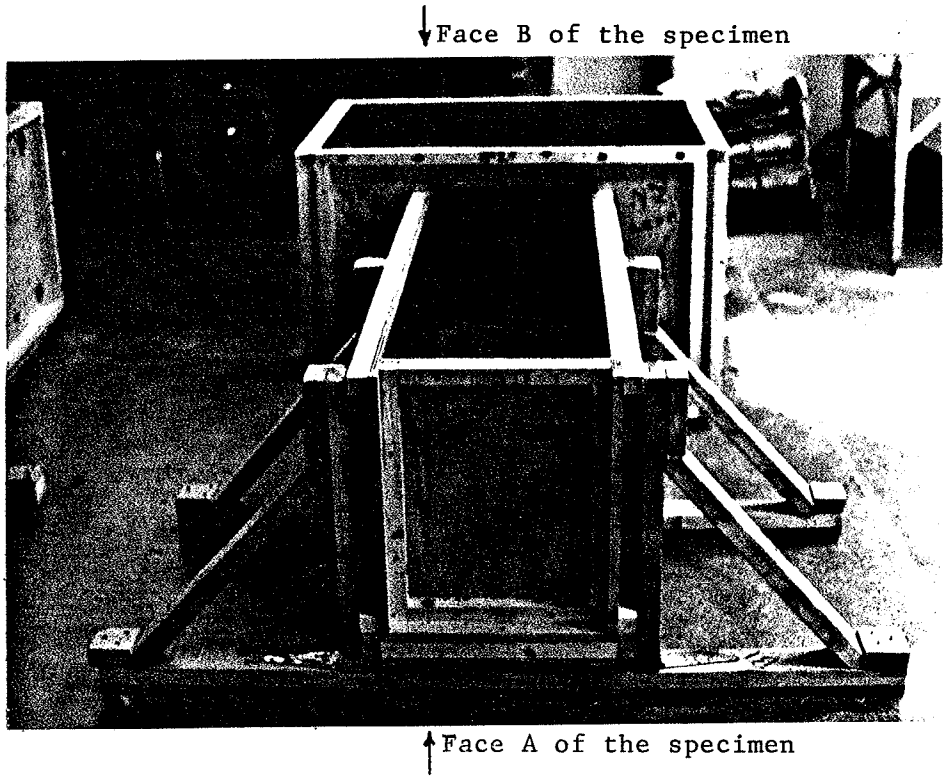

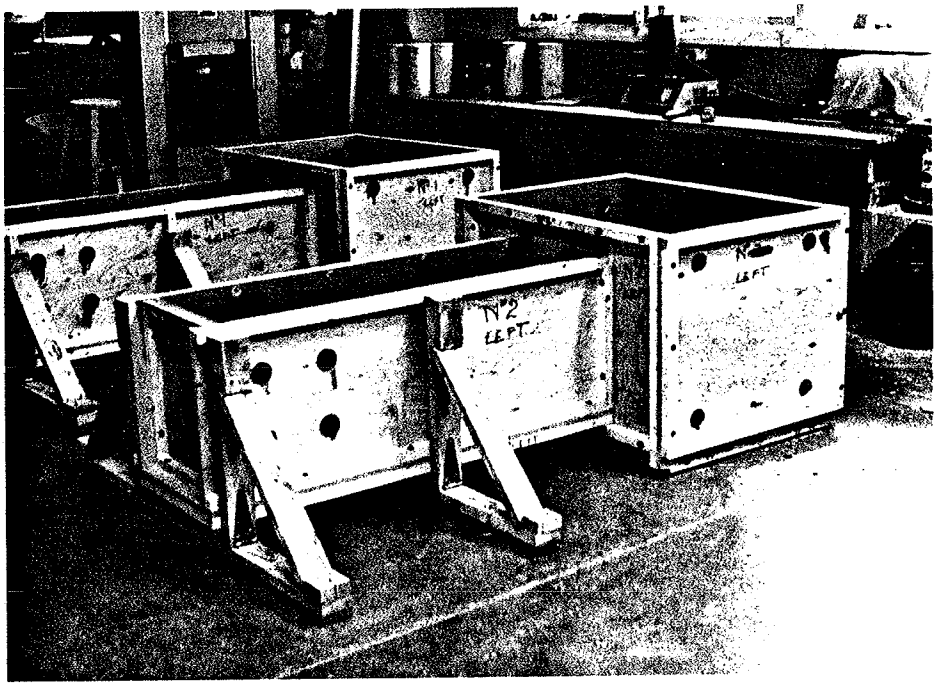

Fig. 3.5 FORMWORK FOR A TYPICAL SPECIMEN

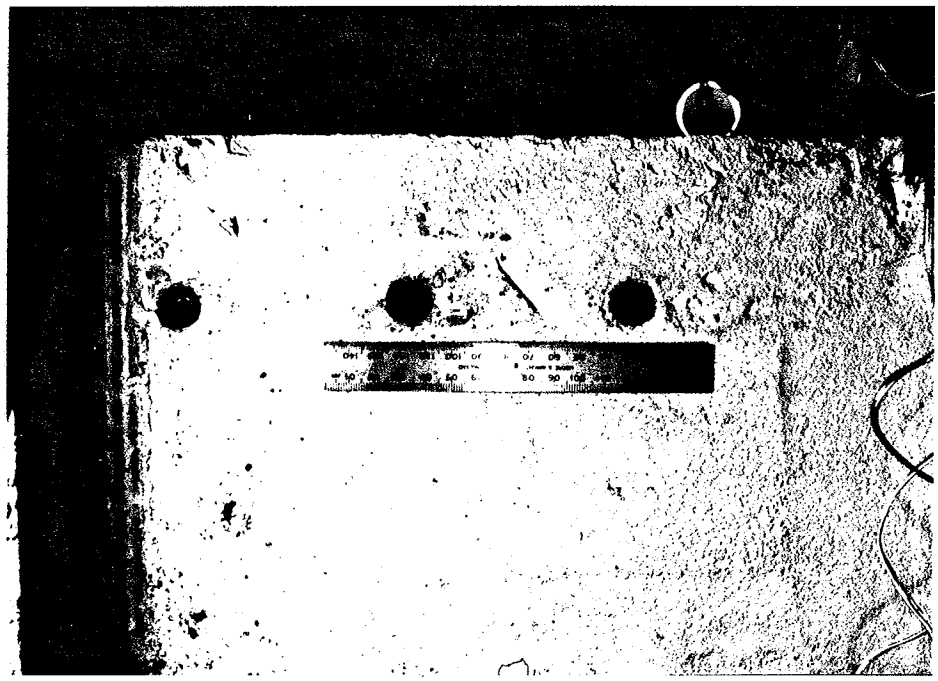

Fig. 3.6 SPACE BETWEEN STUDS AND SURROUNDING CONCRETE

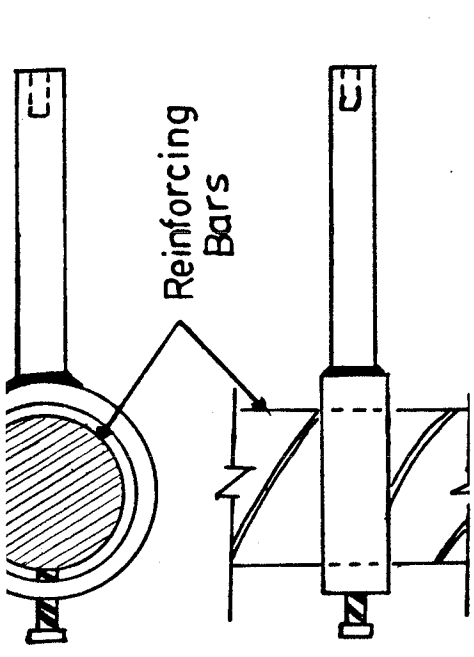

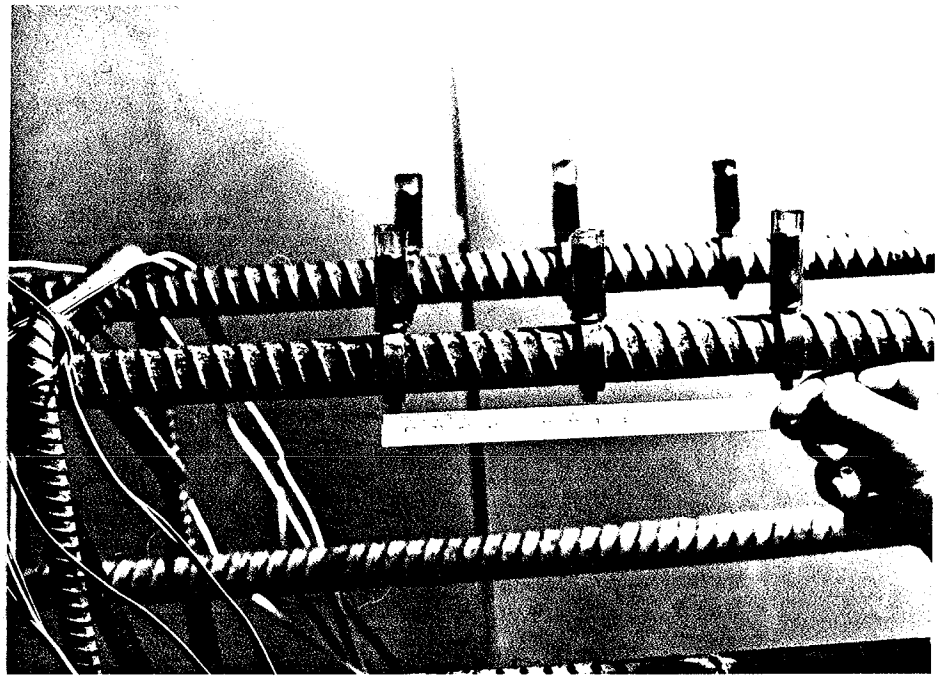

Fig. 3.7 STEEL STUDS ON REINFORCING BARS

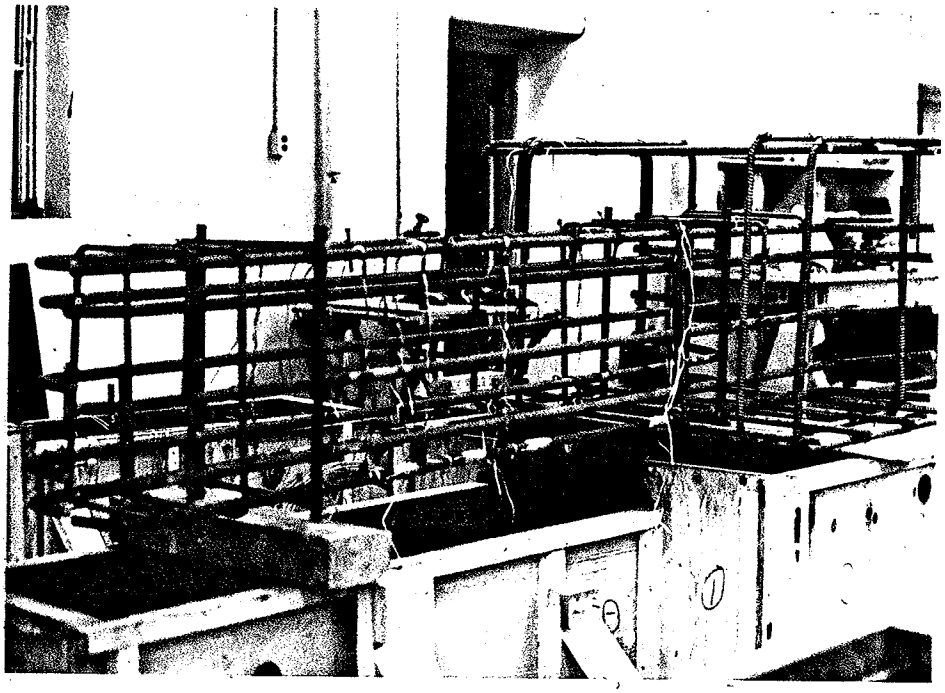

Fig. 3.8 A TYPICAL SPECIMEN REINFORCEMENT

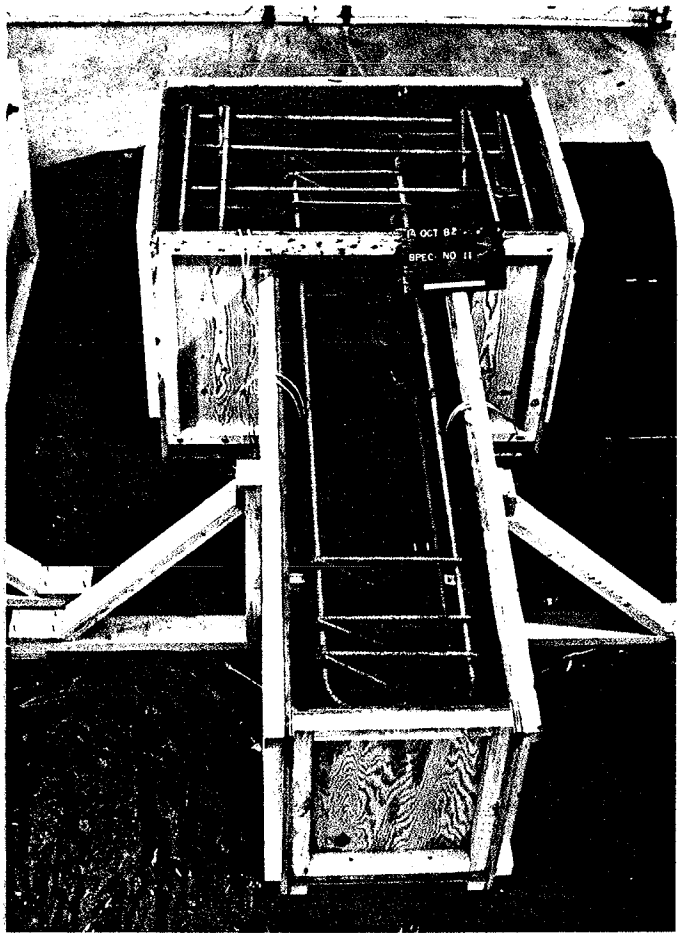

Fig. 3.9 REINFORCEMENT PLACED IN THE FORMS

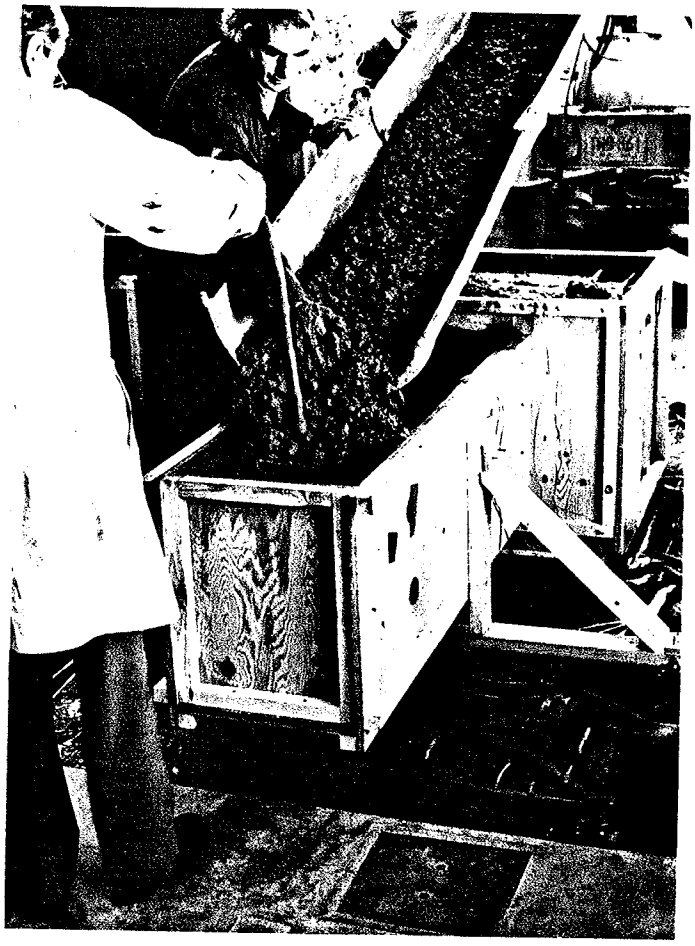

(a)

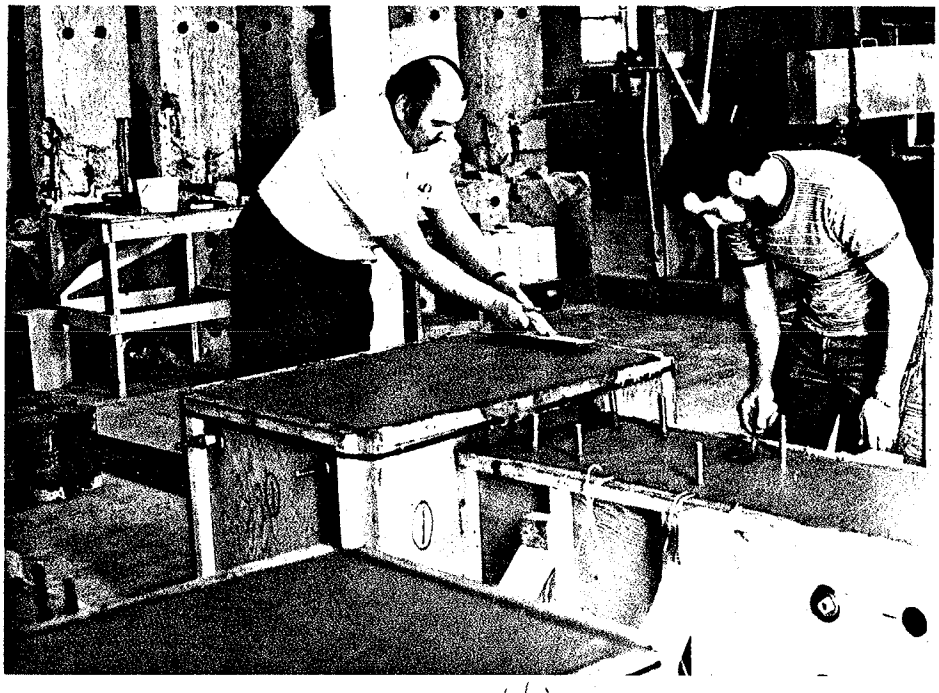

(b)

Fig. 3.10 CASTING OF CONCRETE

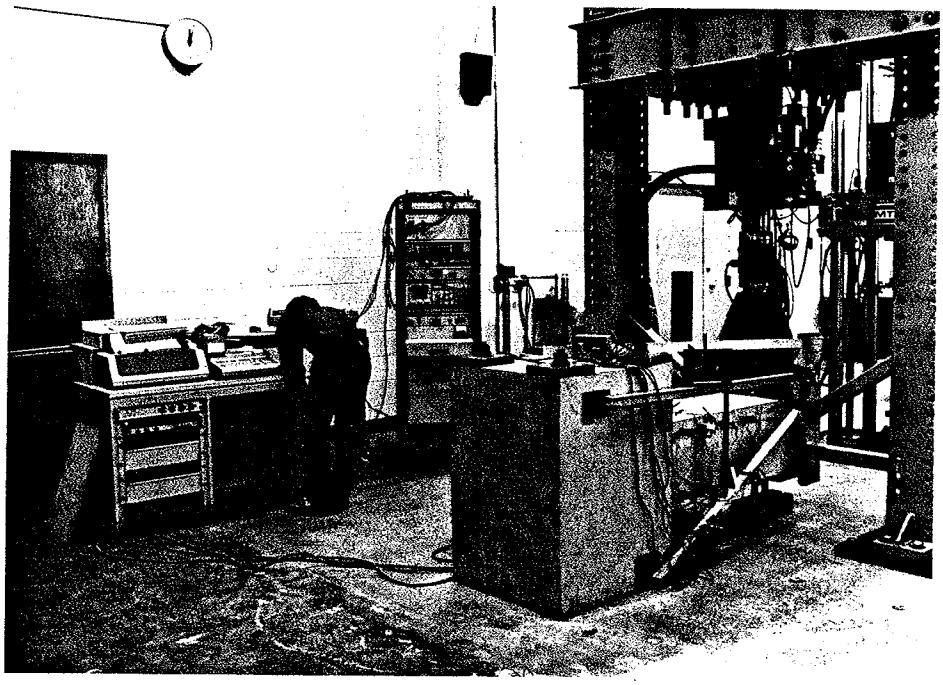

Fig. 3.11 TYPICAL TEST SET-UP

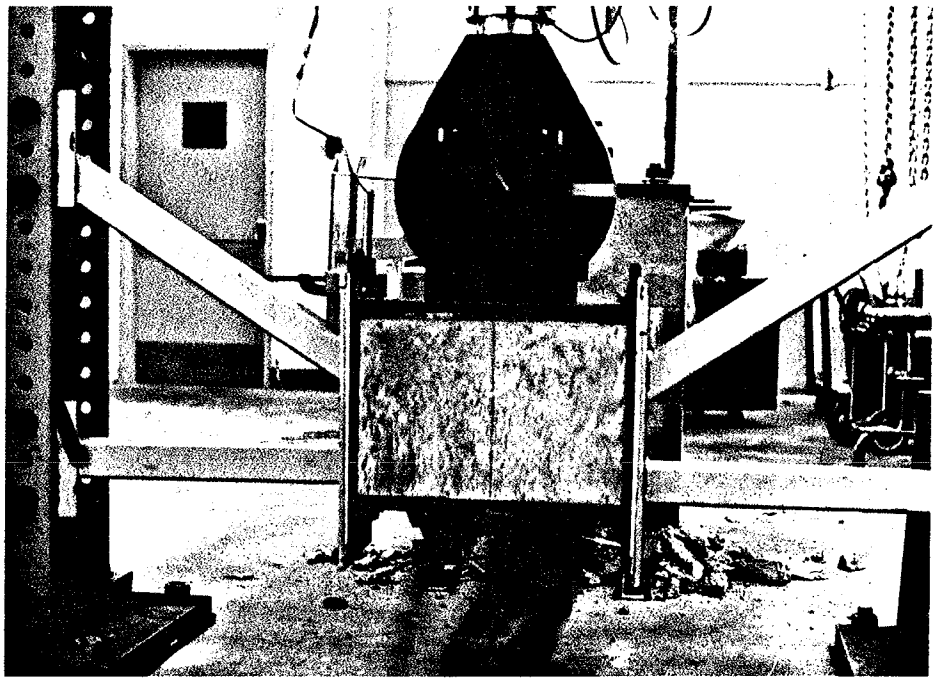

Fig. 3.12 BRACING SYSTEM

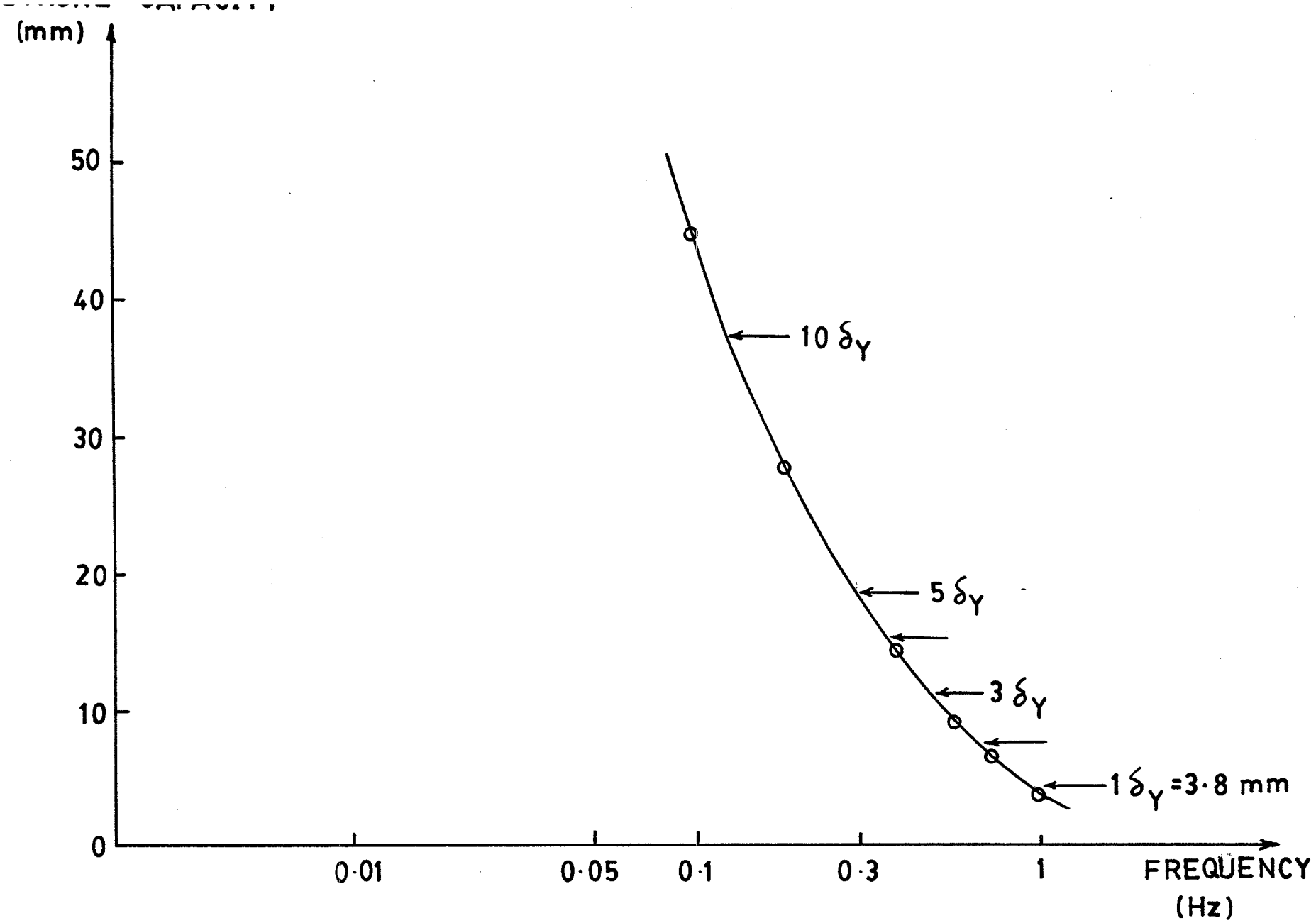

Fig. 3.13 VARIATION OF THE STROKE CAPACITY WITH LOADING FREQUENCY

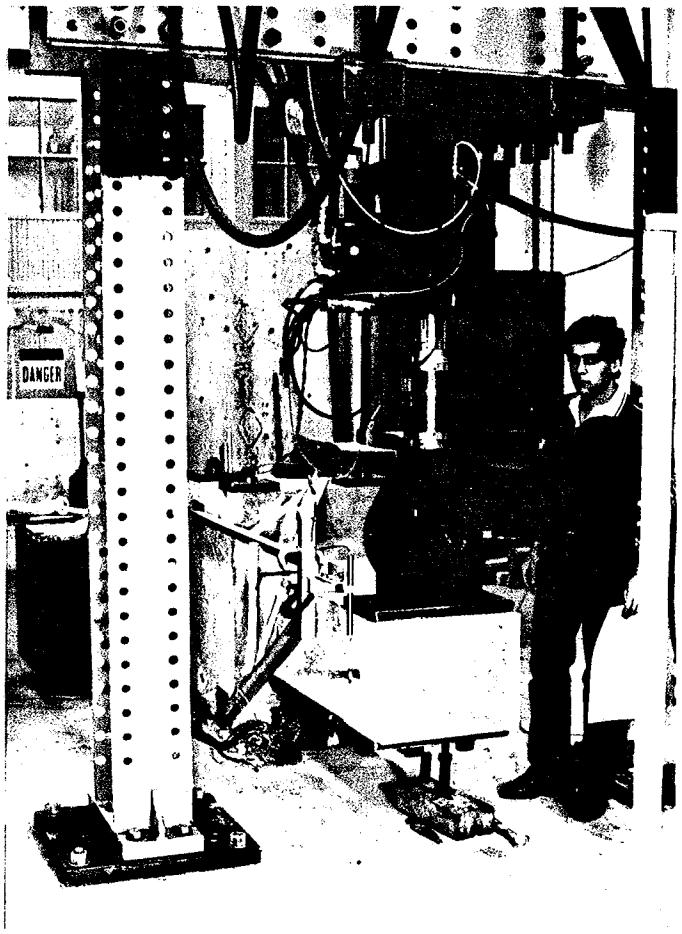

Fig. 3.14 TESTING FRAME TO SUPPORT MTS ACTUATOR

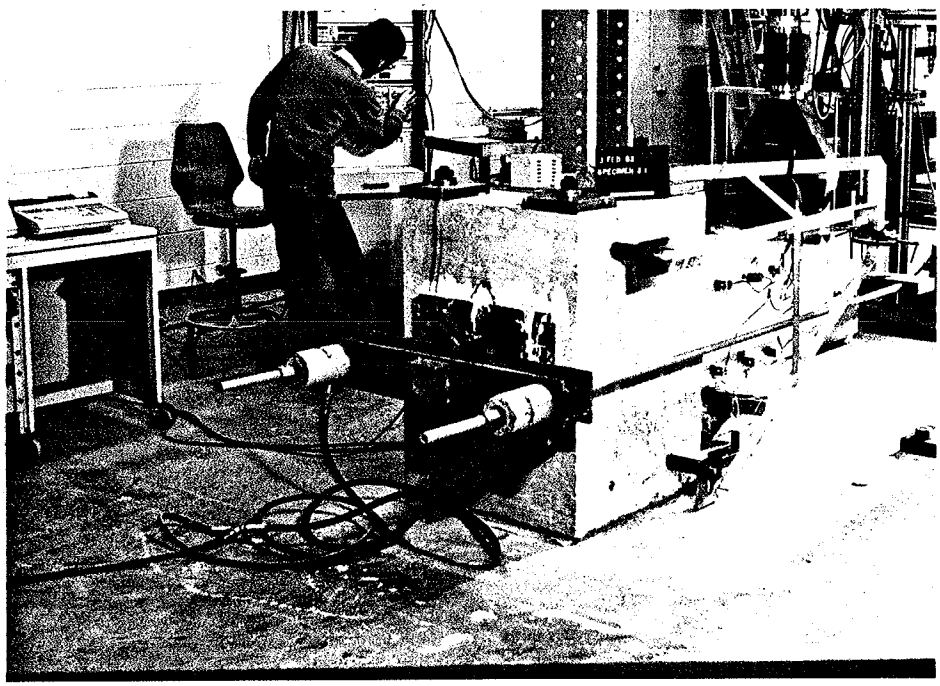

Fig. 3.15 AXIAL LOAD APPARATUS

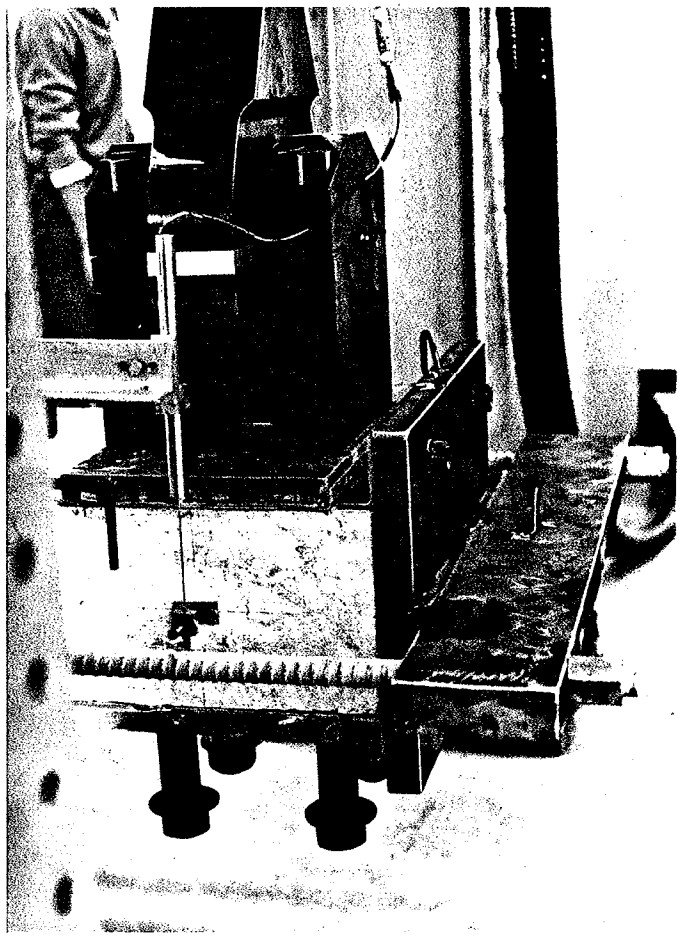

Fig. 3.16 PINNED CONNECTION AT THE FREE END OF CANTILEVER

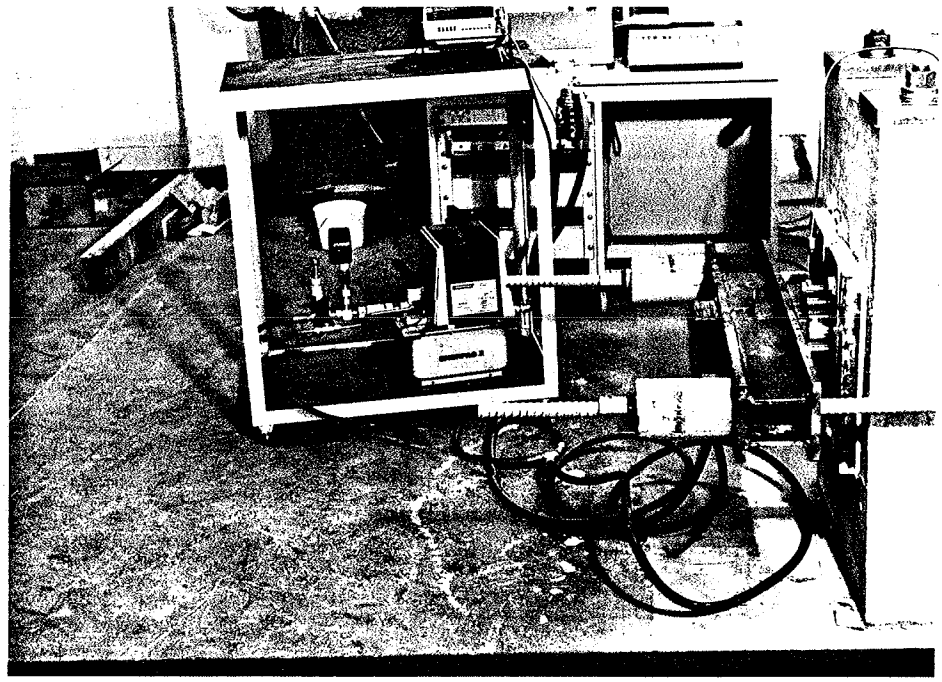

Fig. 3.17 ELECTRIC PUMP CONNECTED TO A PAIR OF HYDRAULIC JACKS

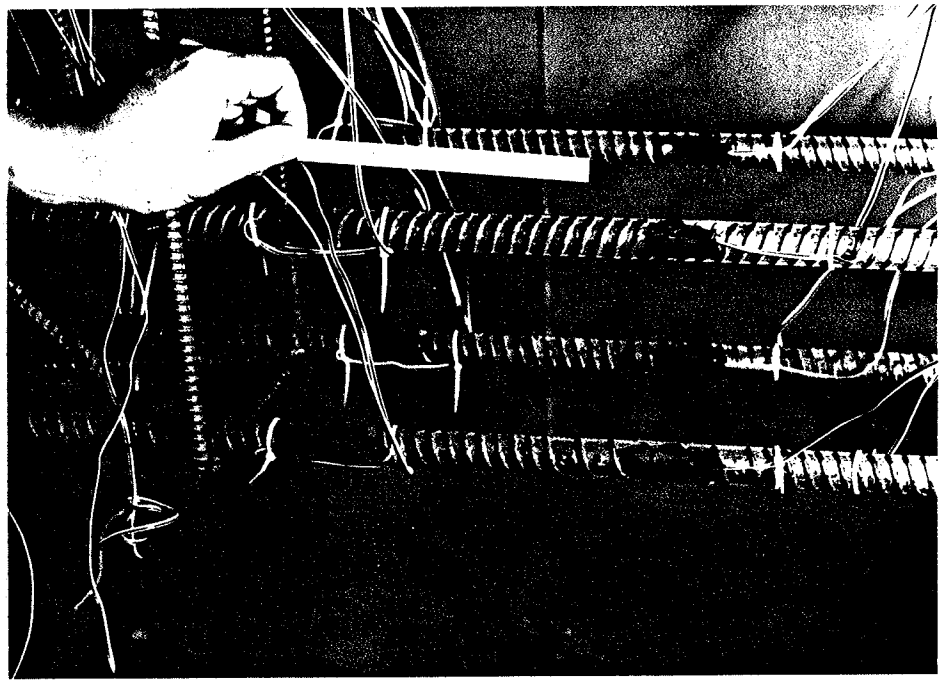

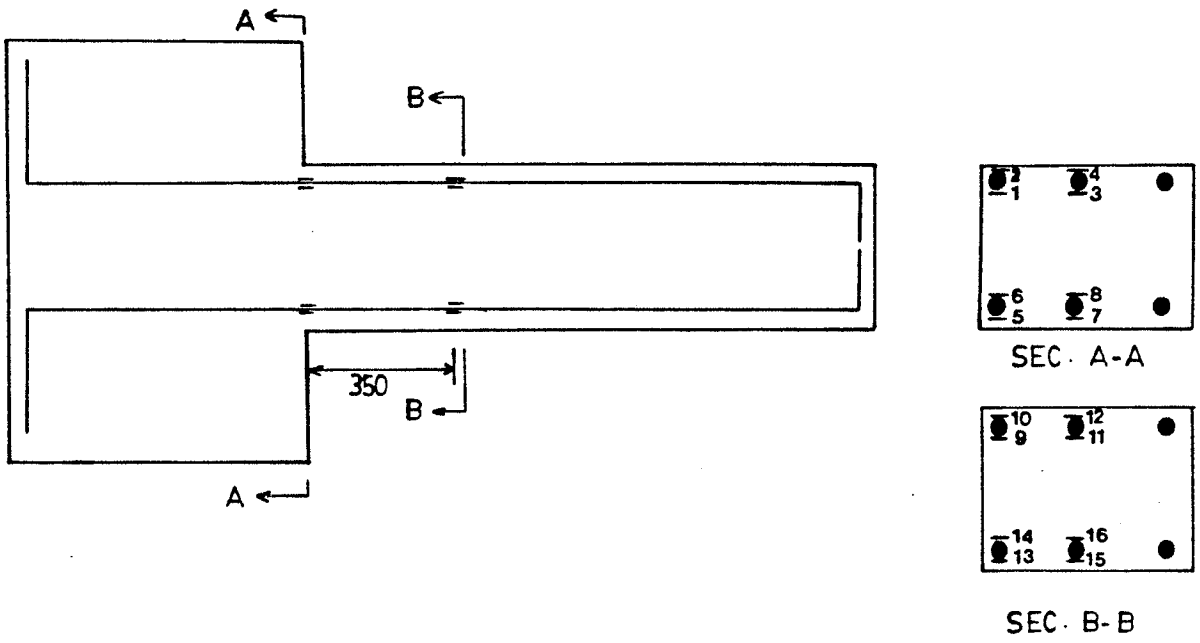

Fig. 3.18 POSITION OF STRAIN GAUGES FOR A TYPICAL SPECIMEN

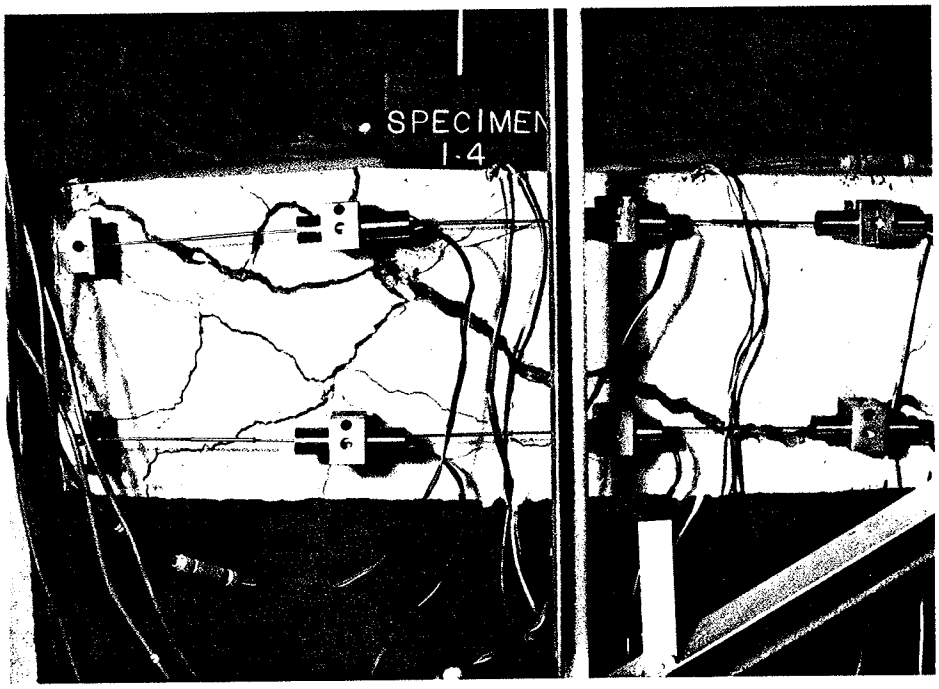

Fig. 3.19 LVDT'S TO MEASURE AVERAGE STRAINS

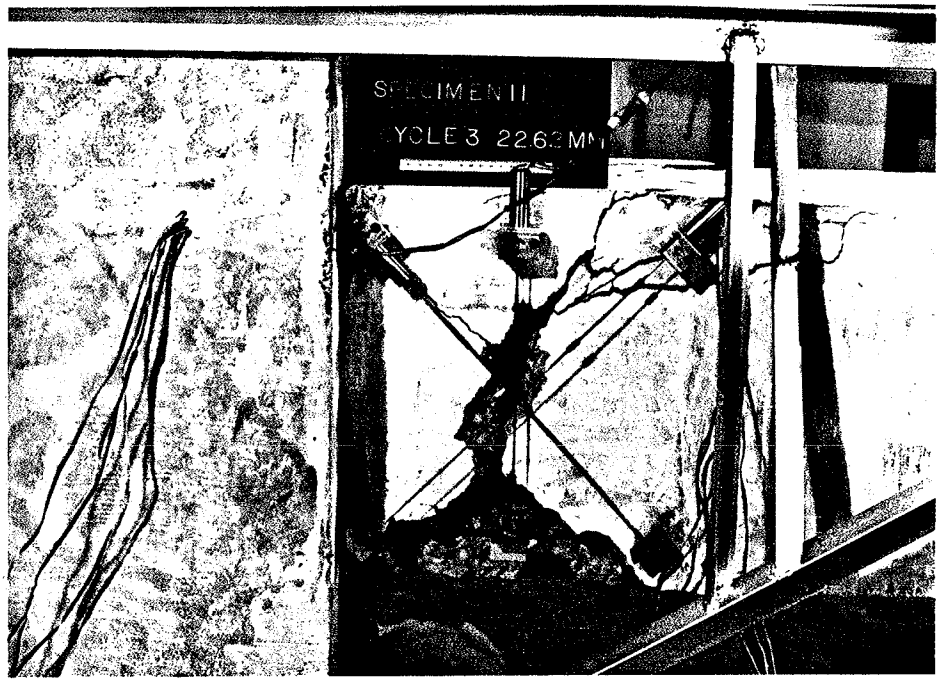

Fig. 3.20 SHEAR LVDT'S TO MEASURE AVERAGE SHEAR STRAIN

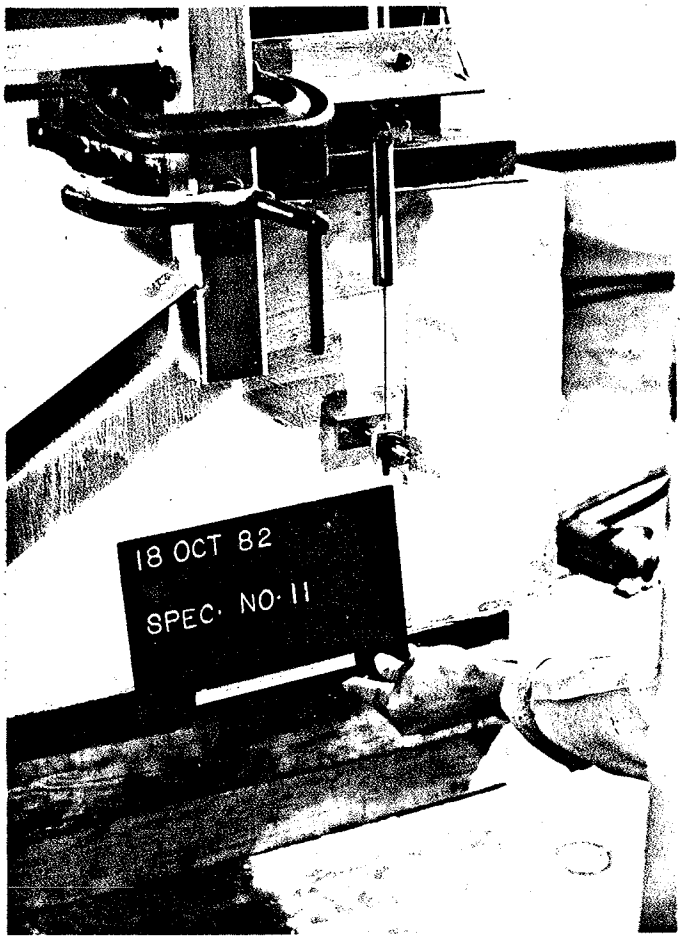

Fig. 3.21 LVDT TO MEASURE THE TIP DEFLECTION

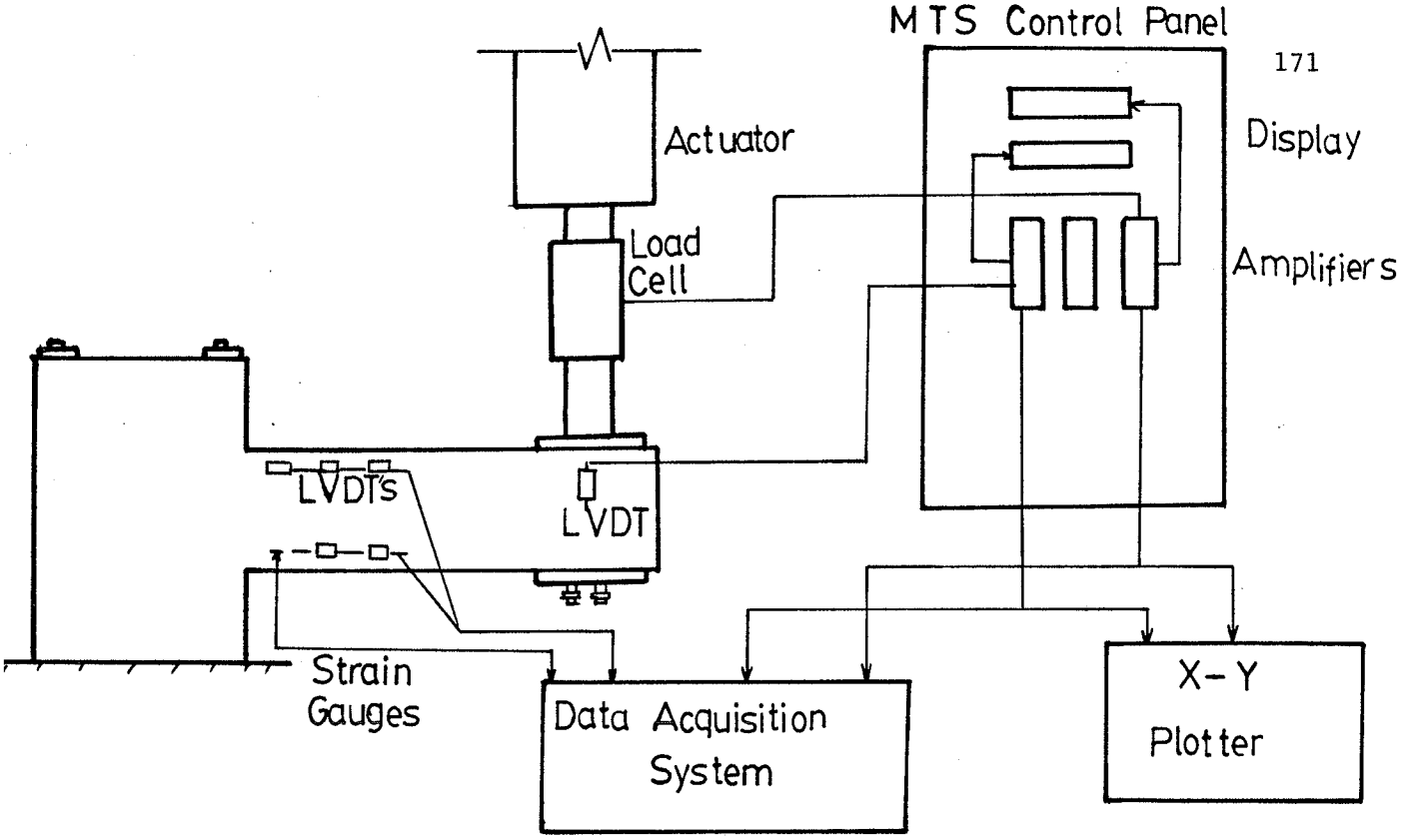

Fig·3·22 SCHEMATIC DIAGRAM FOR THE INSTRUMENTATION IN SERIES I AND III.

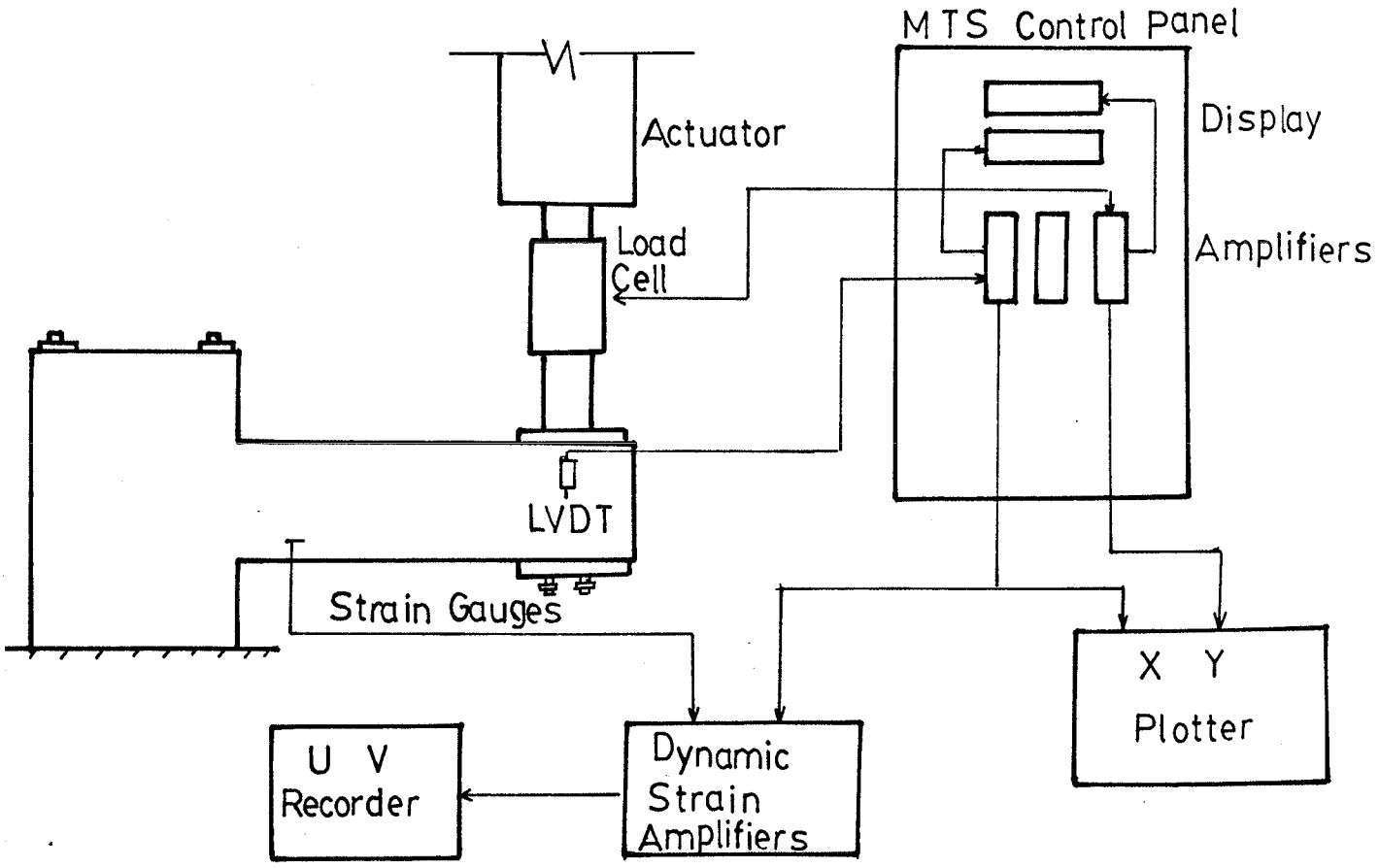

Fig·3·23 SCHEMATIC DIAGRAM FOR THE INSTRUMENTATION IN SERIES II.

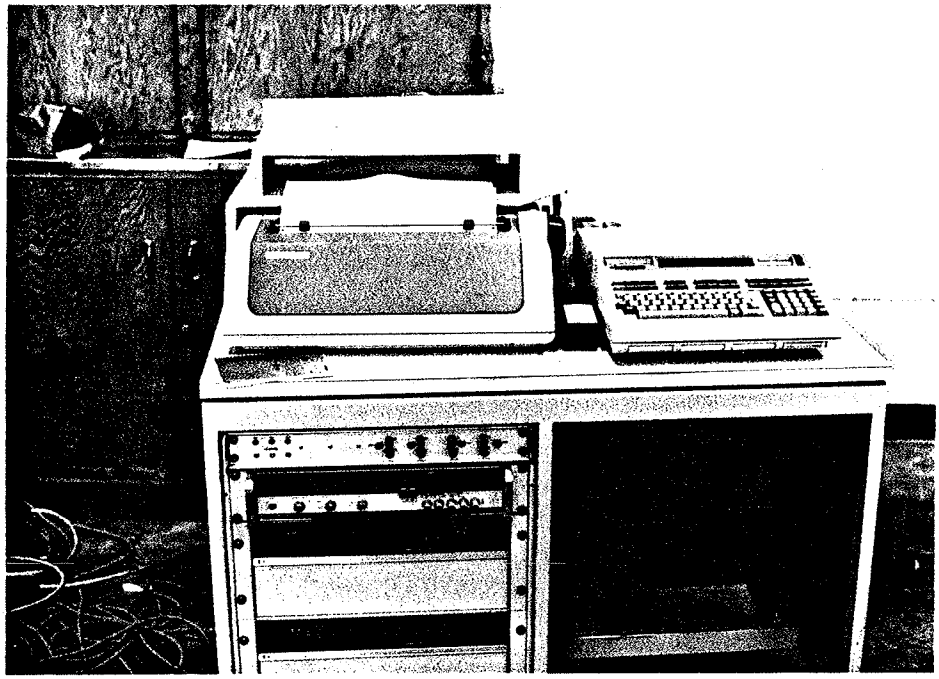

Fig. 3.24 DATA ACQUISITION SYSTEM USED FOR STATIC LOADING

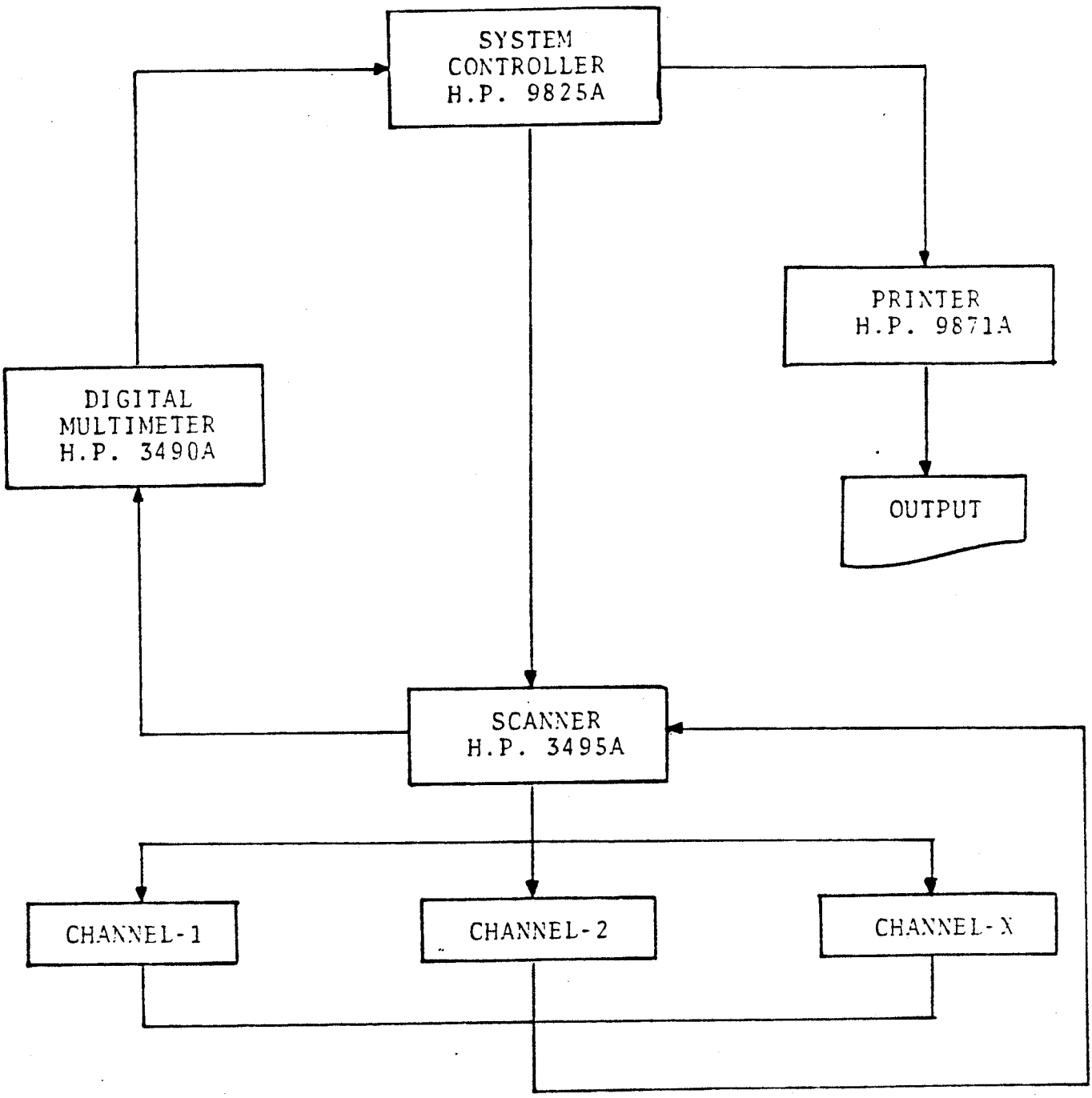

Fig. 3.25 SCHEMATIC DIAGRAM OF DATA ACQUISITION SYSTEM

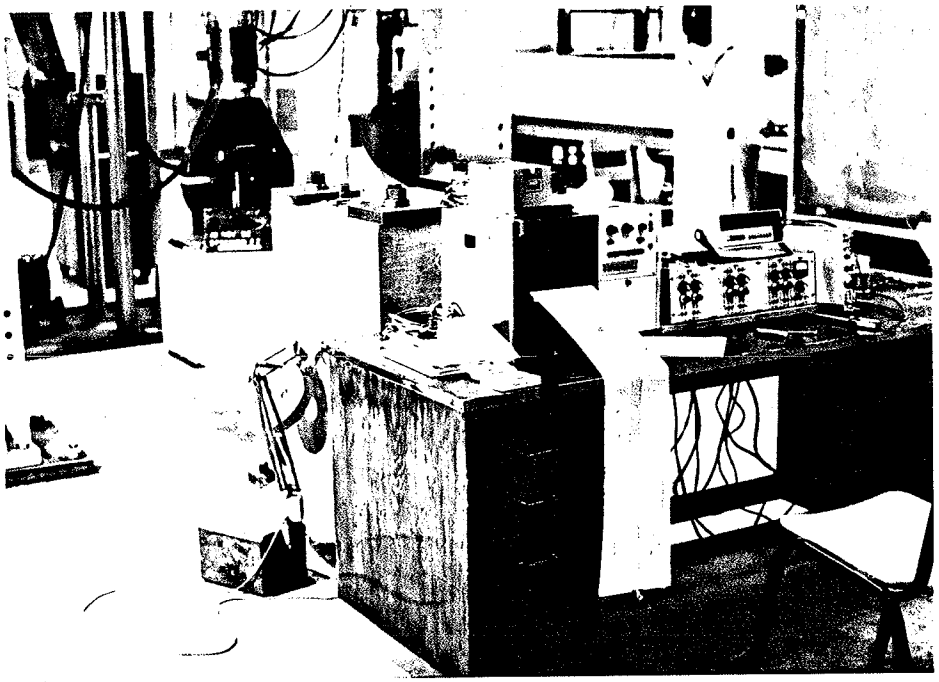

Fig. 3.26 STRAIN AMPLIFIER AND U.V. RECORDER USED FOR THE TEST OF SERIES II

175

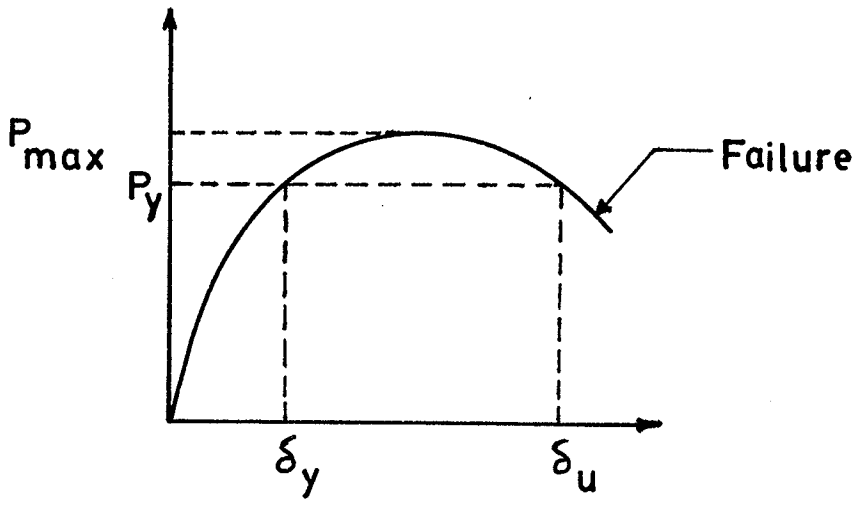

Fig. 4.1 DEFINITION OF DUCTILITY FACTOR AND FAILURE

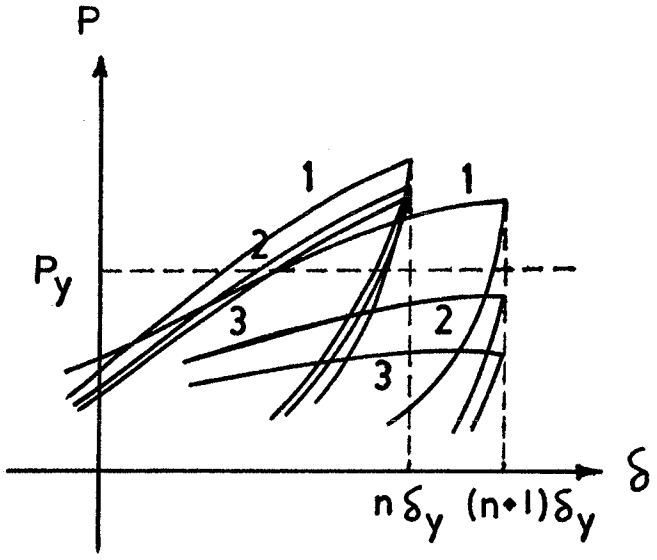

Fig. 4.2 DUCTILITY FACTOR FOR A TYPICAL CASE

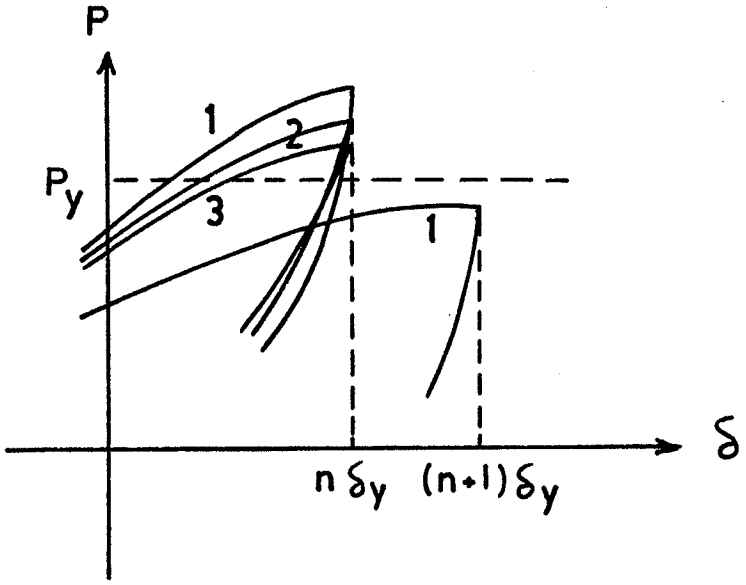

Fig. 4.3 DUCTILITY FACTOR FOR A SPECIAL CASE

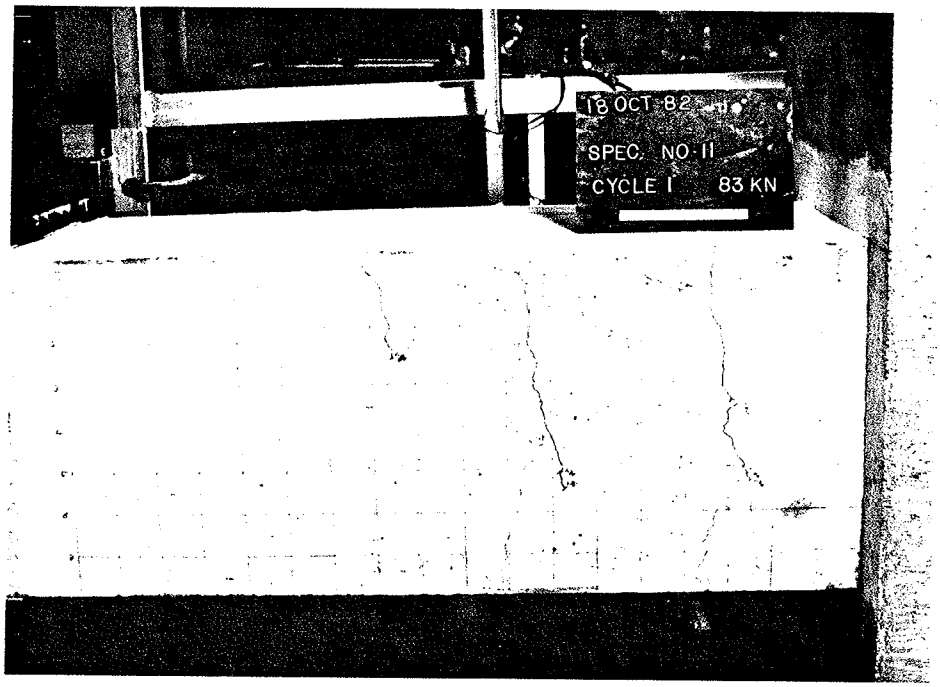

Fig. 4.4 CRACK PATTERN FOR SPECIMEN 1-1 AT 1δy/1

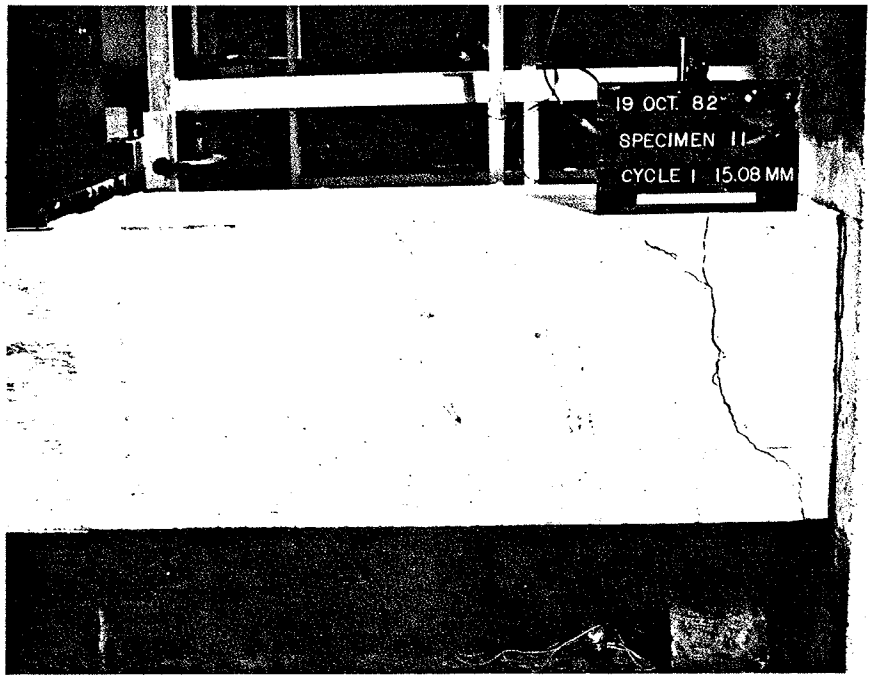

Fig. 4.5 CRACK PATTERN FOR SPECIMEN 1-1 AT $4\delta y/1$

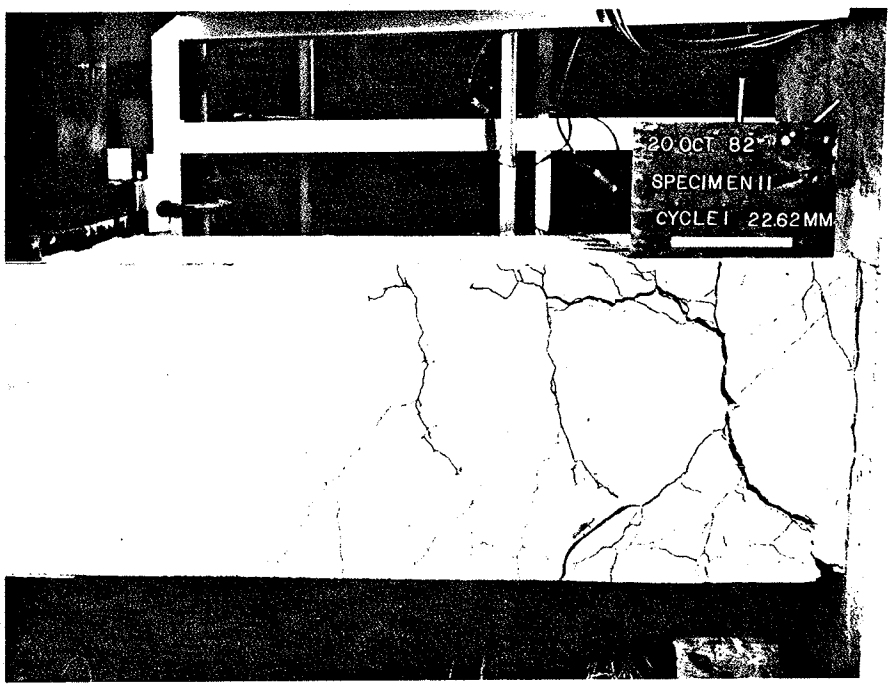

Fig. 4.6 FINAL CRACK PATTERN FOR SPECIMEN 1-1 AT $6\delta y/1$

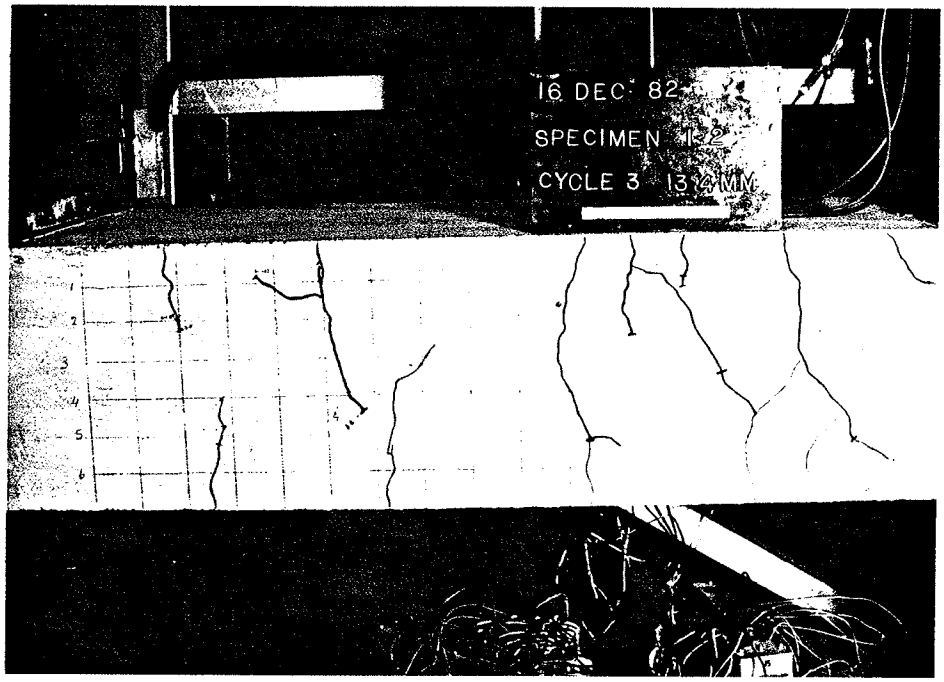

Fig. 4.7 CRACK PATTERN FOR SPECIMEN 1-2 AT $2\delta y/3$

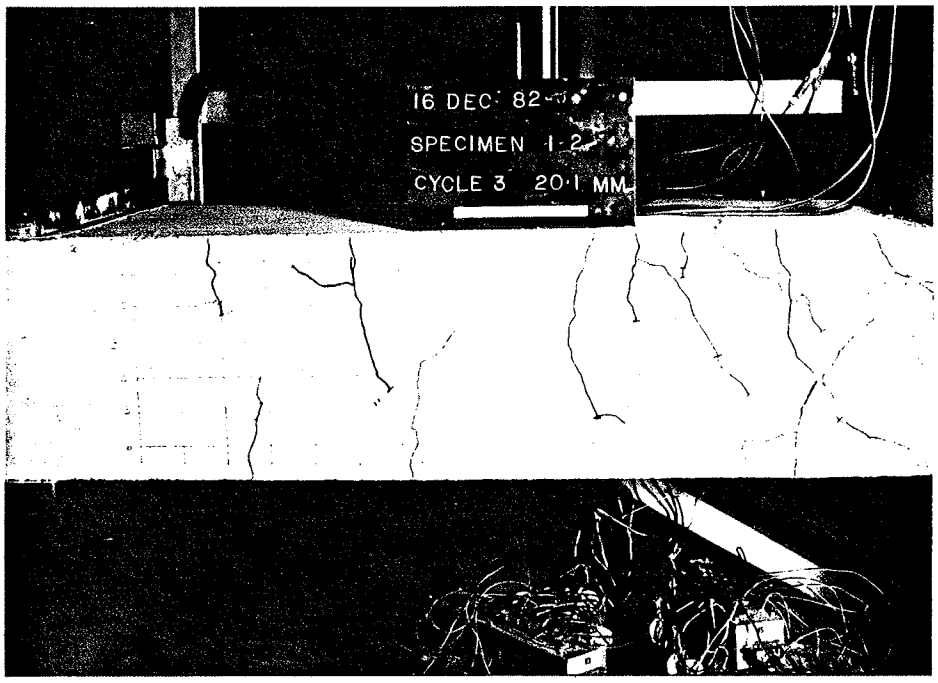

Fig. 4.8 CRACK PATTERN FOR SPECIMEN 1-2 AT $3\delta y/3$

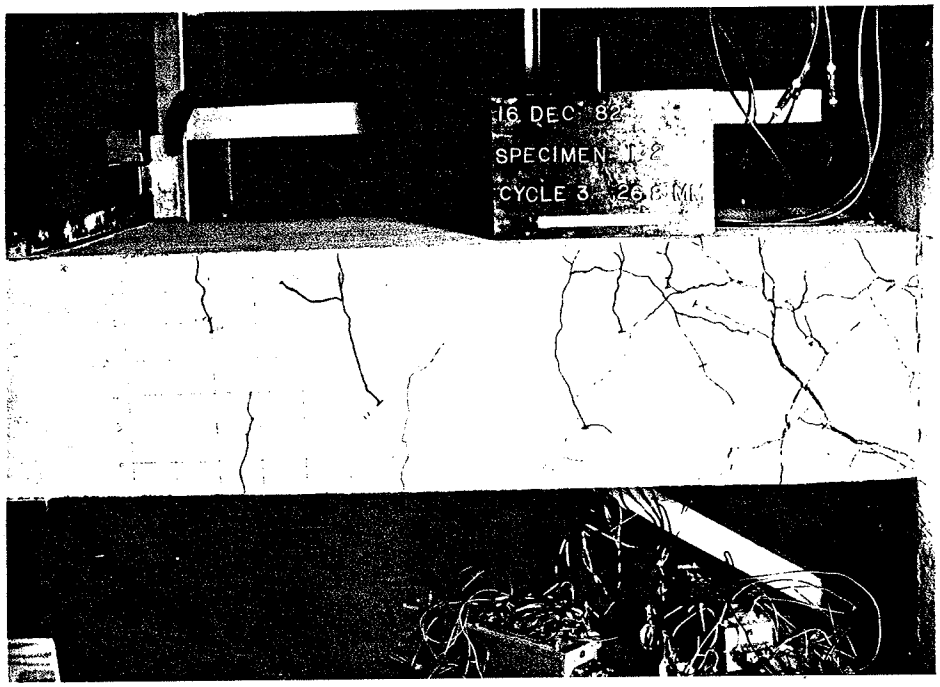

Fig. 4.9 CRACK PATTERN FOR SPECIMEN 1-2 AT $4\delta y/3$

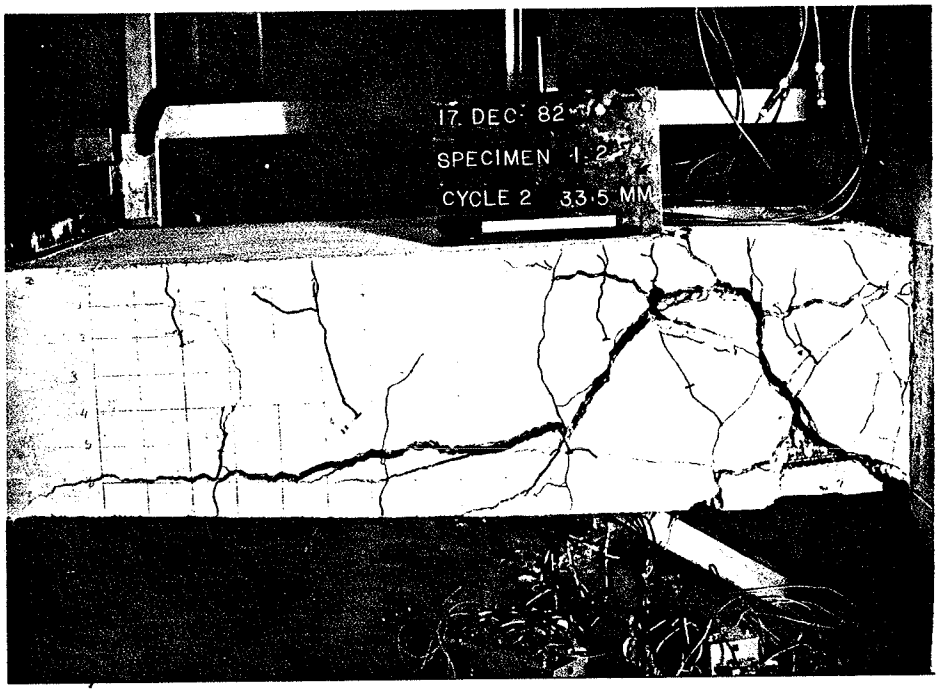

Fig. 4.10 CRACK PATTERN FOR SPECIMEN 1-2 AT $5\delta y/2$

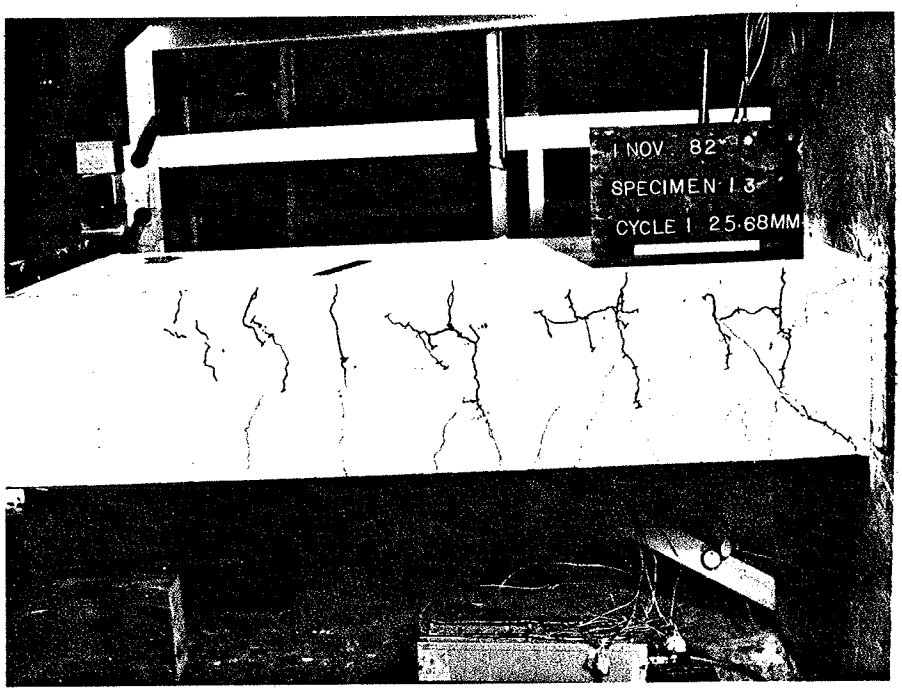

Fig. 4.11 CRACK PATTERN FOR SPECIMEN 1-3 AT $3\delta y/1$

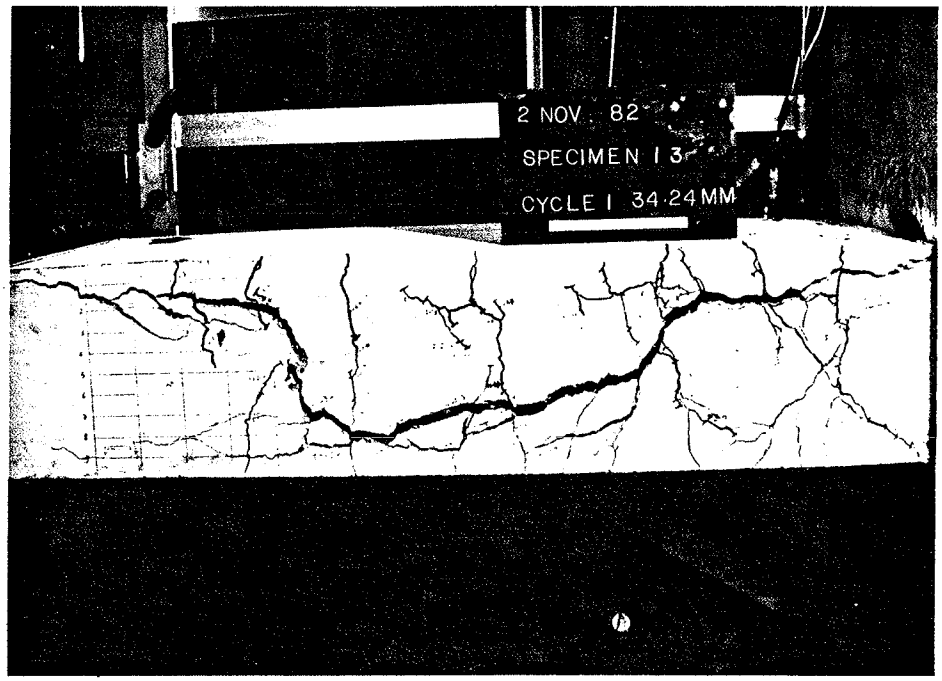

Fig. 4.12 CRACK PATTERN FOR SPECIMEN 1-3 AT $4\delta y/1$

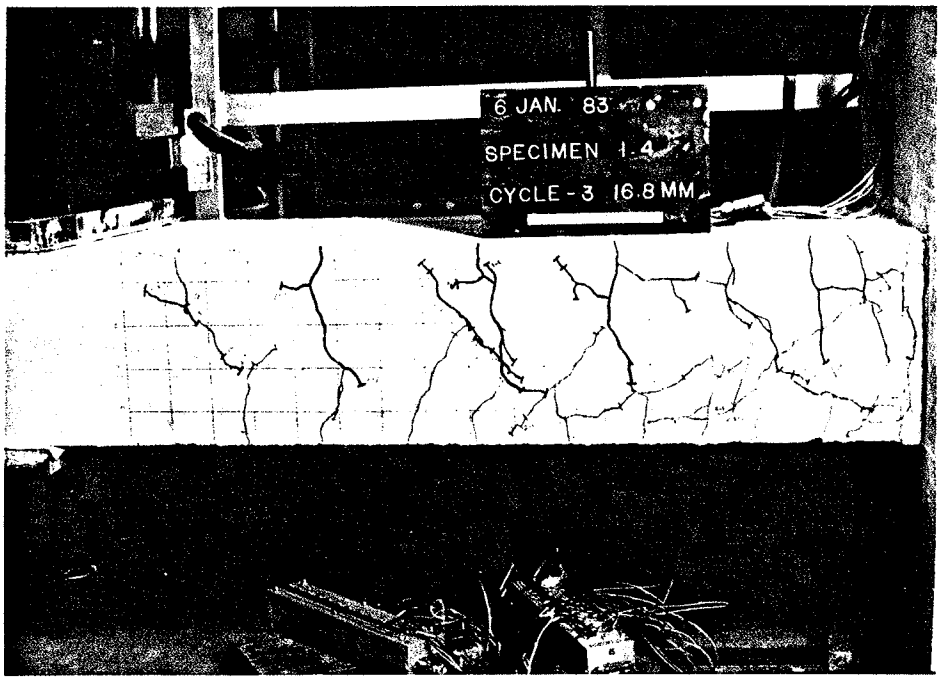

Fig. 4.13 CRACK PATTERN FOR SPECIMEN 1-4 AT $2\delta y/3$

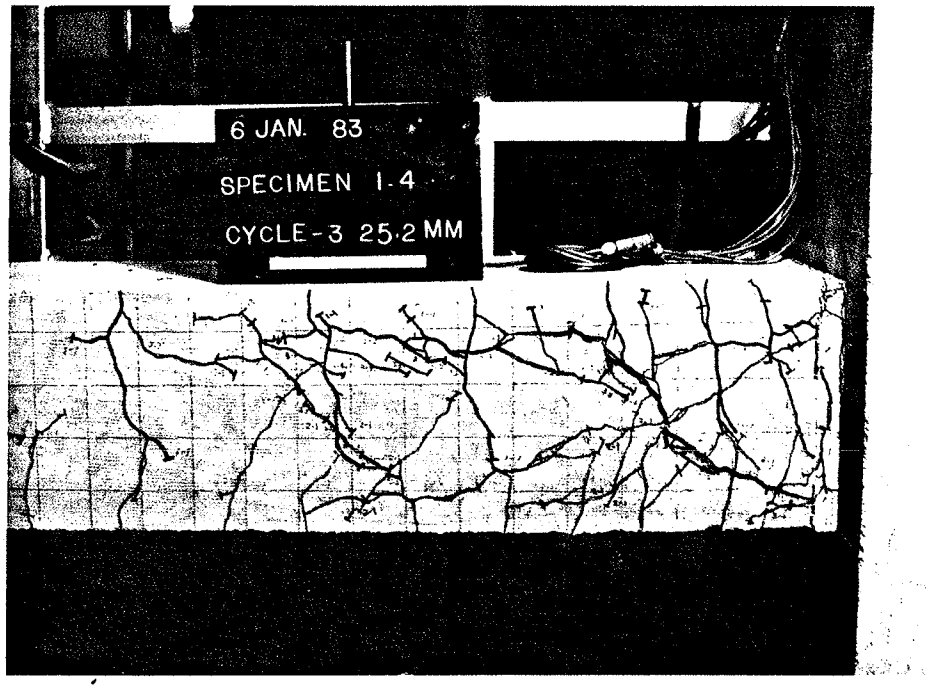

Fig. 4.14 CRACK PATTERN FOR SPECIMEN 1-4 AT $3\delta y/1$

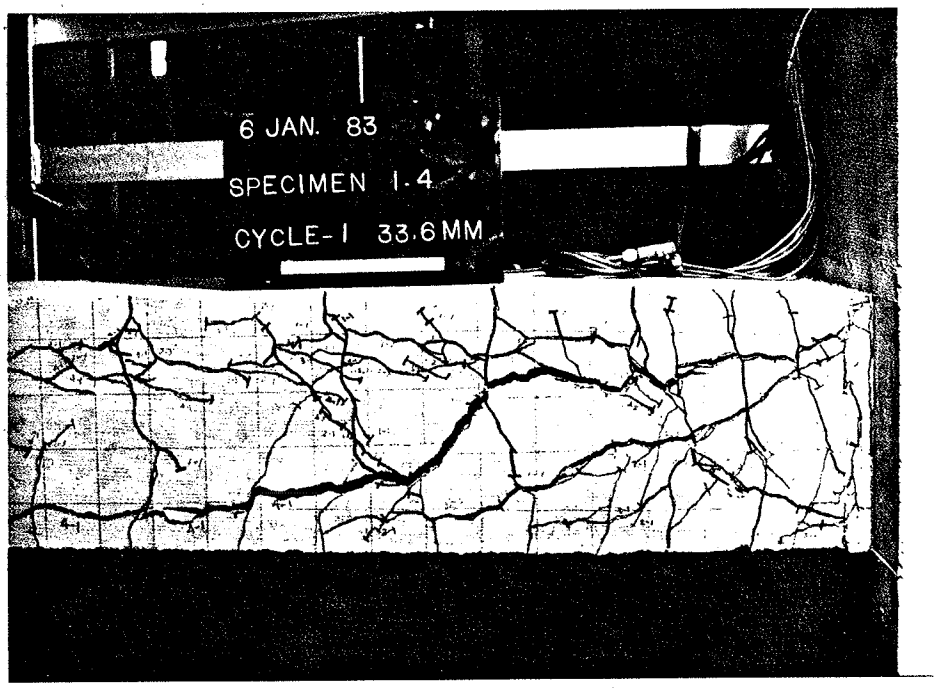

Fig. 4.15 FINAL CRACK PATTERN FOR SPECIMEN 1-4 AT 4δy/1

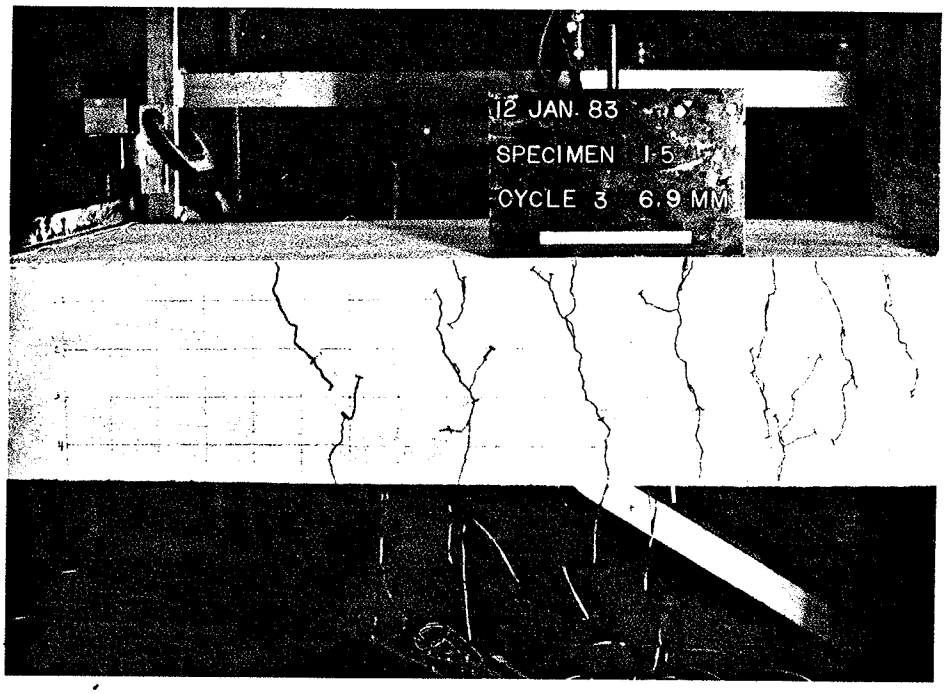

Fig. 4.16 CRACK PATTERN FOR SPECIMEN 1-5 AT 1δy/3

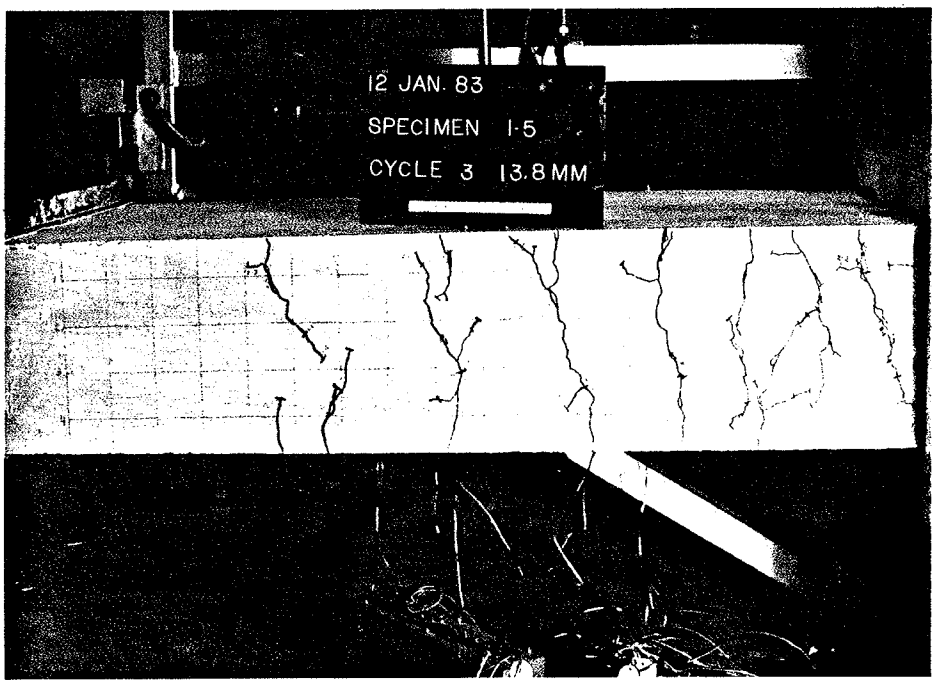

Fig. 4.17 CRACK PATTERN FOR SPECIMEN 1-5 AT $2\delta y/3$

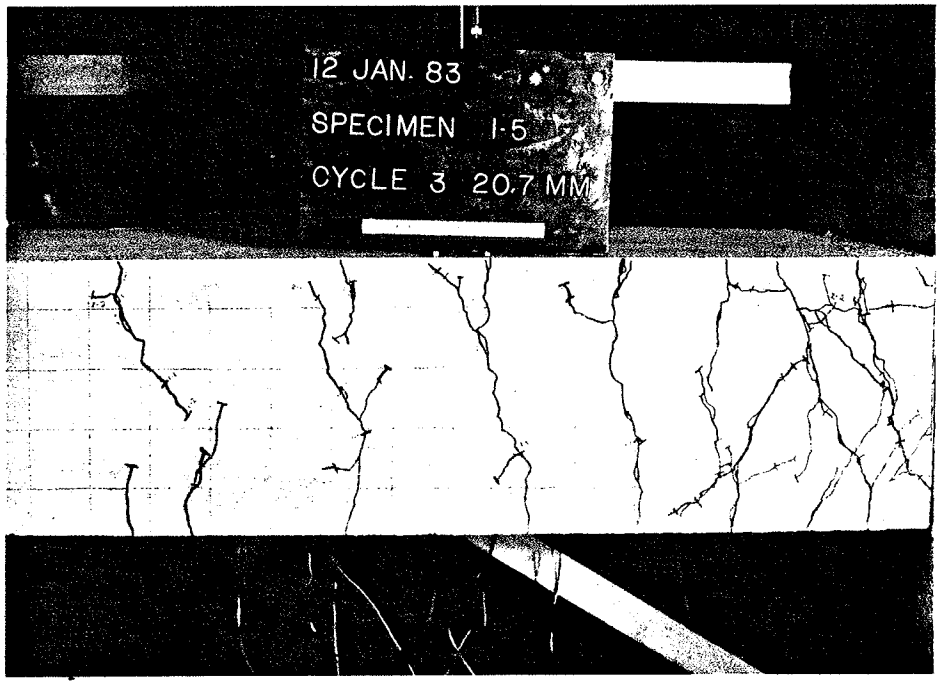

Fig. 4.18 CRACK PATTERN FOR SPECIMEN 1-5 AT $3\delta y/3$

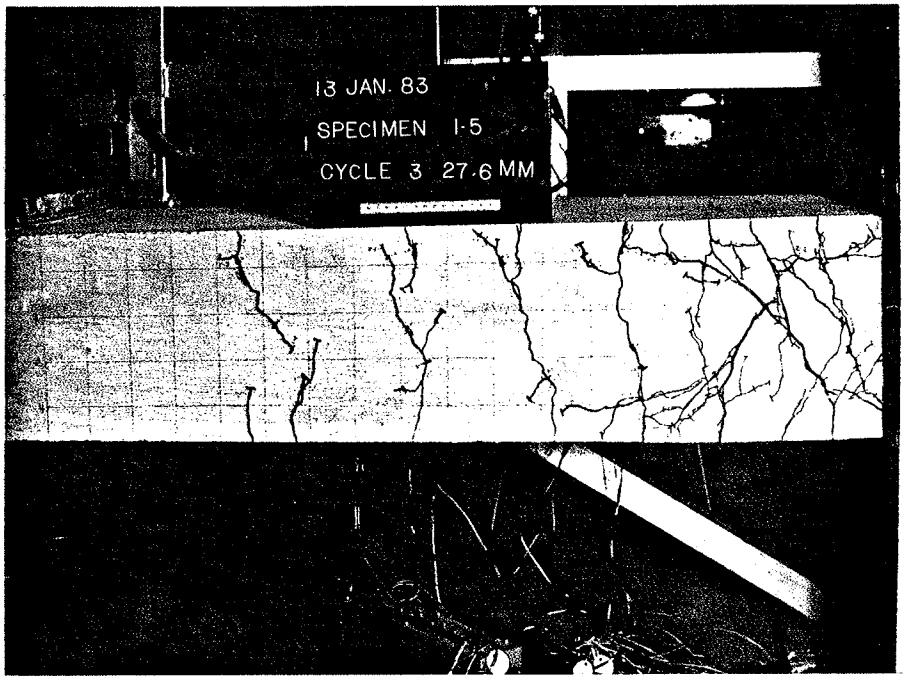

Fig. 4.19 CRACK PATTERN FOR SPECIMEN 1-5 AT $4\delta y/3$

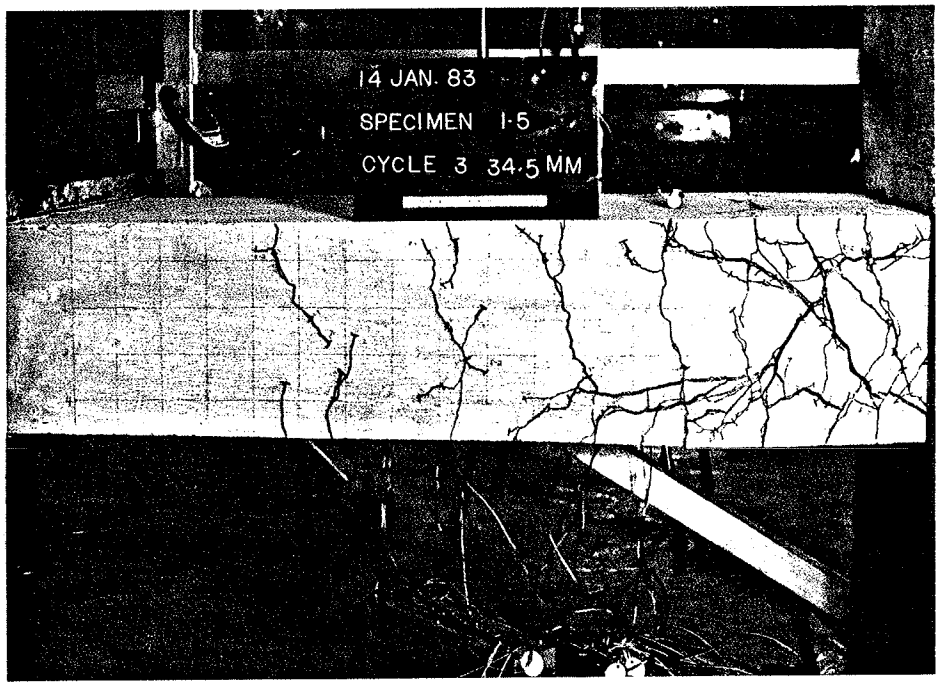

Fig. 4.20 CRACK PATTERN FOR SPECIMEN 1-5 AT $5\delta y/3$

Fig. 4.21 CRACK PATTERN FOR SPECIMEN 1-5 AT $6\delta y/3$

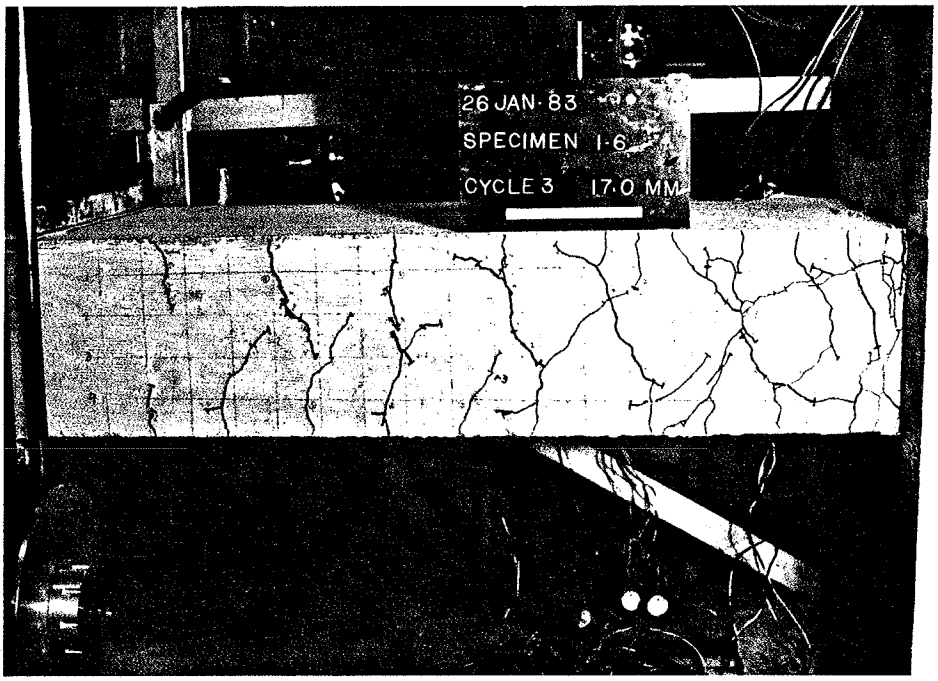

Fig. 4.22 CRACK PATTERN FOR SPECIMEN 1-6 AT $2\delta y/3$

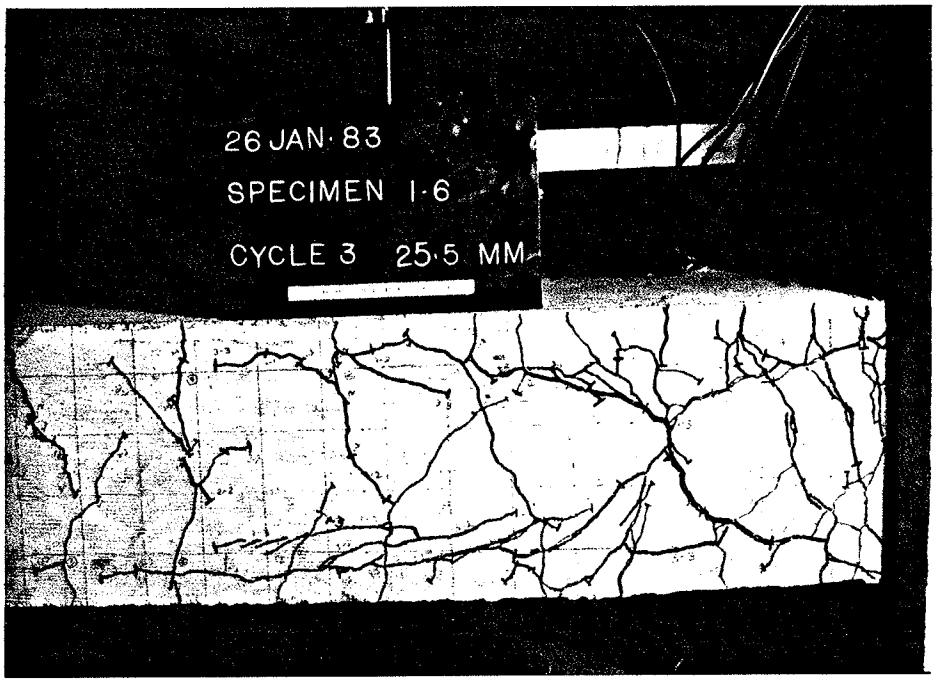

Fig. 4.23 CRACK PATTERN FOR SPECIMEN 1-6 AT $3\delta y/3$

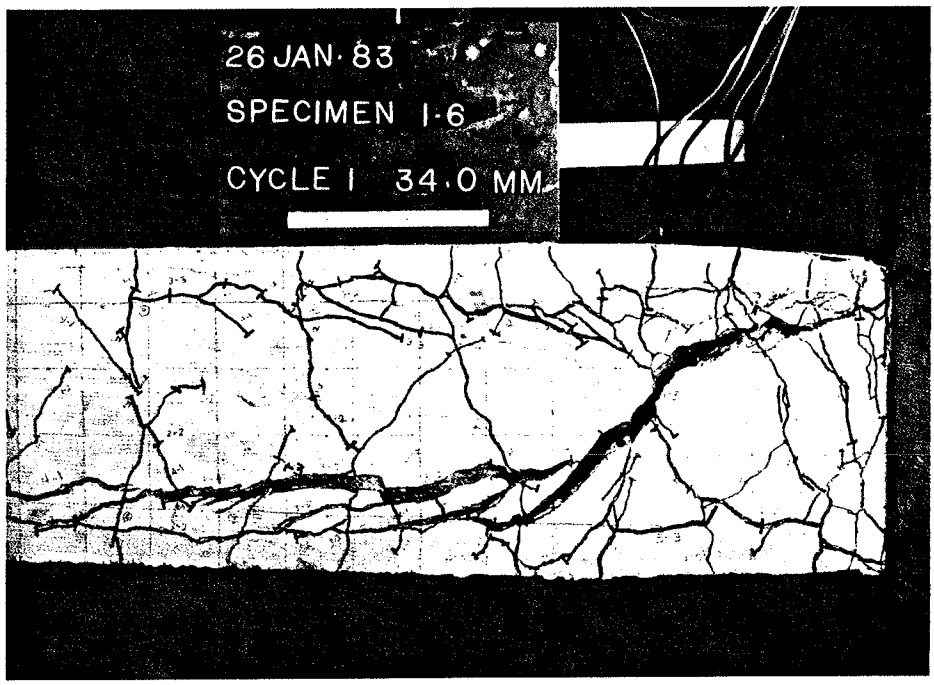

Fig. 4.24 CRACK PATTERN FOR SPECIMEN 1-6 AT $4\delta y/1$

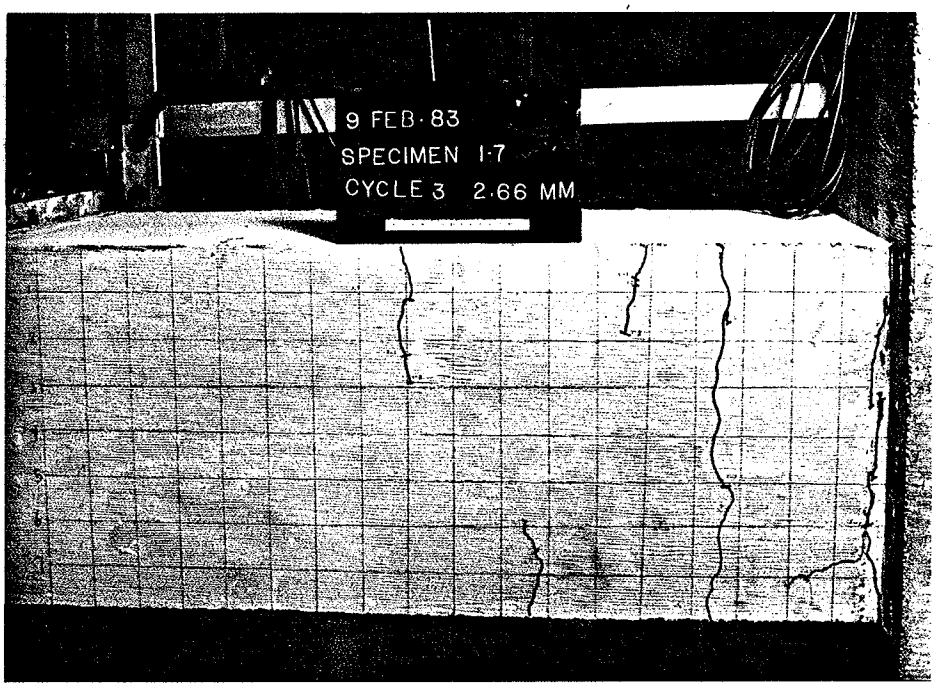

Fig. 4.25 CRACK PATTERN FOR SPECIMEN 1-7 AT $1\delta y/3$

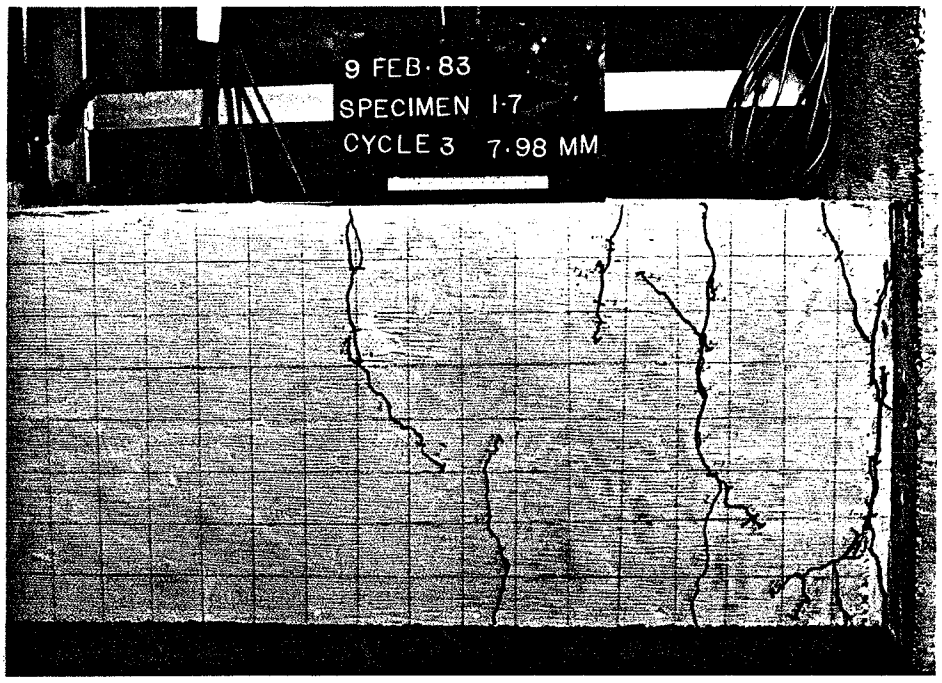

Fig. 4.26 CRACK PATTERN FOR SPECIMEN 1-7 AT $3\delta y/3$

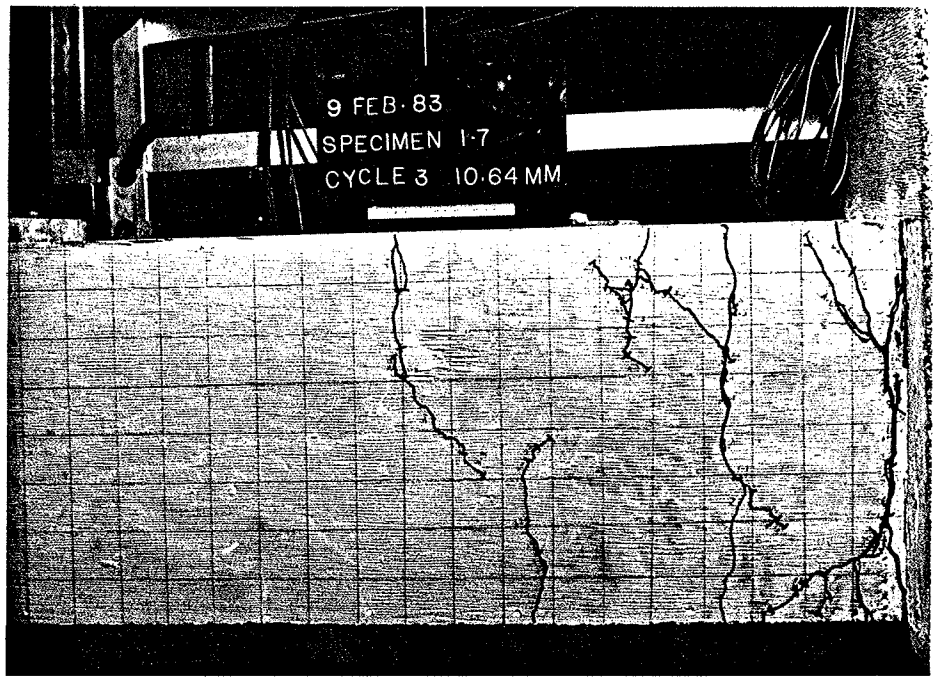

Fig. 4.27 CRACK PATTERN FOR SPECIMEN 1-7 AT 4δy/3

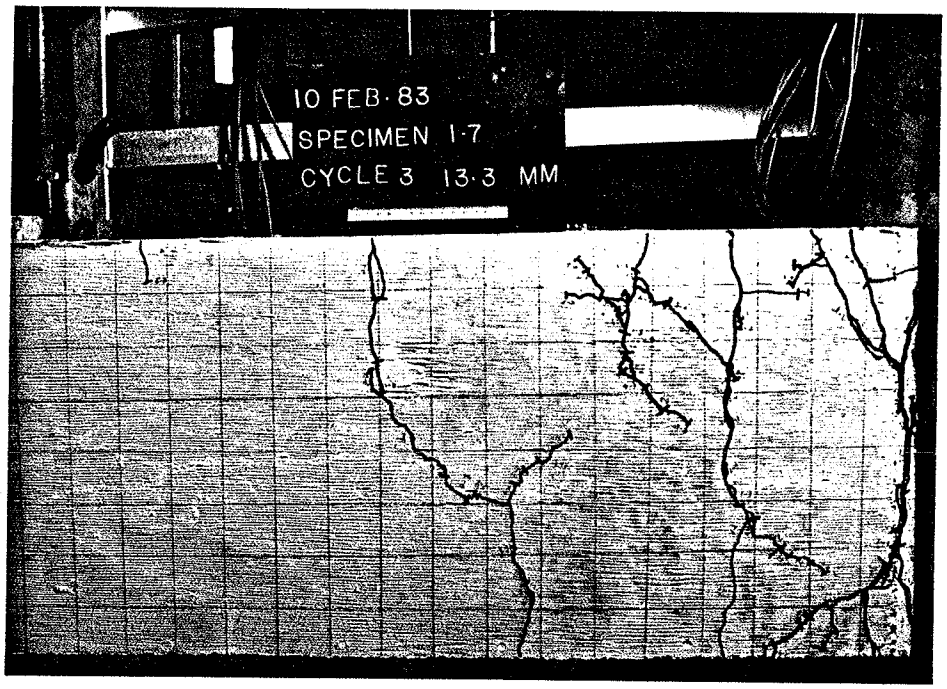

Fig. 4.28 CRACK PATTERN FOR SPECIMEN 1-7 AT 5δy/3

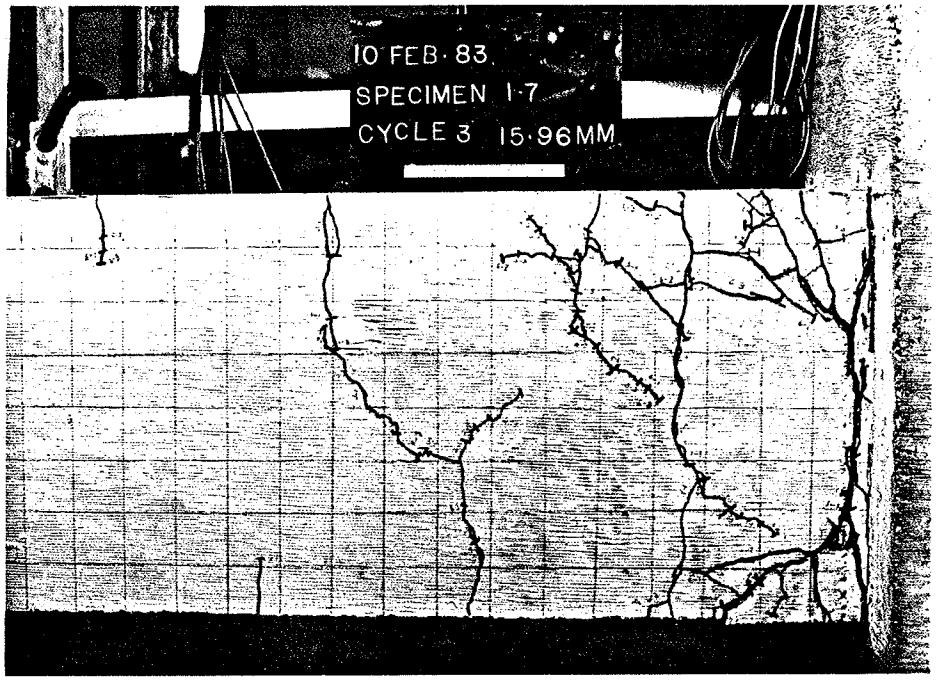

Fig. 4.29 CRACK PATTERN FOR SPECIMEN 1-7 AT $6\delta y/3$

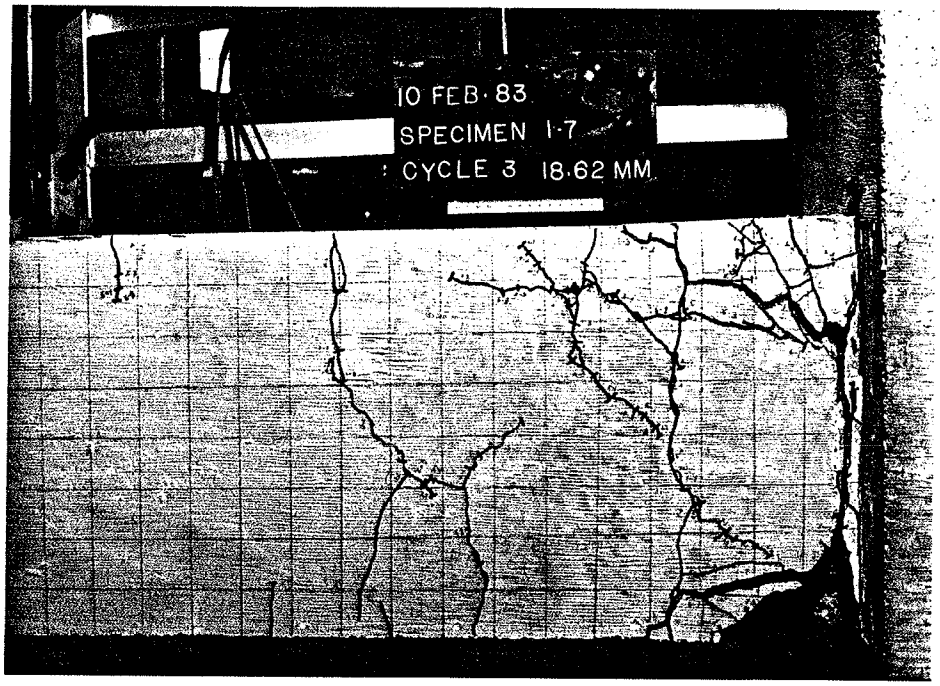

Fig. 4.30 CRACK PATTERN FOR SPECIMEN 1-7 AT $7\delta y/3$

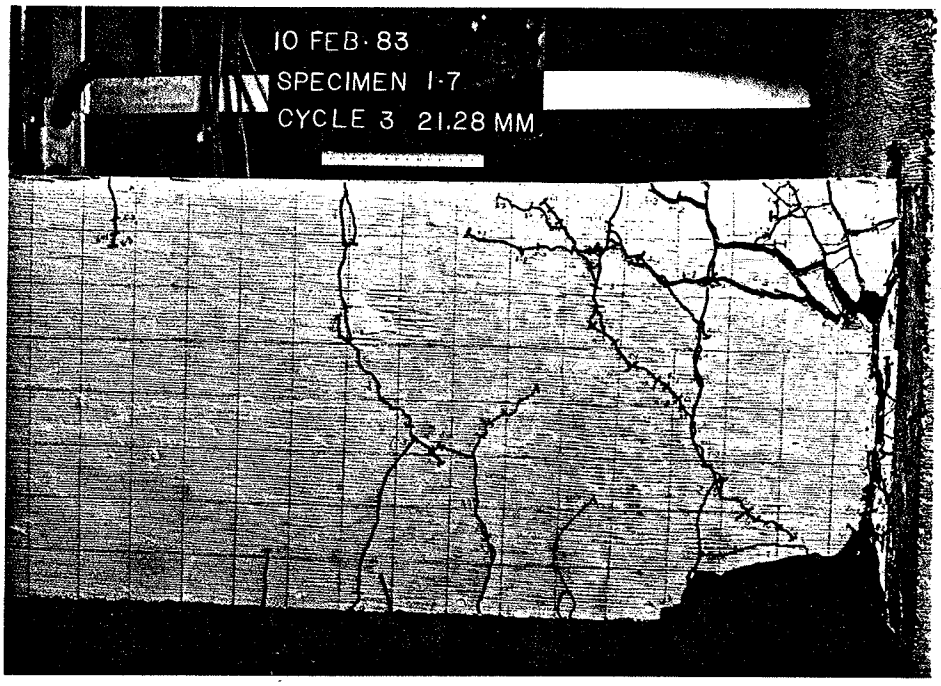

Fig. 4.31 CRACK PATTERN FOR SPECIMEN 1-7 AT $8\delta y/3$

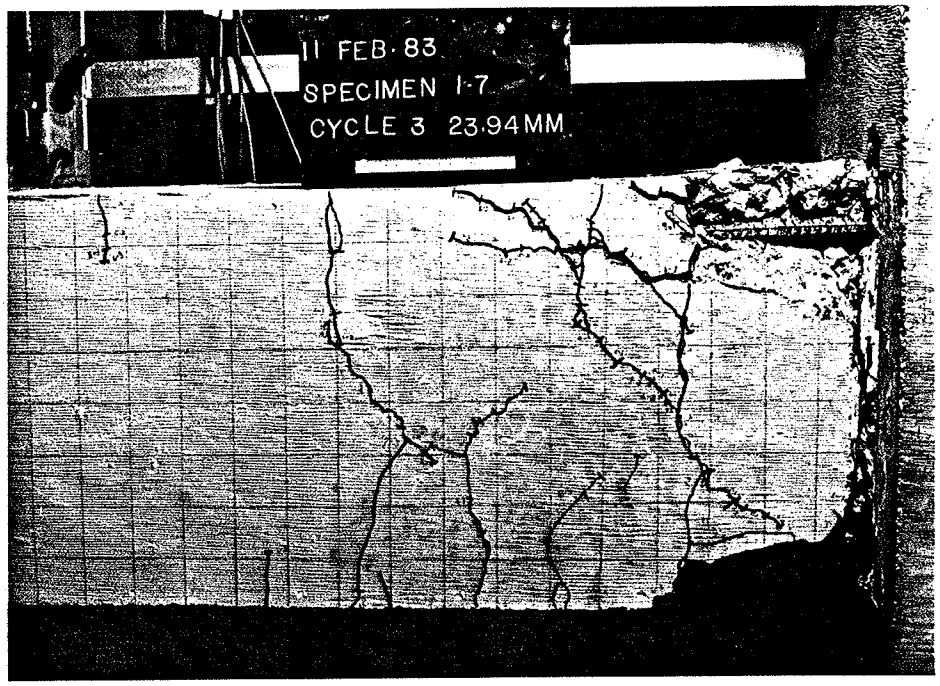

Fig. 4.32 CRACK PATTERN FOR SPECIMEN 1-7 AT $9\delta y/3$

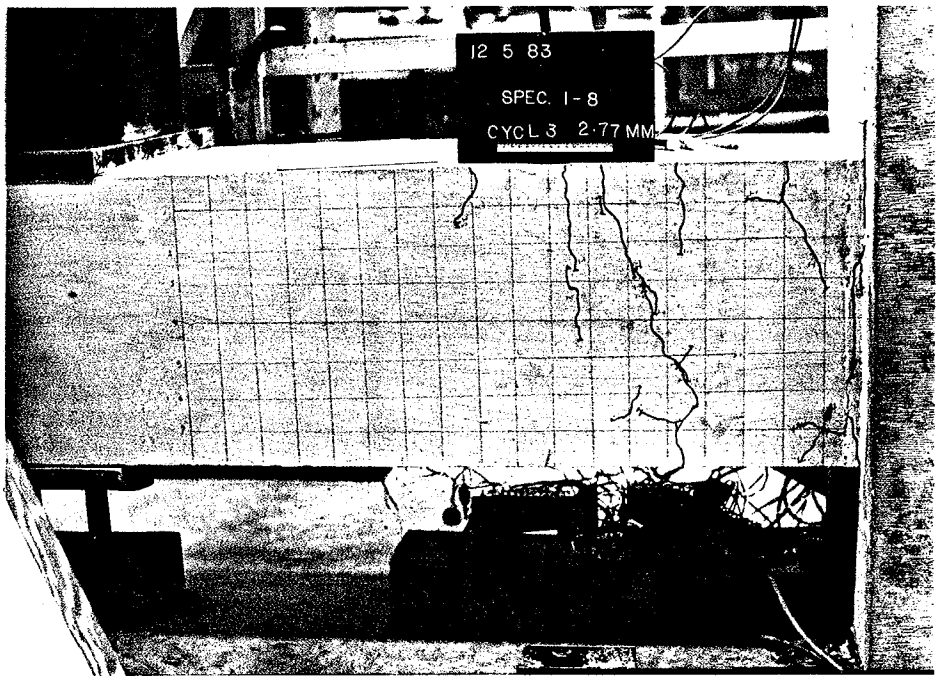

Fig. 4.33 CRACK PATTERN FOR SPECIMEN 1-8 AT $1\delta y/3$

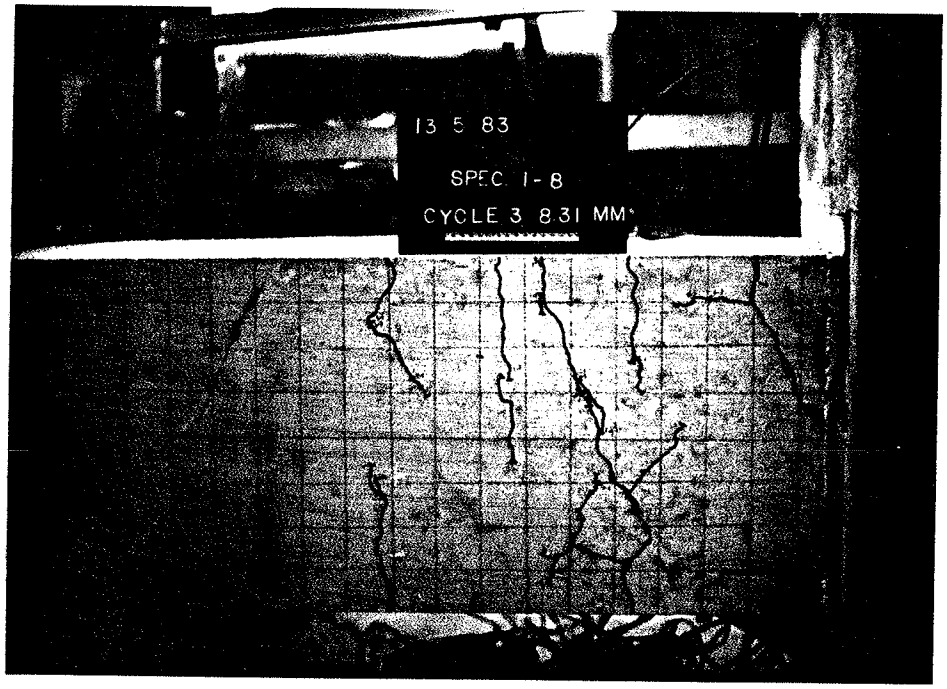

Fig. 4.34 CRACK PATTERN FOR SPECIMEN 1-8 AT $3\delta y/3$

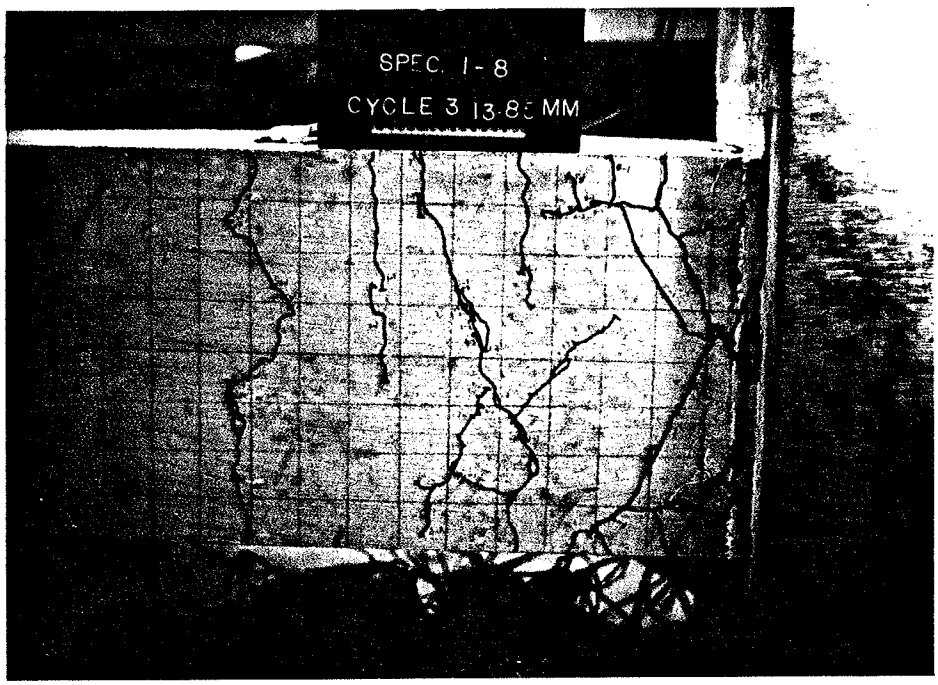

Fig. 4.35 CRACK PATTERN FOR SPECIMEN 1-8 AT 5δy/3

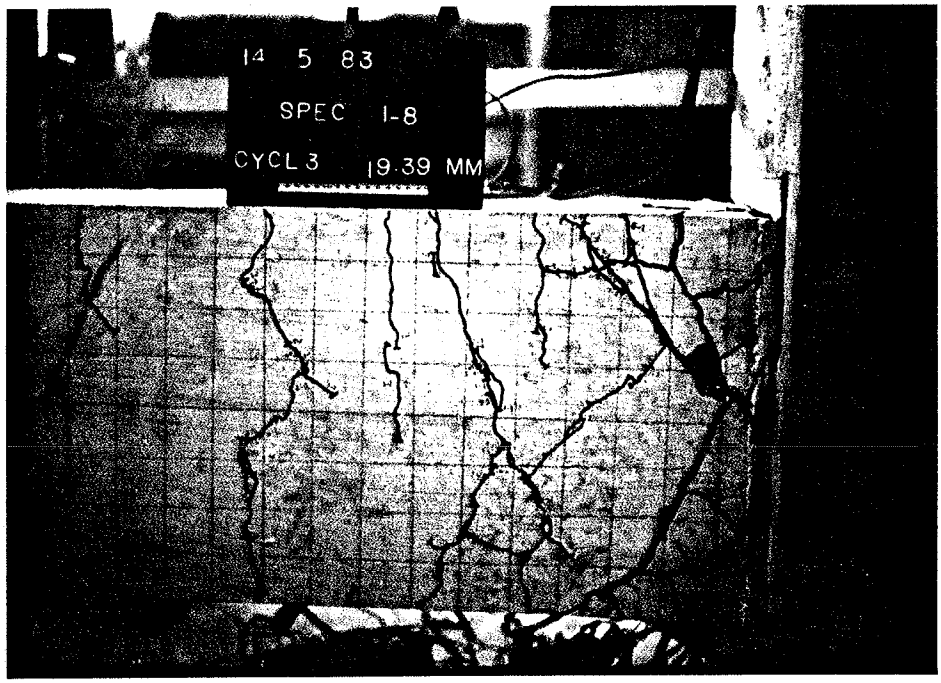

Fig. 4.36 CRACK PATTERN FOR SPECIMEN 1-8 AT 7δy/3

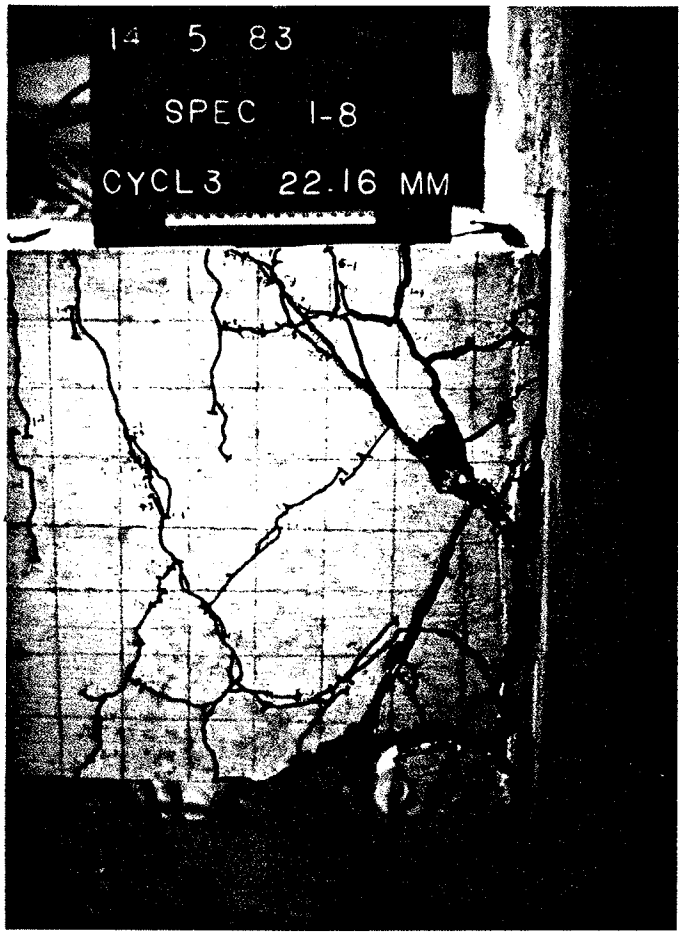

Fig. 4.37 CRACK PATTERN FOR SPECIMEN 1-8 AT 8δy/3

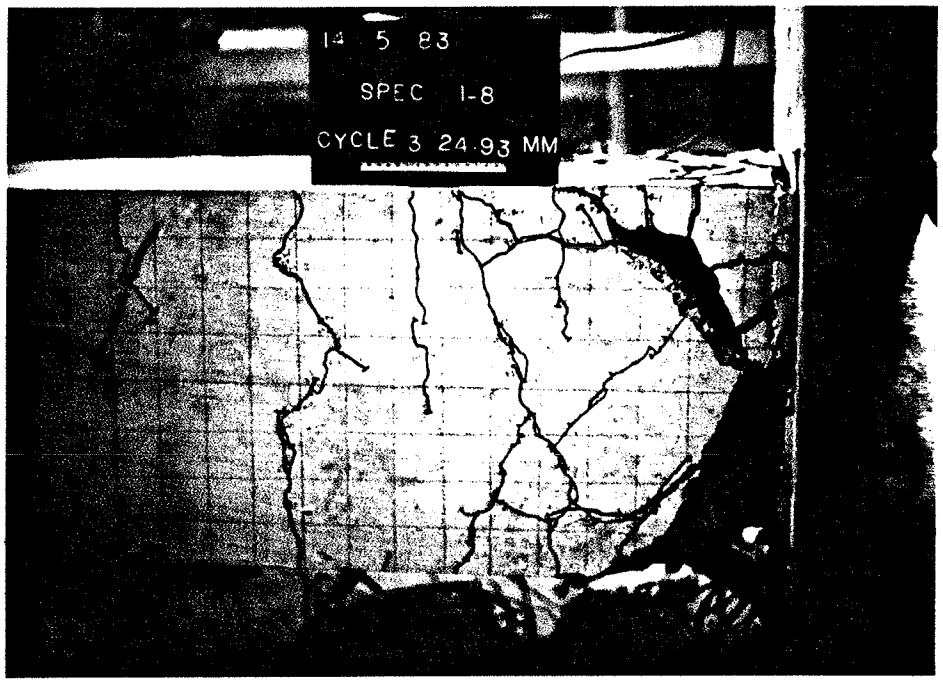

Fig. 4.38 FINAL CRACK PATTERN FOR SPECIMEN 1-8 AT 9δy/3

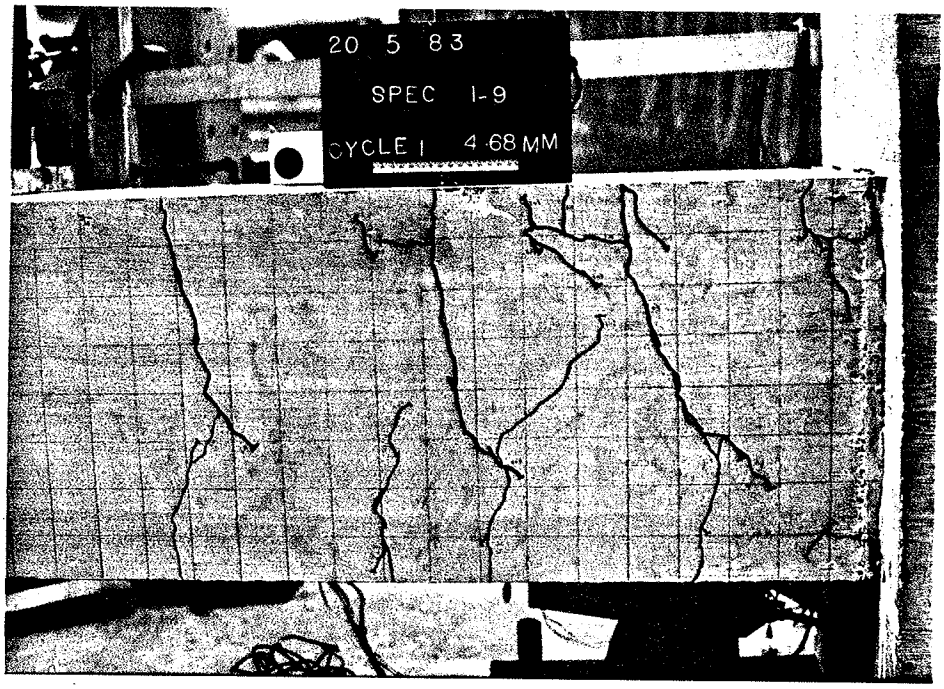

Fig. 4.39 CRACK PATTERN FOR SPECIMEN 1-9 AT 1δy/1

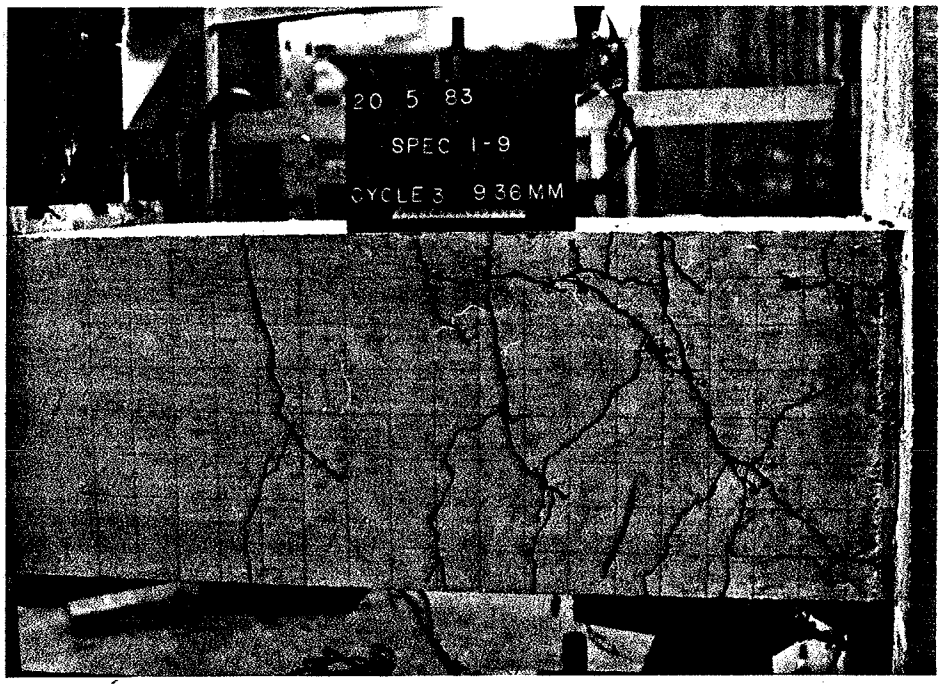

Fig. 4.40 CRACK PATTERN FOR SPECIMEN 1-9 AT 2δy/3

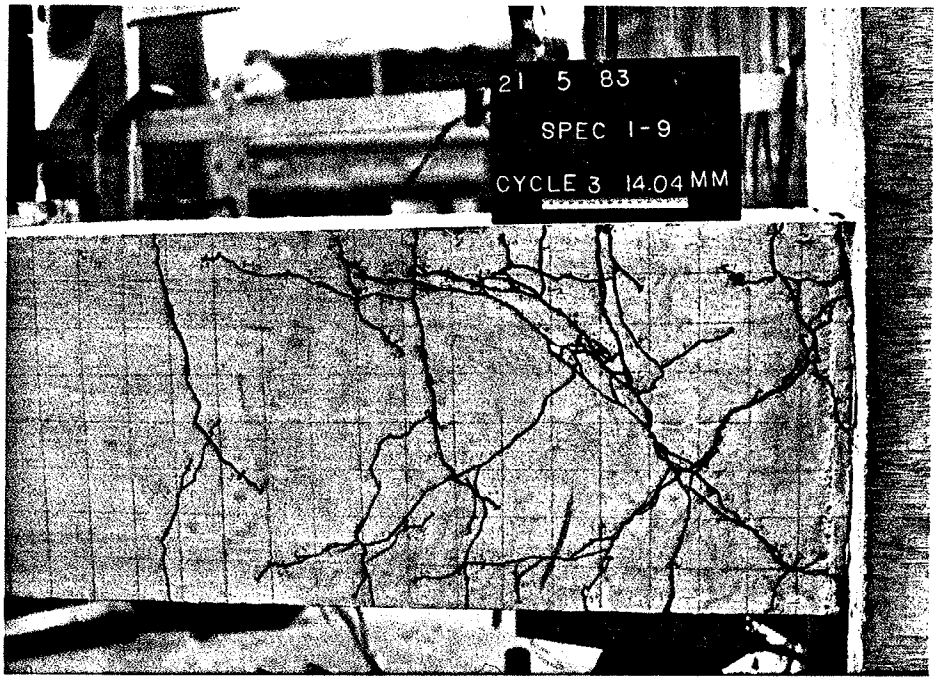

Fig. 4.41 CRACK PATTERN FOR SPECIMEN 1-9 AT $3\delta y/3$

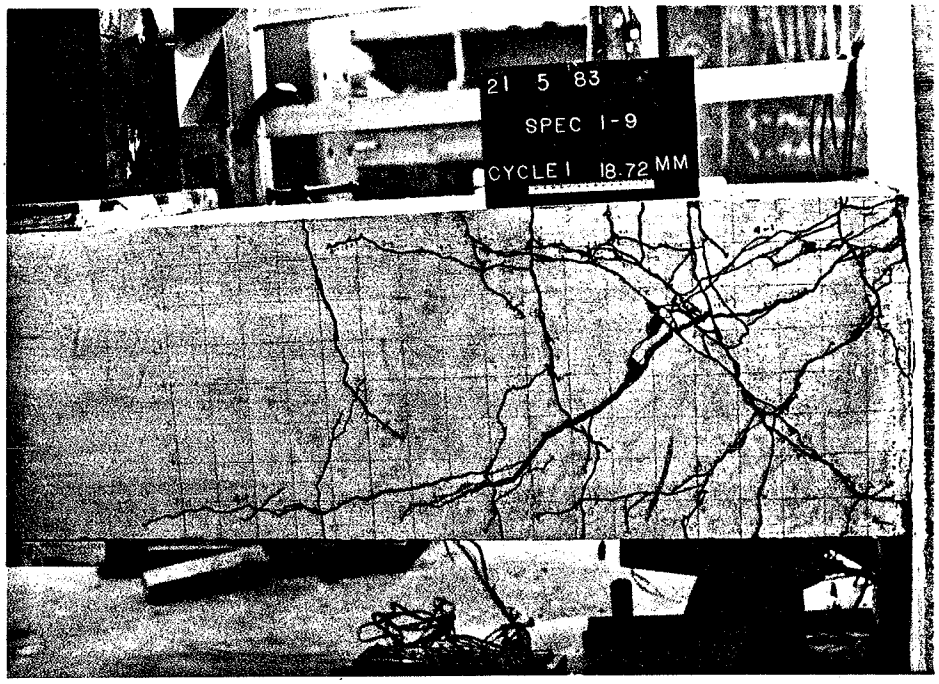

Fig. 4.42 FINAL CRACK PATTERN FOR SPECIMEN 1-9 AT $4\delta y/1$

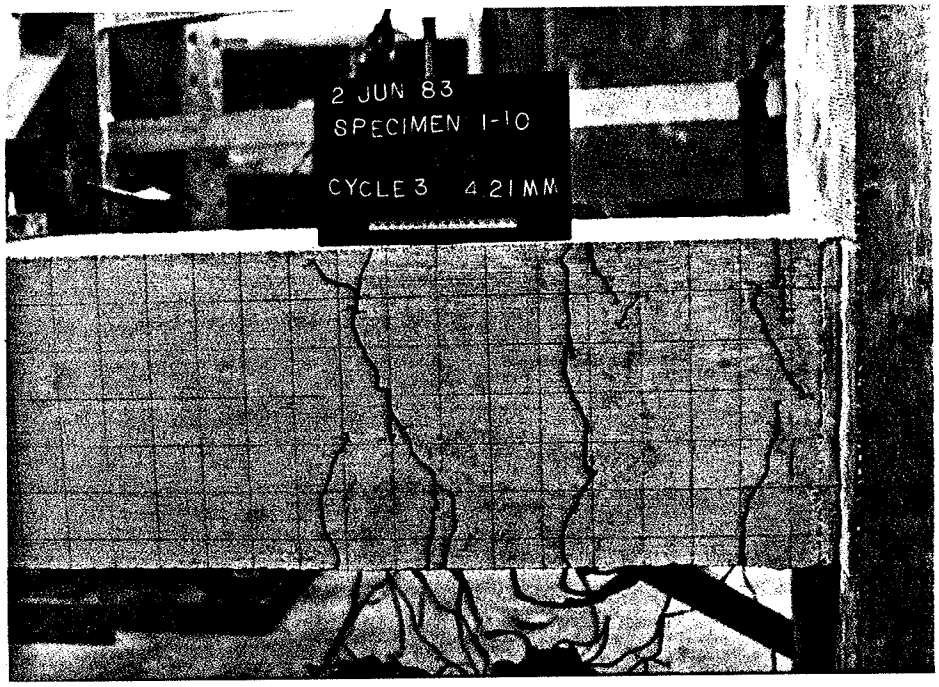

Fig. 4.43 CRACK PATTERN FOR SPECIMEN 1-10 AT $1\delta y/3$

Fig. 4.44 CRACK PATTERN FOR SPECIMEN 1-10 AT $3\delta y/3$

Fig. 4.45 CRACK PATTERN FOR SPECIMEN 1-10 AT 4δy/3

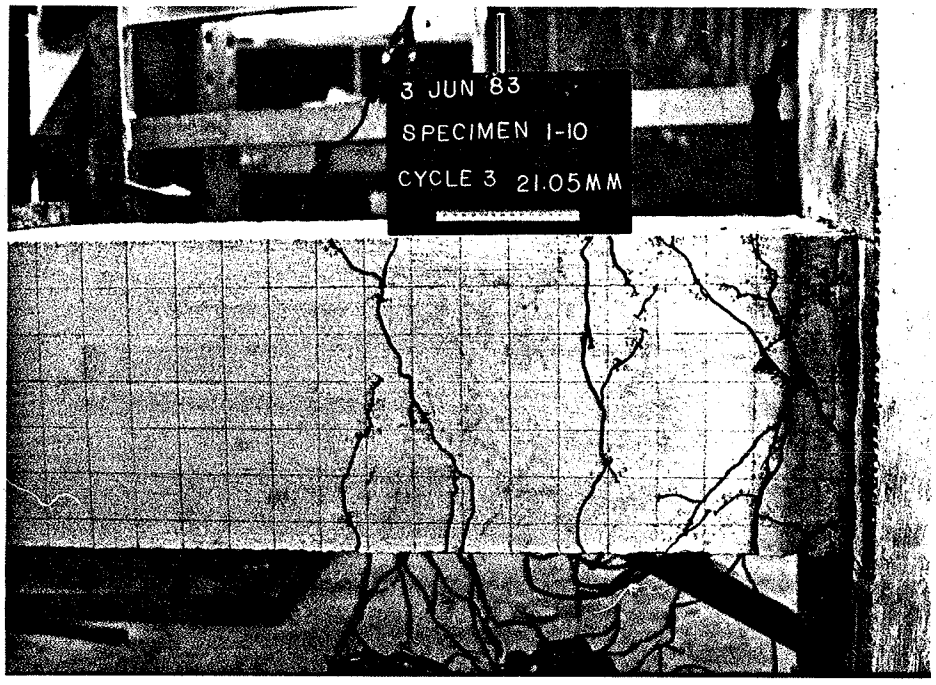

Fig. 4.46 CRACK PATTERN FOR SPECIMEN 1-10 AT 5δy/3

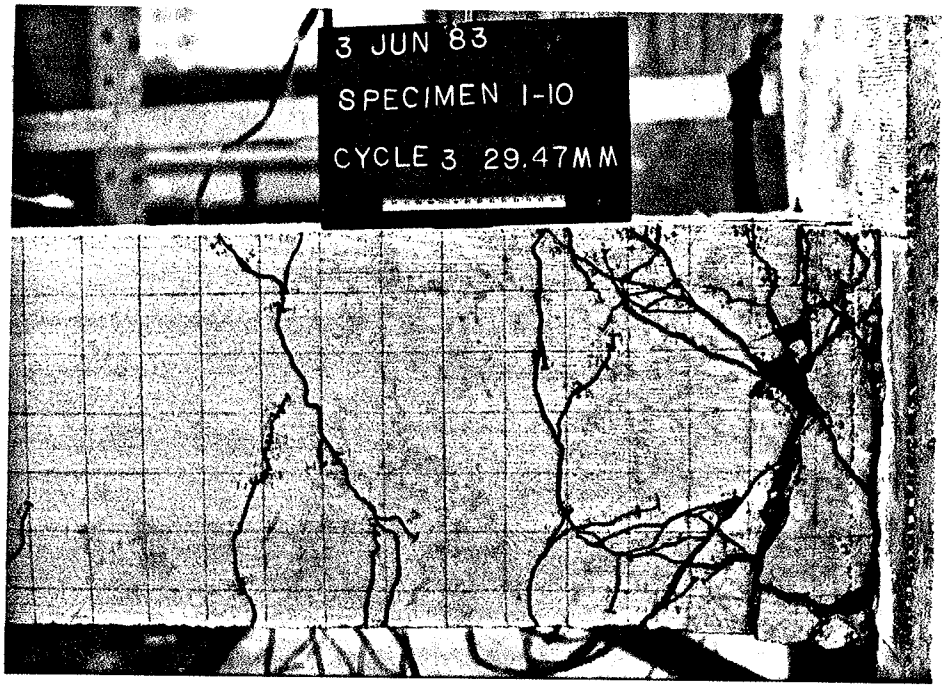

Fig. 4.47 CRACK PATTERN FOR SPECIMEN 1-10 AT $7\delta y/3$

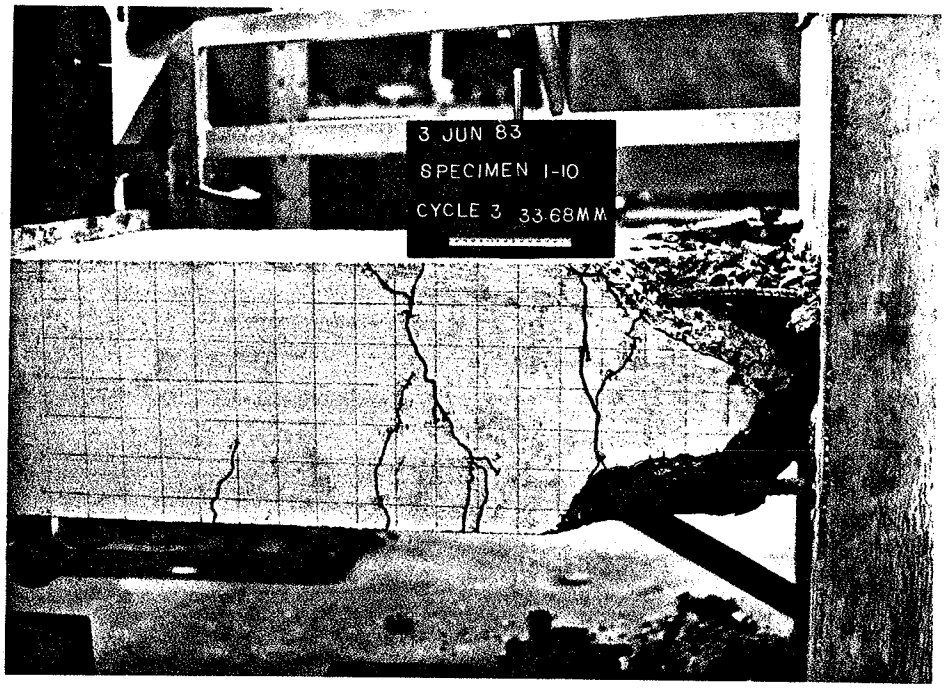

Fig. 4.48 FINAL CRACK PATTERN FOR SPECIMEN 1-10 AT $8\delta y/1$

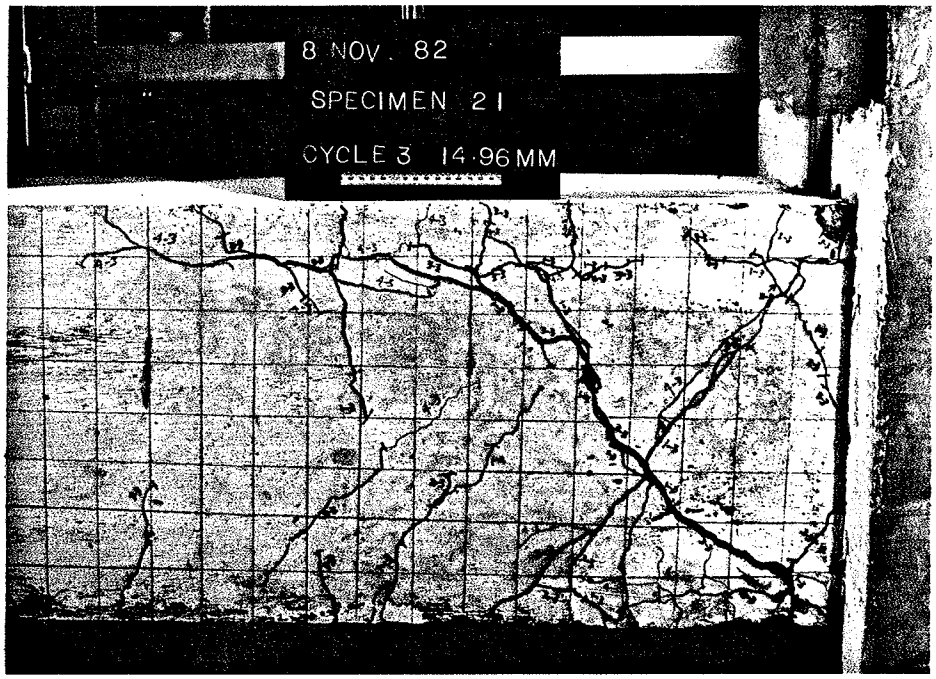

Fig. 4.49 FINAL CRACK PATTERN FOR SPECIMEN 2-1 AT $4\delta y/3$

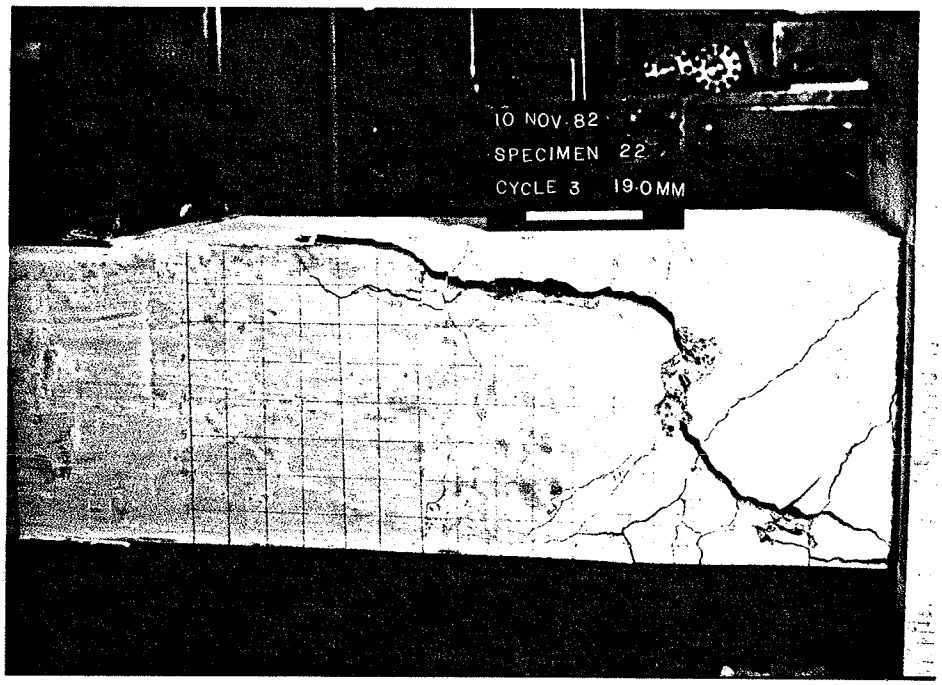

Fig. 4.50 FINAL CRACK PATTERN FOR SPECIMEN 2-2 AT $5\delta y/3$

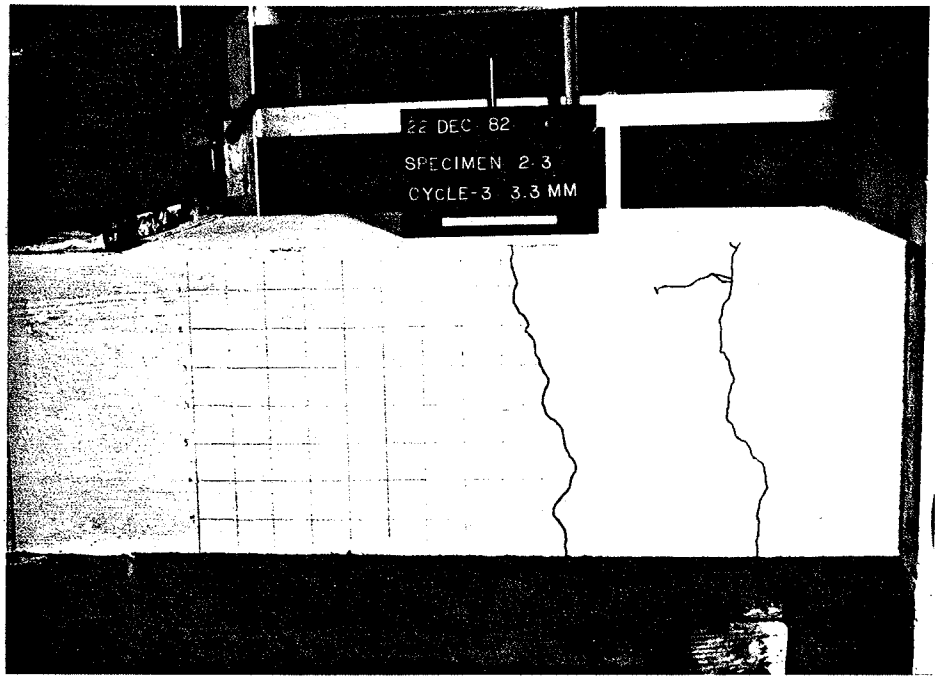

Fig. 4.51 CRACK PATTERN FOR SPECIMEN 2-3 AT $1\delta y/3$

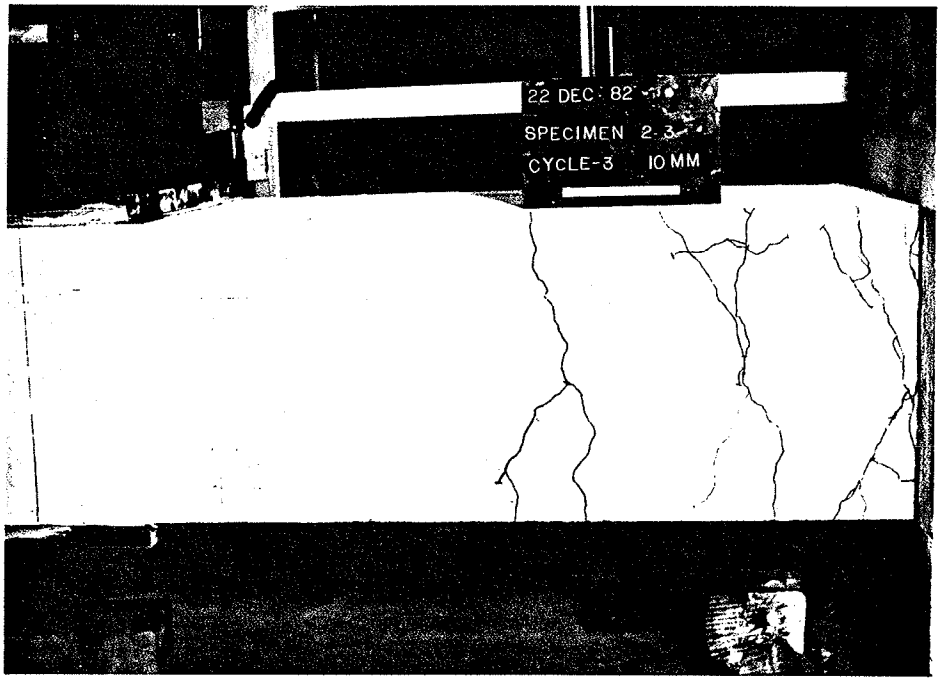

Fig. 4.52 CRACK PATTERN FOR SPECIMEN 2-3 AT $3\delta y/3$

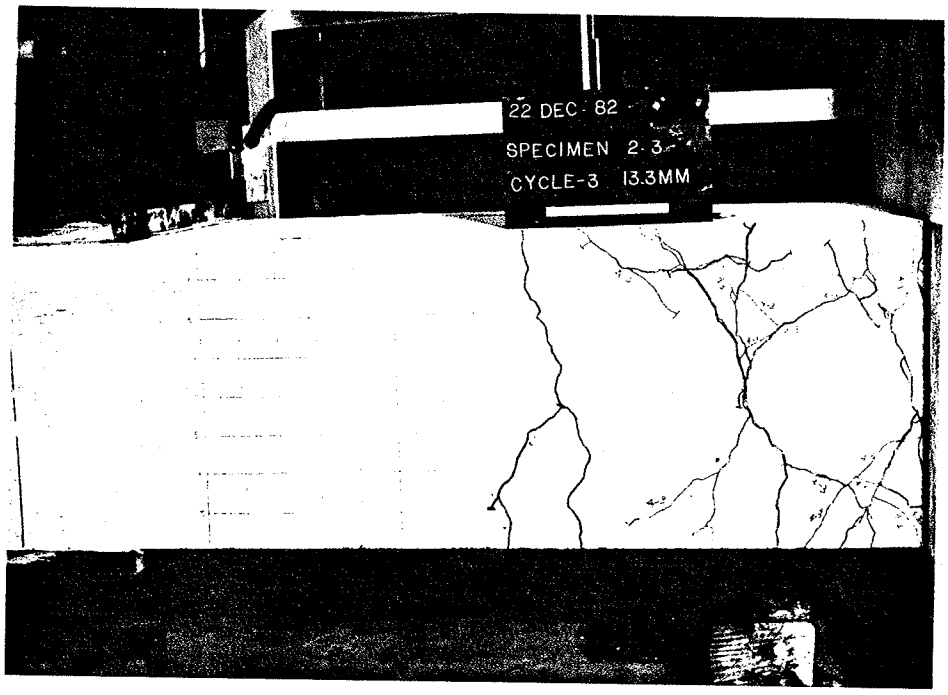

Fig. 4.53 CRACK PATTERN FOR SPECIMEN 2-3 AT 4δy/3

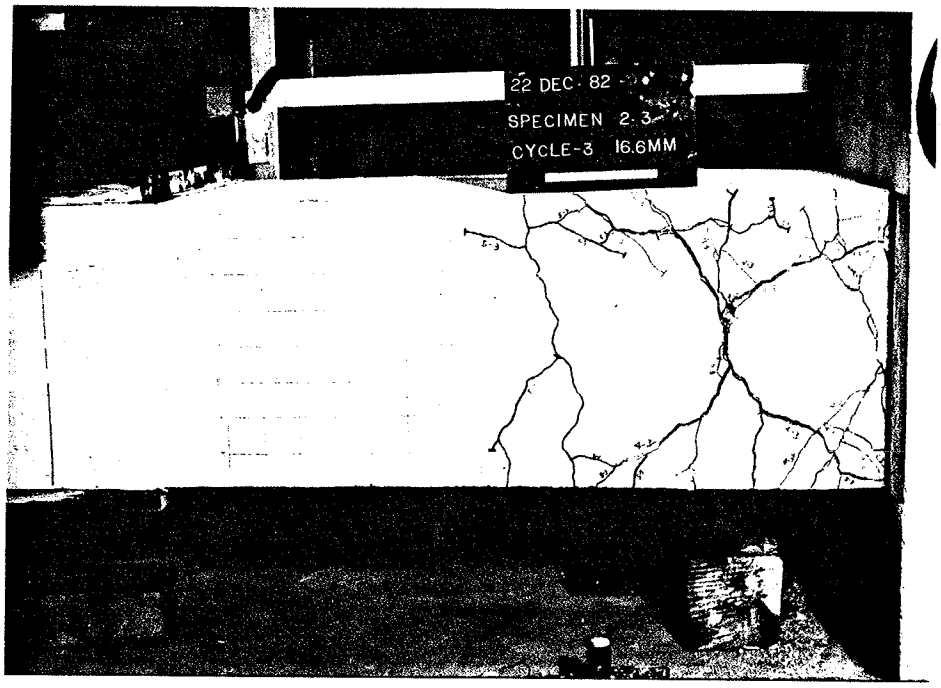

Fig. 4.54 CRACK PATTERN FOR SPECIMEN 2-3 AT 5δy/3

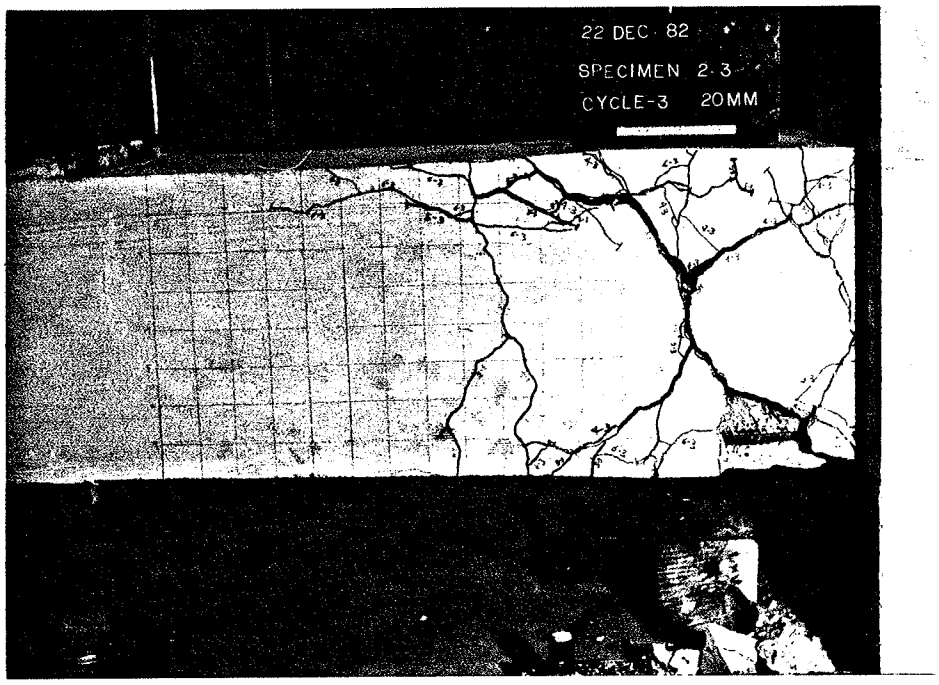

Fig. 4.55 FINAL CRACK PATTERN FOR SPECIMEN 2-3

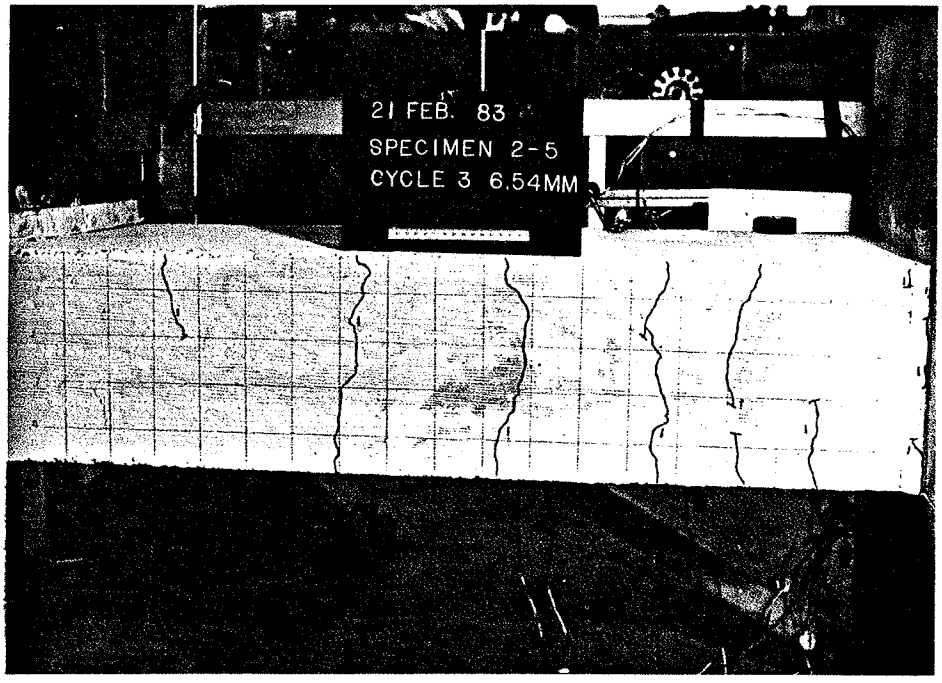

Fig. 4.56 CRACK PATTERN FOR SPECIMEN 2-5 AT $1\delta y/3$

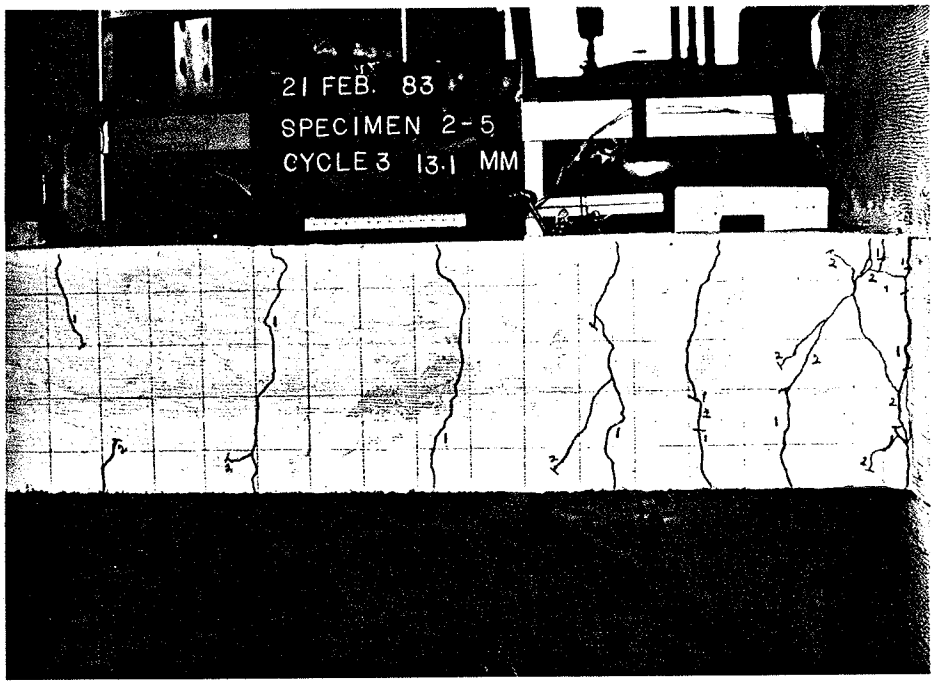

Fig. 4.57 CRACK PATTERN FOR SPECIMEN 2-5 AT $2\delta y/3$

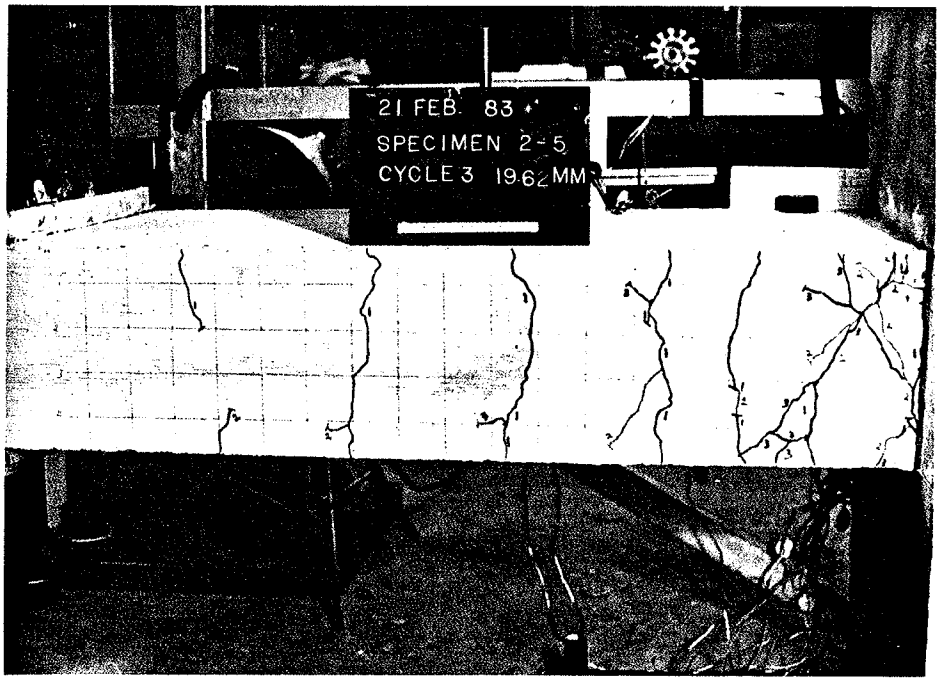

Fig. 4.58 CRACK PATTERN FOR SPECIMEN 2-5 AT $3\delta y/3$

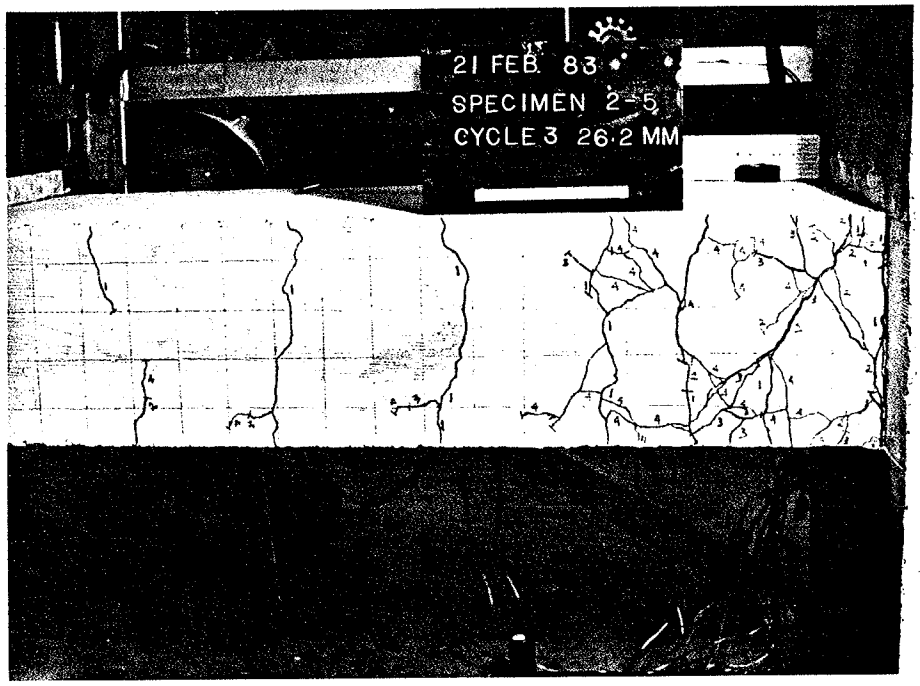

Fig. 4.59 CRACK PATTERN FOR SPECIMEN 2-5 AT $4\delta y/3$

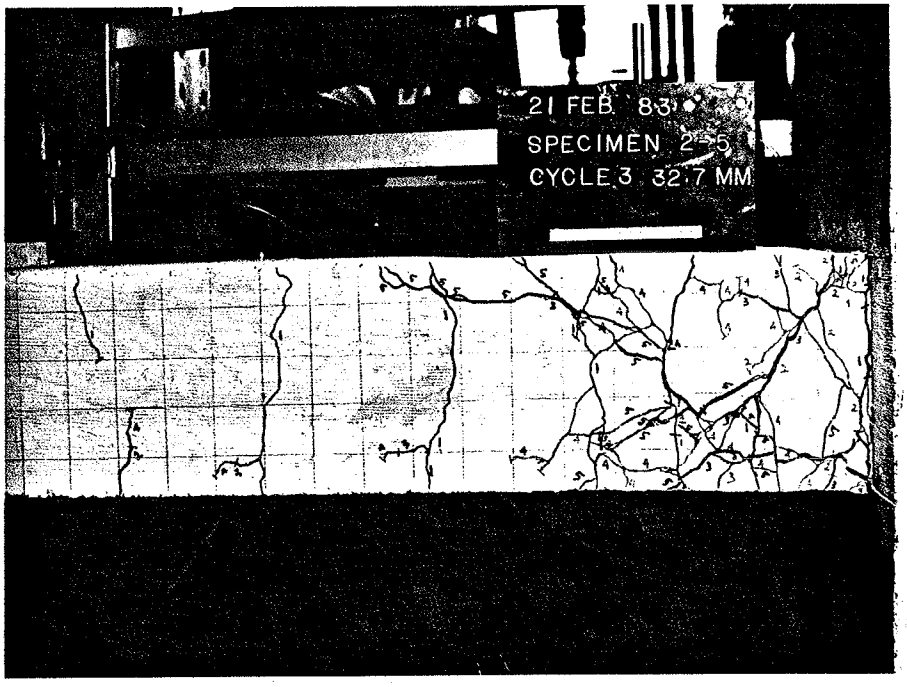

Fig. 4.60 CRACK PATTERN FOR SPECIMEN 2-5 AT $5\delta y/3$

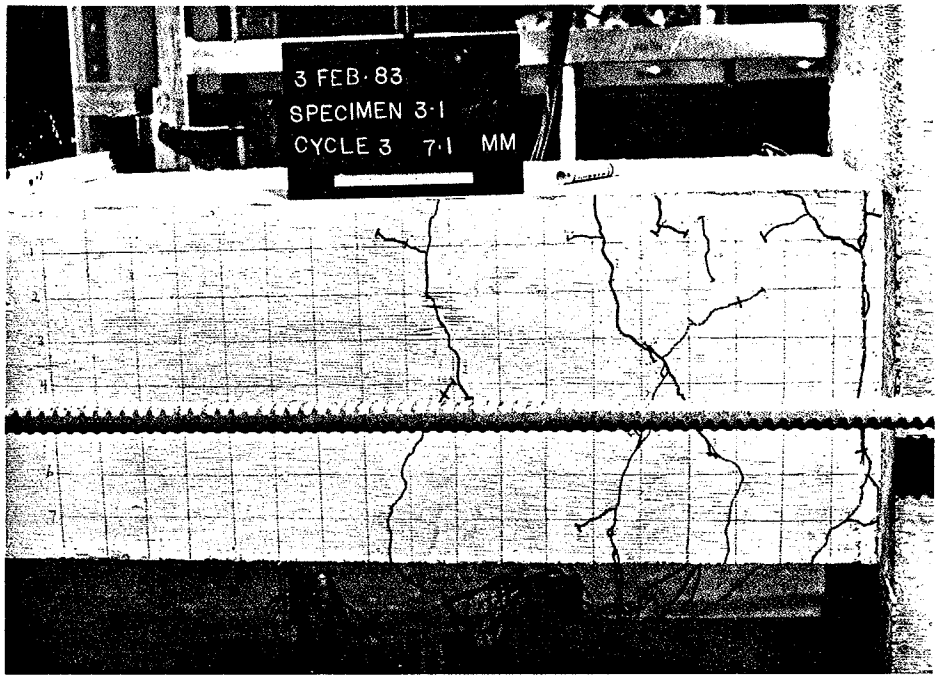

Fig. 4.61 CRACK PATTERN FOR SPECIMEN 3-1 AT $2\delta y/3$

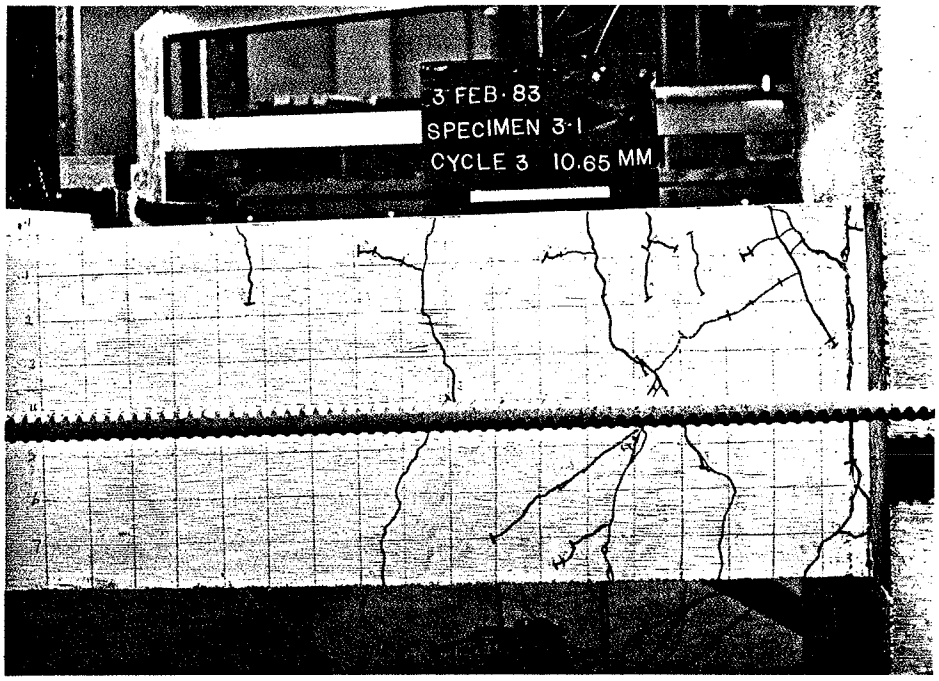

Fig. 4.62 CRACK PATTERN FOR SPECIMEN 3-1 AT $3\delta y/3$

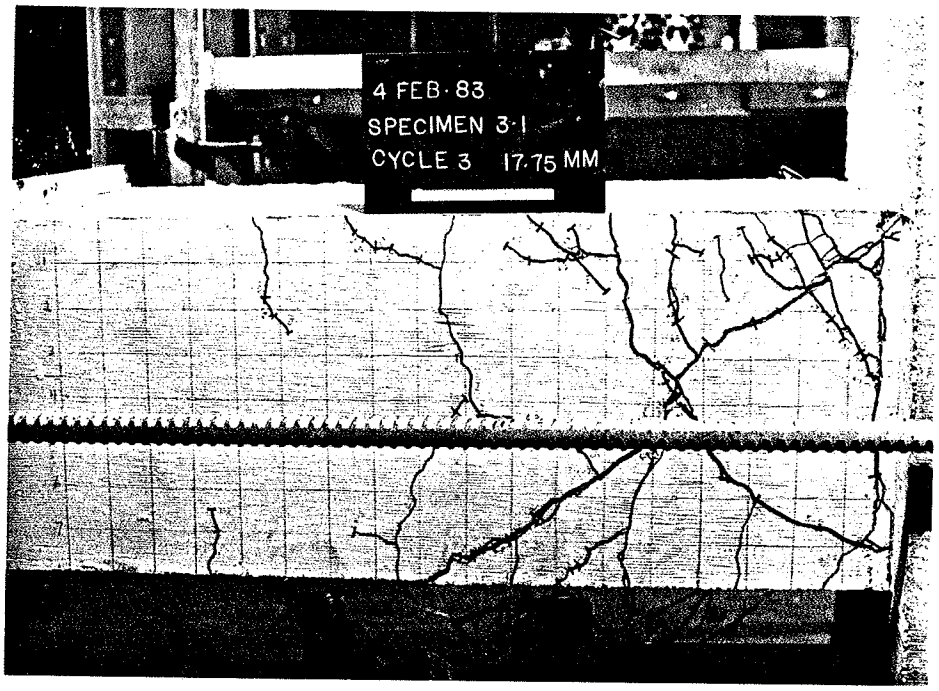

Fig. 4.63 CRACK PATTERN FOR SPECIMEN 3-1 AT 5δy/3

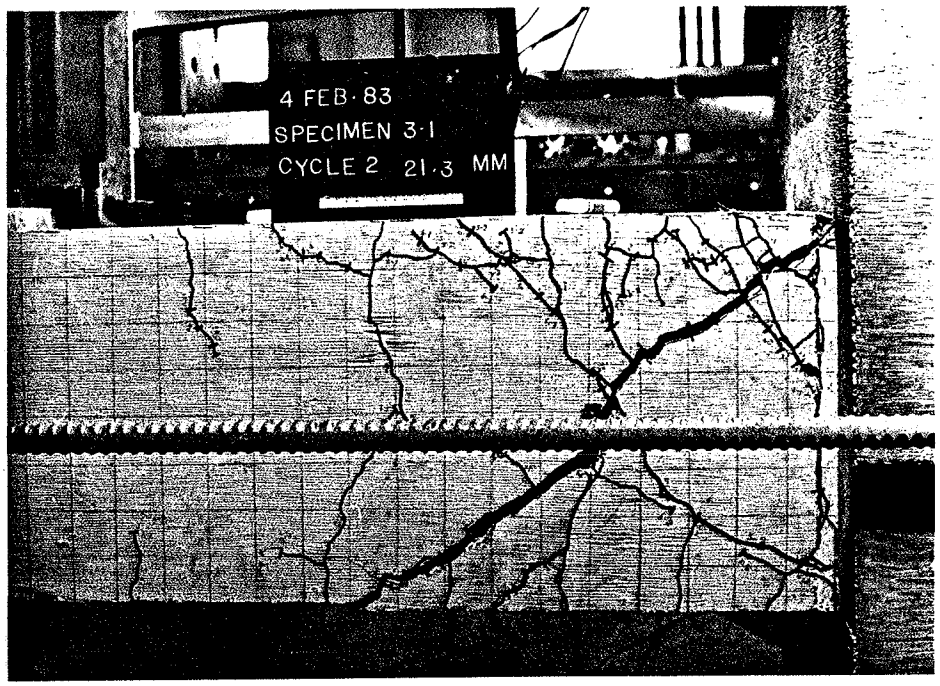

Fig. 4.64 CRACK PATTERN FOR SPECIMEN 3-1 AT 6δy/2

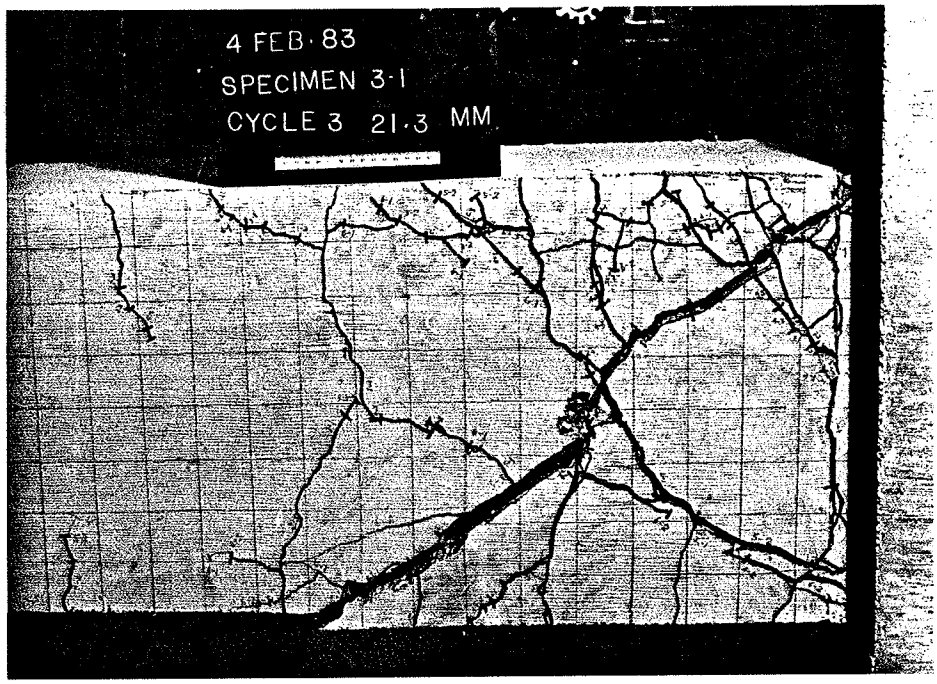

Fig. 4.65 FINAL CRACK PATTERN FOR SPECIMEN 3-1 AT 6δy/2

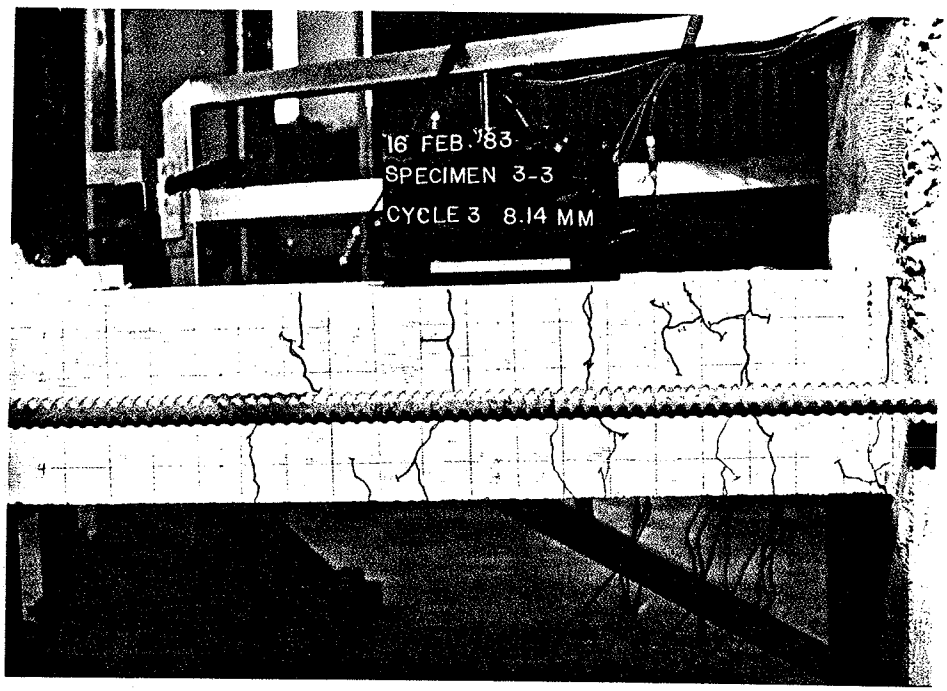

Fig. 4.66 CRACK PATTERN FOR SPECIMEN 3-3 AT 1δy/3

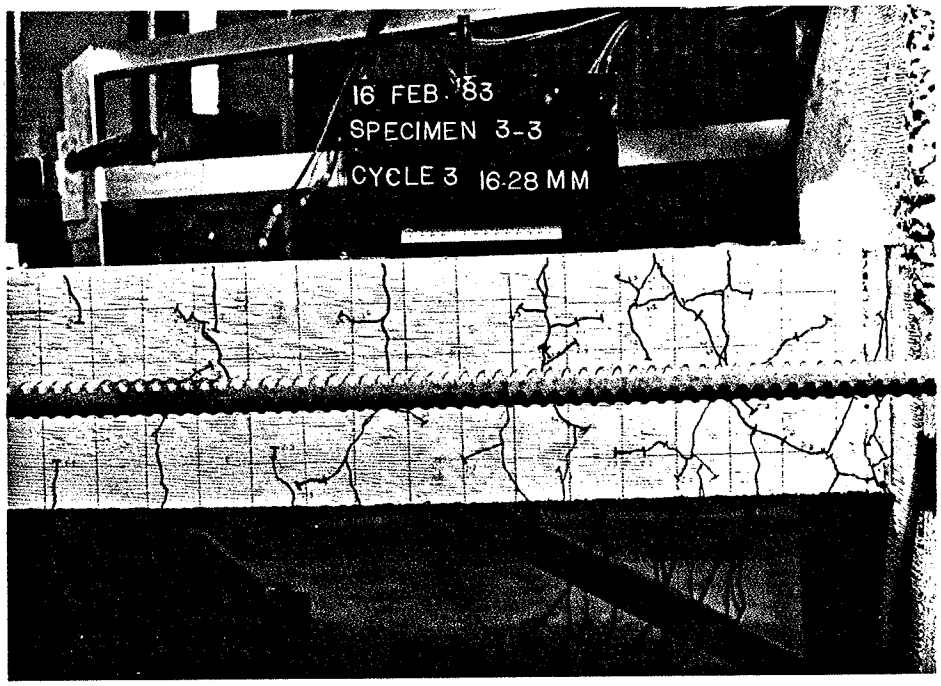

Fig. 4.67 CRACK PATTERN FOR SPECIMEN 3-3 AT $2\delta y/3$

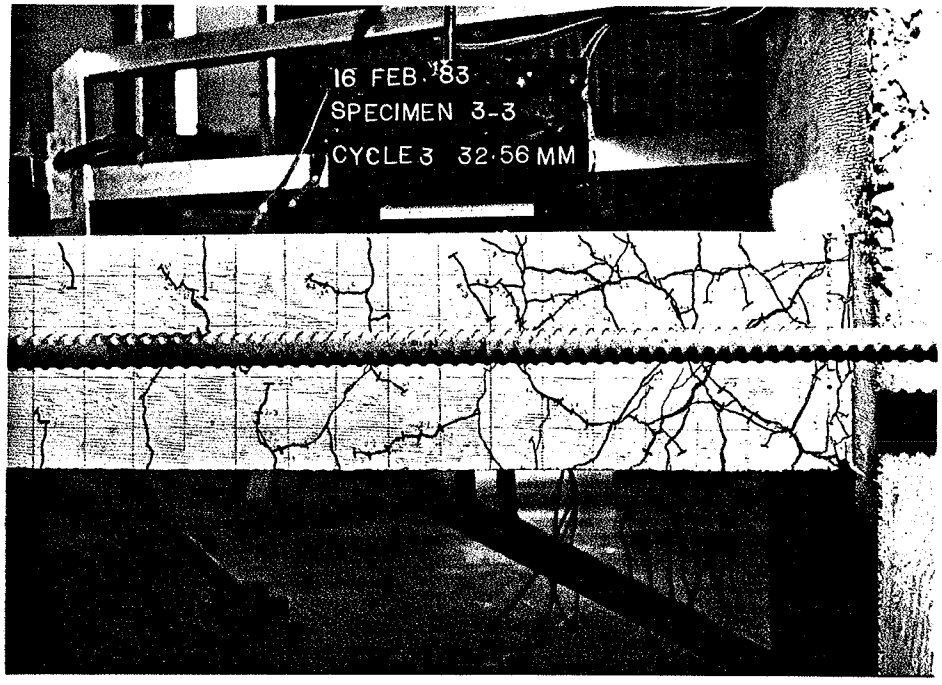

Fig. 4.68 CRACK PATTERN FOR SPECIMEN 3-3 AT $4\delta y/3$

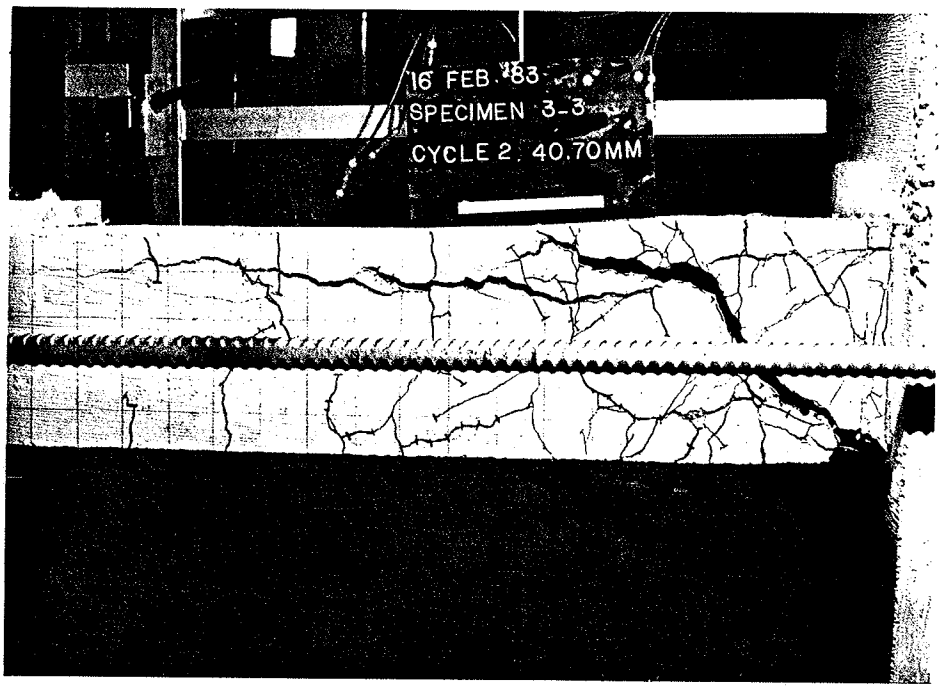

Fig. 4.69 FINAL CRACK PATTERN FOR SPECIMEN 3-3 AT 5δy/2

(a) SPECIMEN 1-1
(P=0·51%)

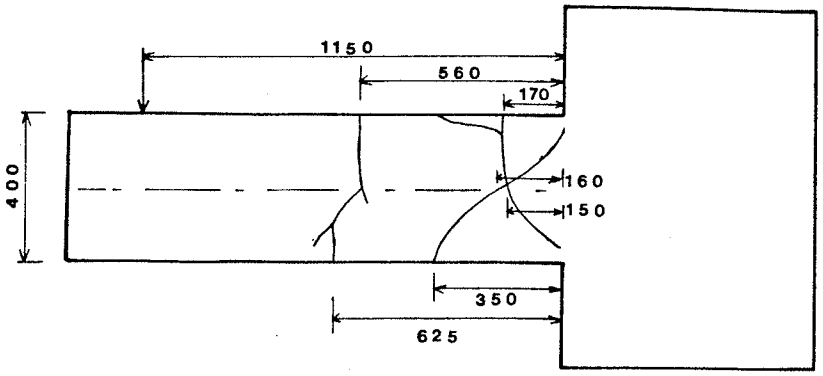

(b) SPECIMEN 1-8
(P=0·46%)

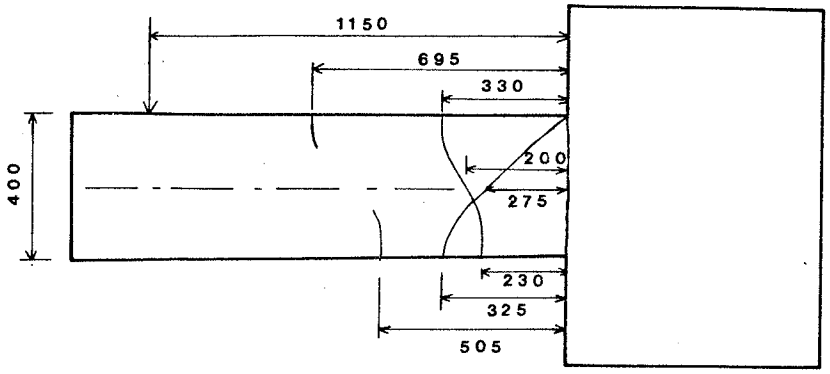

(C) SPECIMEN 1-7
(P= 0·40 %)

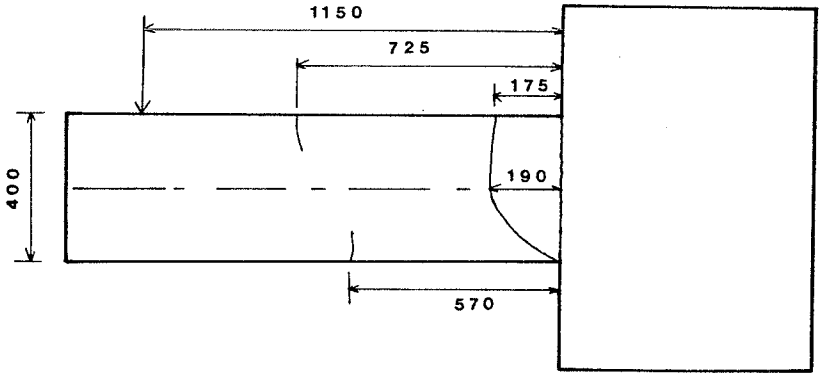

(d) SPECIMEN 1-9
(P= 0·86%)

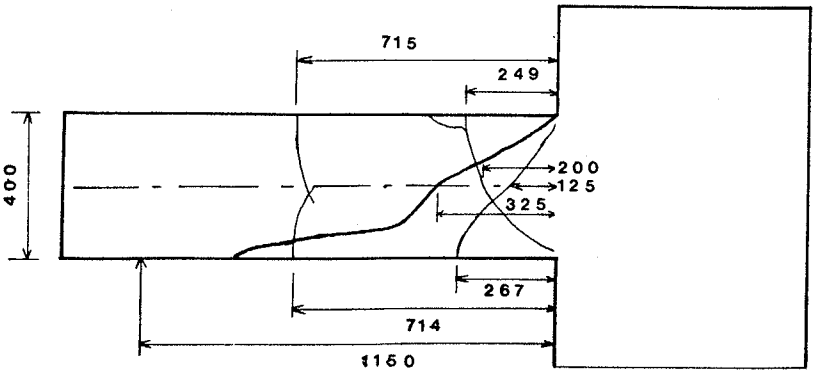

5.1. SUMMARY OF CRACK PATTERN FOR SPECIMEN WITH a/d = 3.29.

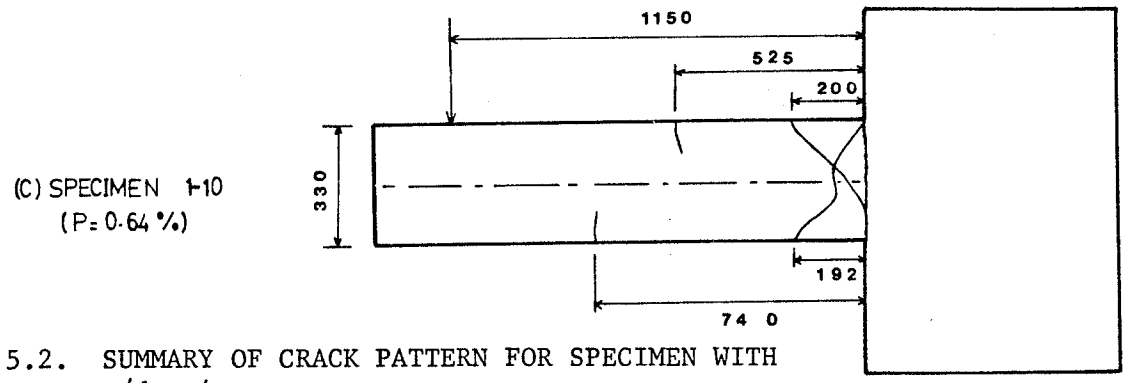

5.2. SUMMARY OF CRACK PATTERN FOR SPECIMEN WITH a/d = 4.

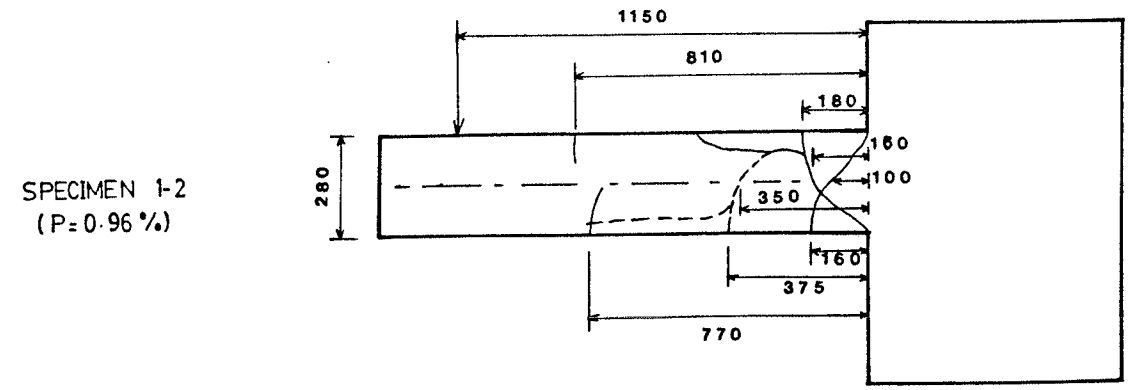

5.3. SUMMARY OF CRACK PATTERN FOR SPECIMEN WITH a/d = 5.

(a) SPECIMEN 1-3
(P=1.26 %)

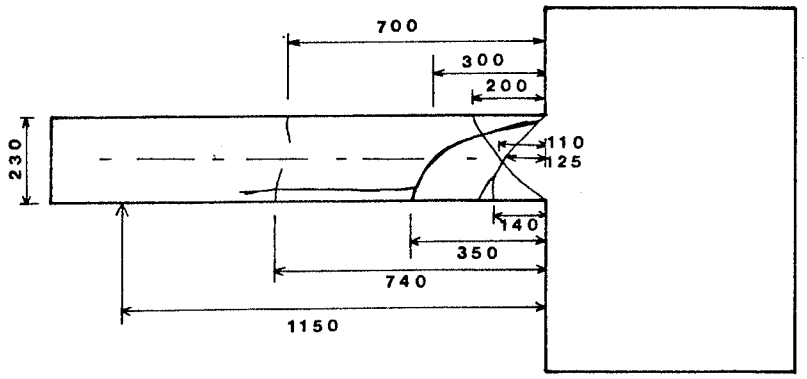

(b) SPECIMEN 1-6
(P=1.58 %)

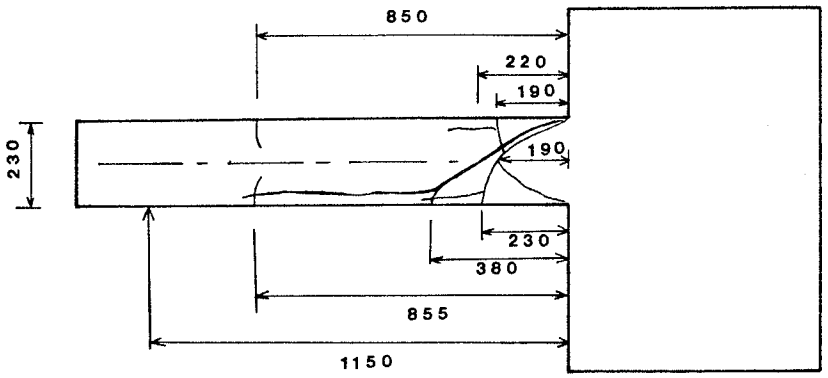

(C) SPECIMEN 1-4
(P= 1.9 %)

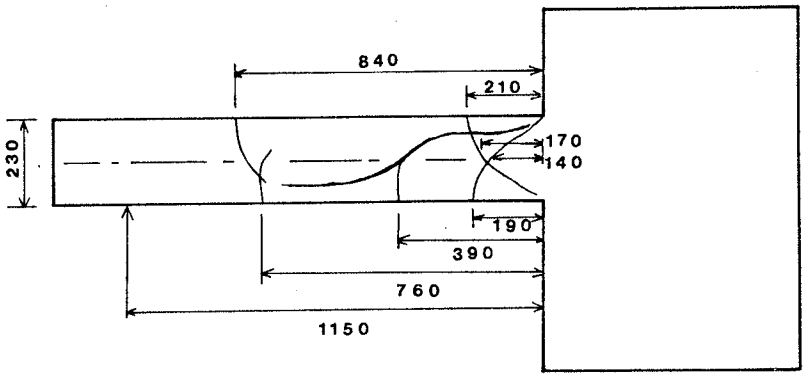

(d) SPECIMEN 1-5
(P=0.95 %)

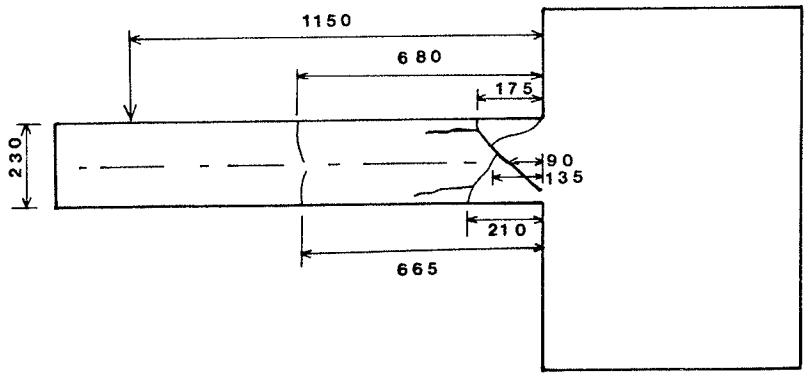

5.4. SUMMARY OF CRACK PATTERN FOR SPECIMEN WITH a/d = 6.05.

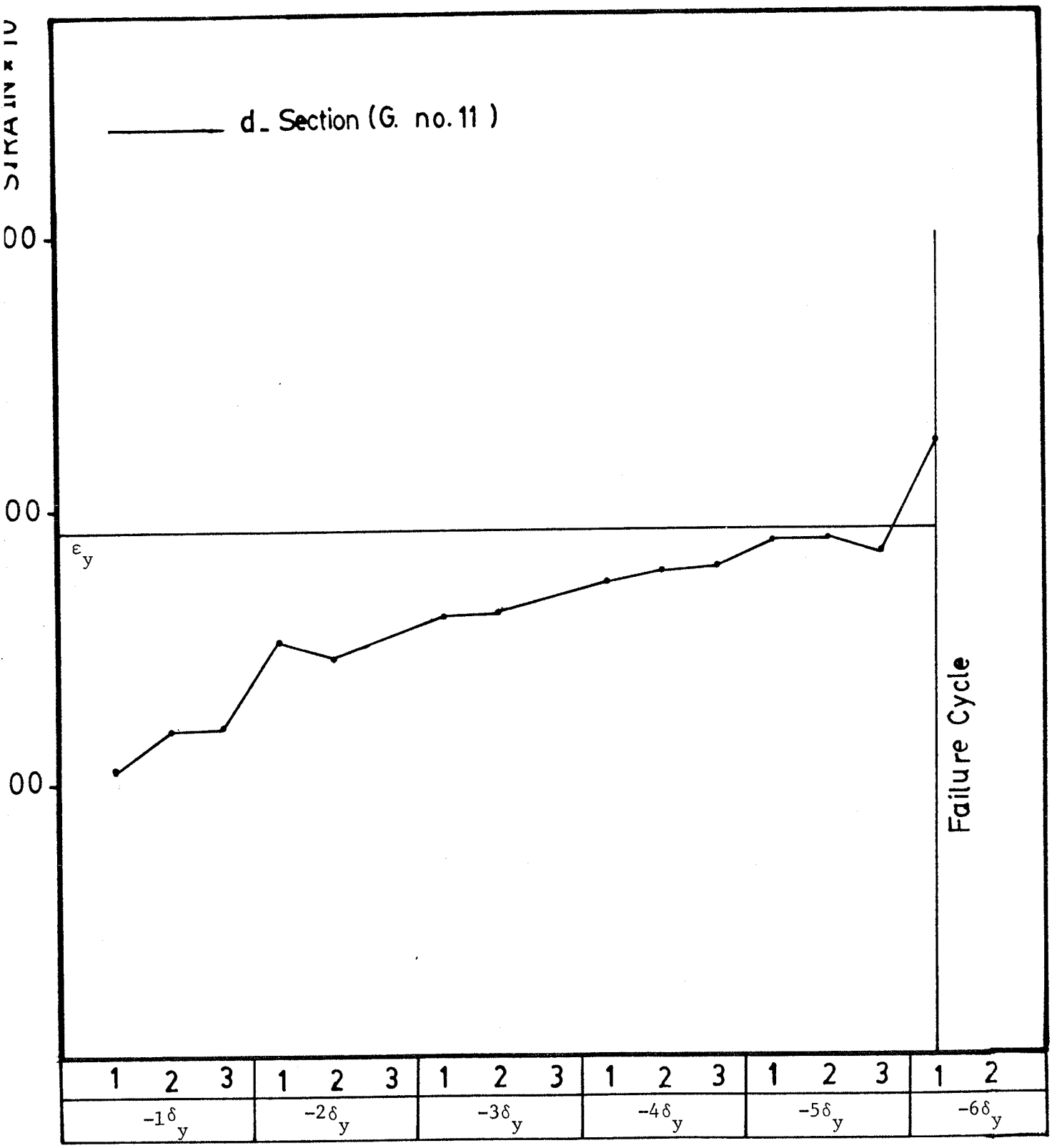

5.5.a. STRAINS OF LONGITUDINAL REINFORCEMENT FOR SPECIMEN 1-1.

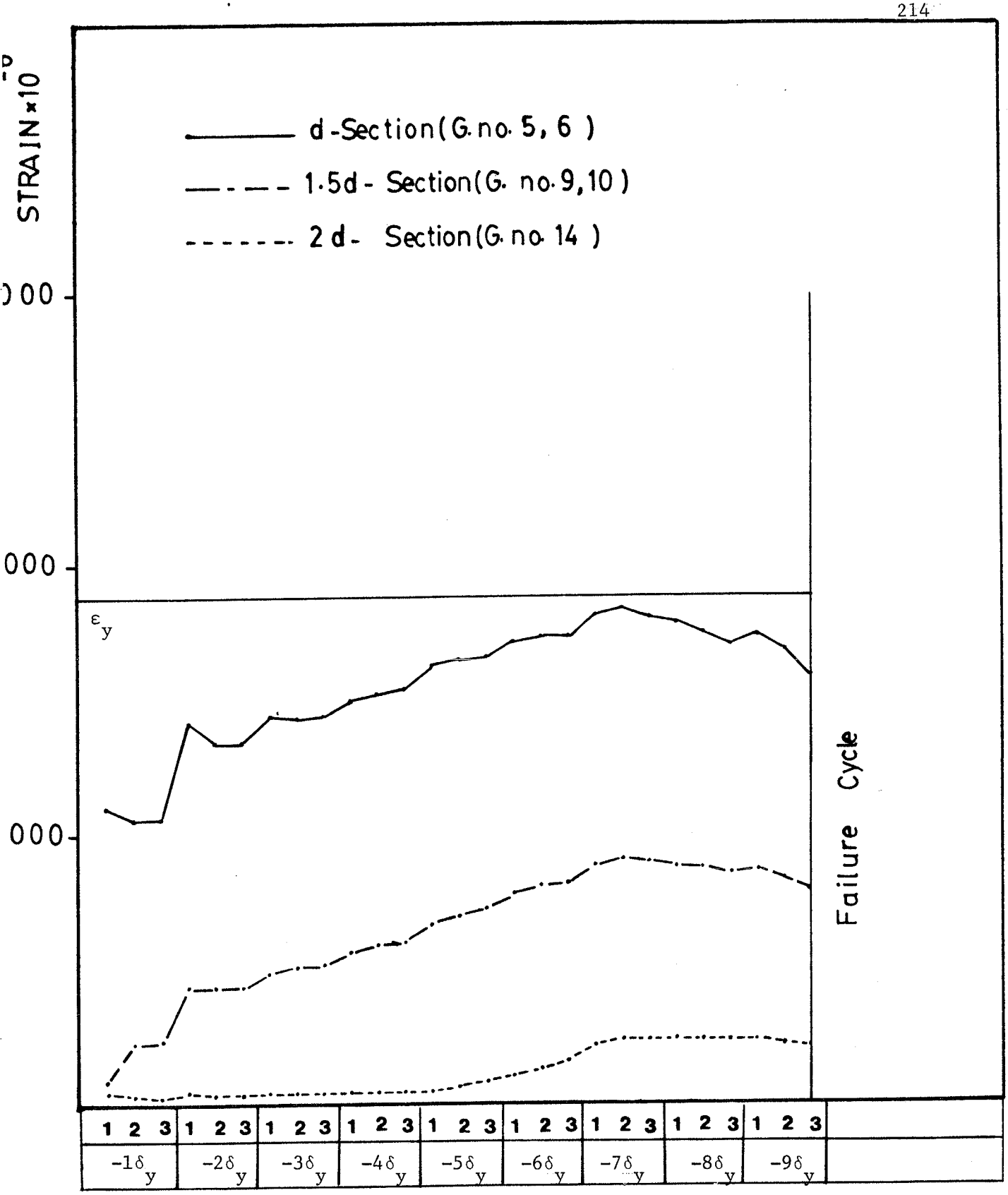

5.5.b. STRAINS OF LONGITUDINAL REINFORCEMENT FOR SPECIMEN 1-8.

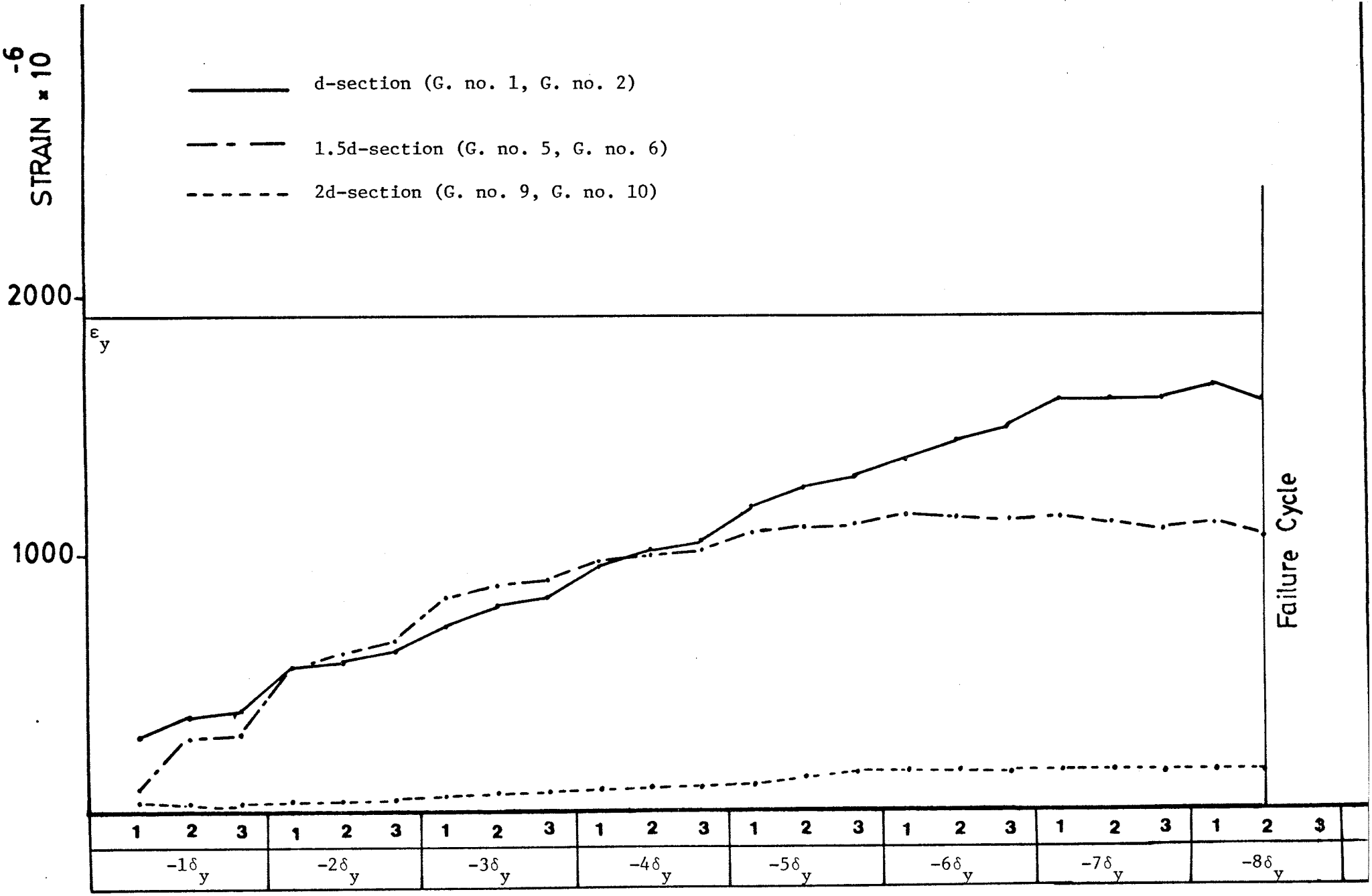

5.5.c. STRAINS OF LONGITUDINAL REINFORCEMENT FOR SPECIMEN 1-7.

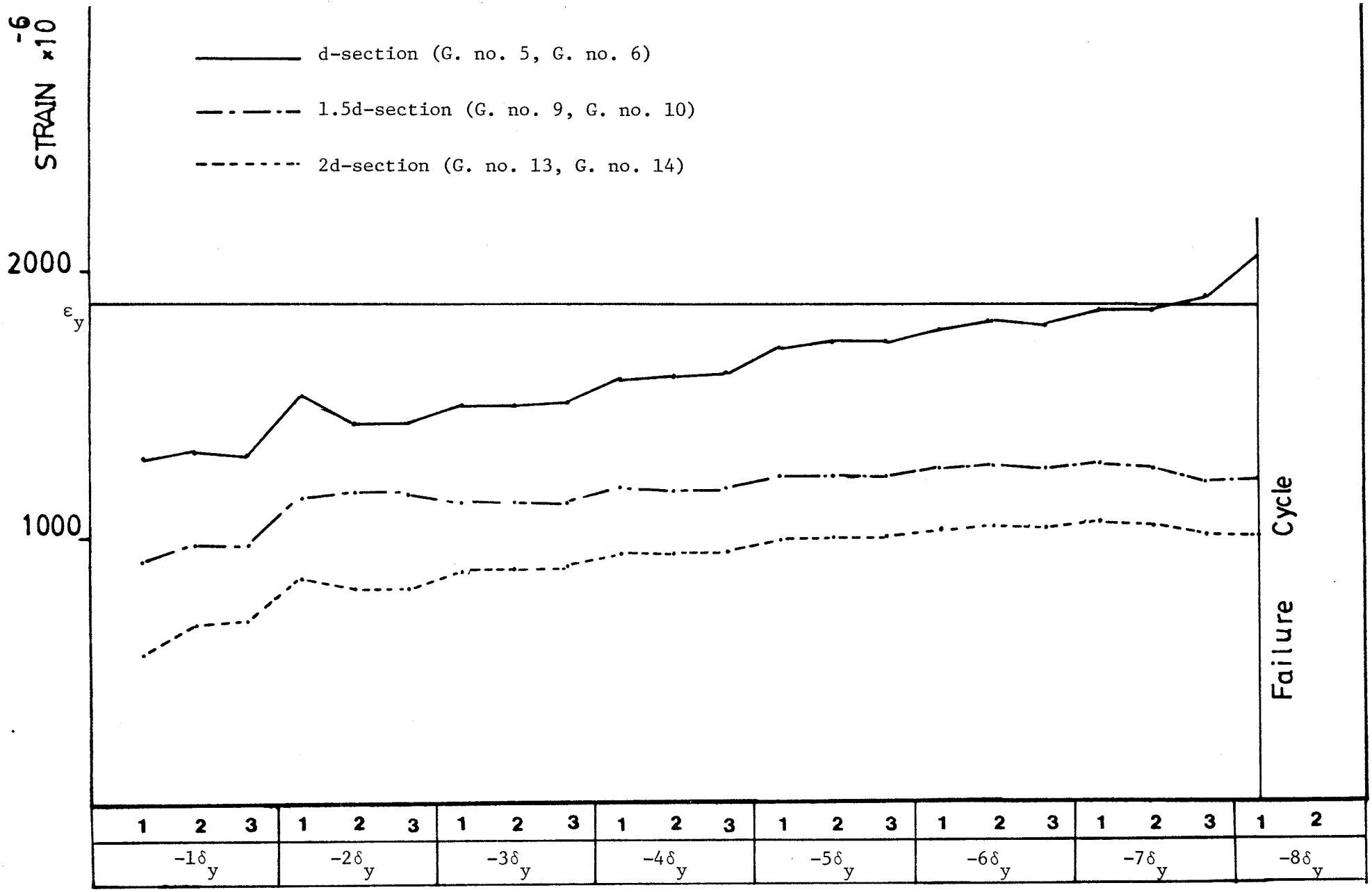

5.5.d STRAINS OF LONGITUDINAL REINFORCEMENT FOR SPECIMEN 1-10.

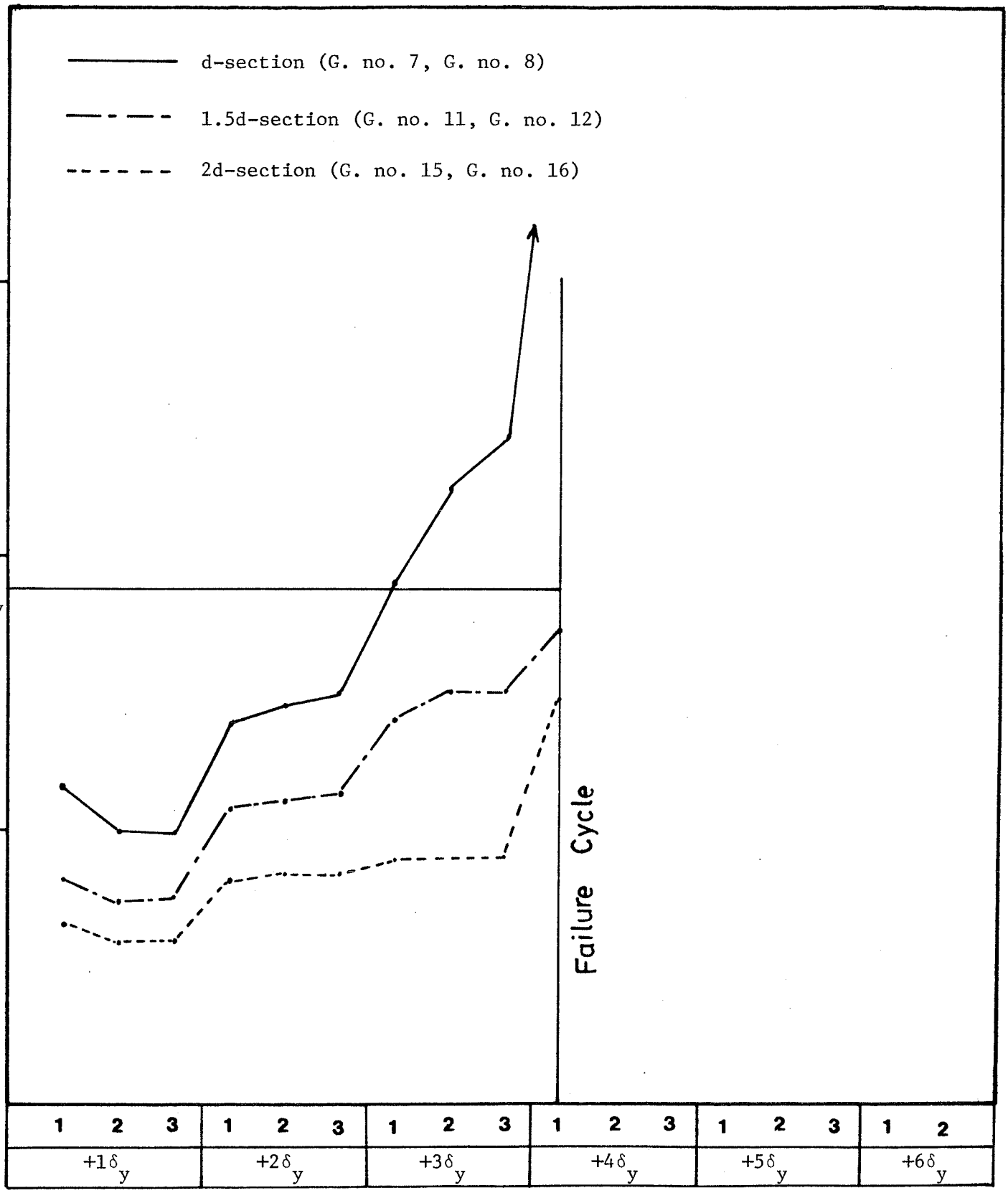

5.5.e. STRAINS OF LONGITUDINAL REINFORCEMENT FOR SPECIMEN 1-9.

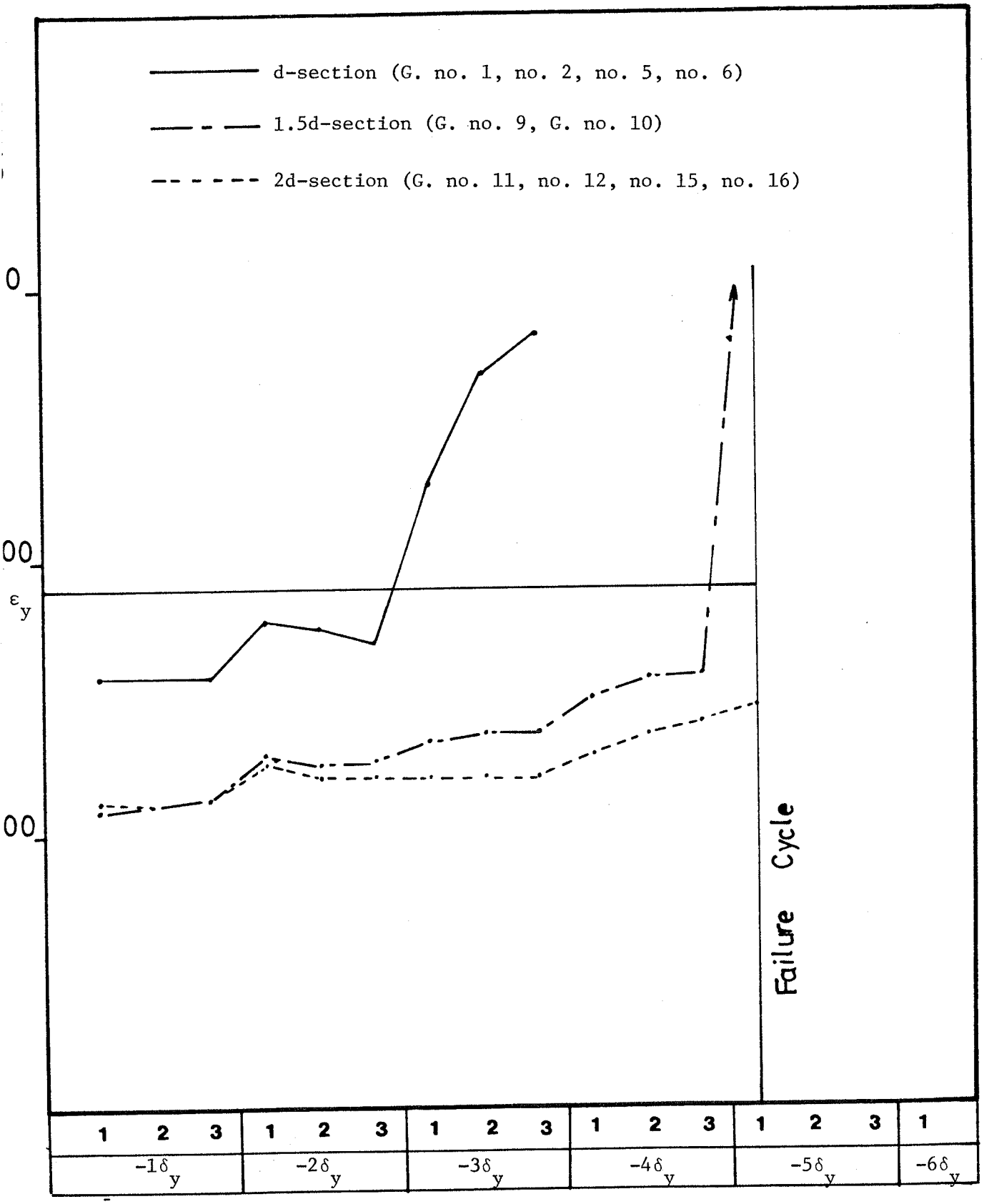

5.6 STRAINS OF LONGITUDINAL REINFORCEMENT FOR SPECIMEN 1-2.

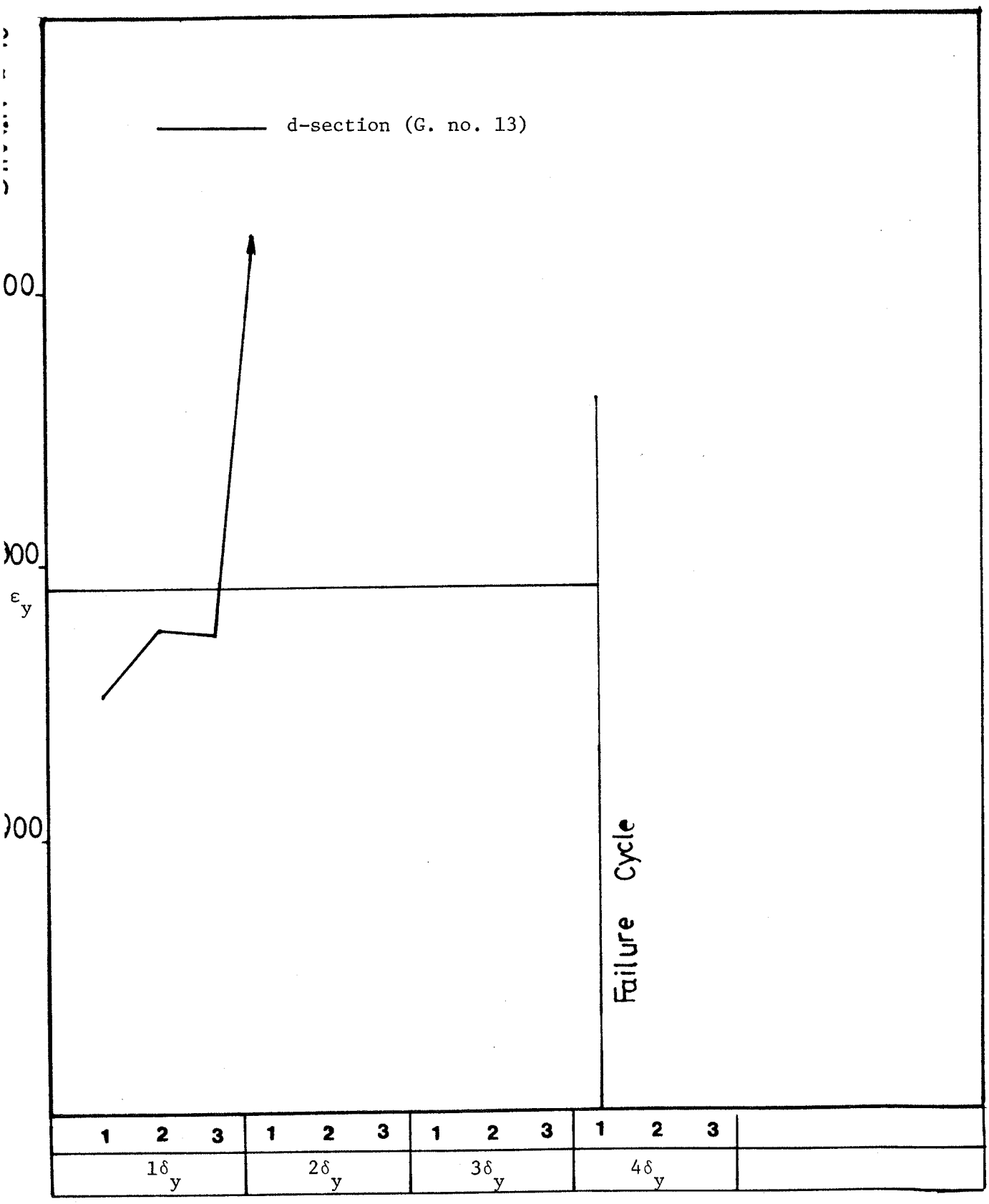

5.7.a. STRAINS OF LONGITUDINAL REINFORCEMENT FOR SPECIMEN 1-3.

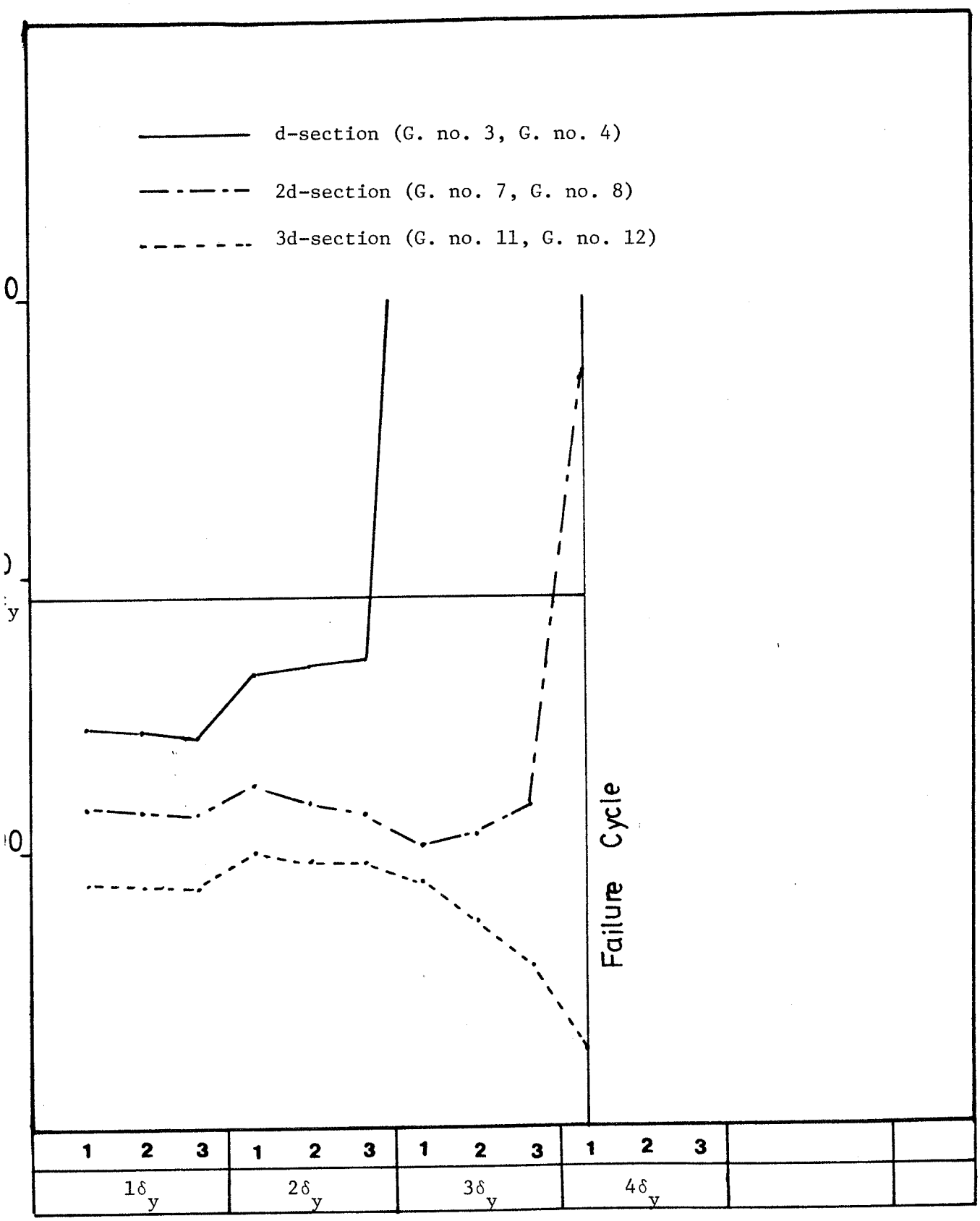

5.7.b. STRAINS OF LONGITUDINAL REINFORCEMENT FOR SPECIMEN 1-6.

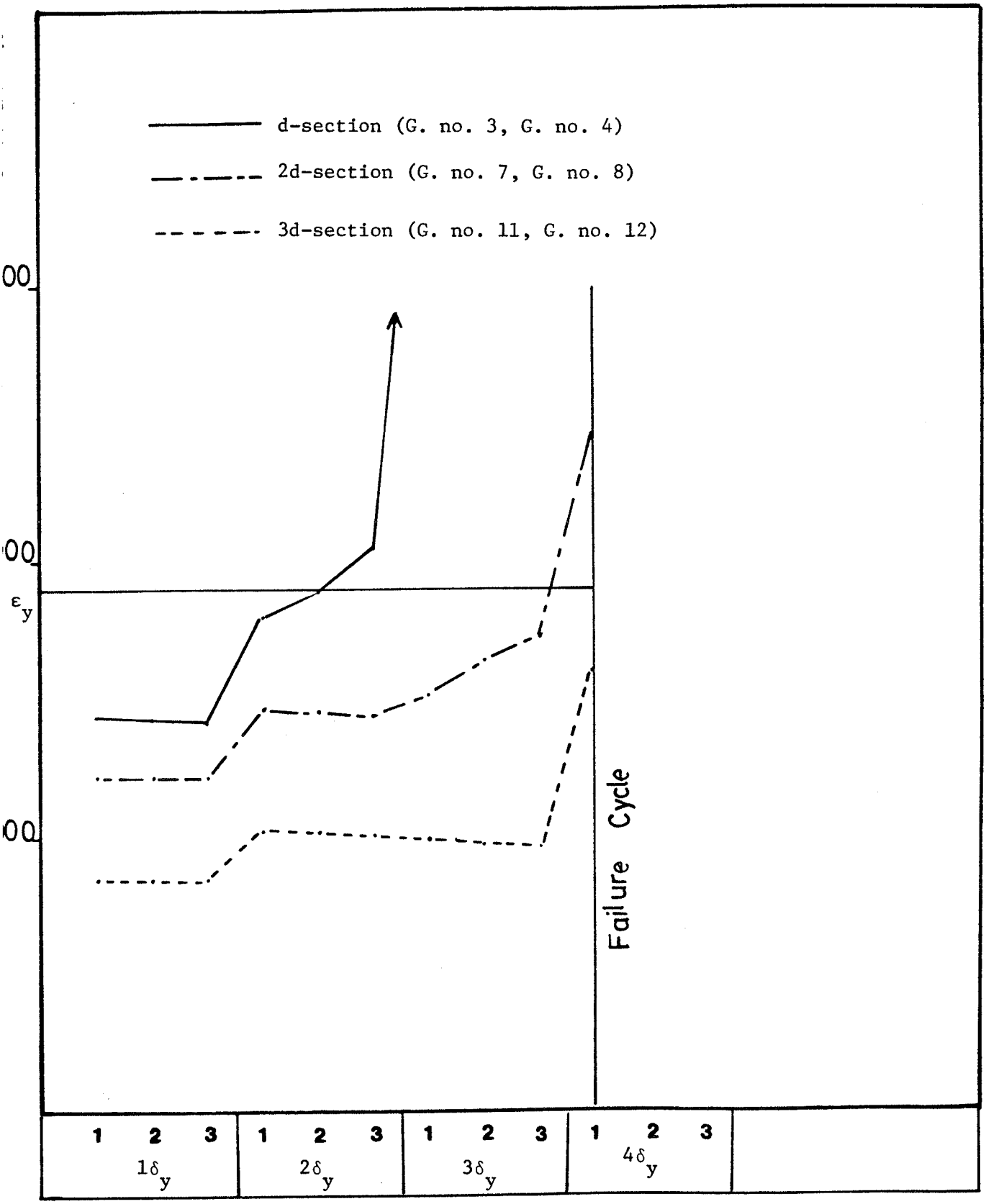

5. 7.c. STRAINS OF LONGITUDINAL REINFORCEMENT FOR SPECIMEN 1-4.

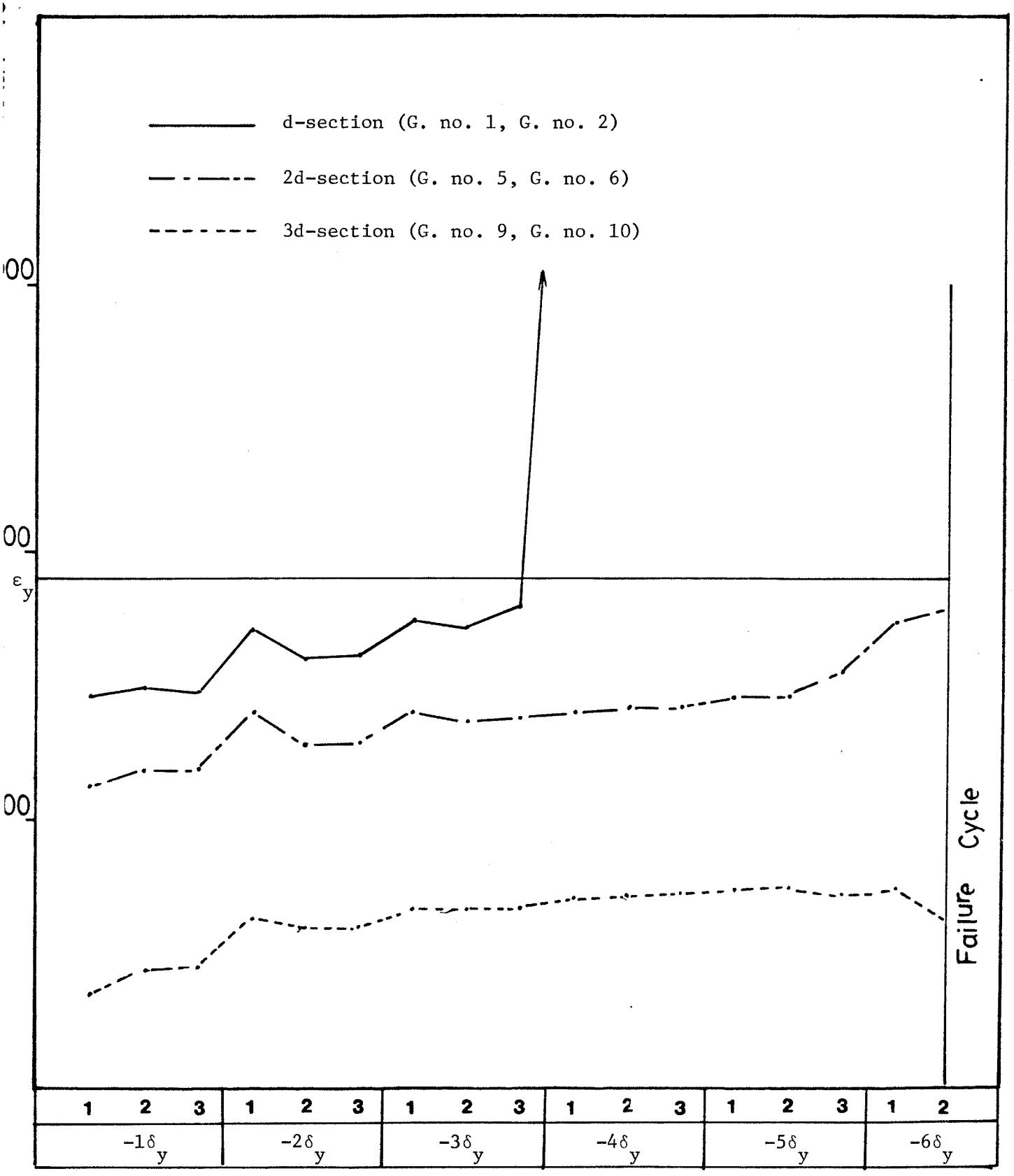

5.7.d. STRAINS OF LONGITUDINAL REINFORCEMENT FOR SPECIMEN 1-5.

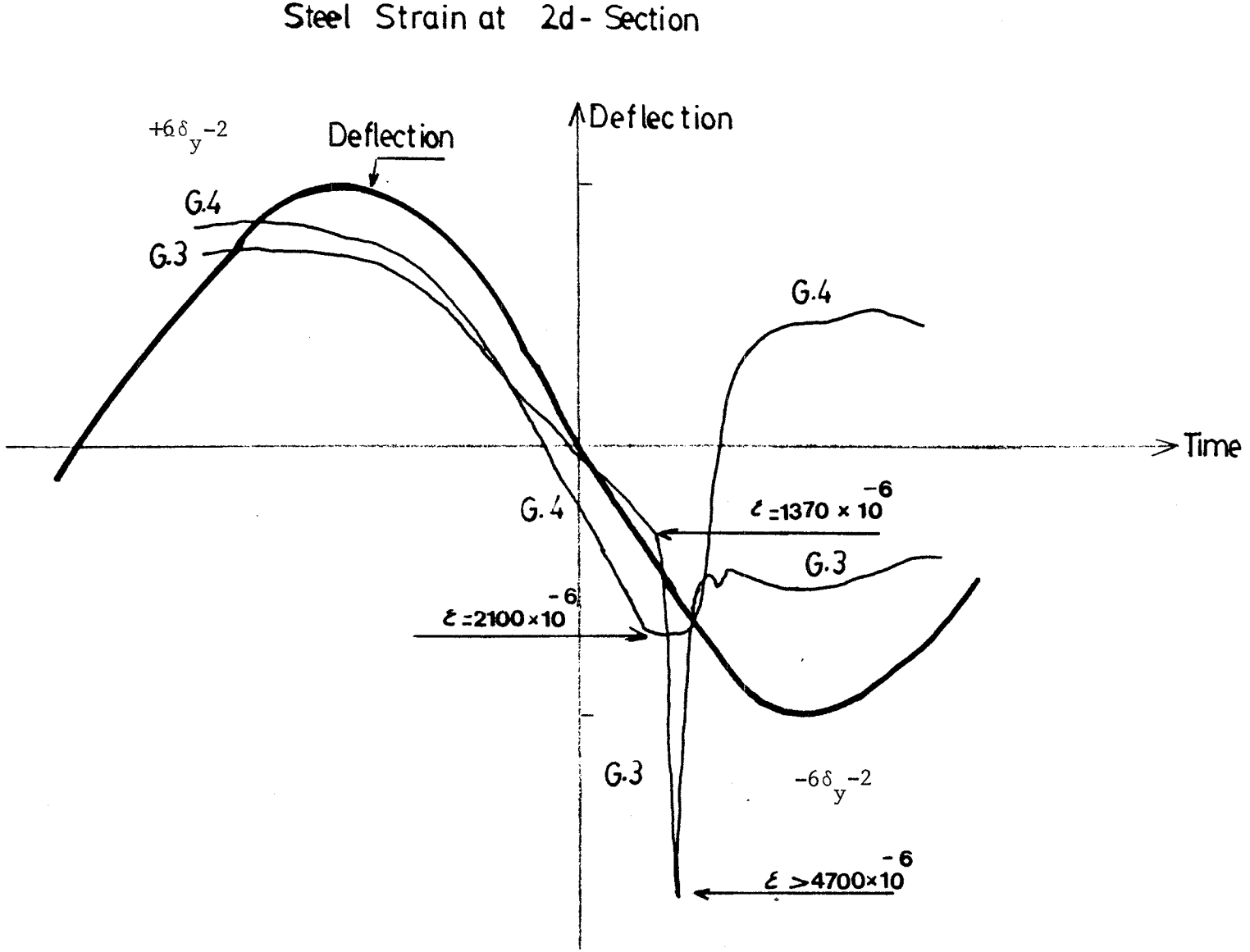

Fig. 5.8. STRAIN RECORD FOR SPECIMEN 2-5 DURING THE FAILURE CYCLE.

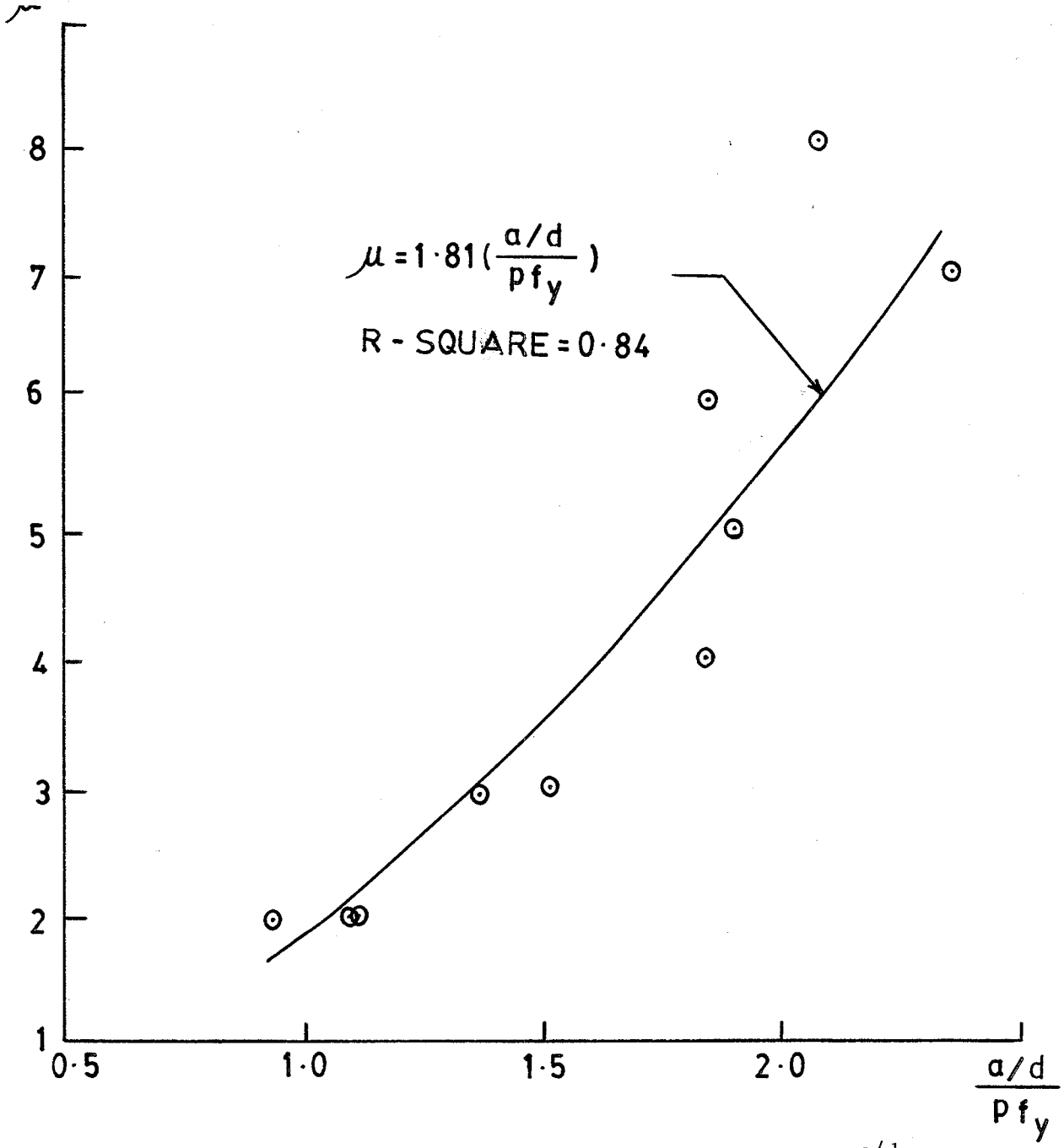

Fig. 5.9 THE RELATIONSHIP BETWEEN THE DUCTILITY FACTOR, μ and $\frac{a/d}{pf_y}$

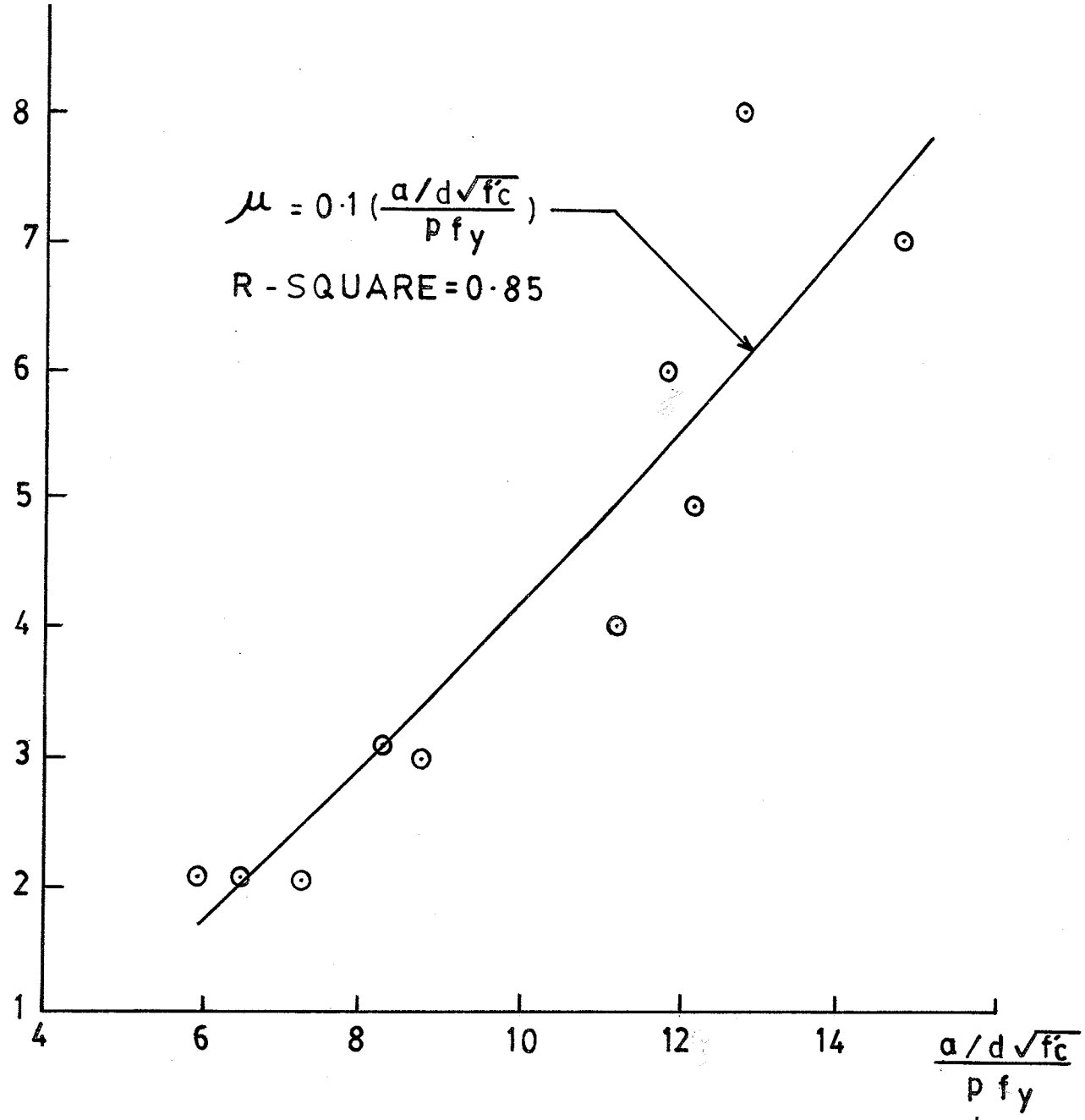

Fig. 5.10 THE RELATIONSHIP BETWEEN THE DUCTILITY FACTOR, μ, and $\frac{a/d \quad f'_c}{pf_y}$

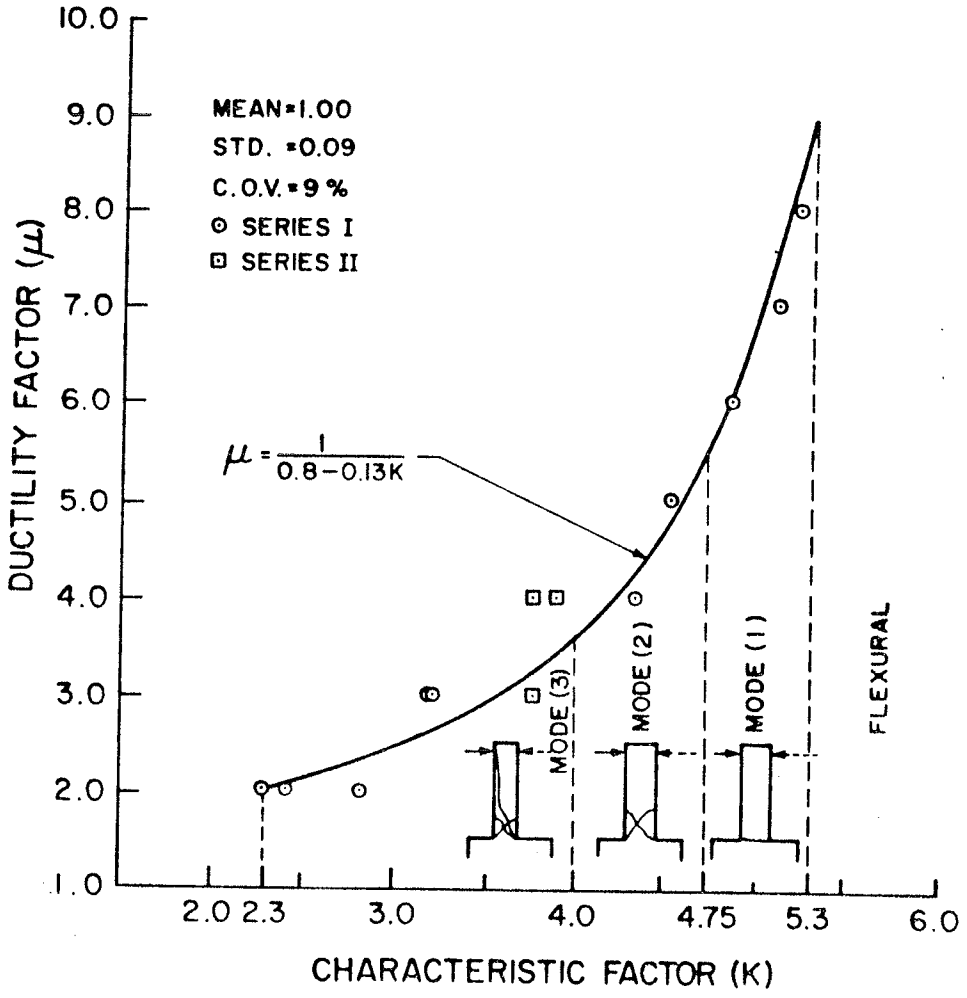

Fig. 5.11 THE RELATIONSHIP BETWEEN THE DUCTILITY FACTOR, μ, AND THE CHARACTERISTIC FACTOR, K

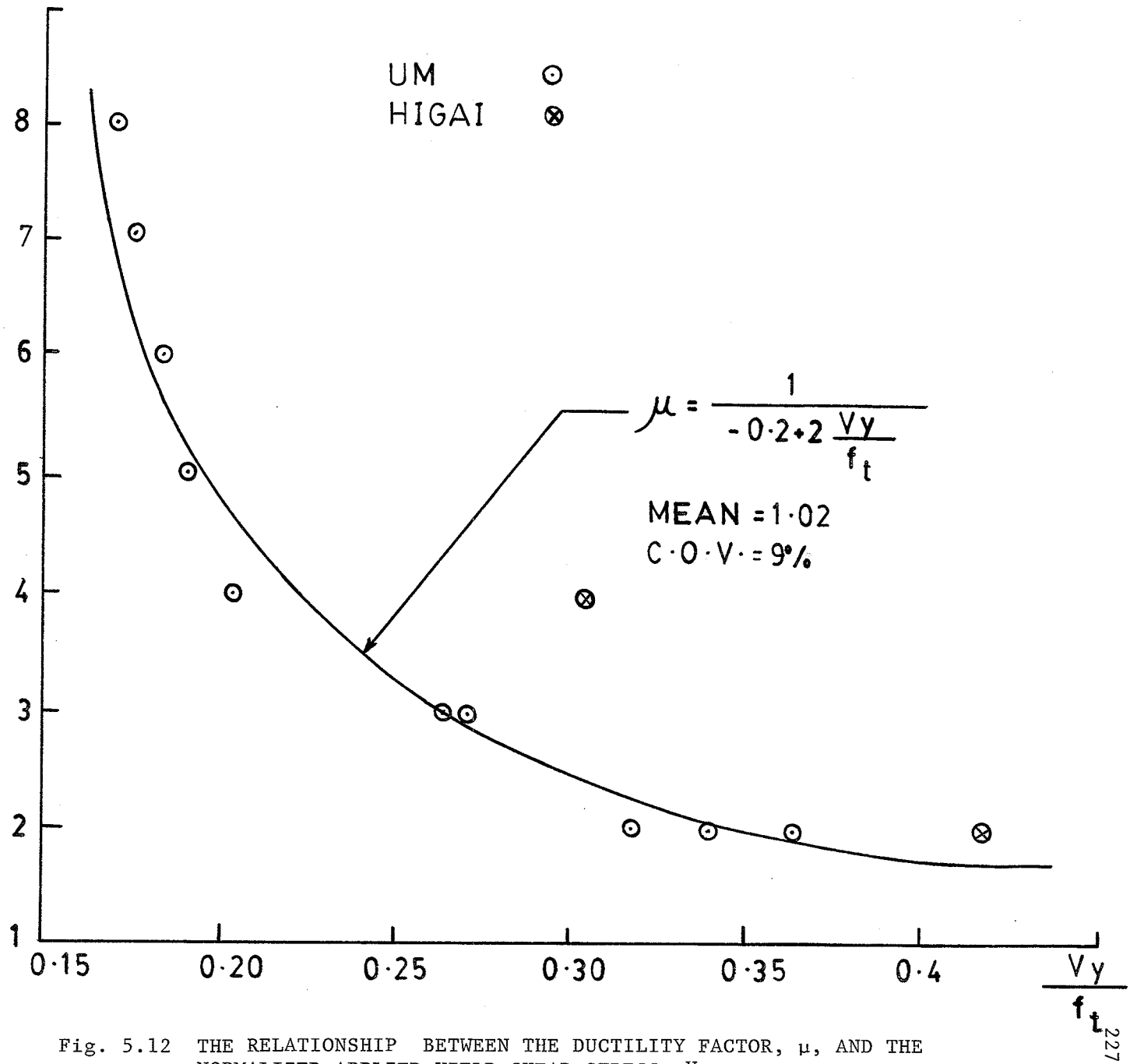

Fig. 5.12 THE RELATIONSHIP BETWEEN THE DUCTILITY FACTOR, μ, AND THE NORMALIZED APPLIED YIELD SHEAR STRESS, $\frac{v_y}{f_t}$

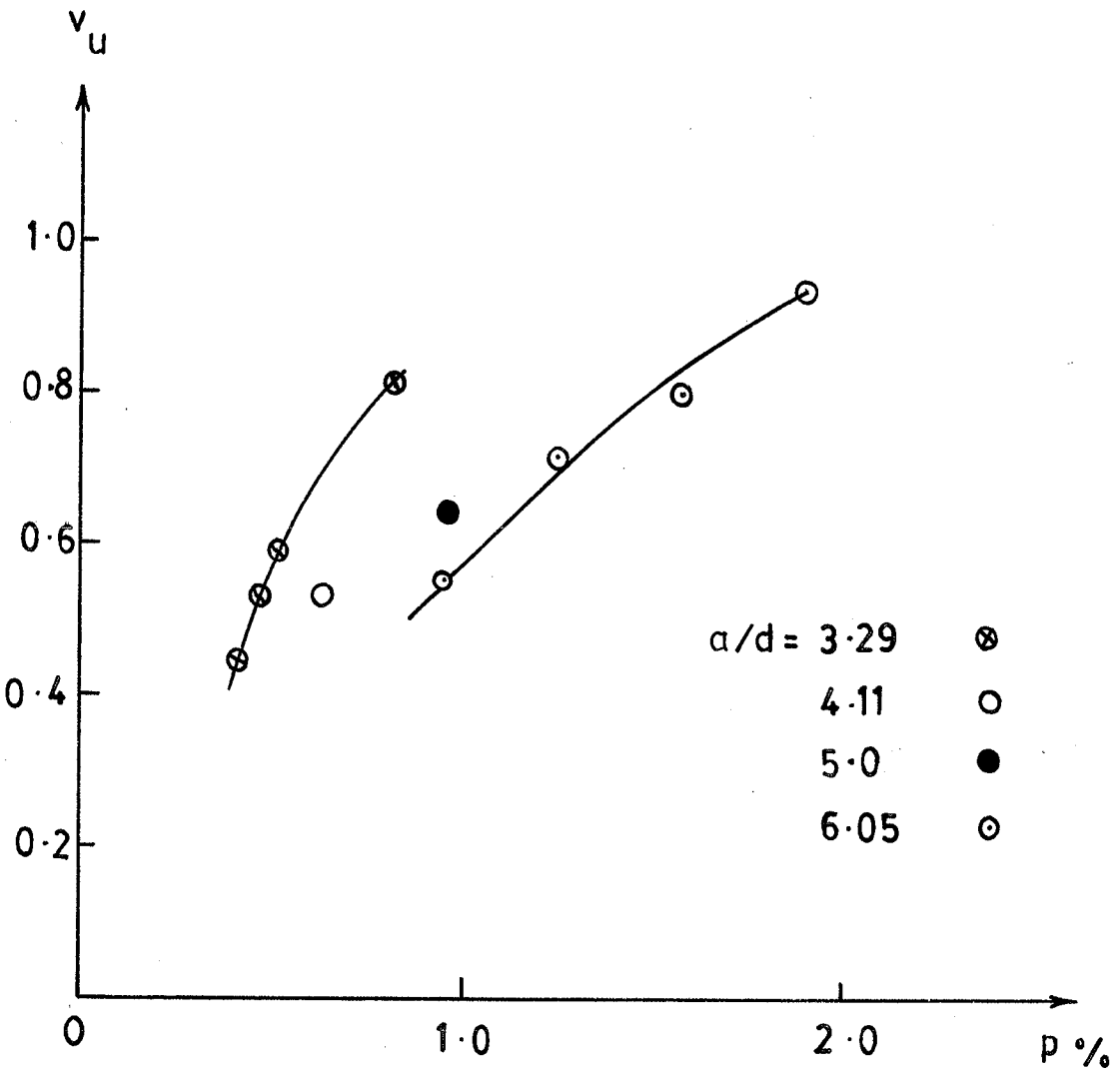

Fig. 5.13 THE RELATIONSHIP BETWEEN THE MAXIMUM SHEAR STRESS, v_u, THE PERCENTAGE OF THE LONGITUDINAL REINFORCEMENT, p

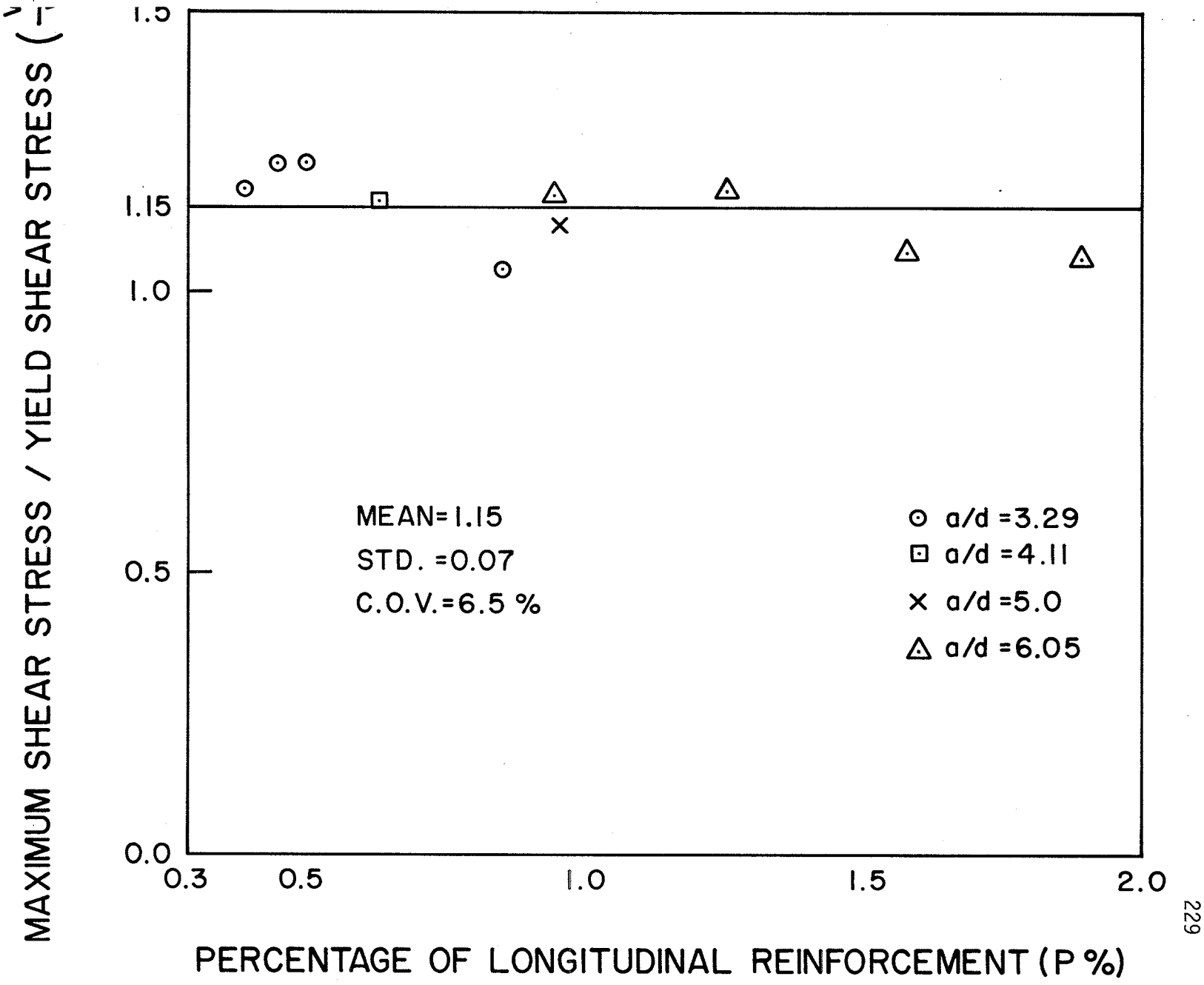

Fig. 5.14 THE RELATIONSHIP BETWEEN THE RATIO OF MAXIMUM SHEAR STRESS TO YIELD SHEAR STRESS, $\frac{v_u}{v_y}$, AND THE PERCENTAGE OF THE LONGITUDINAL REINFORCEMENT, p

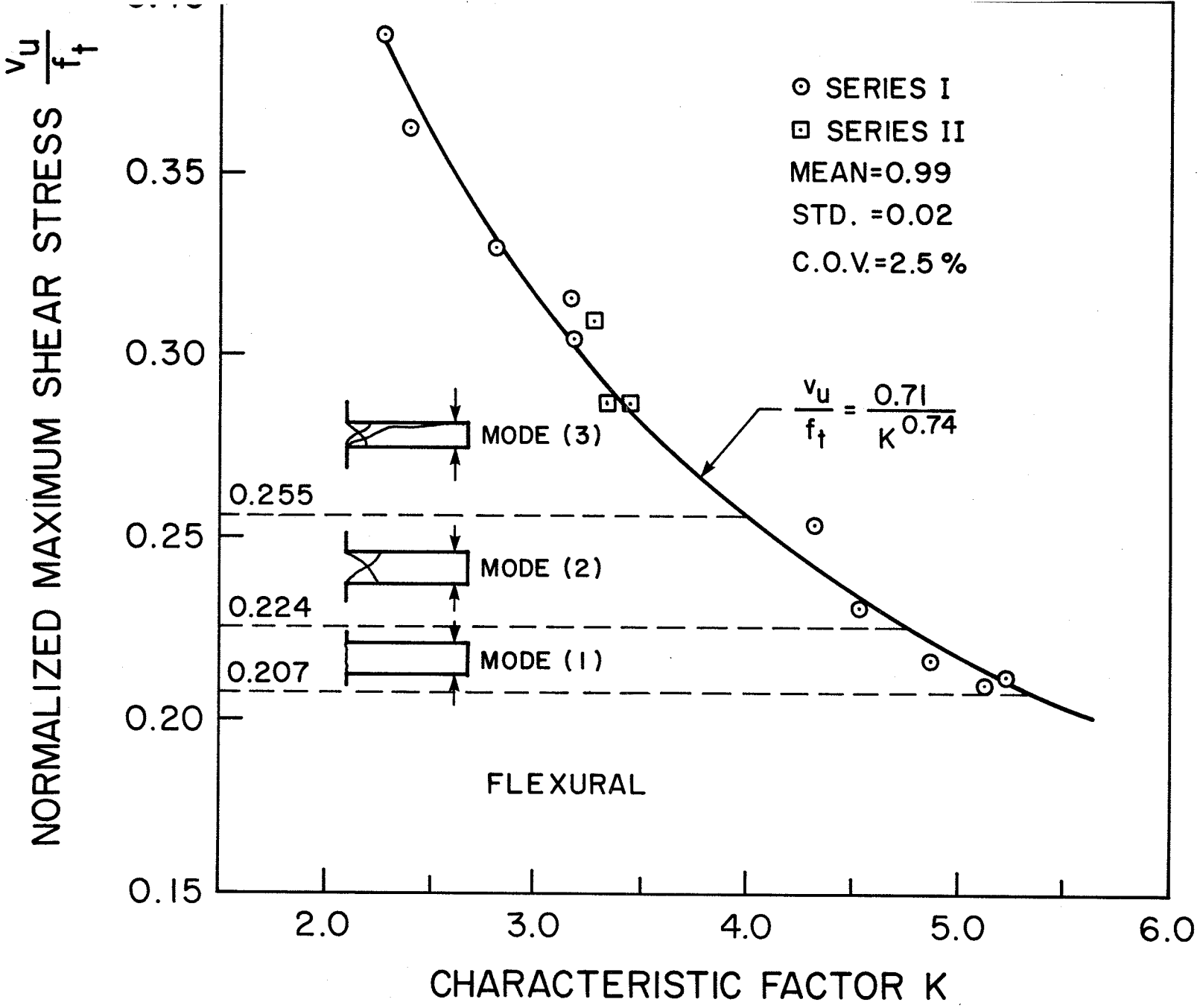

Fig. 5.15 THE RELATIONSHIP BETWEEN THE NORMALIZED MAXIMUM SHEAR STRESS, $\frac{v_u}{f_t}$, AND THE CHARACTERISTIC FACTOR, K

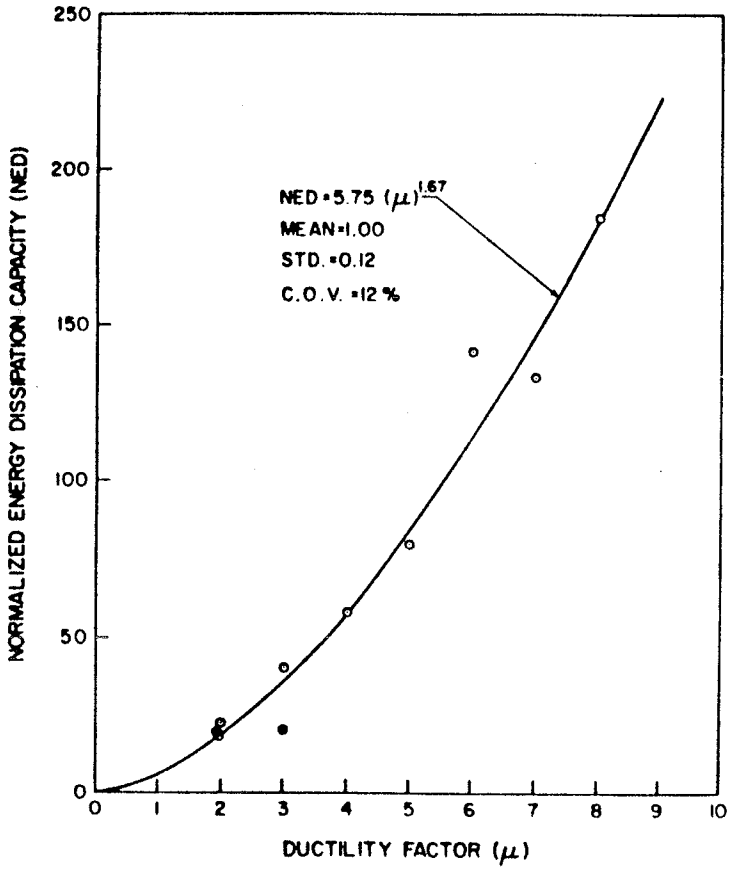

Fig. 5.17 THE RELATIONSHIP BETWEEN THE NORMALIZED ENERGY DISSIPATION CAPACITY AND DUCTILITY FACTOR

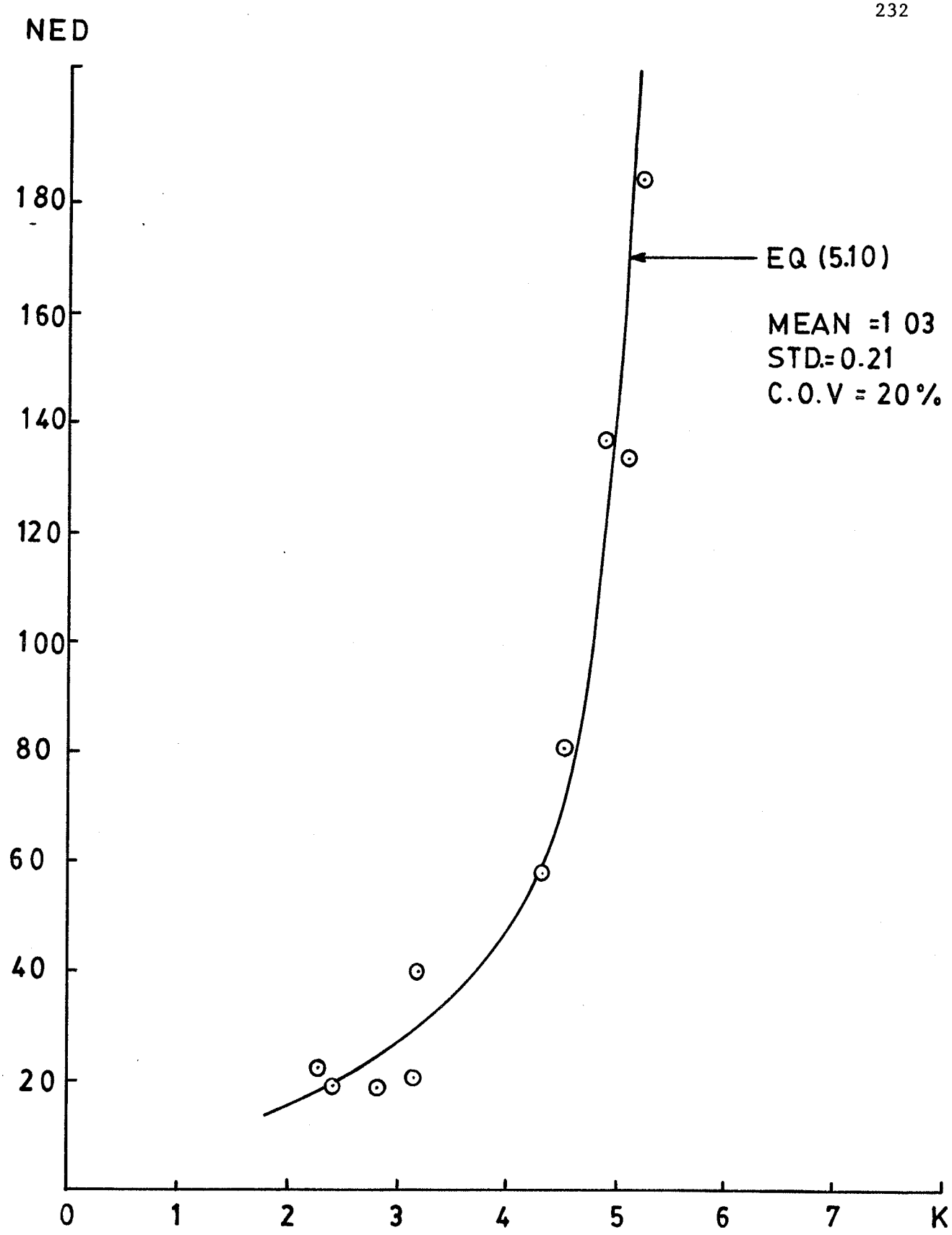

Fig. 5.18 THE RELATIONSHIP BETWEEN THE NORMALIZED ENERGY DISSIPATION, NED, AND THE CHARACTERISTIC FACTOR, K

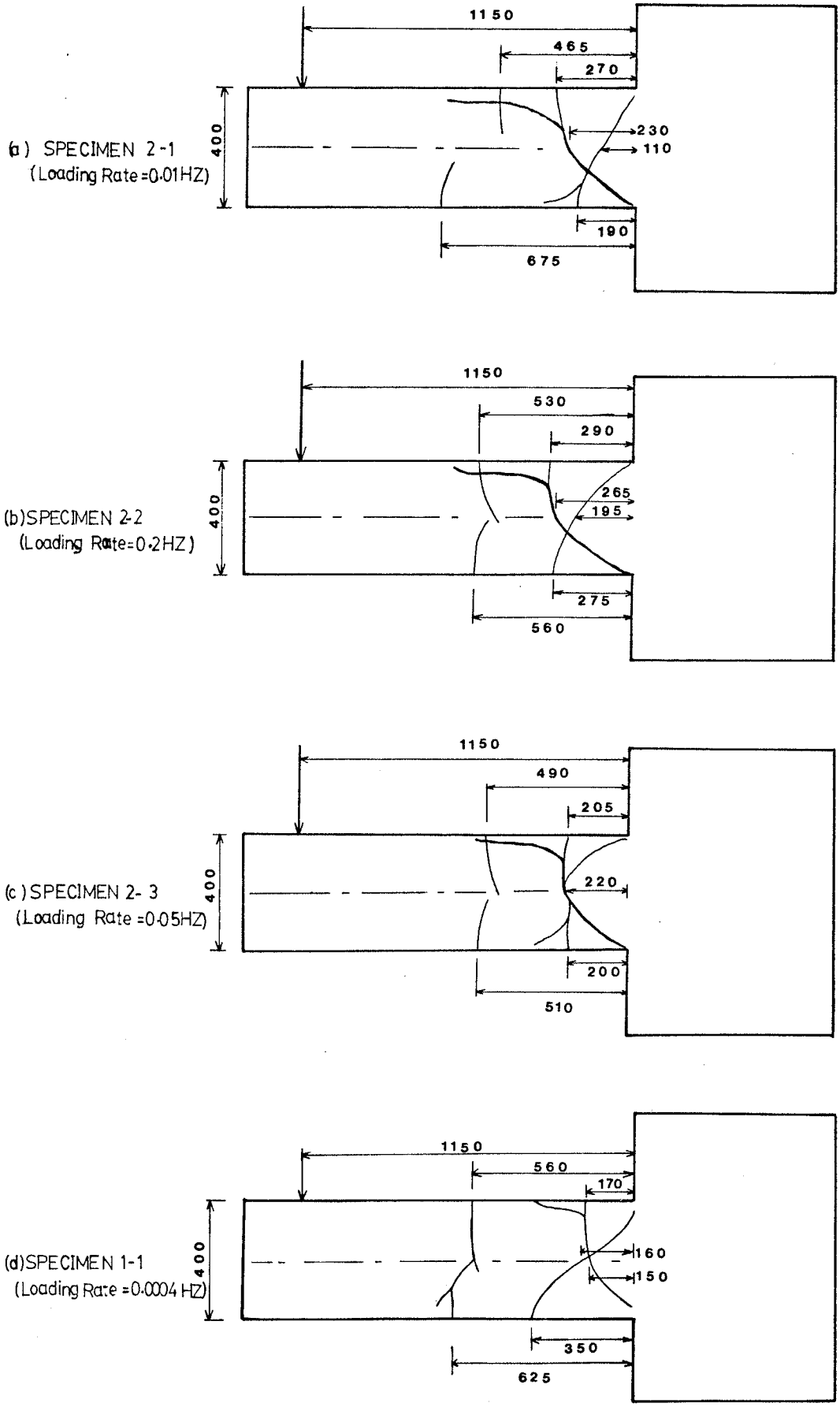

Fig. 5.19. EFFECT OF RATE OF LOADING ON CRACK PATTERN FOR SPECIMEN WITH a/d = 3.29.

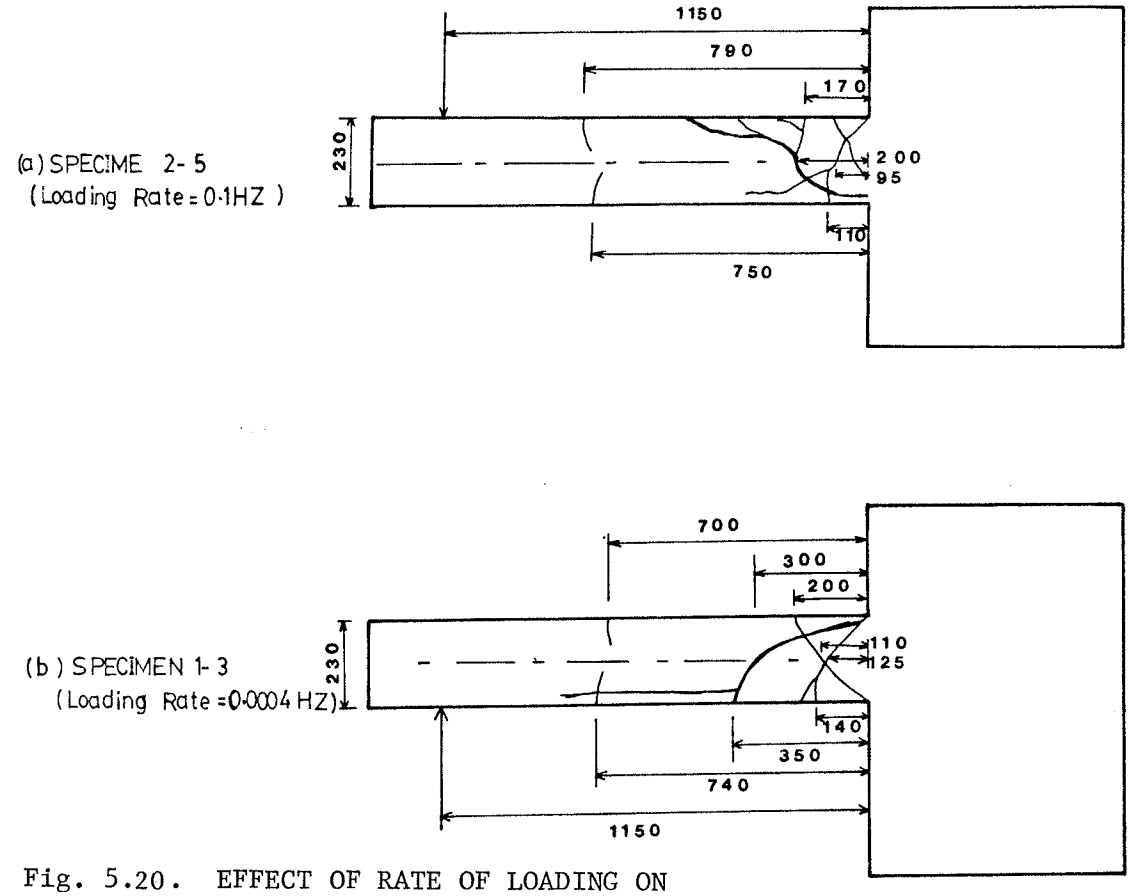

Fig. 5.20. EFFECT OF RATE OF LOADING ON CRACK PATTERN FOR SPECIMEN WITH a/d = 6.05.

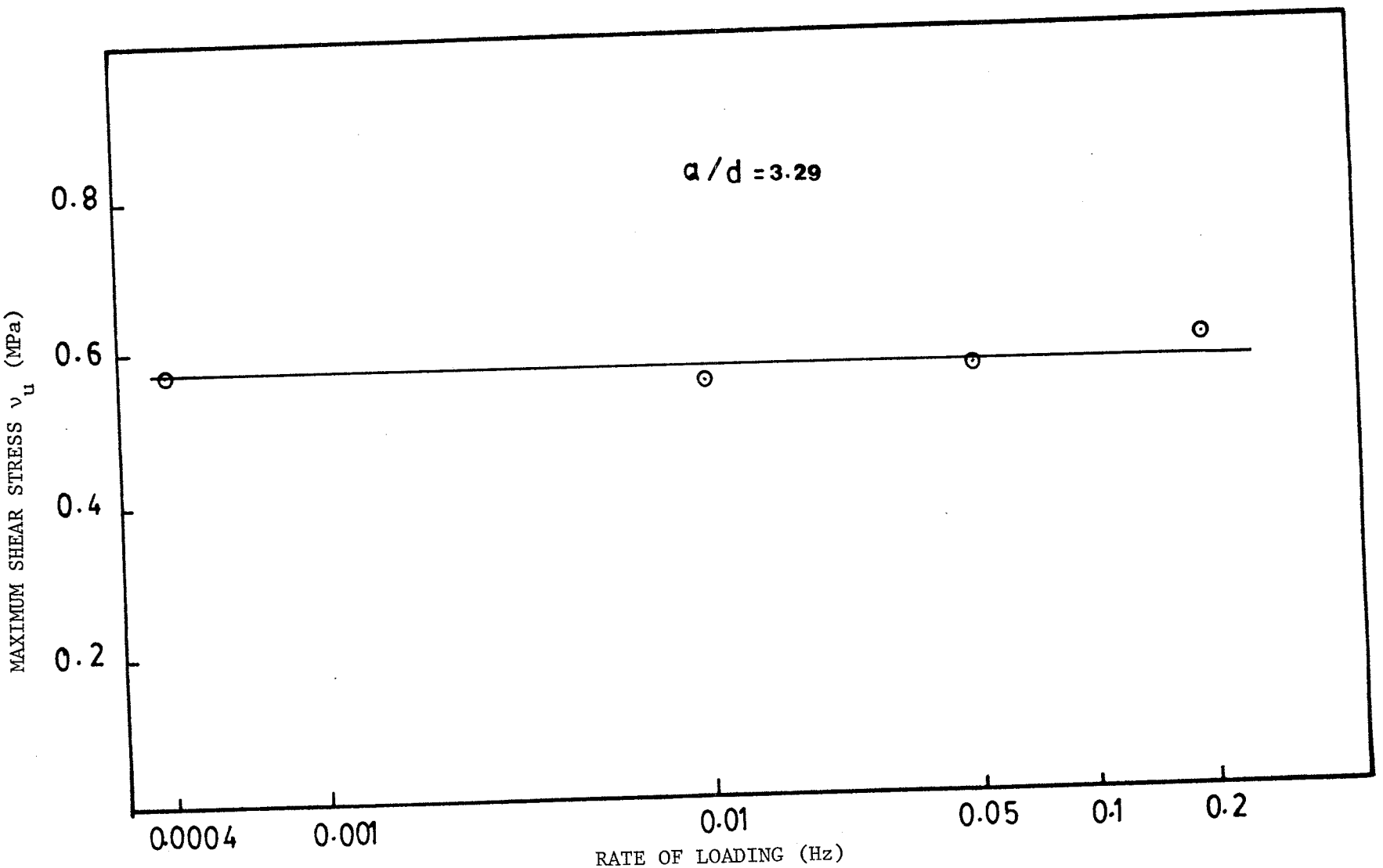

Fig. 5.21. EFFECT OF RATE OF LOADING ON MAXIMUM SHEAR STRENGTH, ν_u.

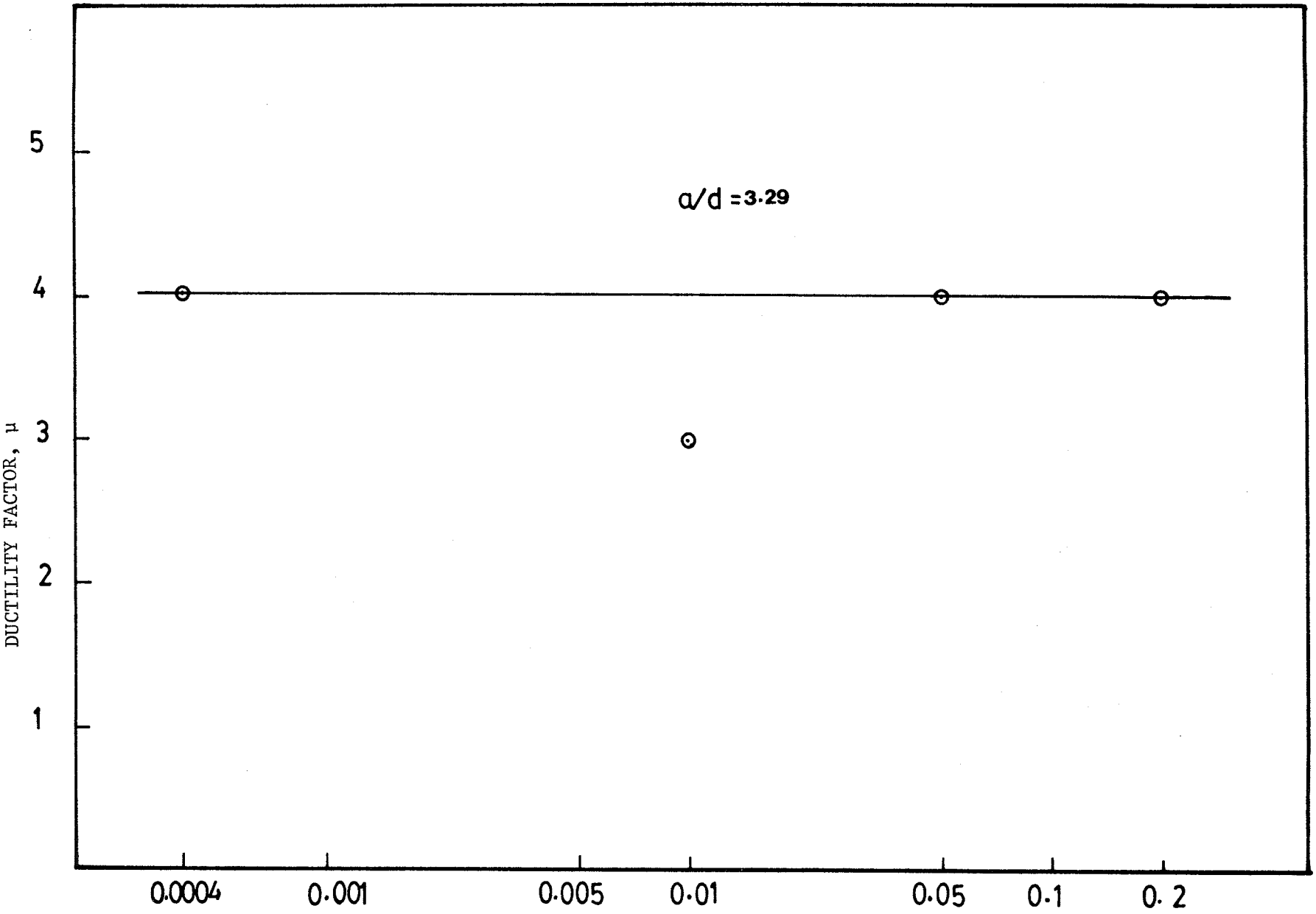

Fig. 5.22. EFFECT OF RATE OF LOADING ON DUCTILITY FACTOR, μ.

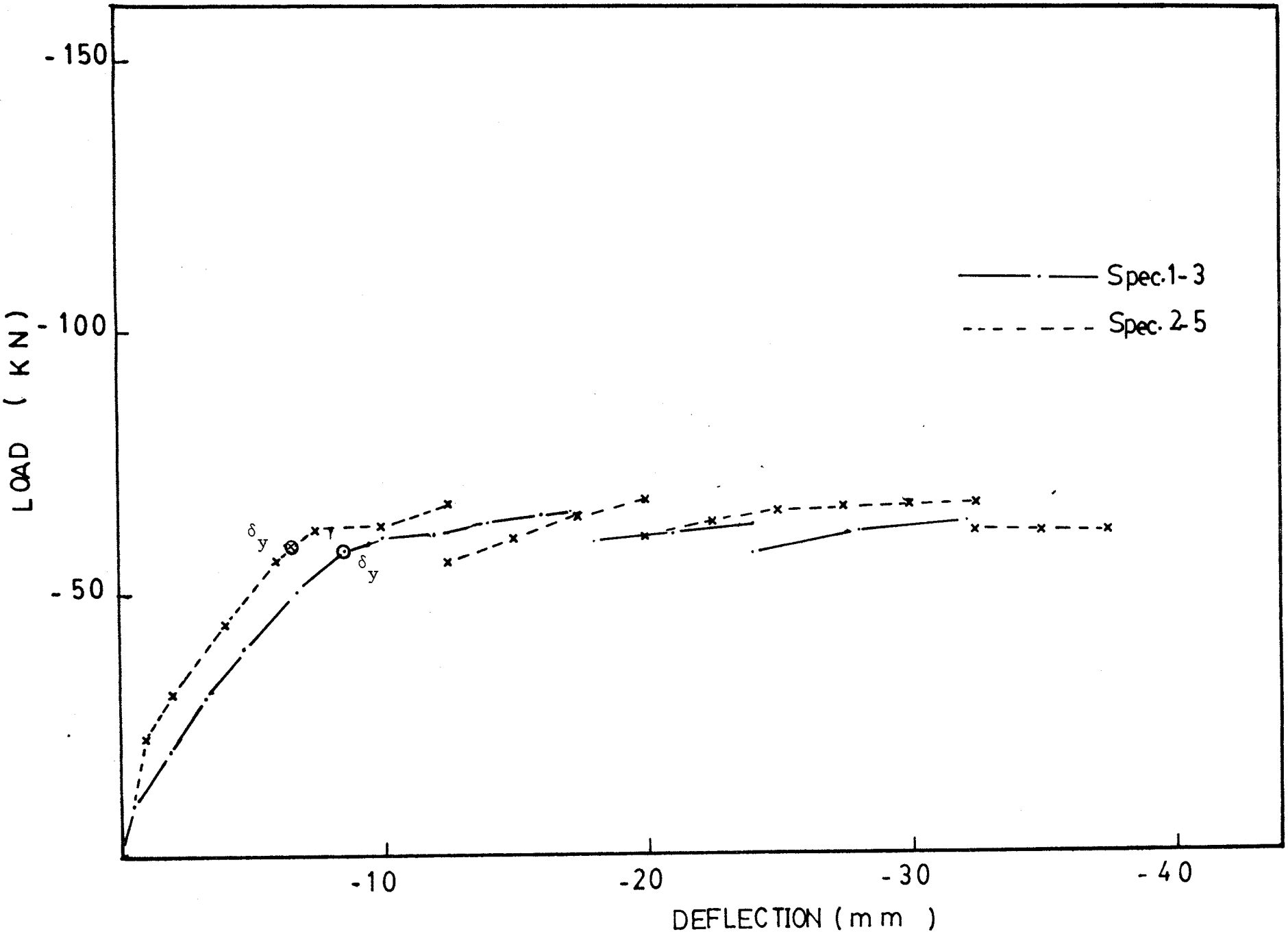

Fig. 5.2.3 COMPARISON BETWEEN LOAD-DEFLECTION CURVES OF SPECIMENS 1-3 AND 1-5.

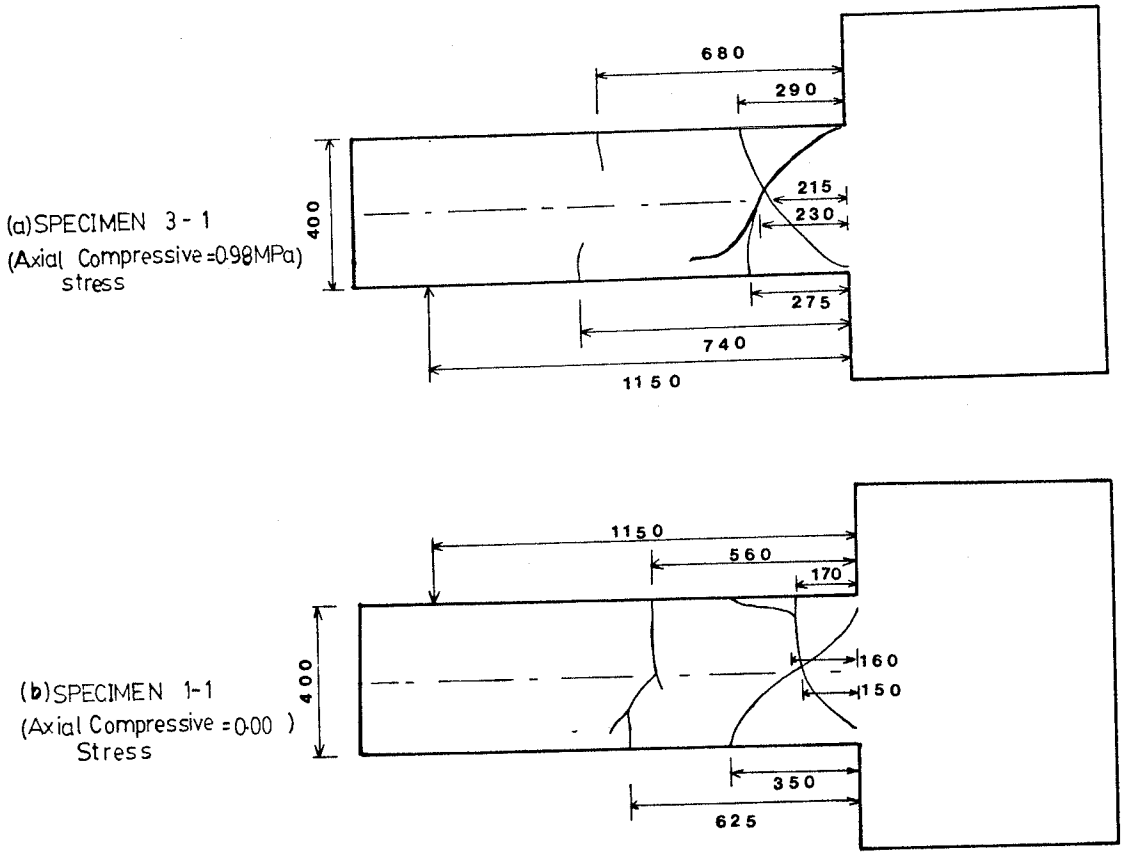

Fig. 5.24. EFFECT OF AXIAL COMPRESSIVE STRESS ON CRACK PATTERN FOR SPECIMEN WITH a/d = 3.29.

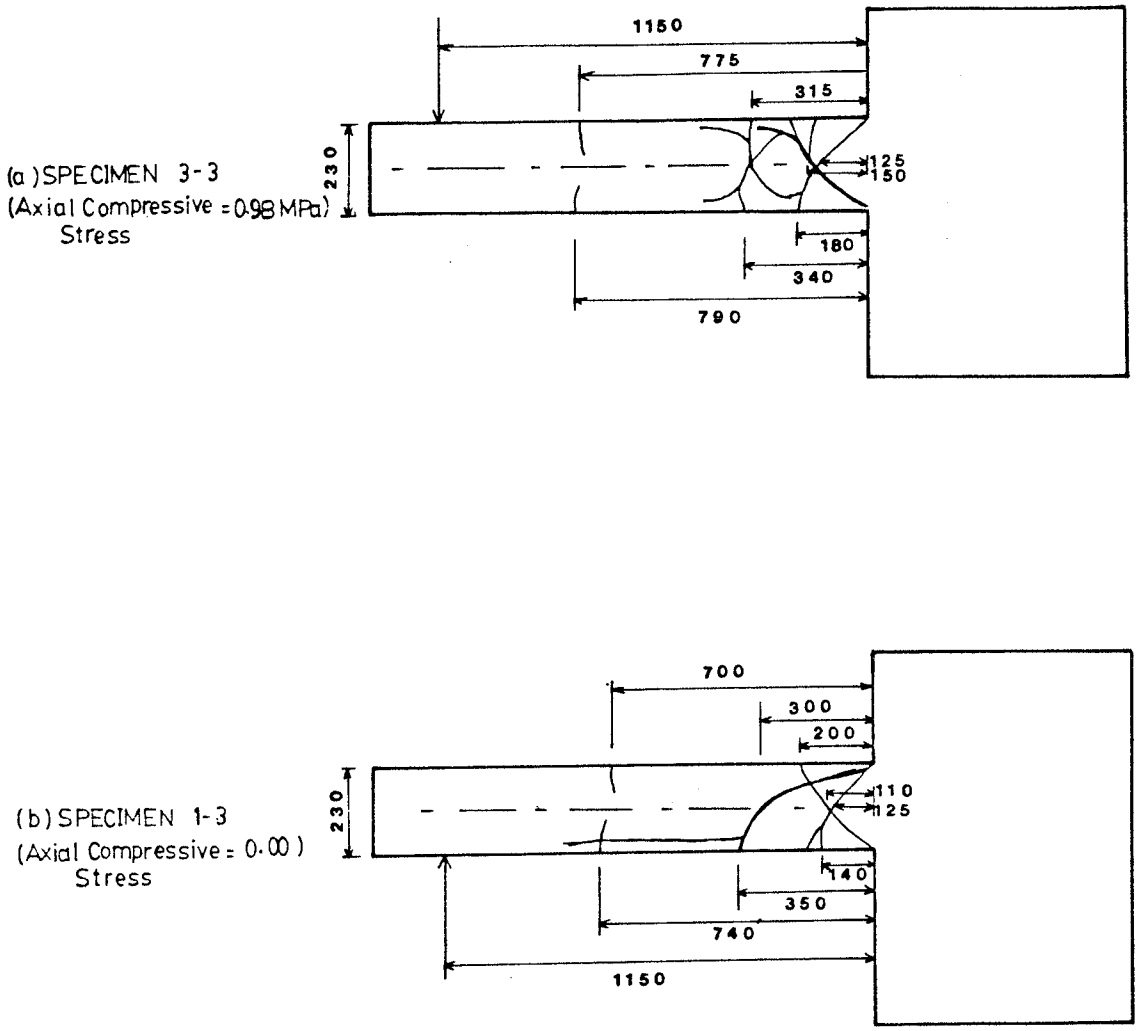

Fig. 5.25. EFFECT OF AXIAL COMPRESSIVE STRESS ON CRACK PATTERN FOR SPECIMEN WITH a/d = 6.05.

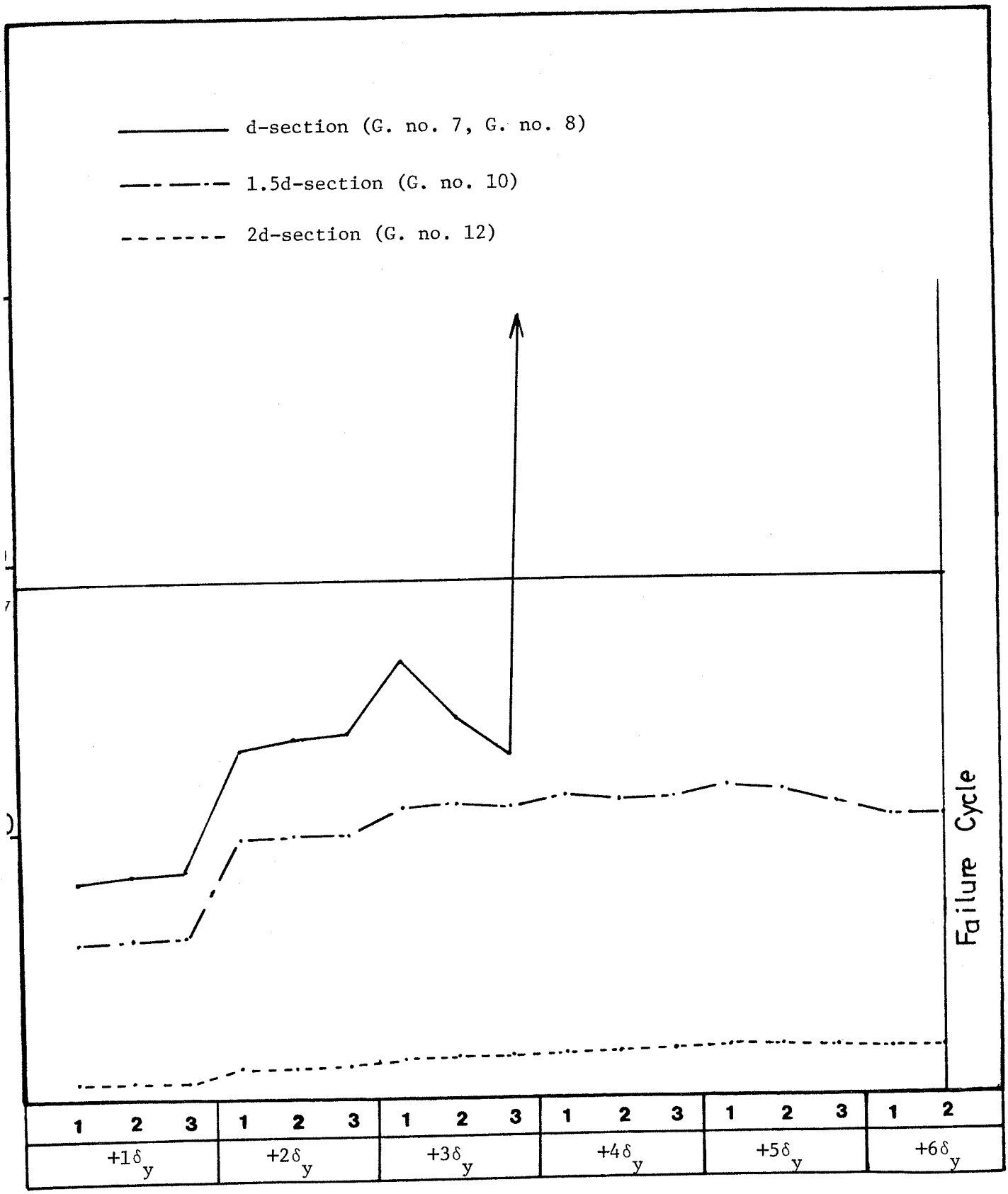

Fig. 5.26. STRAIN OF LONGITUDINAL REINFORCEMENT FOR SPECIMEN 3-1.

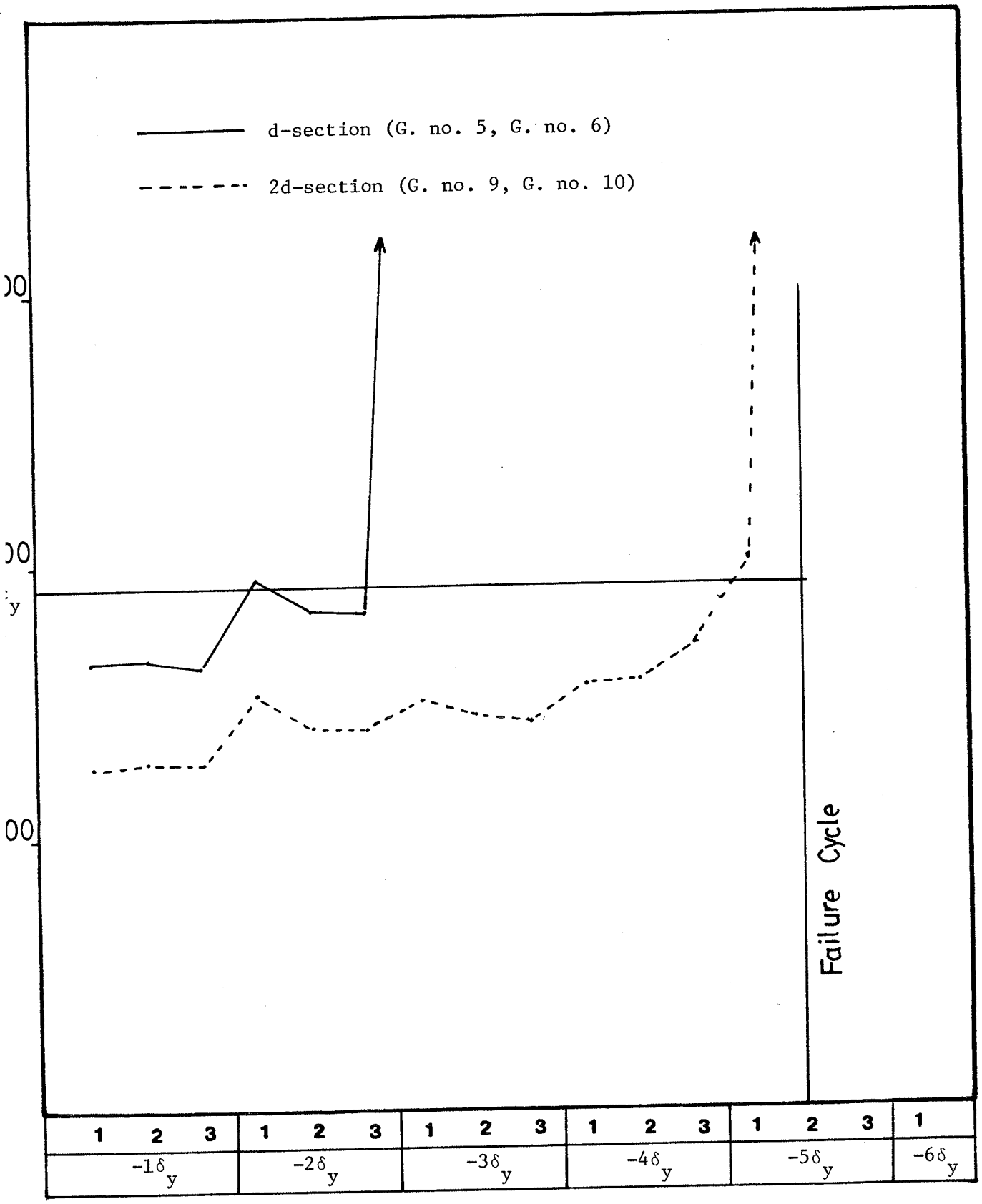

Fig. 5.27. STRAIN OF LONGITUDINAL REINFORCEMENT FOR SPECIMEN 3-3.

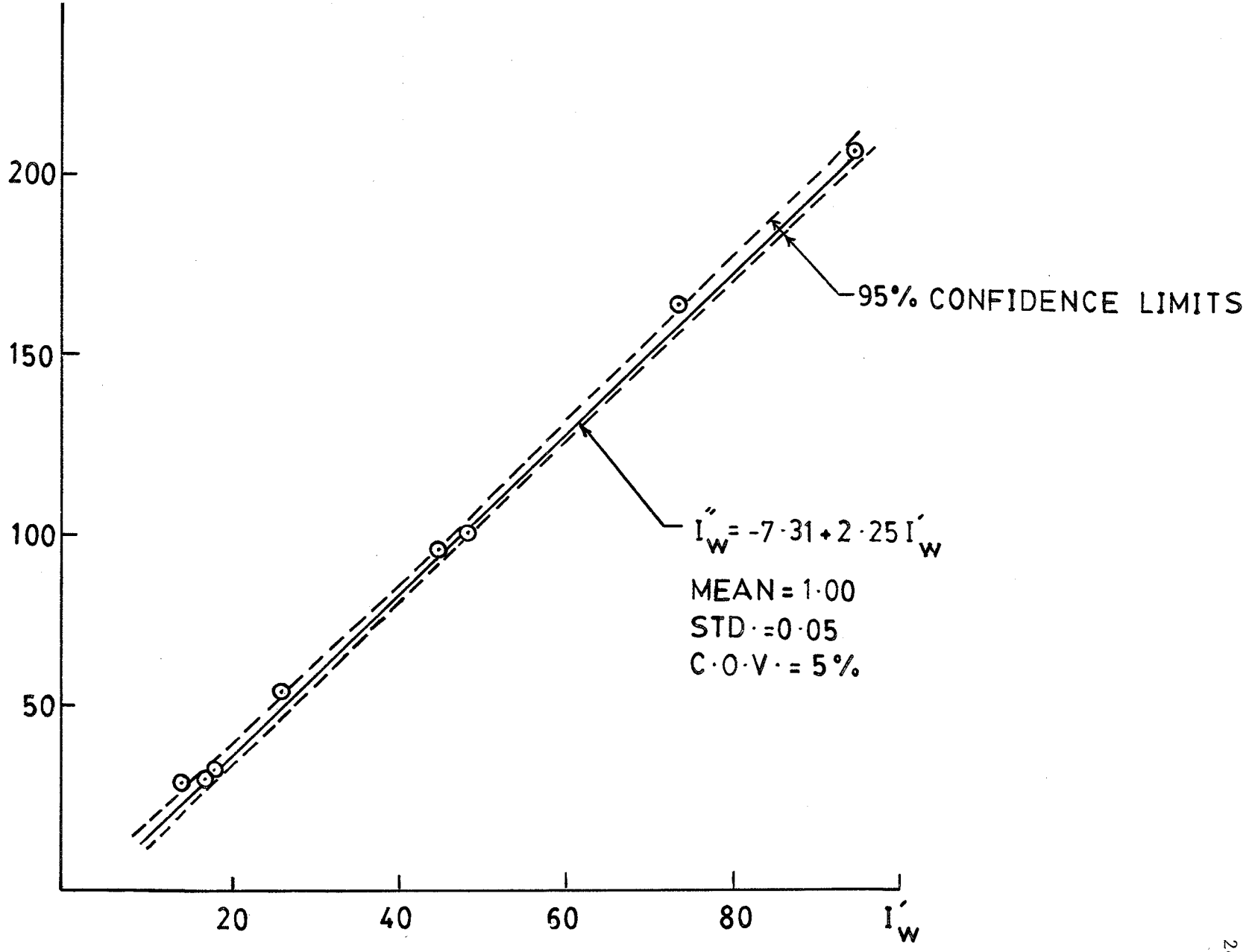

Fig 5.28 THE RELATIONSHIP BETWEEN THE MODIFIED WORK INDEX, I'_w, AND THE NONLINEAR WORK INDEX

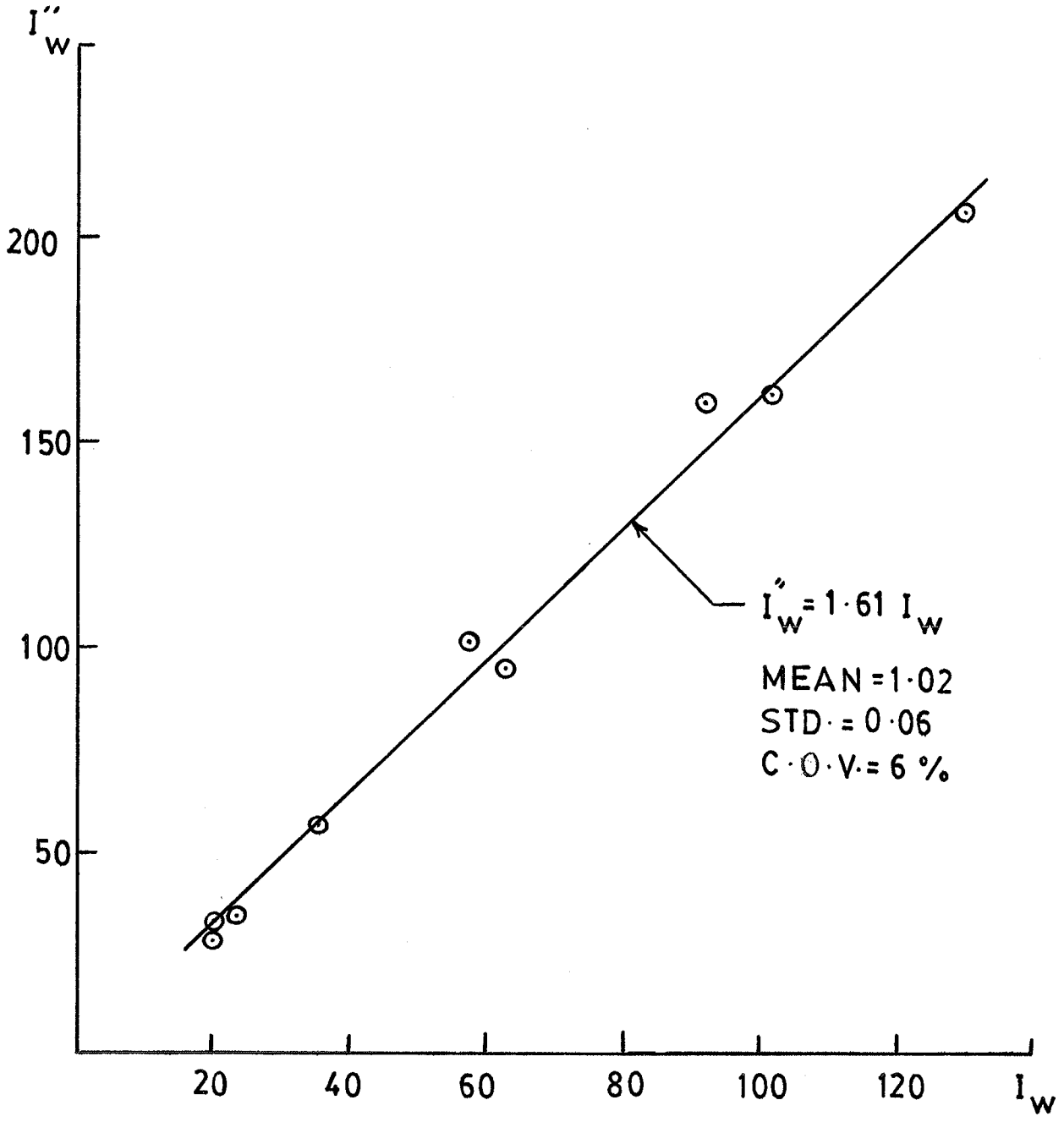

Fig. 5.29 THE RELATIONSHIP BETWEEN THE NONLINEAR WORK INDEX, I''_w, AND THE WORK INDEX, I_w

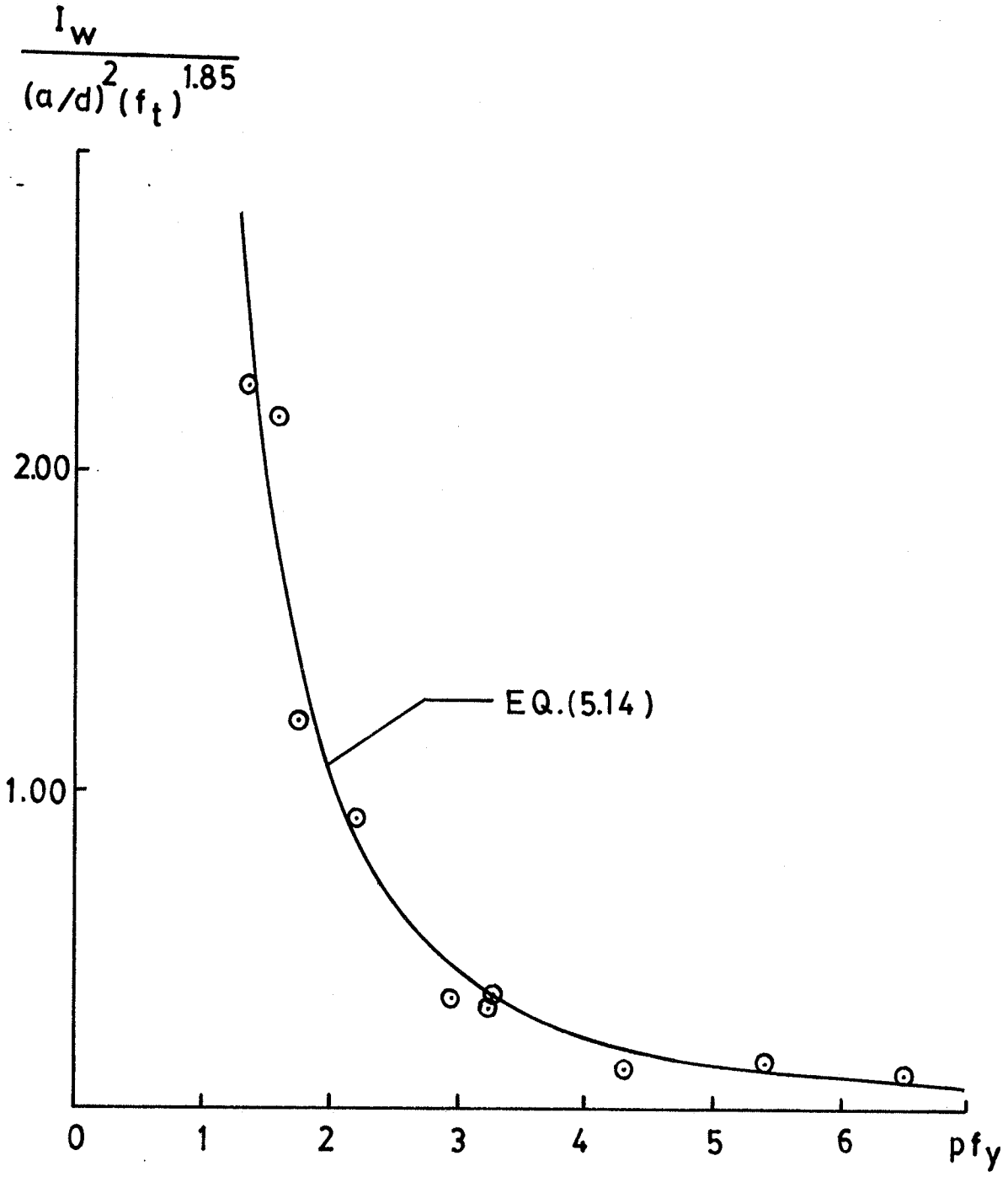

Fig. 5.30 THE EFFECT OF pf_y ON THE WORK INDEX

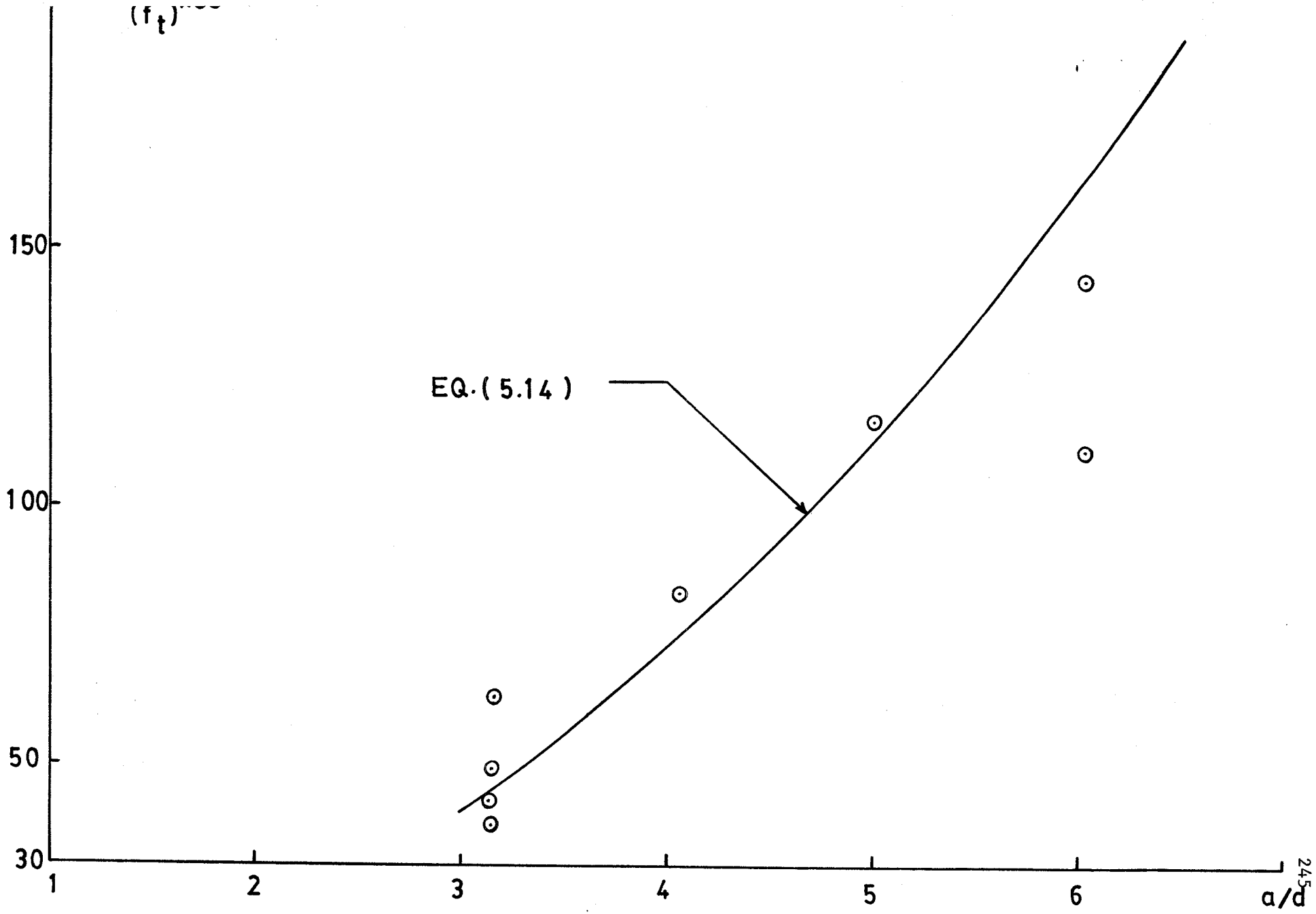

Fig. 5.31 THE EFFECT OF a/d ON THE WORK INDEX

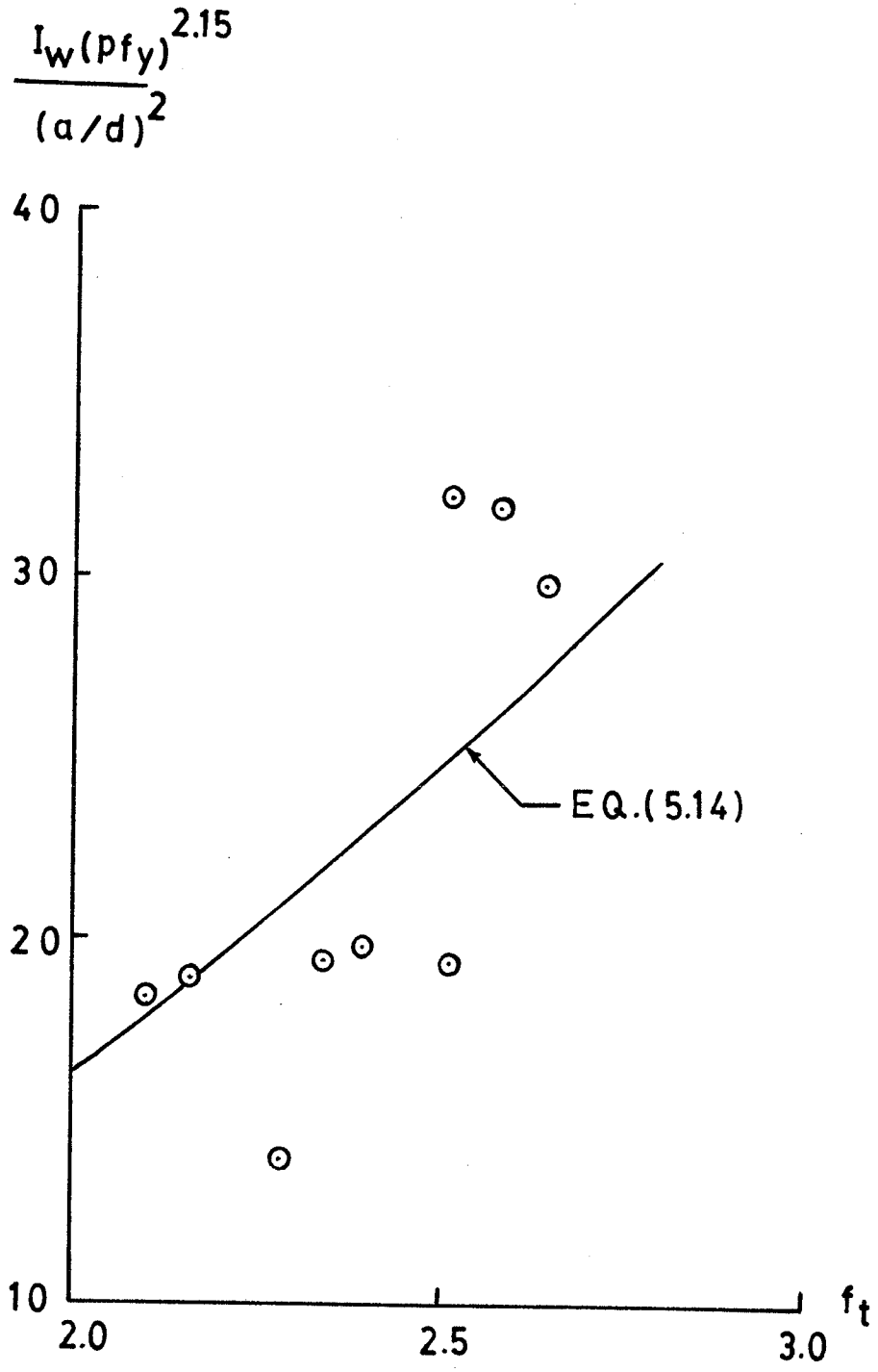

Fig. 5.32 THE EFFECT OF f_t ON THE WORK INDEX

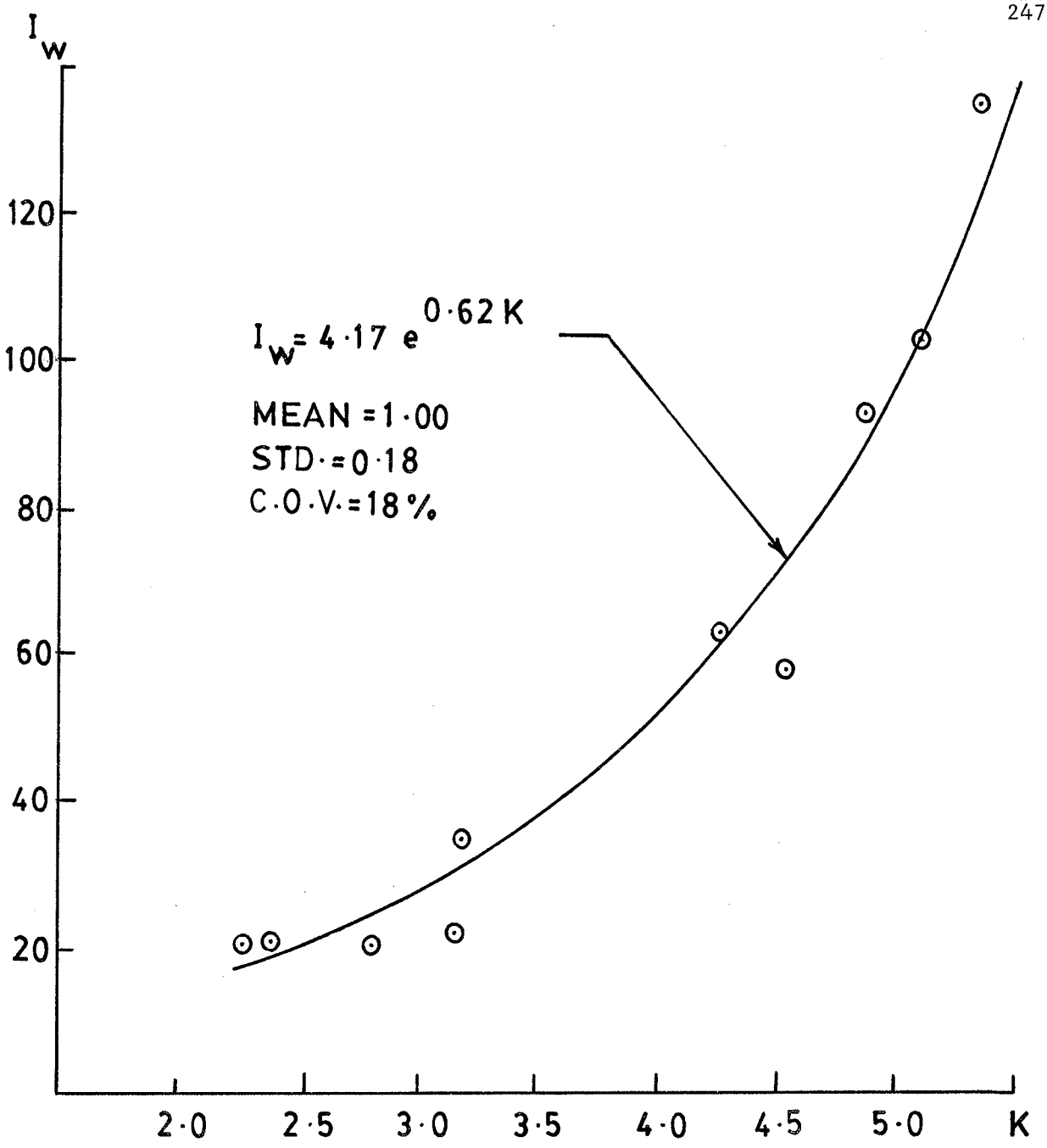

Fig. 5.33 THE RELATIONSHIP BETWEEN THE WORK INDEX, I_w, AND THE CHARACTERISTIC FACTOR, K

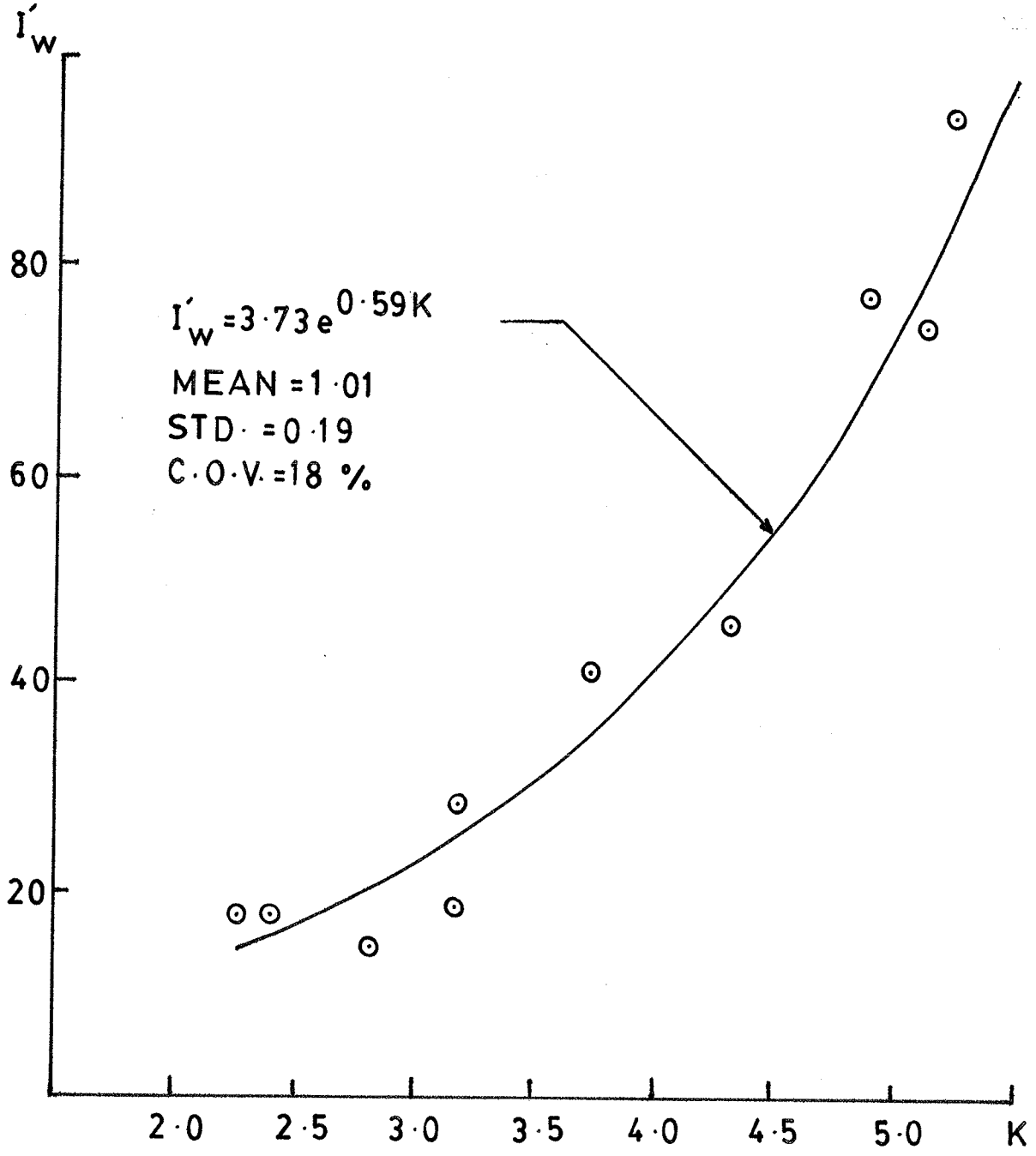

Fig. 5.34 THE RELATIONSHIP BETWEEN THE MODIFIED WORK INDEX, I_w', AND THE CHARACTERISTIC FACTOR, K

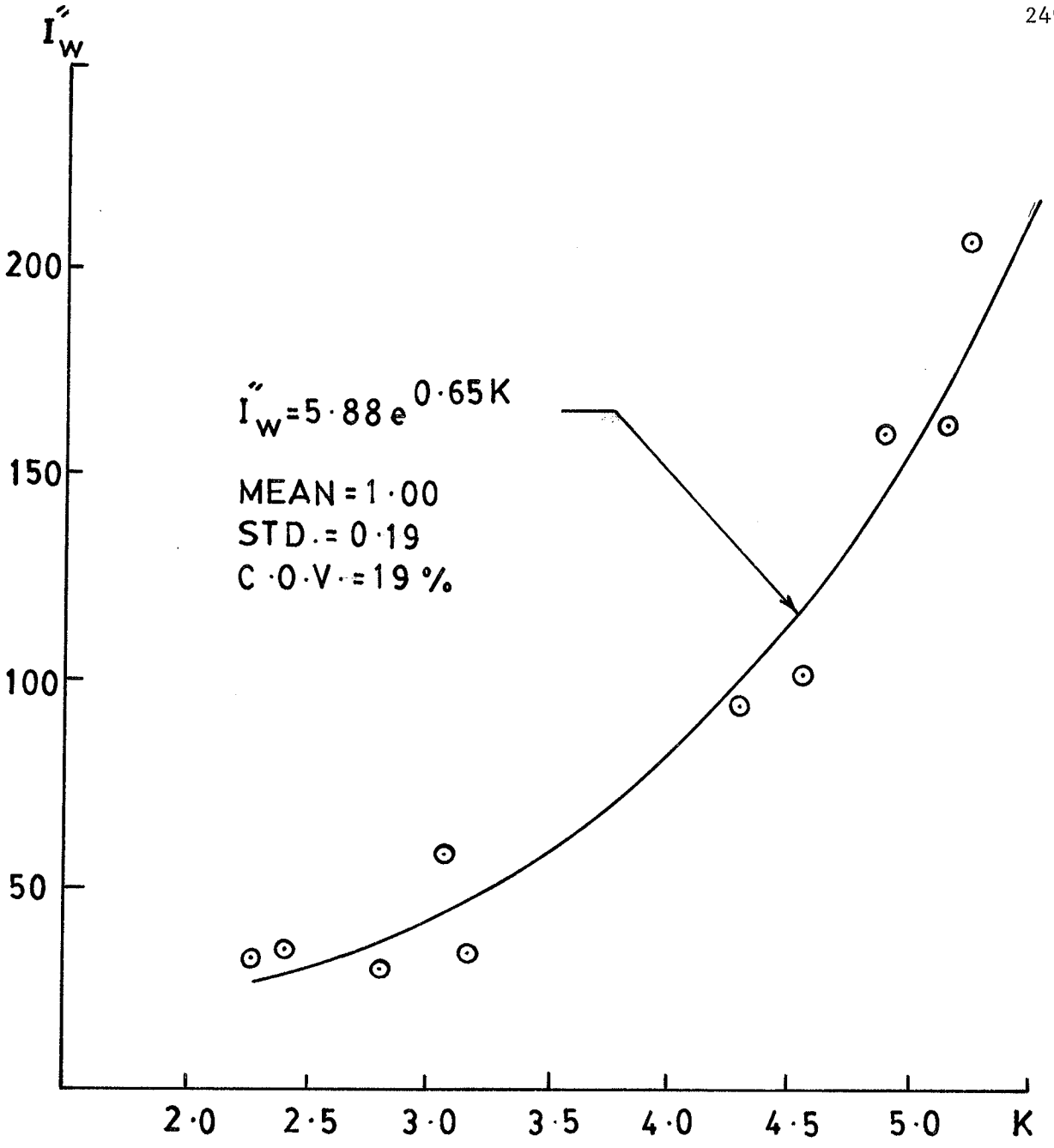

Fig. 5.35 THE RELATIONSHIP BETWEEN THE NONLINEAR WORK INDEX, I''_W, AND THE CHARACTERISTIC FACTOR, K

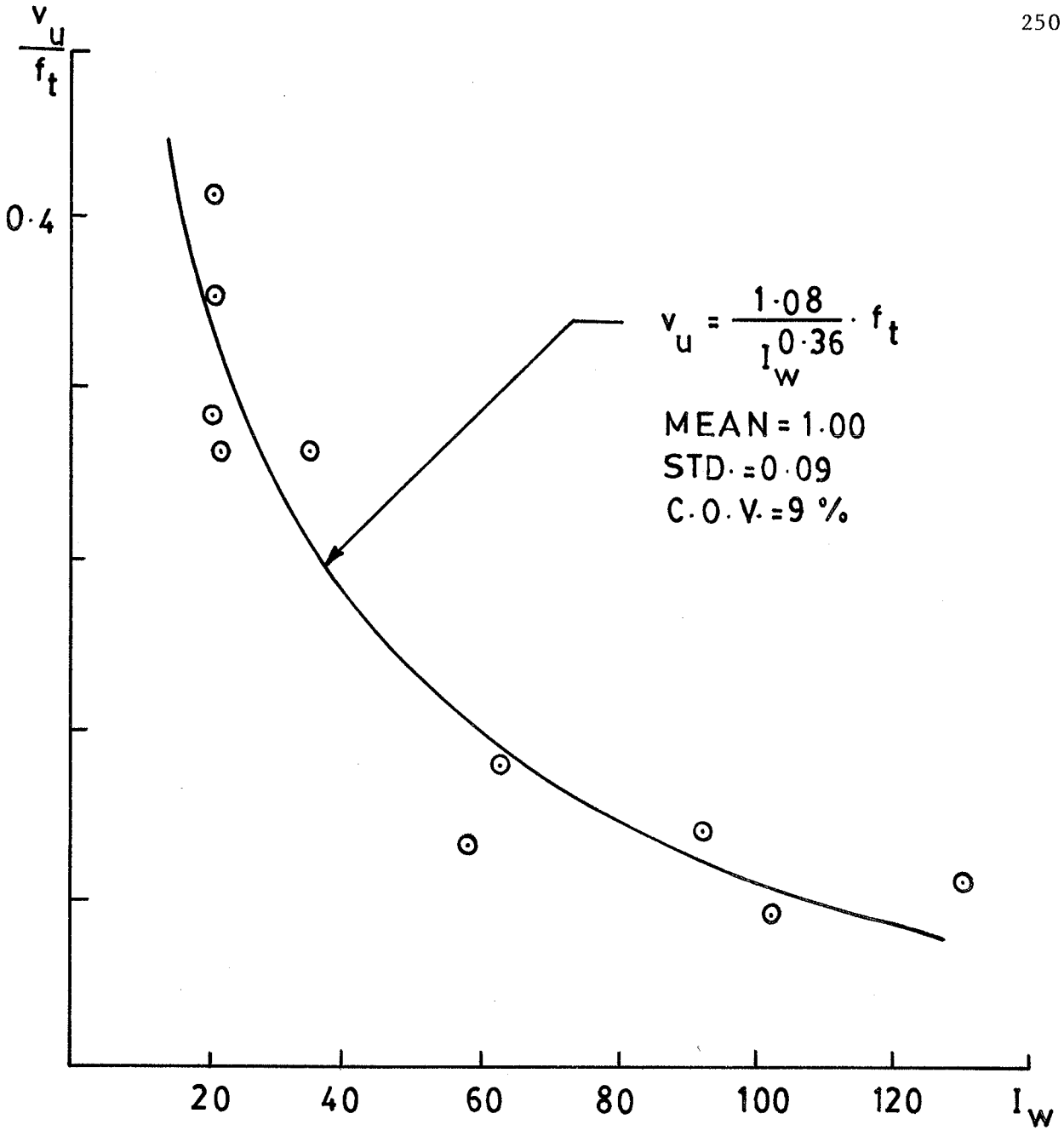

Fig. 5.36 THE RELATIONSHIP BETWEEN THE NORMALIZED MAXIMUM SHEAR STRESS, $\frac{v_u}{f_t}$, AND THE WORK INDEX, I_w

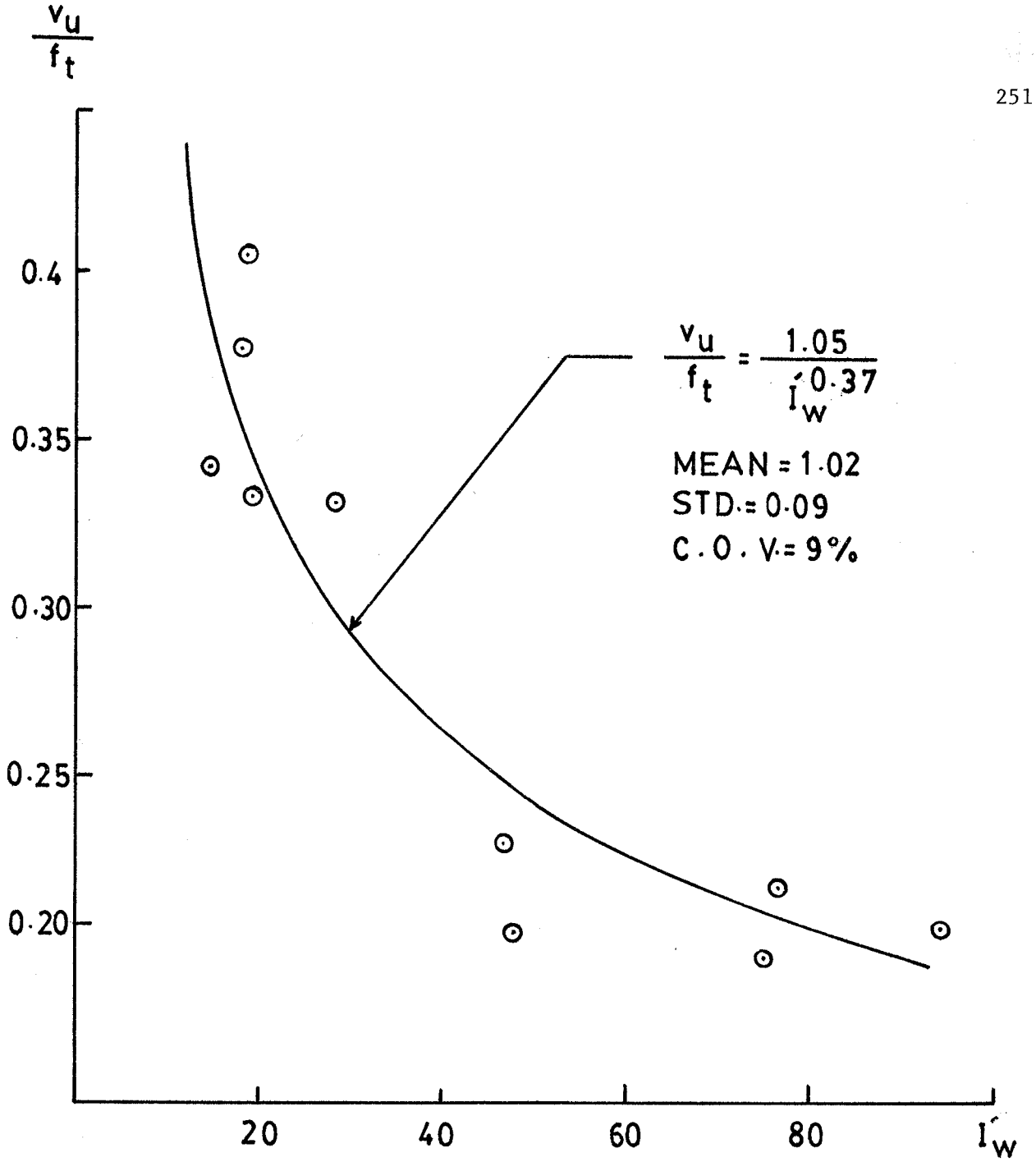

Fig. 5.37 THE RELATIONSHIP BETWEEN THE NORMALIZED MAXIMUM SHEAR STRESS, $\frac{v_u}{f_t}$, AND THE MODIFIED WORK INDEX, I_w'

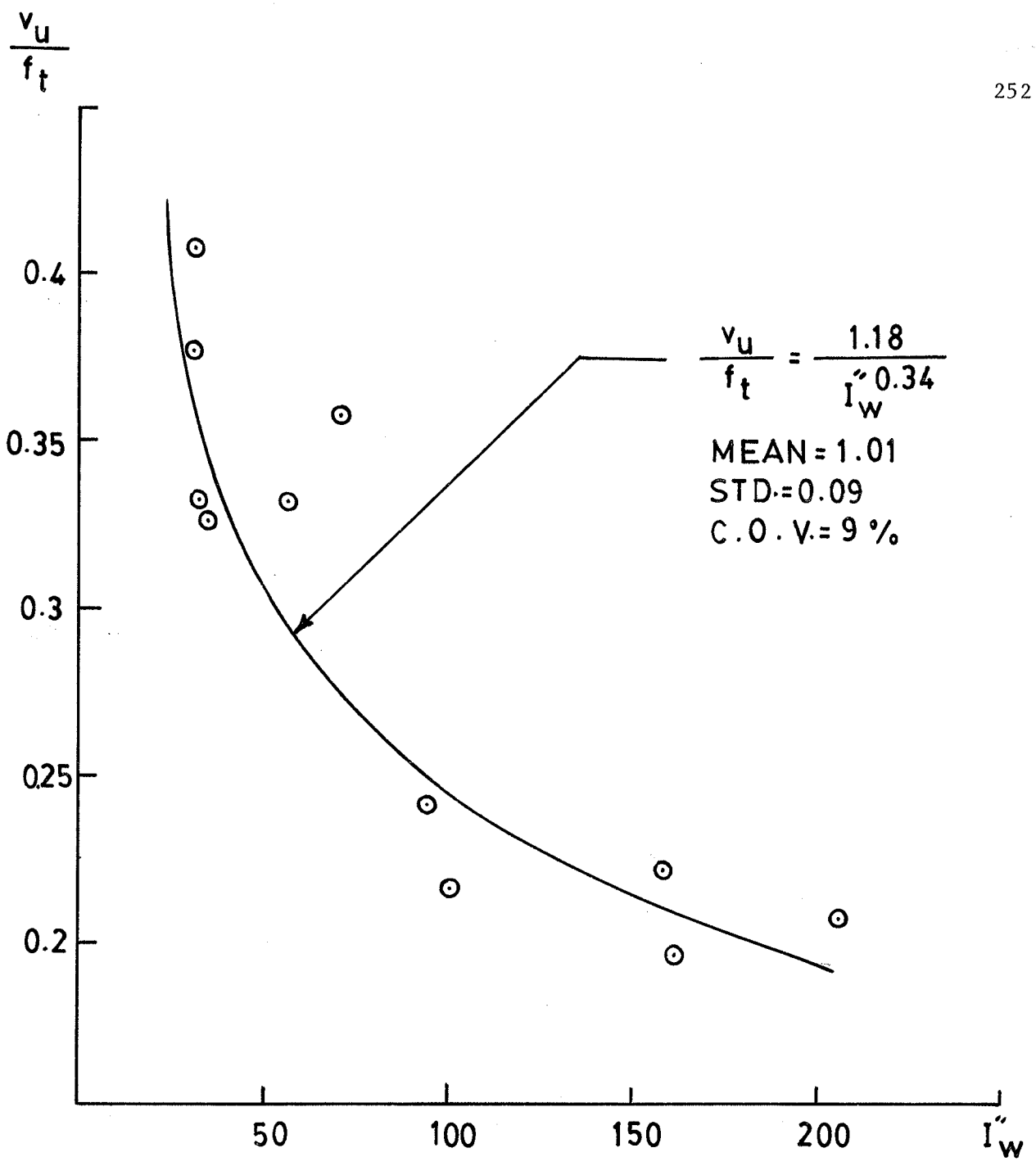

Fig. 5.38 THE RELATIONSHIP BETWEEN THE NORMALIZED MAXIMUM SHEAR STRESS, $\frac{v_u}{f_t}$, AND THE NONLINEAR WORK INDEX, I''_w

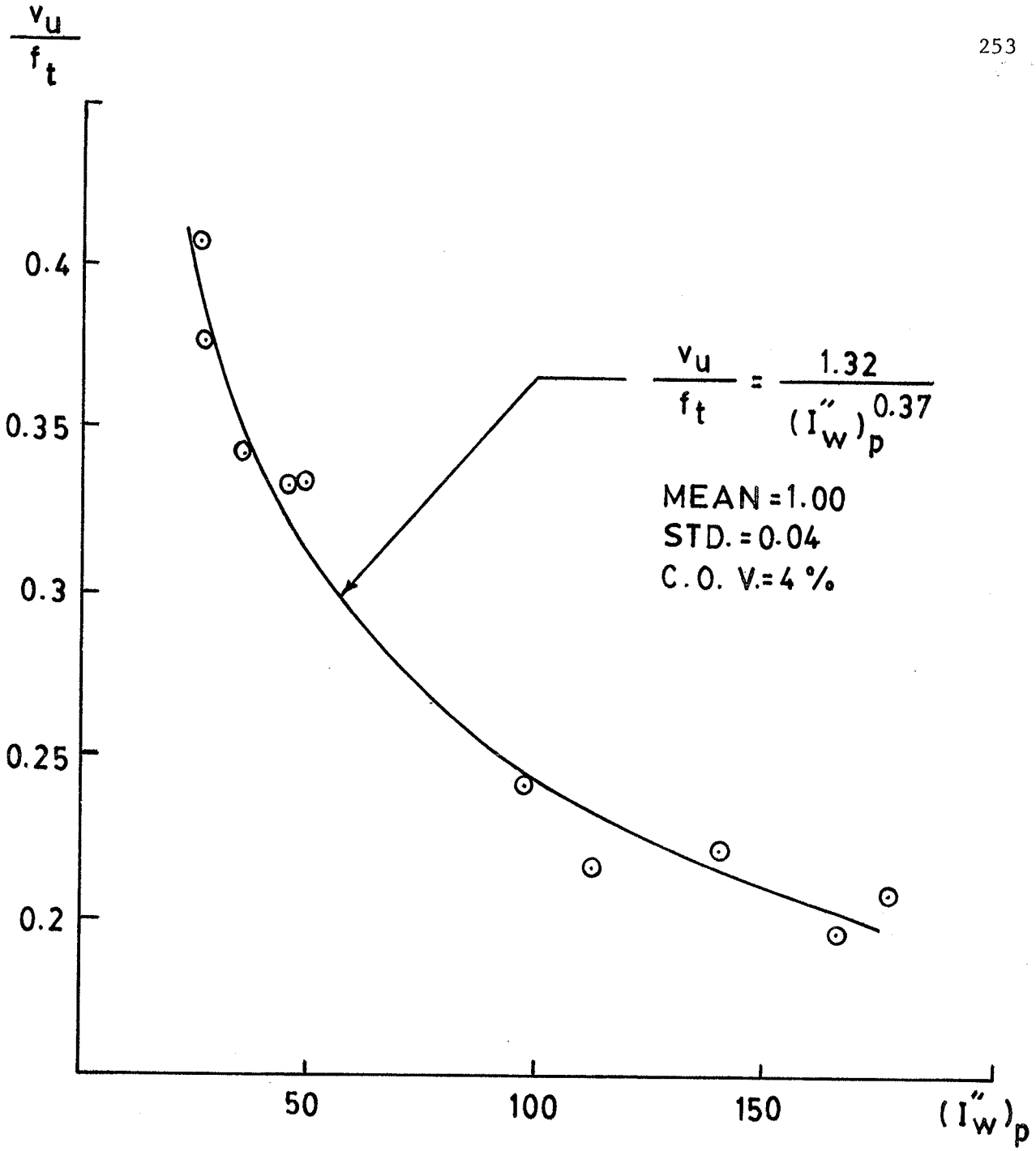

Fig. 5.39 THE RELATIONSHIP BETWEEN THE NORMALIZED MAXIMUM SHEAR STRESS, $\frac{v_u}{f_t}$, AND THE PREDICTED NONLINEAR WORK INDEX, $(I''_w)_p$

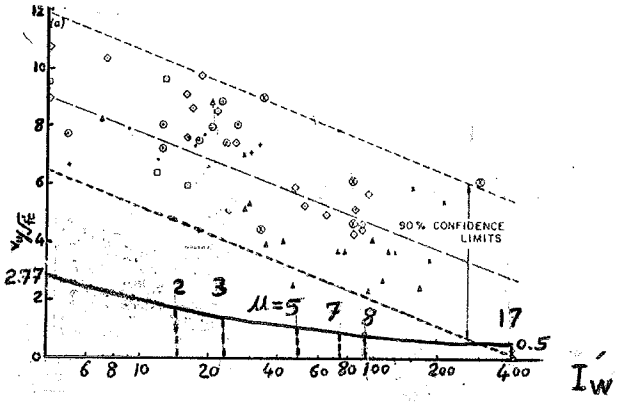

Fig. 5.40 THE COMPARISON BETWEEN THE PROPOSED EQ. (5.19) FOR BRIDGE PIERS WITHOUT WEB REINFORCEMENT AND THE EXPERIMENTAL RESULTS REPORTED FOR THE SPECIMENS WITH WEB REINFORCEMENT [15]

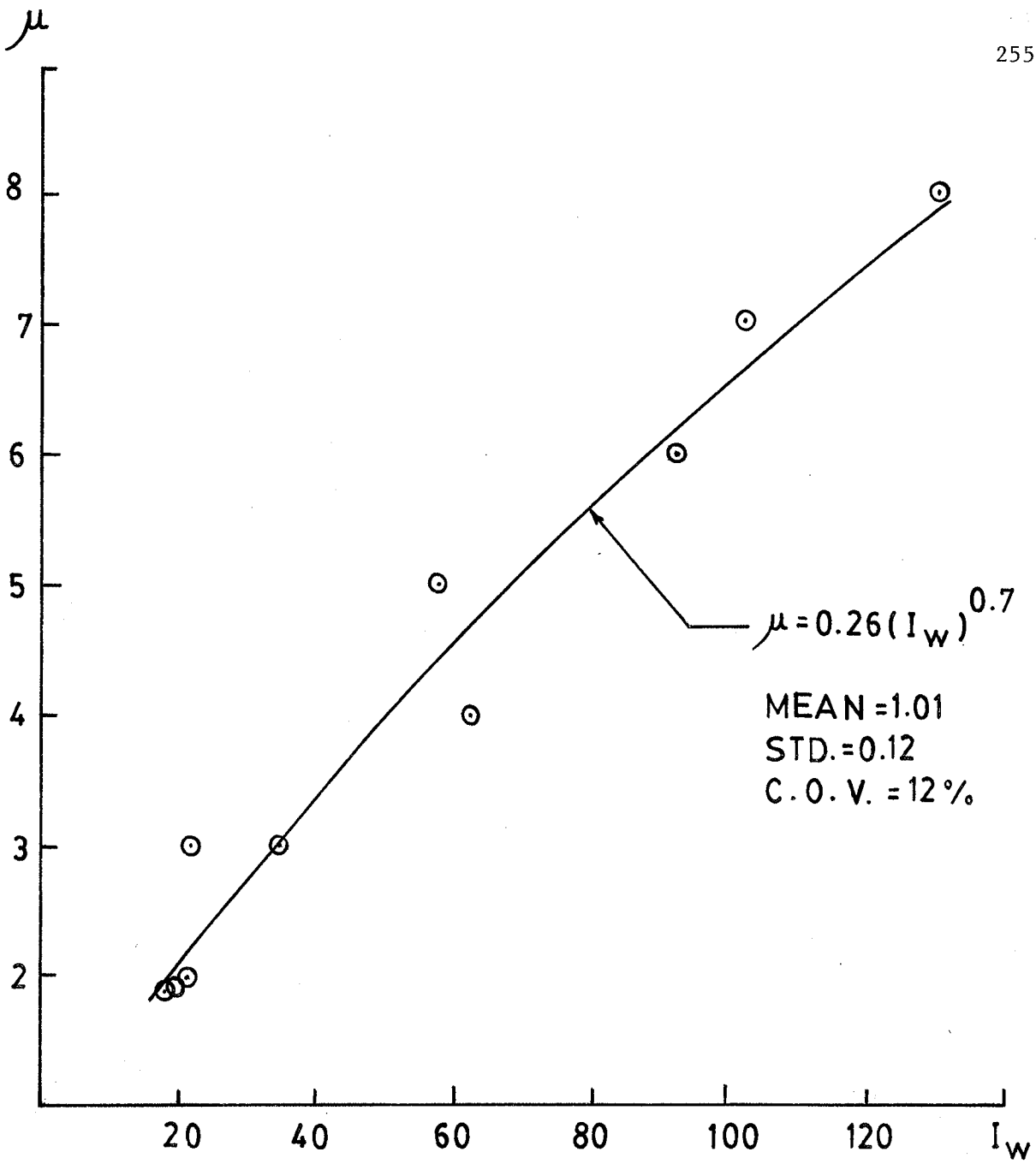

Fig. 5.41 THE RELATIONSHIP BETWEEN THE DUCTILITY FACTOR, μ, AND THE WORK INDEX, I_w

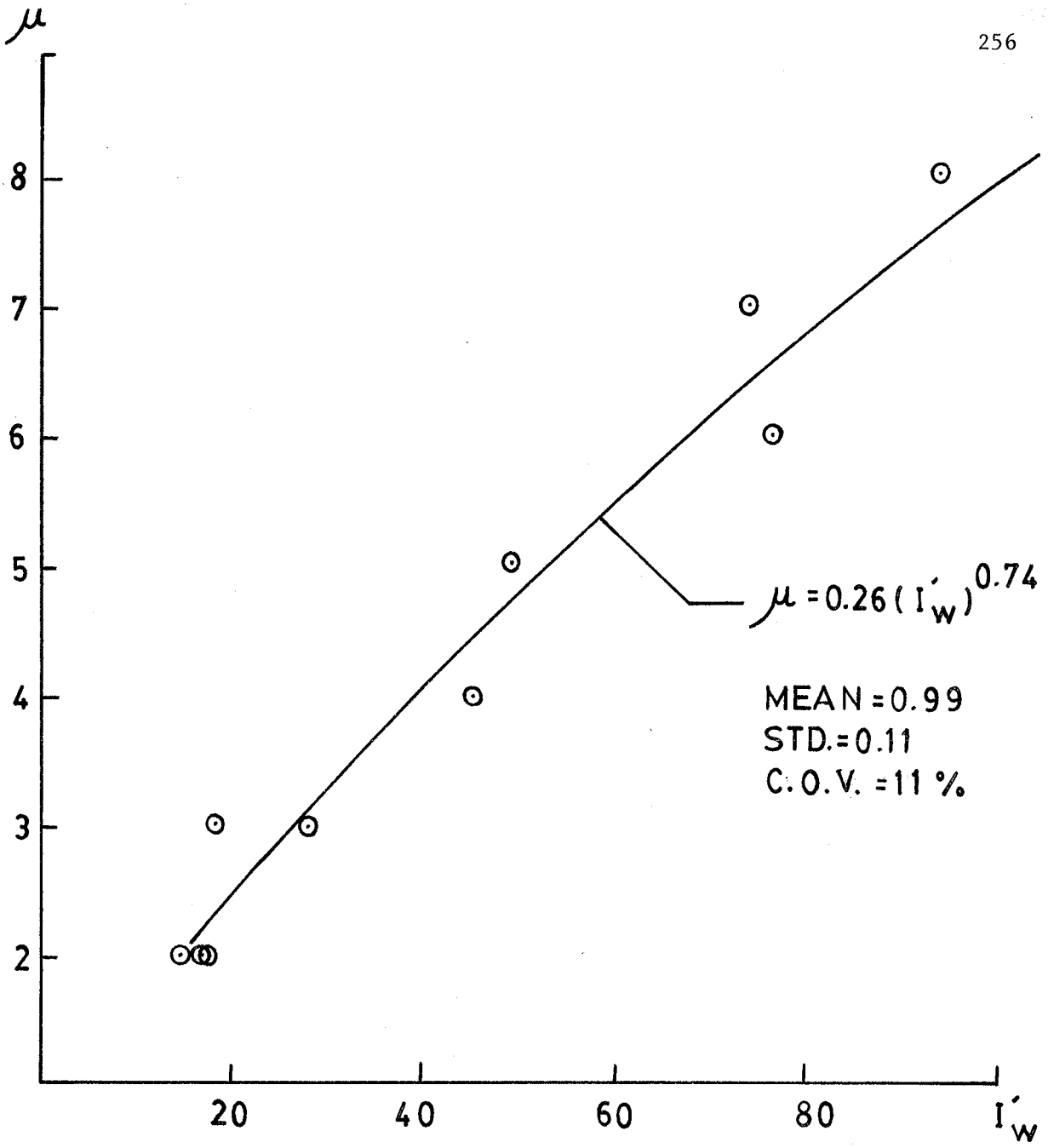

Fig. 5.42 THE RELATIONSHIP BETWEEN THE DUCTILITY FACTOR, μ, AND THE MODIFIED WORK INDEX, I_w'

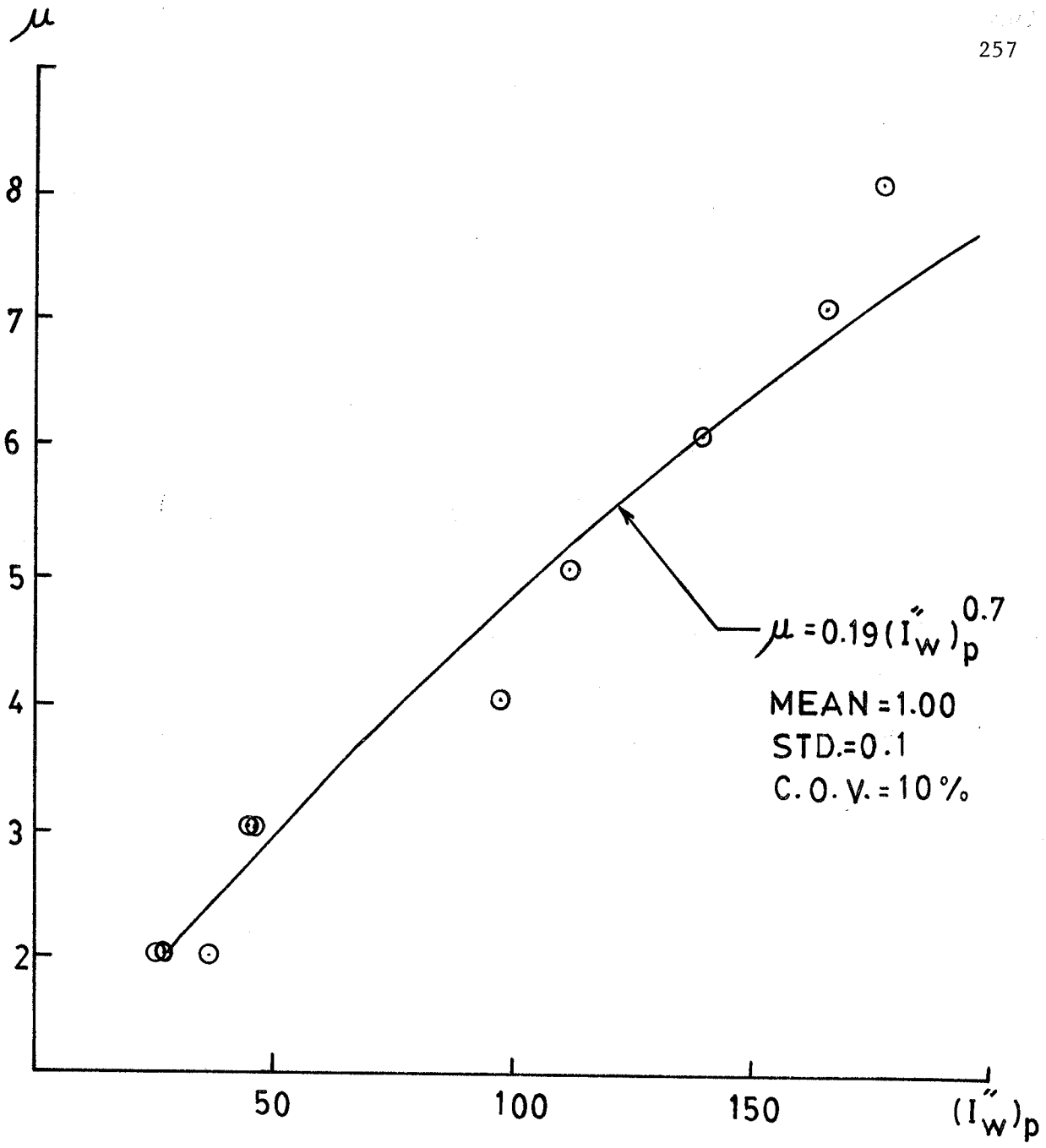

Fig. 5.43 THE RELATIONSHIP BETWEEN THE DUCTILITY FACTOR, μ, AND THE PREDICTED NONLINEAR WORK INDEX

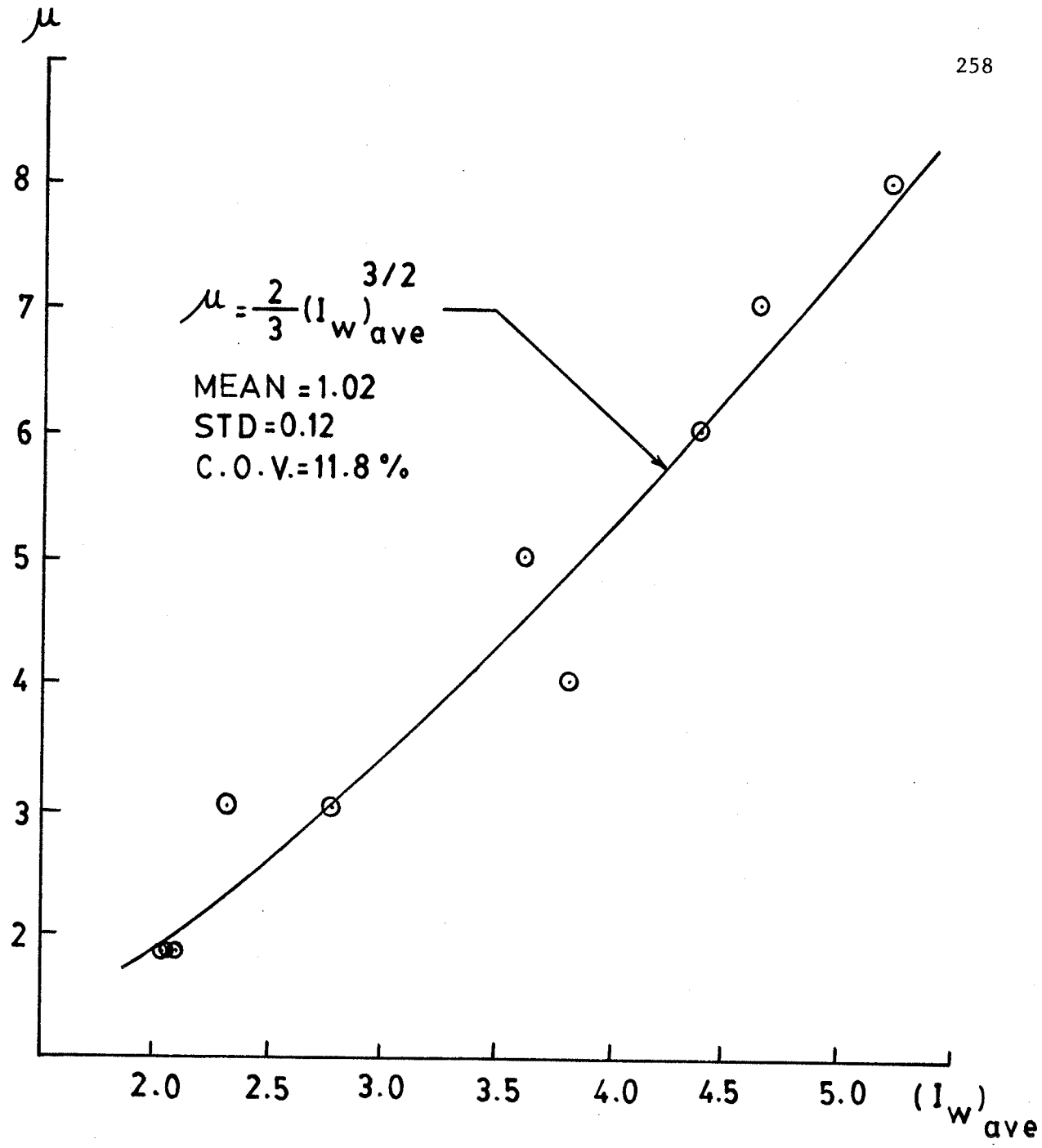

Fig. 5.44 THE RELATIONSHIP BETWEEN THE DUCTILITY FACTOR, μ, AND THE AVERAGE WORK INDEX, $(I_w)_{ave}$

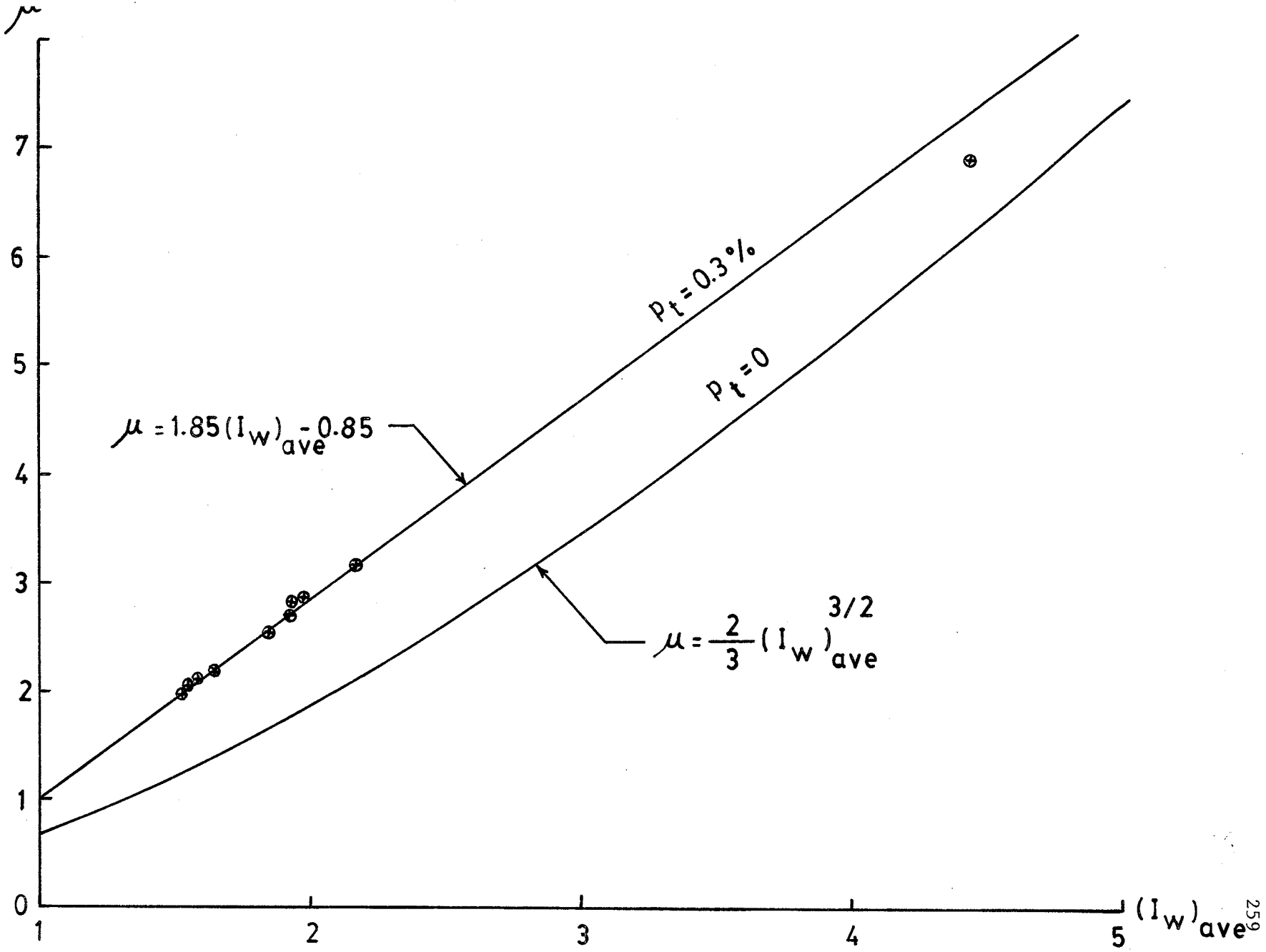

Fig. 5.45 THE COMPARISON BETWEEN THE TEST RESULTS REPORTED [3] FOR SPECIMENS WITH LIGHT TRANSVERSE REINFORCEMENT OF 0.3% AND THE PREDICTIONS OF EQ. 5.24

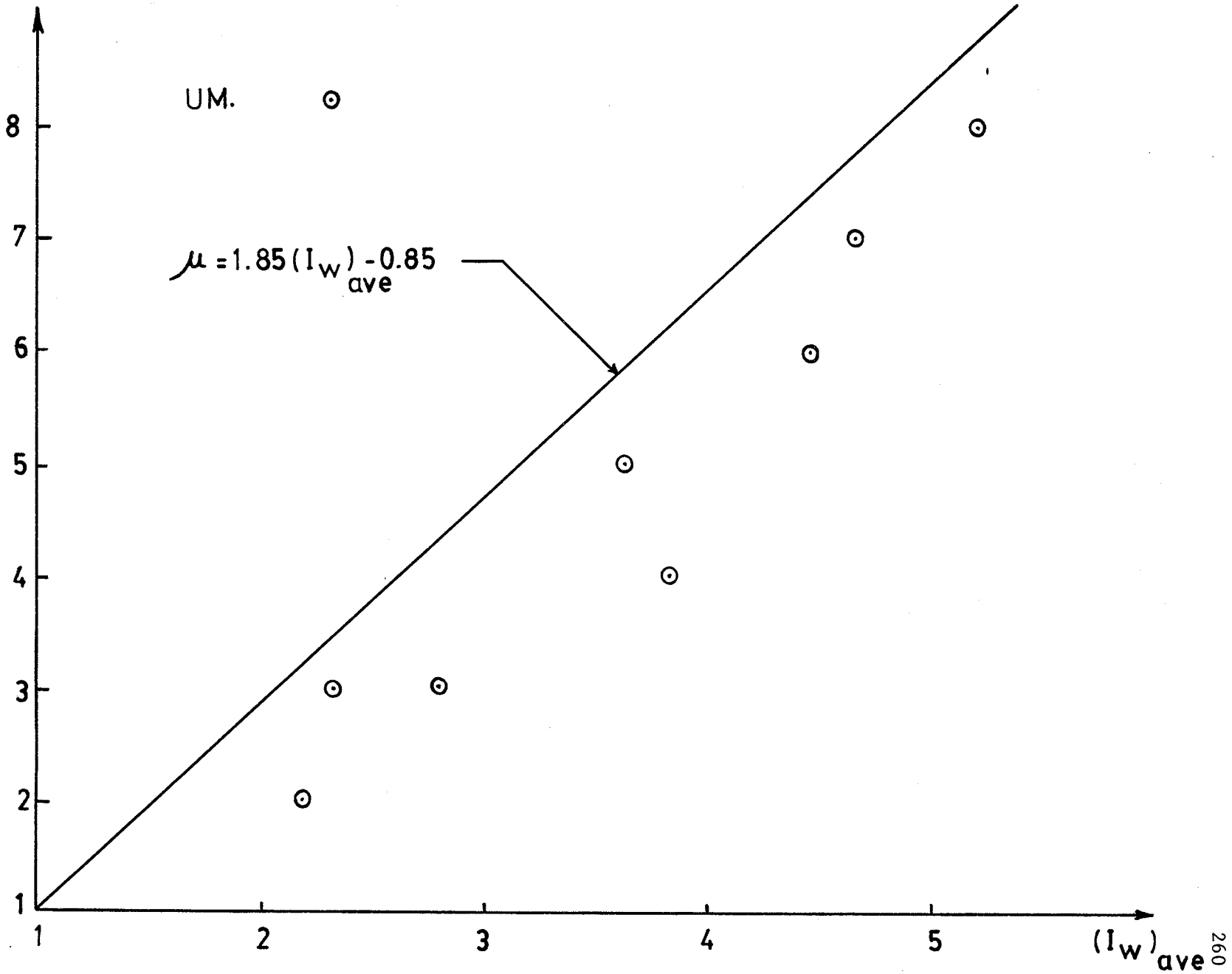

Fig. 5.46 THE COMPARISON BETWEEN THE RESULTS OF ALL THE SPECIMENS TESTED IN SERIES I WITHOUT WEB REINFORCEMENT AND EQ. (5.25) PROPOSED BY ARAKAW, ET AL. [3]

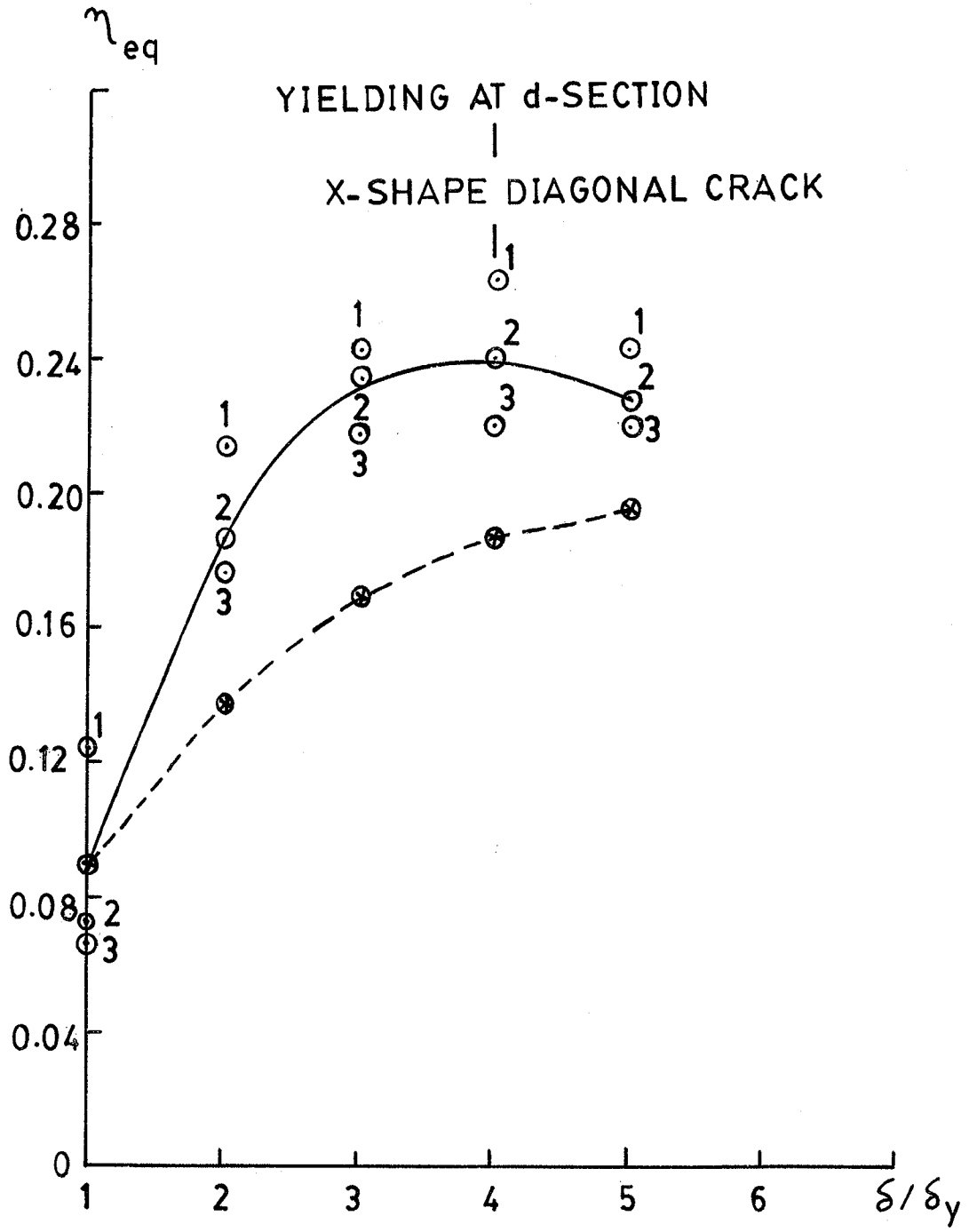

Fig. 5.47 HISTORY OF THE EQUIVALENT DAMPING COEFFICIENT FOR SPECIMEN 1-5

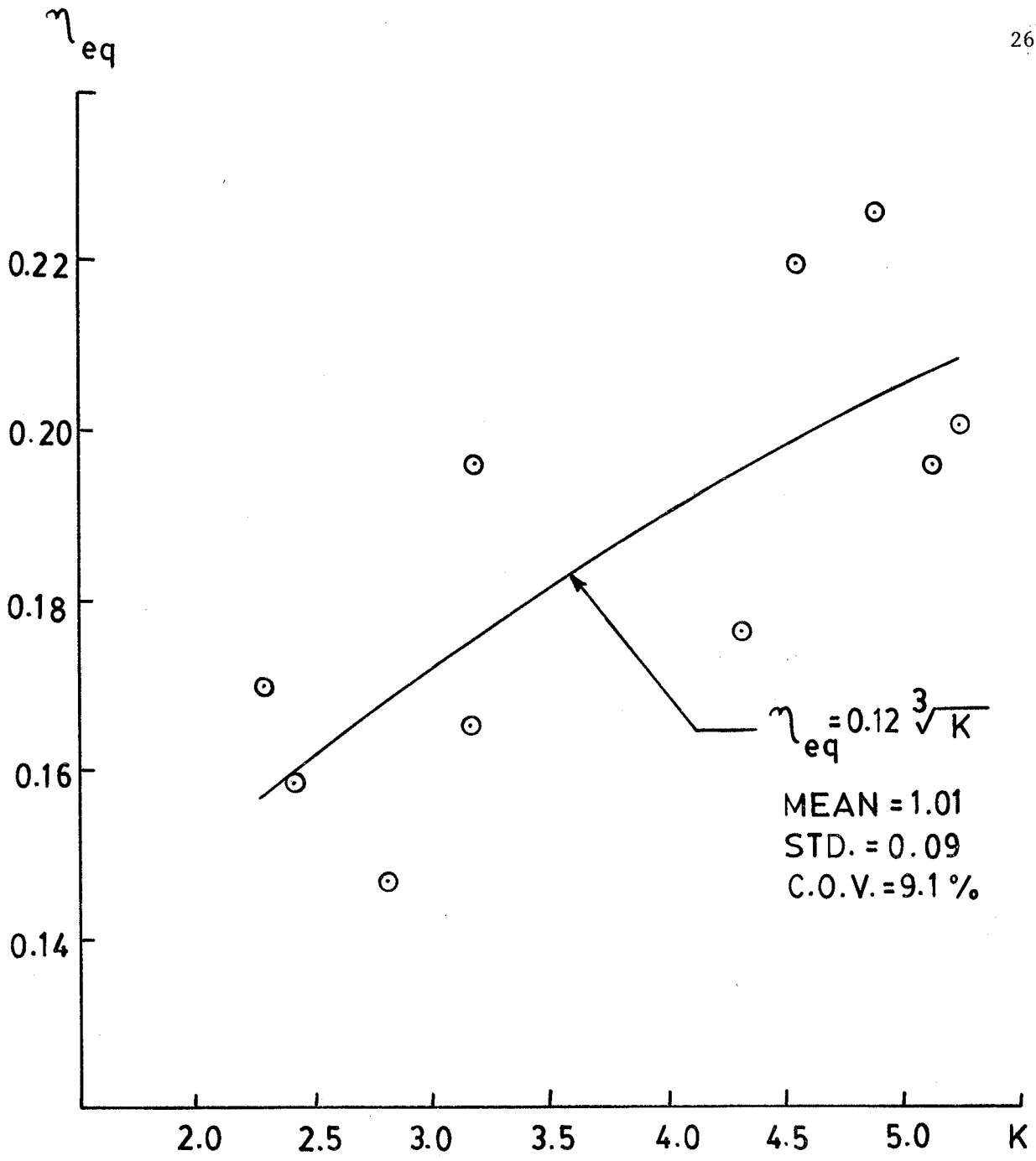

Fig. 5.48 THE RELATIONSHIP BETWEEN THE EQUIVALENT VISCOUS DAMPING COEFFICIENT, η_{eq}, OF ULTIMATE AND THE CHARACTERISTIC FACTOR, K

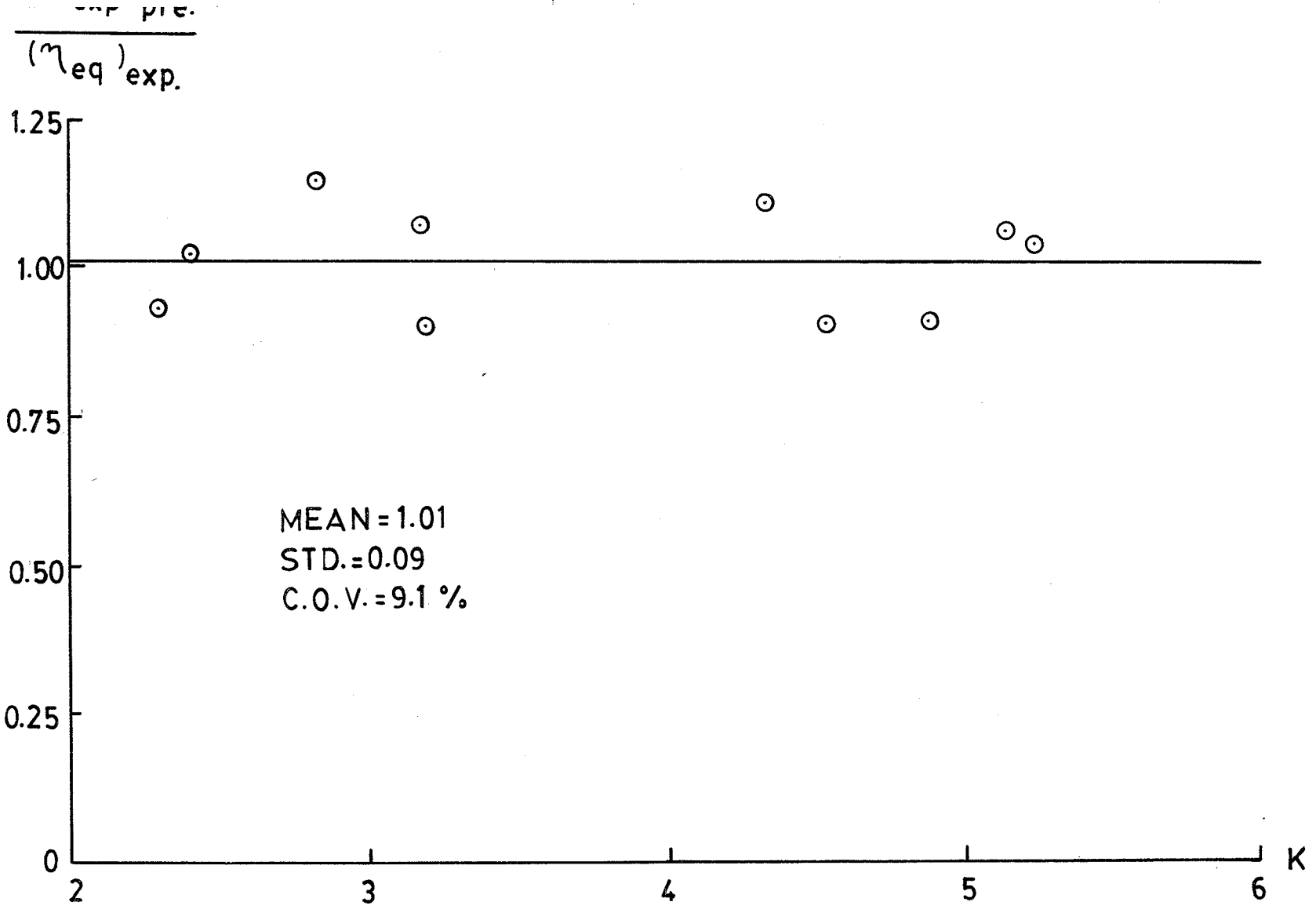

Fig. 5.49 THE VARIATION OF THE RATIO BETWEEN THE PREDICTED AND THE MEASURED VALUES OF THE EQUIVALENT VISCOUS DAMPING COEFFICIENT, $\frac{(\eta_{eq})_{pre}}{(\eta_{eq})_{exp}}$, WITH THE CHARACTERISTIC FACTOR, K

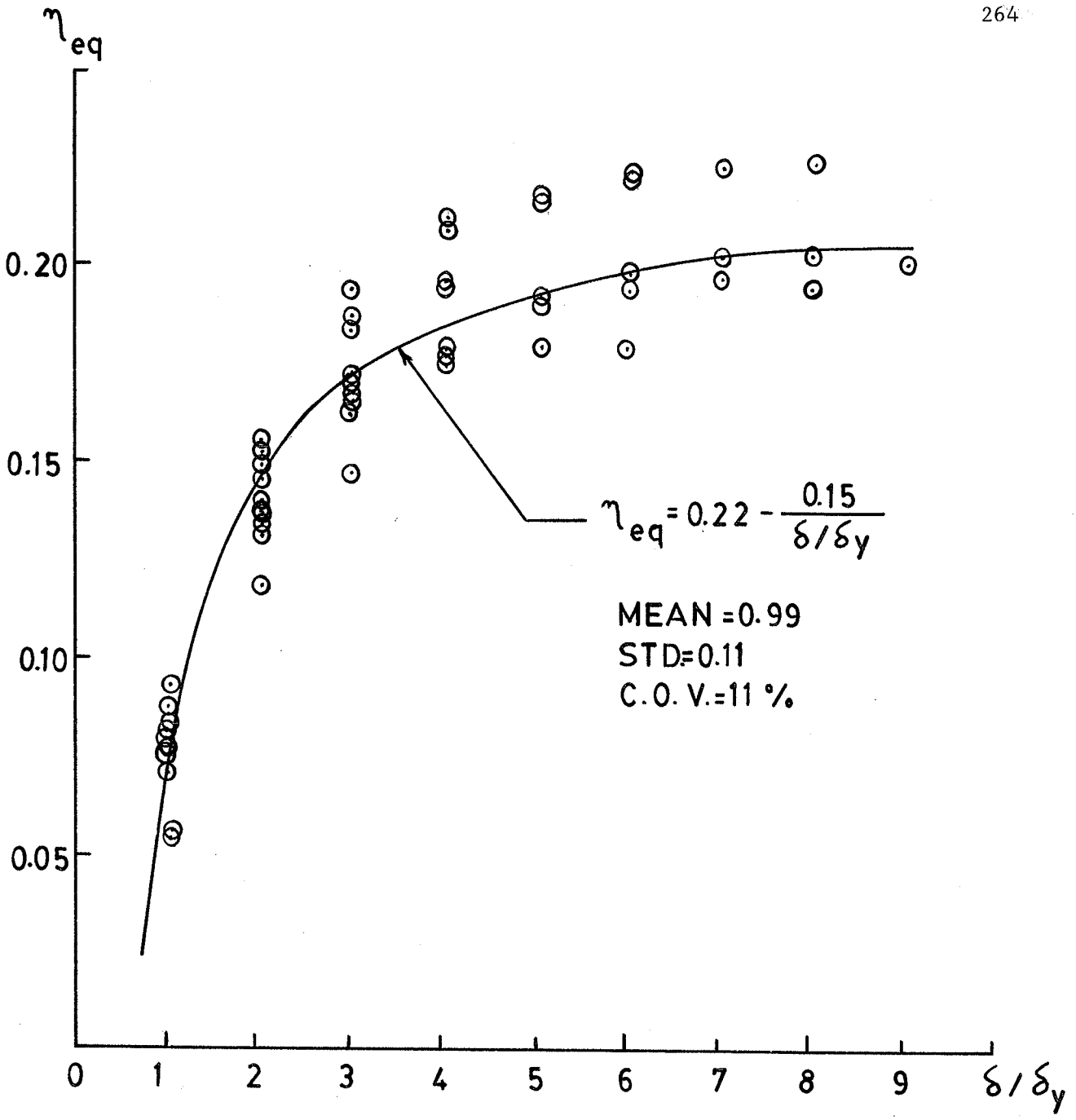

Fig. 5.50 THE VARIATION OF THE EQUIVALENT DAMPING COEFFICIENT, η_{eq}, WITH THE DISPLACEMENT DUCTILITY RATIO, $\frac{\delta}{\delta_y}$

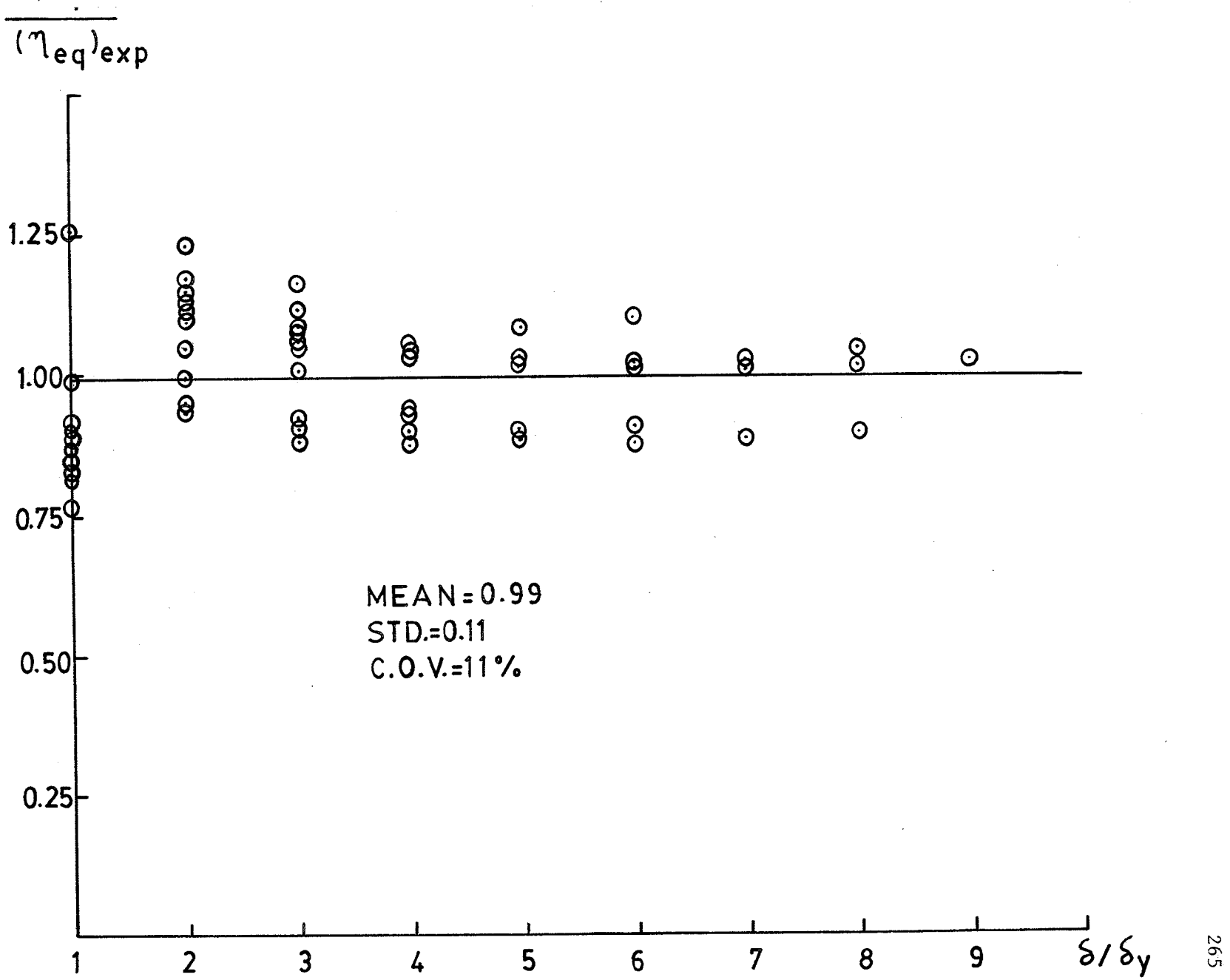

Fig. 5.51 THE VARIATION OF THE RATIO BETWEEN THE PREDICTED AND MEASURED VALUES OF THE EQUIVALENT VISCOUS DAMPING COEFFICIENT, $\frac{(\eta_{eq})_{pre}}{(\eta_{eq})_{exp}}$, WITH THE DISPLACEMENT DUCTILITY RATIO, $\frac{\delta}{\delta_y}$

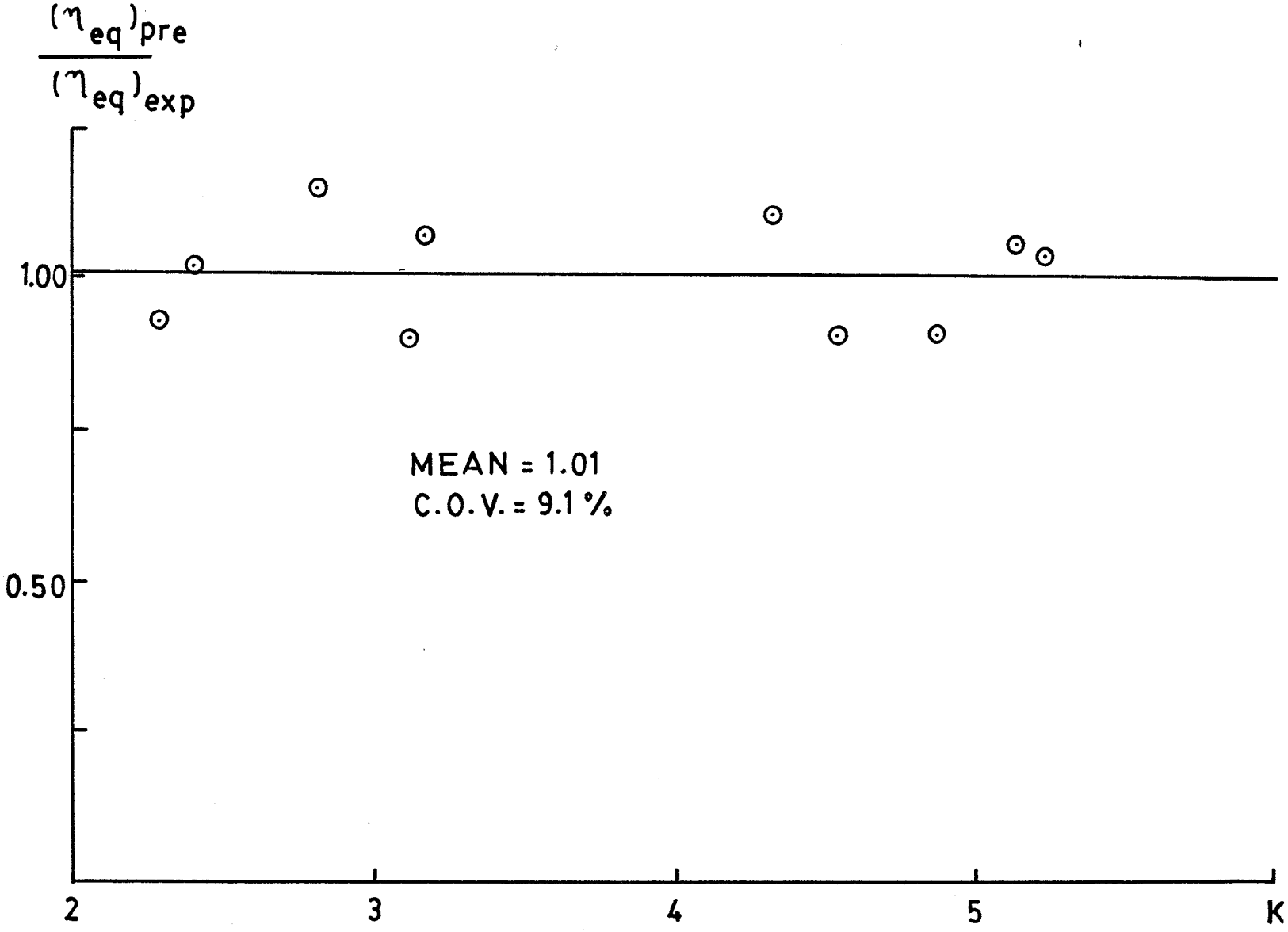

Fig. 5.52 THE VARIATION OF THE RATIO BETWEEN THE PREDICTED AND MEASURED VALUES OF THE EQUIVALENT VISCOUS DAMPING COEFFICIENT, $\frac{(\eta_{eq})_{pre}}{(\eta_{eq})_{exp}}$, AT ULTIMATE WITH THE DISPLACEMENT DUCTILITY RATIO, $\frac{\delta}{\delta_{yy}}$

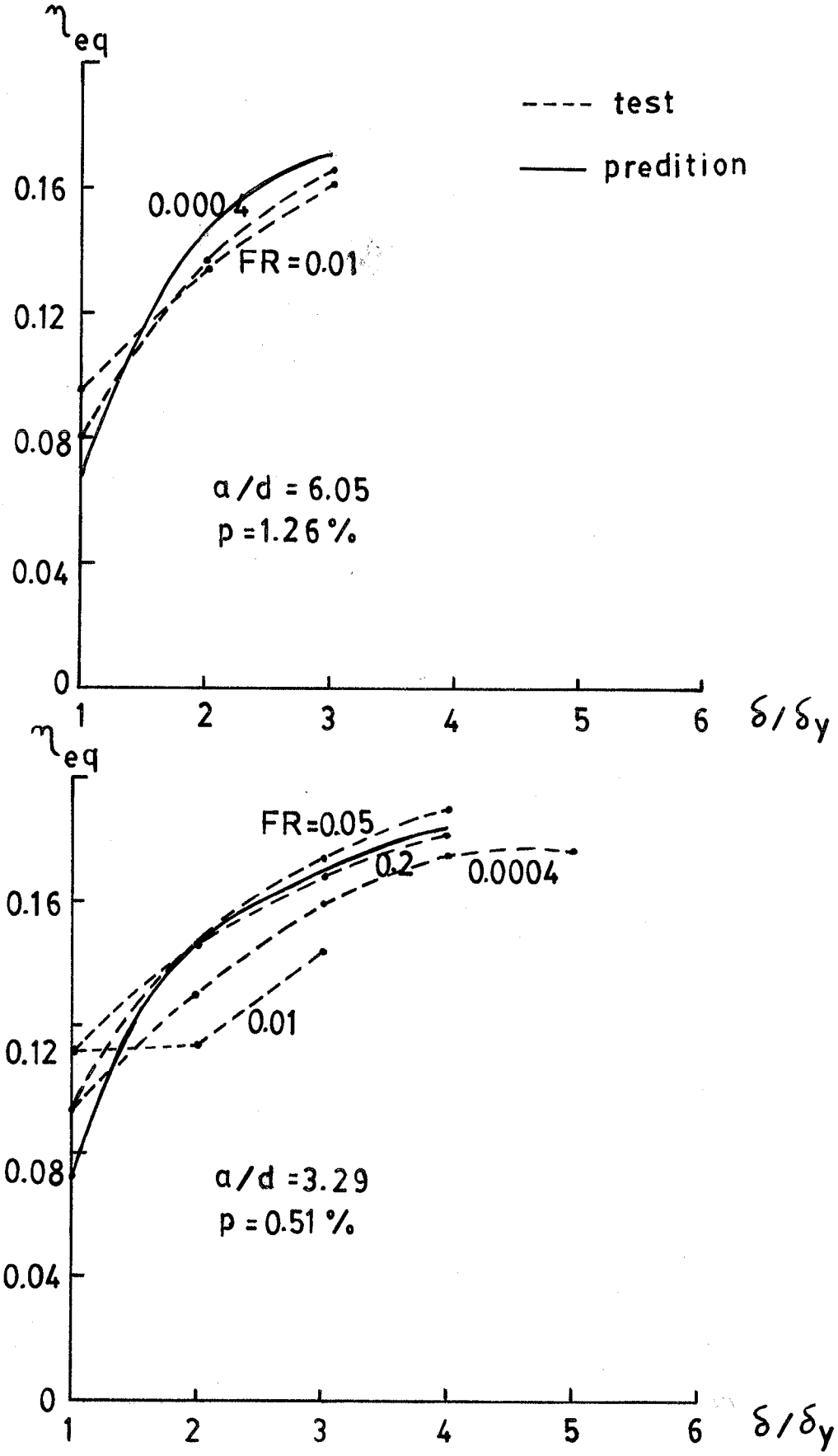

Fig. 5.53 THE COMPARISON OF THE HISTORIES OF THE EQUIVALENT DAMPING COEFFICIENT FOR THE STATIC CASE AND THE LOW-FREQUENCY DYNAMIC CASES

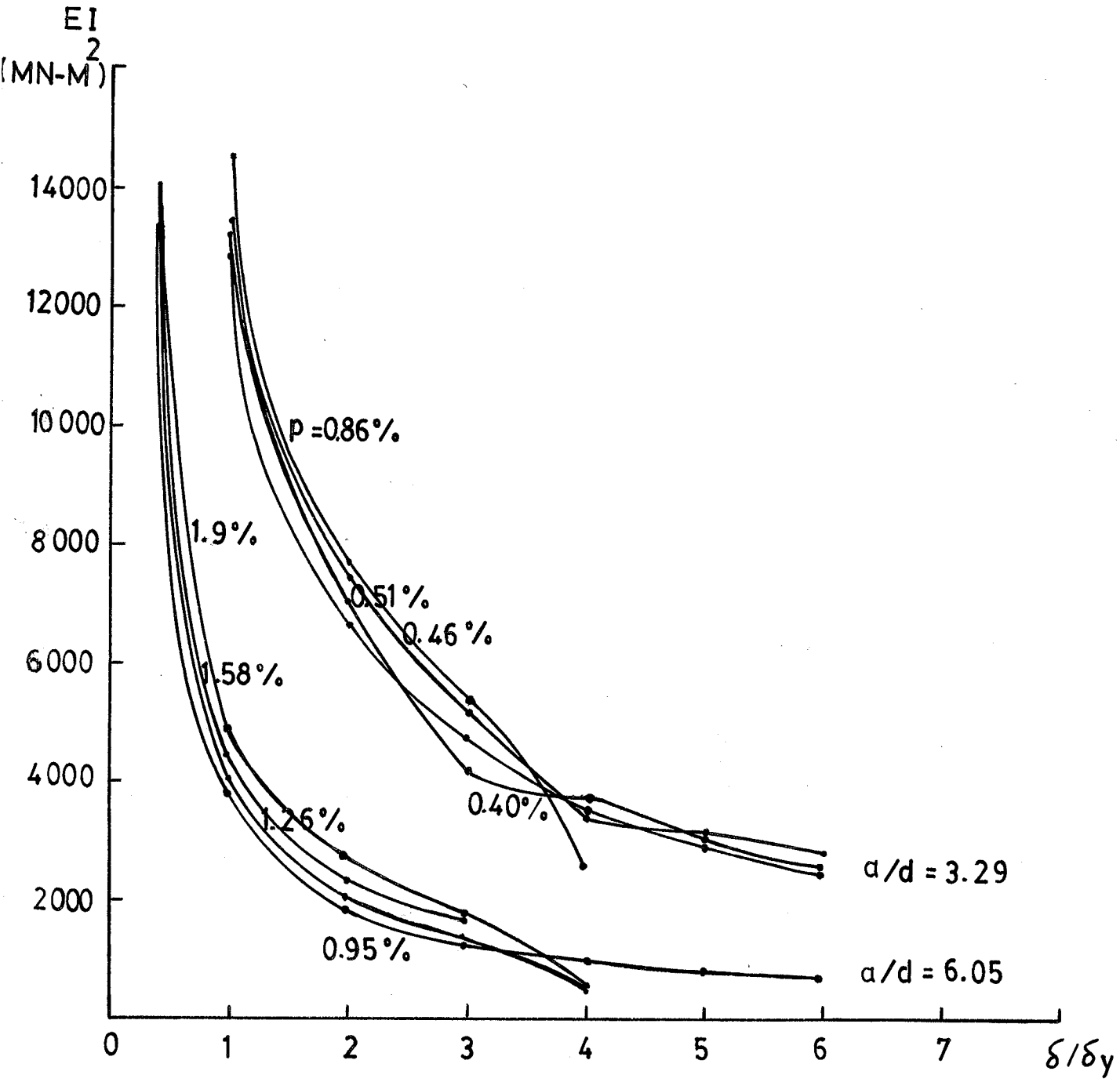

Fig. 5.54 THE VARIATION OF THE STIFFNESS HISTORIES FOR SPECIMENS IN SERIES I WITH a/d OF 3.29 AND 6.05 WITH THE DISPLACEMENT DUCTILITY RATIO, $\frac{\delta}{\delta_y}$

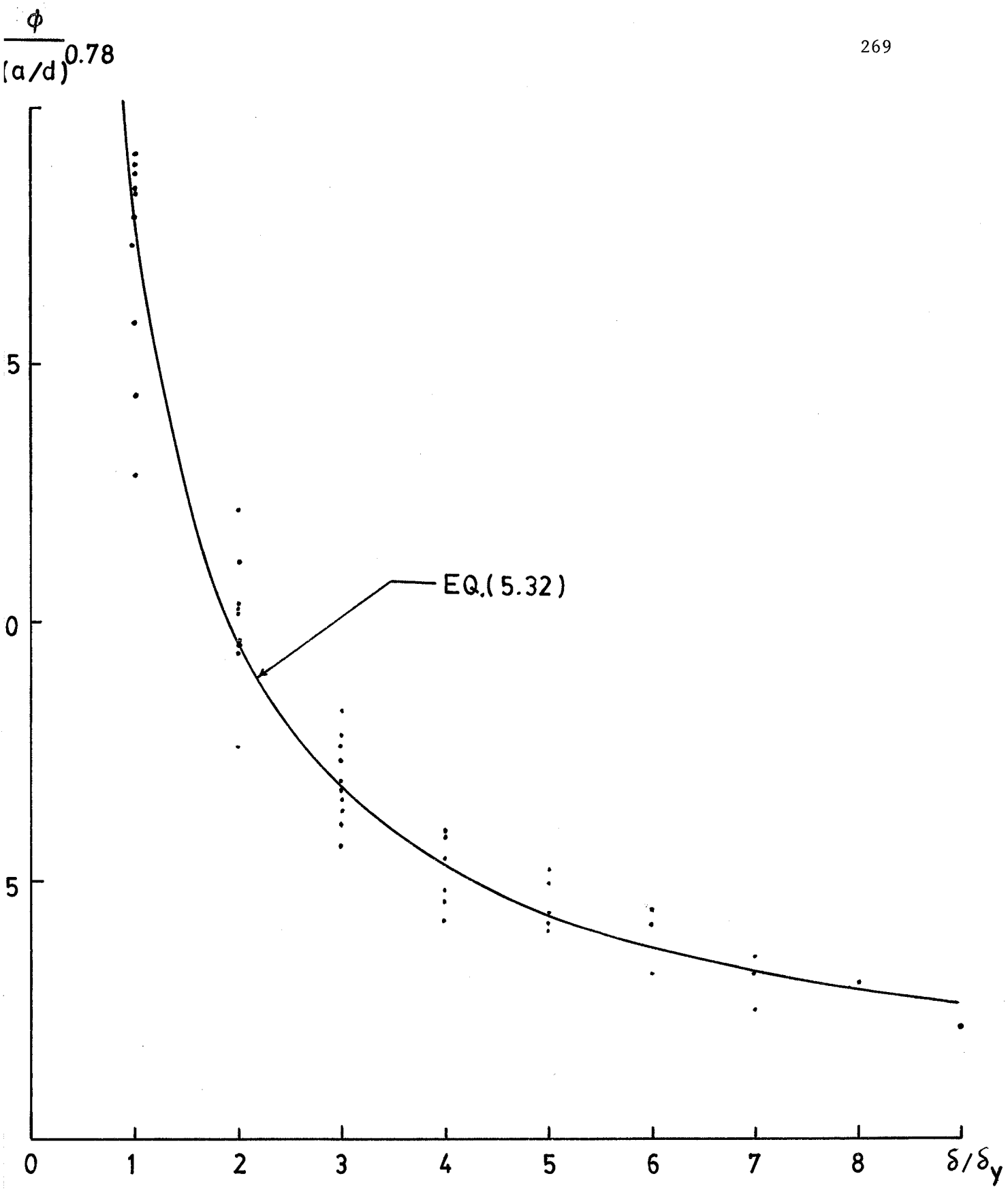

Fig. 5.55 THE RELATIONSHIP BETWEEN THE STIFFNESS RATIO, AND THE DISPLACEMENT DUCTILITY RATIO, $\frac{\delta}{\delta y}$

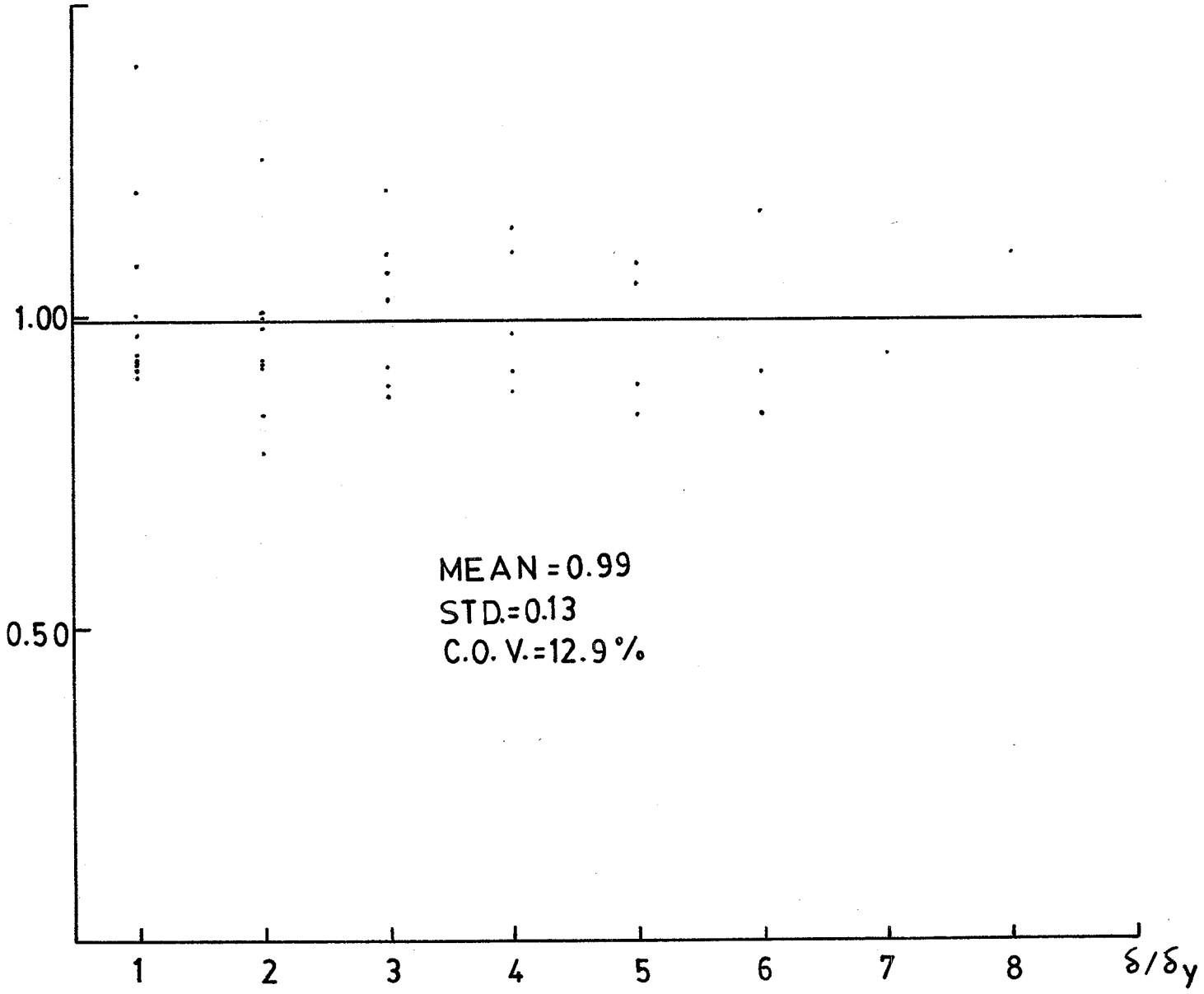

Fig. 5.56 THE VARIATION OF THE RATIO BETWEEN THE PREDICTED AND MEASURED STIFFNESS RATIOS, $\frac{\phi P}{\phi t}$, WITH THE DISPLACEMENT DUCTILITY RATIO, $\frac{\delta}{\delta y}$

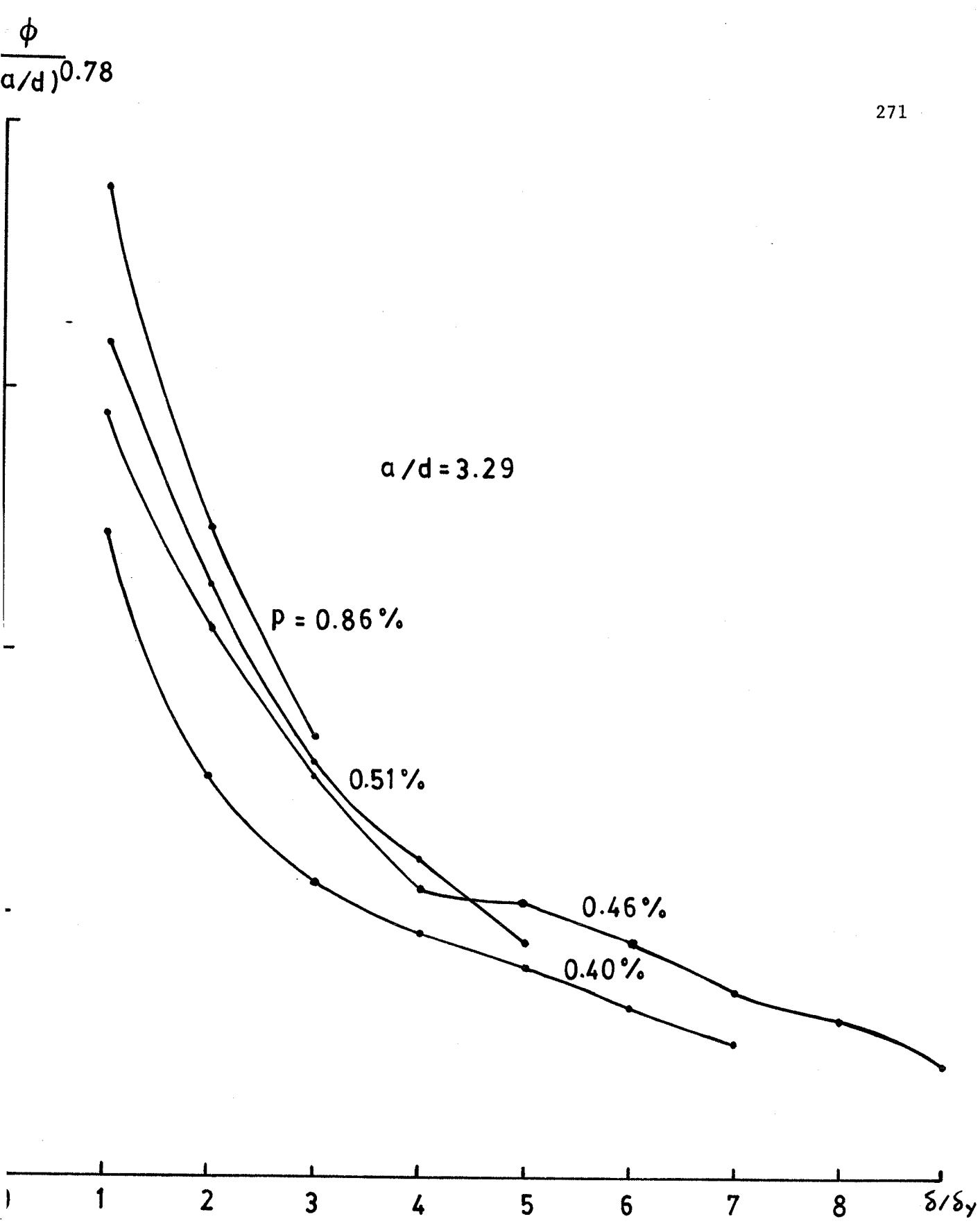

Fig. 5.57 THE VARIATION OF THE MEASURED STIFFNESS RATIO, , WITH THE DISPLACEMENT DUCTILITY RATIO, $\frac{\delta}{\delta_y}$, AND THE LONGITUDINAL REINFORCEMENT PERCENTAGE, p, FOR SPECIMENS TESTED IN SERIES I WITH a/d RATIO OF 3.29

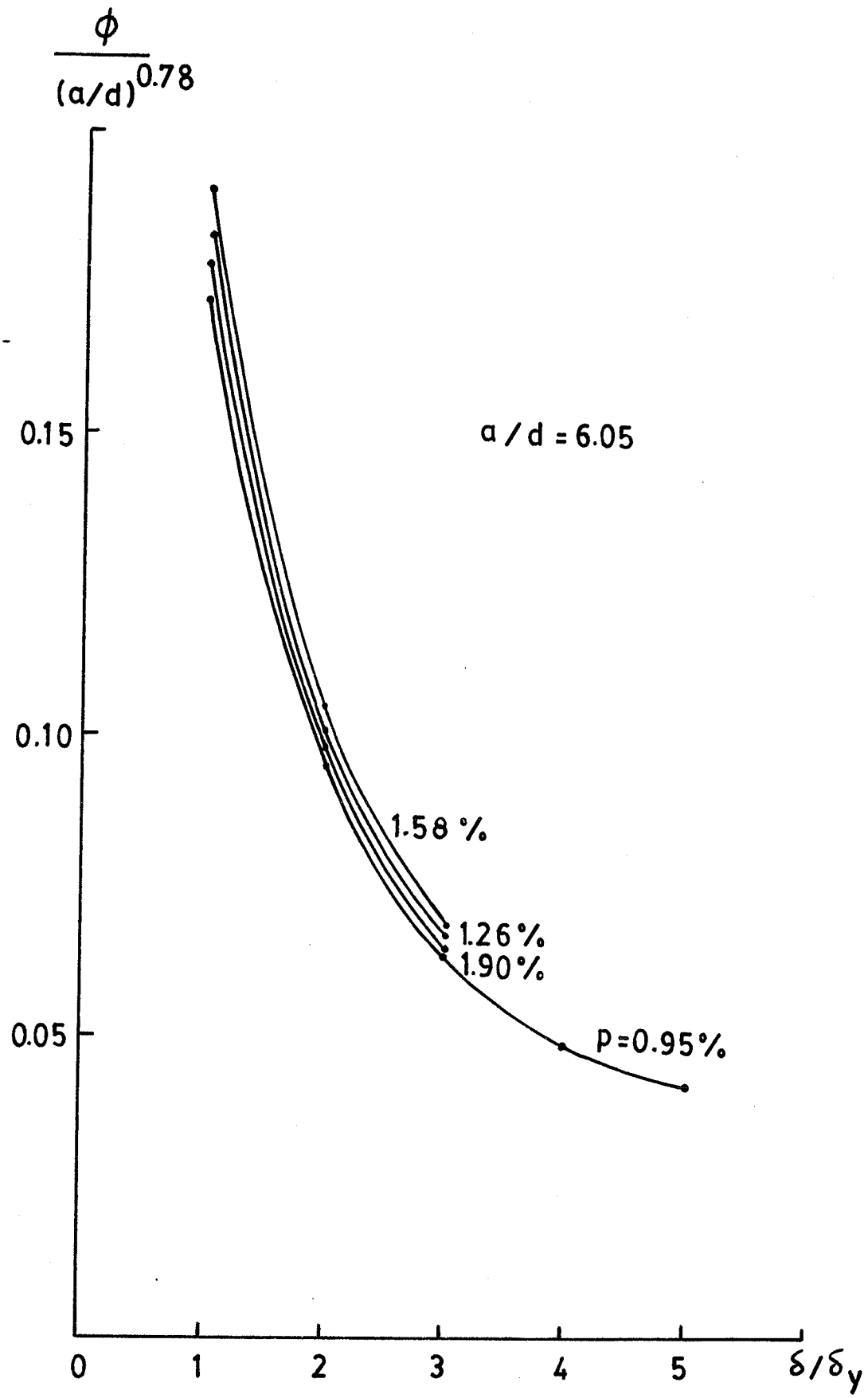

Fig. 5.58 THE VARIATION OF THE MEASURED STIFFNESS RATIO, ϕ, WITH THE DISPLACEMENT DUCTILITY RATIO, $\frac{\delta}{\delta y}$, AND THE LONGITUDINAL REINFORCEMENT PERCENTAGE, p, FOR SPECIMENS TESTED IN SERIES I WITH a/d RATIO OF 6.05

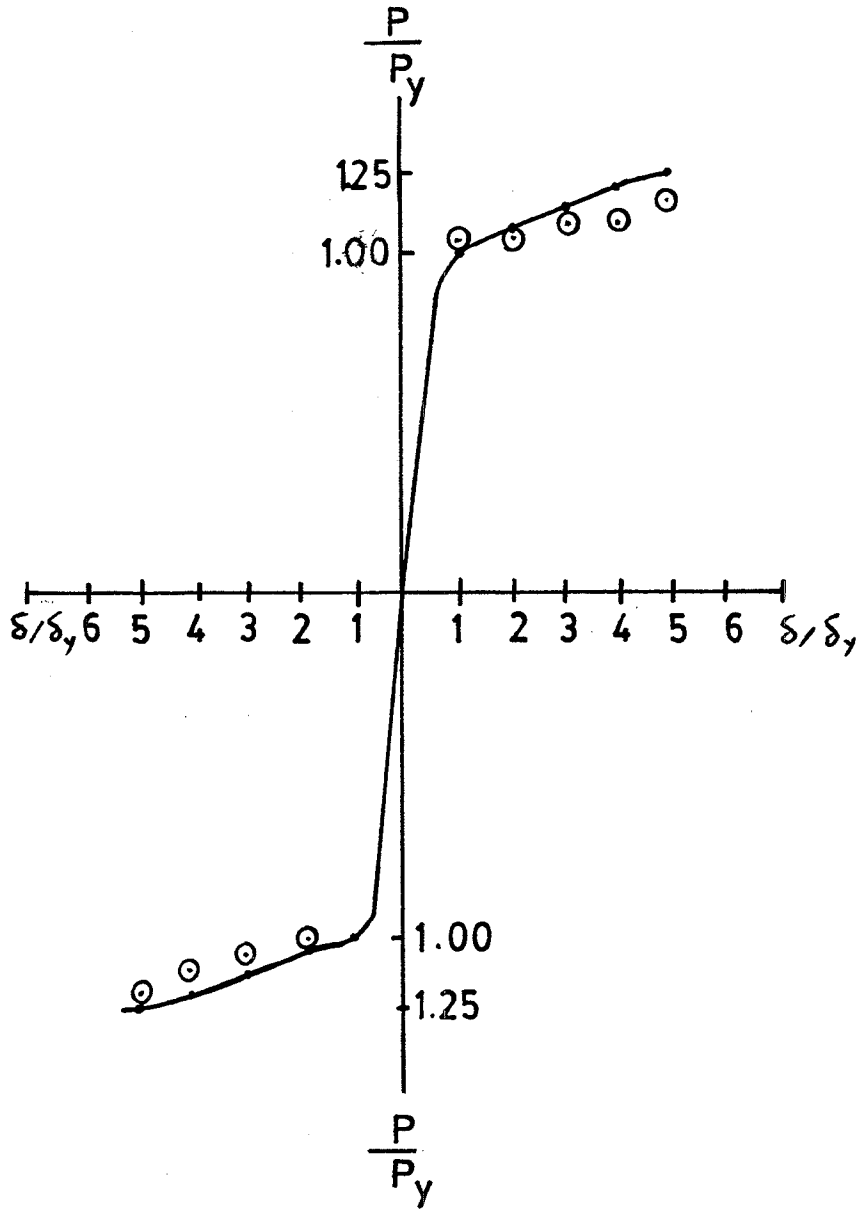

FIG. 5.59 LOAD-DEFLECTION ENVELOPE FOR SPECIMEN 1-5